Diffraction study of mechanical properties and residual stresses resulting from surface processing of polycrystalline materials.

Marianna Marciszko

2013-ENAM-0037

École doctorale n° 432 : Science des Métiers de l'ingénieur

Doctorat ParisTech

T H È S E

pour obtenir le grade de docteur délivré par

l'École Nationale Supérieure d'Arts et Métiers

Spécialité " Mécanique-Matériaux"

présentée et soutenue publiquement par

Marianna MARCISZKO

11 octobre 2013

Diffraction study of mechanical properties and residual stresses resulting from surface processing of polycrystalline materials

Co-Directeur de thèse : **Andrzej BACZMANSKI**
Co-Directeur de la thèse : **Chedly BRAHAM**

Jury

M. Wojciech LUZNY, Professeur, WFIIS, AGH University of Science and Technology, Krakow	Président
M. Manuel FRANCOIS, Professeur, LASMIS, Université de Technologie de Troyes	Rapporteur
Mme Malgorzata KAROLUS, HDR, University of Silesia, Katowice	Rapporteur
M. Olivier CASTELNEAU, HDR, PIMM, Ecole Nationale Supérieure d'Arts et Métiers, Paris	Examinateur
M. Andrzej BACZMANSKI, Professeur, WFIIS, AGH University of Science and Technology, Krakow	Examinateur
M. Chedly BRAHAM, HDR, PIMM, Ecole Nationale Supérieure d'Arts et Métiers, Paris	Examinateur
M. Krzysztof WIERZBANOWSKI, Professeur, WFIIS, AGH, University of Science and Technology, Krakow	Examinateur

T H È S E

Arts et Métiers ParisTech - Centre de Paris
AGH, University of Science and Technology, Krakow

Acknowledgements

Foremost, I would like to thank my supervisors prof. Andrzej Baczmański and prof. Chedly Braham for providing me with the opportunity to complete my PhD thesis.

I especially want to thank prof. Andrzej Baczmański for his valuable guidance, scholarly inputs and consistent encouragement I received throughout the research work. I consider it as a great honor to have an opportunity to do my doctoral programme under his guidance and to learn from his research experience.

Thank you Sir, for all your help and support. I could not have imagined having a better supervisor and mentor.

I would also like to thank Prof. Chedly Braham, for the academic support and the facilities provided to carry out the research work, for all his advices, discussions and suggestions.

The thesis would not have come to a successful completion, without the help I received from dr hab. Mirosław Wróbel and dr Wilfrid Seiler. I would like to express my special appreciation and gratitude to dr hab. Mirosław Wróbel for discussions, sample preparation, ideas and encouragement. I would like to thank dr. Wilfrid Seiler for assistance in carrying out experiments using X-ray diffraction and all valuable advises.

I am most grateful to prof. Krzysztof Wierzbanowski, prof. Olivier Castelnau and dr Sebastian Wroński for their kindness and support during my PhD studies.

I want to thank all members of the Group of Condensed Matter Physics (Faculty of Physics and Applied Computer Sciences, AGH, Kraków, Poland).

Last but not the least I would like to thank my family and my friends for their support and encouragement.

I dedicate this thesis to my Mother, my Aunt, Dorota and my beloved husband. Thank you for your constant support and unconditional love.

TABLE OF CONTENTS

1. Introduction 5

2. Strains and stresses measured by diffraction 9

2.1. Residual stresses and strains 9

2.2. Diffraction 14

2.3. Determination of stresses from diffraction data 23

2.3.1. Determination of first and second order stresses 24

2.3.2. Determination of third order strains and crystallite size 34

3. Methodology of stress measurements using X-rays 39

3.1. Methods with variable penetration depth 46

3.1.1. Standard geometries of stress measurement 46

3.1.2. Universal plot method 49

3.1.3. Scattering vector method 50

3.2. Methods with constant penetration depth 51

3.2.1. Multi-reflection grazing incidence X-ray diffraction 51

3.2.2. Multi-wavelength method 55

3.2.3. Multiple χ - method (pseudo-grazing) 55

3.3. X-ray diffraction elastic constants and stress factors 57

4. Aims of the Thesis 63

5. Tests, limits and experimental developments of the MGIXD method 65

5.1. Corrections of determined peak position 66

5.1.1. Intensity corrections 66

5.1.2. Peak shift due to refractive index smaller than 1 69

5.2. Tests of the experimental configuration 82

5.2.1. Uncertainty of peak position 86

5.2.2. Testing incident beam optics 88

5.2.3. Influence of 2θ - zero position on the measured stress 91

5.2.4. Influence of z- position on the measured stress 92

5.3. Conclusions 94

6. New interpretations of MGIXD measurements and verification of X-ray Stress Factors (XSFs) 95

6.1. Self - consistent fitting of c/a parameter 95

6.2. Peak displacement caused by stacking faults 100

6.3. Verification of XSF used in MGIXD 104

6.3.1. Tensile test 105

6.3.2. Measurements of residual stresses 119

6.4. Conclusions 131

7. MGIXD method using different wavelengths of synchrotron radiation 133

7.1. X-ray measurements 134

7.2. Synchrotron measurements using MGIXD with different wavelengths and incident angles. 149

7.3. Energy dispersion measurement using synchrotron radiation. 177

7.4. Conclusions 181

8. General conclusions 183

List of publications published by author 187

References 189

1. INTRODUCTION

The stress state is a characteristic parameter of the material state, together with the microstructure and the texture, it influences the material properties. That is why the stress analysis is of the great significance in industry and technology and became an important part of materials science. Progress in materials science and technology brought new challenges for stress analysis and various destructive and nondestructive methods have been developed.

Residual stresses are the stresses that remain after the original cause of the stresses (external forces, heat gradient) has been removed [1]. They can result from temperature or deformation gradients which are present in almost every step of material processing. Residual stresses can occur as a consequence of various technological treatments and manufacturing processes, but they can also arise in the component during its service life. Both the magnitude and the spatial distribution of residual stresses play key role in the behaviour of the material subjected either to heat treatment or plastic deformation. The strain - stress analysis is of particular utility for elucidating causes of failure. Depending on the orientation and value of the residual stresses superimposed by the external loads they can be unfavorable or beneficial for the component. The failure of a component in most cases starts in the near-surface area and occurs due to the initiation of plastic deformation or fracture when material is subjected to tensile loads. What is more all kinds of scratches, notches, etc. concentrate additional applied tensile stress near the surface which can cause the initiation of a crack. That is why; usually it is favorable with respect to the component lifetime to create compressive residual stresses in the near-surface area, which can stop fatigue crack propagation [2]. The basic mechanical surface treatments which allow gaining compressive residual stresses are deep-rolling and shot-peening [2, 3].

One of the ways to improve surface properties of the material are coatings. They can be beneficial in example for corrosion or wear resistance and can provide the long-term surface protection. The lifetime of a coating is strongly dependent on the residual stresses profile in the surface area.

Residual stresses influence the strength and fatigue behavior of the materials, but also they affect the chemical, electrical behavior of the thin films and can be very important in stress corrosion process [2, 3]. That is why residual stresses have to be taken into account while designing the structural parts especially in view of the improvement of their properties and increase of their lifetime. Stress analysis is important for constructions of and especially after various mechanical surface treatments. Studying the residual stresses of these materials is challenging issue due to depth gradients of micro and macro residual stresses and the influence of different parameters on their stability or relaxation. Consequently, reliable experimental methods for residual stress determination are of great practical importance. That is why diffraction method, which allow to separate micro- and macro-residual stresses and to study stress distribution in the sample are an indispensible tool. Despite great progress in stress analysis there are many questions which remain unsettled.

In the first part of this thesis (chapters 1-3), the diffraction methods of stress determination are introduced. The principles of lattice distortion, crystallite size and stress analysis based on the diffraction peak profile and measured lattice strain are described in chapter 2. Next, chapter 3 is devoted to a short characterization of different methodologies for stress determination using X-ray radiation (classical and synchrotron). The experimental methods are divided into two groups, i.e.: these in which the penetration depth of X-rays is constant or these for which penetration varies during measurement. On the basis of first three chapters the aims of the thesis are specified in chapter 4.

In chapters 5 – 7 the original results of this work, concerning development and testing of the multireflection grazing incidence X-ray diffraction (MGIXD) method for stress determination are presented. At first, the most important corrections of experimental data and tests of experimental setups are described (chapter 5).

In chapter 6 two important theoretical developments of the MGIXD method are presented. The first one enabling determination of *c/a* parameter and significantly

improving quality of experimental data analysis for hexagonal structure has been proposed and tested. The second one in which density of stacking faults is taken into account is applied. What is more a verification of different types of X-ray stress factors (XSF), which can be applied to interpret the experimental data obtained using MGIXD method, is presented. Finally, examples of stress determination in surface layer for materials having high and low single crystal elastic constants anisotropy are shown.

In chapter 7 the methodology of data interpretation is developed in order to treat data obtained not only for different incident angles but also using simultaneously different wavelengths. It is shown that the new elaborated method is not only ‘multi-reflection’ but also ‘multi-wavelength’. Moreover, application of different wavelengths enables verification of the MGIXD measurements.

Chapter 8 concludes all the results presented in the thesis and formulates practical recommendations for the users of MGIXD method.

2. STRAINS AND STRESSES MEASURED BY DIFFRACTION

The advantage of the diffraction method is its non-destructive character and the possibility of direct measurements of strains in precisely defined volumes of the material. Not only stresses can be determined from the diffraction methods. Intensities of the diffraction lines gives us the information about the crystallographic texture and the broadening of the diffraction lines allows to determine the size of the diffracting domains and the content of the crystalline defects such as dislocations and stacking faults [1]. Presence of stacking faults causes the diffraction peak shift and it depends on the probability of finding fault (Wagner 1966) [4].

The great need of precise stress determination has involved the introduction of new measuring methods and devices into experimental world. This progress would not have been possible without a detailed understanding of the theoretical principles of the used methodologies. In this work the diffraction methods of stress measurement will be used and developed. Because these methods are based on measurements of crystallographic lattice strains, the present chapter is devoted to explain how diffraction sees the strains caused by different kinds of stresses.

2.1. RESIDUAL STRESSES AND STRAINS

All solid materials are deformed when subjected to external loads. The deformation is manifested in displacement of points in the body under load from their initial positions. When a body underlies certain stresses, the strain response depends on the elastic properties of the material. The strain can be of elastic and of plastic kind. As long as the forces acting on the body are below a certain limit, the deformation is reversible and is called elastic deformation. For this kind of deformation, when the load is removed the displacements vanish and the body returns to its unloaded configuration. However, when

the forces acting on the material are higher than the limit, the material undergoes plastic deformation. In this case some permanent deformation remains after the load is removed. If the deformation of the material is homogeneous the deformation of all points of the body is the same. However, when the deformation varies from point to point along any direction in the material volume, the deformation distribution is considered heterogeneous [1, 3].

The relation between the stresses and elastic strain tensor for elastic body is given by generalized Hooke's law [1]:

$$\sigma_{ij} = c_{ijkl}\varepsilon_{kl} \quad \text{or} \quad \varepsilon_{kl} = s_{klij}\sigma_{ij} \tag{2.1}$$

where: σ_{ij} and ε_{kl} are the components of stress and elastic strain tensors, while c_{ijkl} (s_{klij}) are the components of stiffness (compliance) tensor.

The stress component σ_{ij} is defined to be the force per area acting on the i-face in direction j (Fig. 2.1). The σ_{ii} components for which i-forces are normal to the i-faces are called normal components, and the σ_{ij} components (where $i \neq j$) for which j-forces are parallel to the i-faces are called shear components. Stresses form a 9 component symmetrical 2nd rank tensor which can be written in the matrix notation [1]:

$$\sigma_{ij} = \begin{pmatrix} \sigma_{11} & \sigma_{12} & \sigma_{13} \\ \sigma_{21} & \sigma_{22} & \sigma_{23} \\ \sigma_{31} & \sigma_{32} & \sigma_{33} \end{pmatrix} \tag{2.2}$$

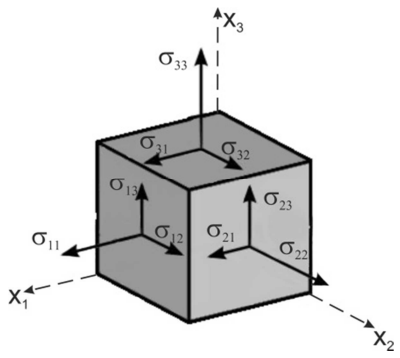

Fig. 2.1. Orientations of stress tensor components with respect to definition surfaces

In static conditions, the principle of conservation of angular momentum implies that $\sigma_{ij} = \sigma_{ji}$ and only 6 of the 9 components are independent [1].

The external forces acting on the material causes the deformation which can be described by the strain tensor:

$$\varepsilon_{ij} = \begin{pmatrix} \varepsilon_{11} & \varepsilon_{12} & \varepsilon_{13} \\ \varepsilon_{21} & \varepsilon_{22} & \varepsilon_{23} \\ \varepsilon_{31} & \varepsilon_{32} & \varepsilon_{33} \end{pmatrix} \tag{2.3}$$

where:

$$\varepsilon_{ii} = \lim_{\delta x_i \to 0} \frac{\delta w_i}{\delta x_i} \qquad and \qquad \varepsilon_{ij} = \frac{1}{2}\left(\lim_{\delta x_i \to 0} \frac{\delta v_j}{\delta x_i} + \lim_{\delta x_j \to 0} \frac{\delta v_i}{\delta x_j} \right) \qquad for \quad i \neq j$$

while i, j = 1, 2, 3 (the displacements for two dimentions are defined in Fig. 2.2).

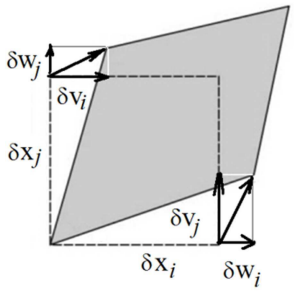

Fig. 2.2. Displacement of the body used in strain definition.

The proportionality constants c_{ijkl} in Eq 2.1 describe physical property of the elastic substance under load. The c_{ijkl} tensor relating strains and stresses (Eq. 2.1) is a 4-th rank tensor of elastic stiffnesses, and it has 81 components. Because of stress and strain symmetries it is possible to reduce the number of the components to 36 independent ones. In the case of monocrystal this number furthermore can be reduced taking into consideration the symmetry of the crystal lattice [1]. For isotropic body the c_{ijkl} constants depend only on two parameters (E – Young's modulus and Poisson's ratio), and they do not change with direction in the body. However, for anisotropic materials these properties vary with orientation and more elastic constants are needed to describe elastic properties [3].

By definition, the residual stresses are self-equilibrated stresses [2]. The residual stresses must fulfill the equilibrium condition in each point of the material [2, 3]:

$$\frac{\partial \sigma_{ij}}{\partial x_i} = 0 \tag{2.4}$$

And surface condition:

$$\vec{\sigma} \cdot \vec{n} = 0 \qquad \text{i.e.} \quad \sigma_{ij} \cdot n_i = 0 \tag{2.5}$$

where $\vec{n}$ is the normal versor to sample surface.

When flat samples are taken into consideration the 'plane stress' condition can be assumed. It is possible due to their small expansion in one direction (e.g., x_3) as compared to the other two directions, so often stresses in the x_3-direction can be assumed to be negligible ($\sigma_{13} = \sigma_{23} = \sigma_{33} = 0$). The stress equilibrium conditions imply that tensile residual stresses in a certain direction within one part of a body are always balanced by matching compressive residual stresses in another part. Thus, the residual stress state of a component can never be expressed by a single residual stress tensor, but only by residual stress distribution. This also implies the presence of residual stress gradients. Strong residual stress gradients are often present in the near-surface area of components, due to surface treatment, or because the residual stress component normal to the surface needs to vanish but stress continuity has to be observed in the bulk material [2].

Due to granular structure of polycrystalline aggregates, the stress and strain states in these materials should be considered and described at different scale. It is possible to distinguish residual stresses of Ist type (macrostresses) and IInd type, IIIrd type (microstresses). The residual stress distribution in a material is the sum of type I, type II, and type III residual stresses:

$$\sigma(\vec{r}) = \sigma^{I} + \sigma^{II} + \sigma^{III}(\vec{r}) \tag{2.6}$$

$$\int_{V_{tot}} \sigma(\vec{r}) dV = 0 \tag{2.7}$$

where: V_{tot} is the total volume of the sample and $\vec{r}$ describes position.

Type I residual stresses σ^I represent the average residual stresses acting within all phases and crystallites in the gauge volume V_{ga}. These stresses are defined by mean value over volume of considered part of the sample (V_{ga}, for example gauge volume in diffraction experiment), i.e.:

$$\sigma^I = \frac{1}{V_{ga}} \int_{V_{ga}} \sigma(\vec{r}) dV \tag{2.8}$$

The gauge must be large enough to represent macroscopic material containing a sufficient number of crystallites and all phases present in the material.

Type I residual stresses (or first order) result from long range strain incompatibilities introduced, e.g., by strain or temperature gradients in a manufacturing process. The distribution and magnitude of type I residual stresses often can be controlled by modifying the process parameters of a production process [2].

Type II residual stresses (σ^{II}, second order) describe the mean deviation from the macroscopic residual stress level σ^I calculated over the volume of individual polycrystalline grain (V_{gr}), i.e.:

$$\sigma^{II} = \frac{1}{V_{gr}} \int_{V_{gr}} [\sigma(\vec{r}) - \sigma^I] dV \tag{2.9}$$

In a multiphase material type II residual stresses (or second order) are taken as the volume weighted average residual stresses σ^α calculated over the volume of crystallites belonging to a phase α (V_α) or as the average residual stresses for those crystallites of the phase α which contribute to the measurement:

$$\sigma^\alpha = \frac{1}{V_\alpha} \int_{V_\alpha} [\sigma(\vec{r}) - \sigma^I] dV \tag{2.10}$$

Type II residual stresses arise for instance due to deformation misfits between neighboring grains and due to temperature or deformation induced misfits between different phases in a multiphase material [2].

Type III residual stresses $\sigma^{III}(\vec{r})$ represent the local deviation of the residual stresses within an individual crystallite from its average residual stresses in the grain

(variation on the atomic scale). Thus, the average type III residual stresses does not result in macroscopic distortions. Type III residual stresses are caused, e.g., by voids, solute atoms, or dislocations in the crystal lattice [1, 2].

The all three types are present, for example, in mechanically machined samples. The microstructure of materials subjected to plastic deformation changes significantly. Due to twinning mechanism and slips occurring on the crystallographic planes plastic deformation of the grain occurs. In general, this irreversible deformation it is slightly different for neighboring grains, which leads to compression or stretching of single grains. This mechanism is a primary source of internal second order stresses. In addition, during the plastic deformation, a large amount of point defects and dislocations is generated. The latter phenomena lead to creation of internal stress fields. Accumulation of dislocation inside the grains produces the third order stresses.

Each type of stresses existing in material influences crystallographic lattice causing its distortion. The first and second order stresses cause mean elastic lattice strains for particular polycrystalline grains. The third order stresses leads to distortion and strain heterogeneity within grains. Both effects can be seen in diffraction experiment as the shift and broadening of the diffraction peaks. To present methods for strain measurement, at first the diffraction phenomenon must be described.

2.2. DIFFRACTION

Diffraction on crystallographic lattice is associated with certain phase relationships between waves scattered in all directions by the atoms. The phases of the scattered rays are relatively shifted in the most of directions. However, in some particular directions the reflected waves exhibit the same phase and due to constructive interference they are strengthened, creating a diffracted beam.

In order to describe the diffraction phenomenon using kinematic theory, crystal can be treated as a periodic arrangement of atomic planes, which act like a mirror for the incident radiation [5]. The incident beam strikes the crystallographic planes at an angle θ and it is reflected from them also at an angle θ (see Fig. 2.3b). Therefore, the total angle of deflection of the diffracted beam is equal 2θ. If the distance between adjacent planes is

equal to *'d'* the difference of the paths for the rays reflected from these planes is equal to *2d sinθ* (Fig. 2.3a). Constructive interference will occur when the waves have the same phase, so when the path difference between them will be equal to an integer multiples (*m*) of the wavelength (λ), so when the equation:

$$m\lambda = 2d\sin\theta \tag{2.11}$$

is fulfilled. The above equation is called Bragg's law [1] and it is a basic geometrical diffraction condition.

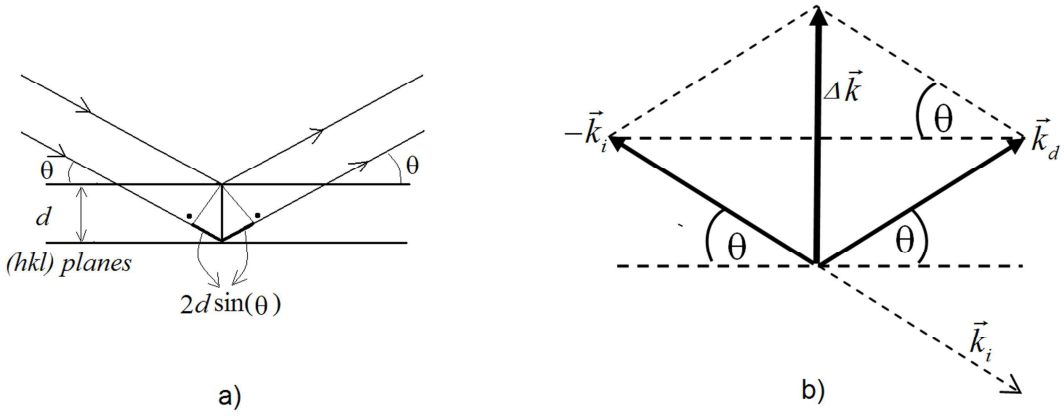

Fig. 2.3. Difference between paths of the beams reflected from neighboring crystallographic planes (a) and construction of the scattering vector (b), where $\vec{k}_i$ and $\vec{k}_d$ denotes wave vectors for the incident and diffracted beams, respectively.

Bragg's equation can be expressed also in an equivalent way. Let us denote by $\vec{k}_i$ a wave vector of the incident beam and by $\vec{k}_d$ a wave vector of diffracted beam. Diffraction vector can be defined as: $\Delta\vec{k} = \vec{k}_d - \vec{k}_i$ and it is perpendicular to the plane of reflection (Fig2.3 b). The length of the diffraction vector is given by:

$$\left|\Delta\vec{k}\right| = \left|\vec{k}_d - \vec{k}_i\right| = \frac{4\pi\sin\theta}{\lambda} \tag{2.12}$$

Considering Bragg's law, the above equation can be rewritten as:

$$\left|\Delta\vec{k}\right| = \frac{2\pi}{d_{hkl}} \tag{2.13}$$

where: *hkl* are the indices of reflection which for the first order reflection (i.e., for the lowest *hkl* and *m*=1 in Bragg' law) are equal to Miller indices of the of the reflecting planes, while for the *m-th* order of reflections $d_{hkl}=d/m$ where *d* is the interplanar space.

Because $d_{hkl} = \frac{2\pi}{\left|\vec{G}_{hkl}\right|}$ (where $\vec{G}_{hkl}$ is the reciprocal lattice vector), so the general condition for the occurrence of diffraction (when both vectors $\Delta\vec{k}$ and $\vec{G}_{hkl}$ have the same orientations, i.e., they are perpendicular to the reflecting plane) can be written as:

$$\Delta\vec{k} = \vec{G}_{hkl} \tag{2.14}$$

Expressing the $\vec{G}_{hkl}$ vector by primitive translation vectors of the reciprocal lattice $\vec{G}_{hkl} = h\vec{b}_1 + k\vec{b}_2 + l\vec{b}_3$ and multiplying both sides of Eq. (2.14) by primitive translation vectors $\vec{a}_1, \vec{a}_2, \vec{a}_3$ (where the latter basis vectors are defined for the real lattice) the Laue equations can be obtained [7]:

$$\vec{a}_1\Delta\vec{k} = 2\pi h \qquad \vec{a}_2\Delta\vec{k} = 2\pi k \qquad \text{and} \qquad \vec{a}_3\Delta\vec{k} = 2\pi l \tag{2.15}$$

The Miller indices of crystallographic plane in the real space (*h*,*k*,*l*) correspond to the coordinates of lattice point in the reciprocal space.

Bragg or Laue equations give the geometrical condition of the diffraction; however, they do not contain the information about the intensity of the diffracted beam. The intensity will depend on the kind of the diffracting atoms and their arrangement in the unit cell. In the case of X-ray diffraction electrons are responsible for coherent scattering of the electro-magnetic wave. During the diffraction each of the electrons in the atom scatters elastically part of the incident beam. In order to describe the ability of diffraction for each atom the atomic factor *f* depending on the *Z* (atomic number) of the element is used [8]. In the direction of diffraction, specified by the Bragg condition, the ability of diffraction by the unit cell is described using the structural factor F_{hkl}. The complex value of this factor is

calculated as a sum of the amplitudes of the coherently diffracted rays from the atoms in the unit cell (assuming unit amplitude of the incident beam) [8]. For unit cell having *M* atoms at positions described with the coordinates (x_n, y_n, z_n), the structural factor can be expressed as [6]:

$$F_{hkl} = \sum_{n=1}^{M} f_n e^{2\pi i(hx_n + ky_n + lz_n)} \tag{2.16}$$

where: *hkl* are the indices of considered reflection, f_n is the atomic factor of the *n-th* atom and *M* denotes number of atoms in unit cell

The intensity of the beam diffracted from all the atoms in the unit cell in the direction described with the Braggs law is proportional to the square of the amplitude of the resultant beam, and consequently, it is proportional to $| F_{hkl} |^2$. The above equation allows calculating the intensity of each *hkl* reflection when the atomic positions are known. Analyzing intensities of the beams diffracted on different plains (i.e., knowing the values of $| F_{hkl} |^2$ from experiment) the arrangement of the atoms in unit cell can be refined. In this aim the numerical Rietveld method can be used [9].

In description of diffraction experiment it should be remembered that the crystals are not ideal and the incident beam is not strictly parallel and monochromatic. The actual X-ray beam contains rays divergent and convergent as well as parallel, so the intensity of diffracted beam will be registered not only for the Bragg angle but also in same small range around this angle. This effect is known as the instrumental broadening of registered diffraction peak. Also, the microstructure of the material significantly influences the profile of the measured peak, i.e. the broadening of the peak is affected by the size of diffracting crystal and its real internal structure containing defects of the lattice.

To explain the role of finite crystal size the ideal crystallite having *N* points (equal to number of unit cells) can be considered. The positions of *n*-th point of the real lattice can be defined by the vector:

$$\vec{\rho}_n = m_1\vec{a}_1 + m_2\vec{a}_2 + m_3\vec{a}_3 \tag{2.17}$$

where: $\vec{a}_1, \vec{a}_2, \vec{a}_3$ are the basis translation vectors and m_1, m_2 , m_3 are the integer or zero numbers.

Next, the diffraction vector $\Delta\vec{k}$ can be expressed as the linear combination of the basis vectors in reciprocal space:

$$\Delta\vec{k} = h_1\vec{b}_1 + h_2\vec{b}_2 + h_3\vec{b}_3 \tag{2.18}$$

where h_1, h_2, h_3 are the $\Delta\vec{k}$ vector coordinates given by real values. These values are chosen close to the point of reciprocal lattice corresponding to the considered reflection *hkl*, i.e. $h_1=h$, $h_2=k$, $h_3=l$ when Eq. 2.14 is fulfilled and $\Delta\vec{k}$ determines the position of the reciprocal lattice point.

If the point of the observation (detector counting intensity of diffracted beam) is far away from the crystal the phase difference of the waves from two scattering centers is equal: $\Delta\phi_n = \Delta\vec{k}\vec{\rho}_n$. Assuming amplitude of incident beam equal to unity, the amplitude A_n of the wave diffracted on a lattice point (representing unit cell) in the position $\vec{\rho}$ can be expressed as :

$$A_n = A_e F_{hkl} \exp[-i\Delta\phi_n] = A_e F_{hkl} \exp[-i\Delta\vec{k}\vec{\rho}_n] \tag{2.19}$$

where F_{hkl} stands for an amplitude of the beam diffracted on the unit cell which is equal to the structural factor defined by Eq. 2.16 and A_e is an amplitude of wave scattered by one electron. In order to gain the amplitude from all scattering centers it is necessary to sum up over all lattice points [:

$$A_{total} = A_e F_{hkl} \sum_n^N \exp\left[-i\vec{\rho}_n\Delta\vec{k}\right] \tag{2.20}$$

Following the calculations given by for example Kittel [10], the dependence of diffracted intensity on the length and direction of scattering vector ($\Delta\vec{k} = h_1\vec{b}_1 + h_2\vec{b}_2 + h_3\vec{b}_3$) can be derived:

$$I(h_1,h_2,h_3) = \left|A_{total}\right|^2 = \left|A_e F_{hkl}\right|^2 \frac{\sin^2\pi N_1 h_1}{\sin^2\pi h_1}\frac{\sin^2\pi N_2 h_2}{\sin^2\pi h_2}\frac{\sin^2\pi N_3 h_3}{\sin^2\pi h_3} \tag{2.21}$$

where: N_1, N_2 and N_3 are the numbers of real lattice point in directions of $\vec{a}_1, \vec{a}_2, \vec{a}_3$ and $N= N_1 N_2 N_3$.

Integrating the above equation around point of reciprocal lattice (e.g. $\Delta\vec{k} = \vec{G}_{hkl} = h\vec{b}_1 + k\vec{b}_2 + l\vec{b}_3$ the total diffracted intensity proportional to the number of unit cells (*N*) can be calculated, i.e.:

$$I_{tot}(hkl) = \int_{h-1/2}^{h+1/2}\int_{k-1/2}^{k+1/2}\int_{l-1/2}^{l+1/2} I(h_1,h_2,h_3)dh_1dh_2dh_3 = \left|A_N\right|^2 = \left|A_eF_{hkl}\right|^2 N_1N_2N_3 = \left|A_eF_{hkl}\right|^2 N \quad (2.22)$$

To see the intensity distribution around given point in reciprocal lattice the particular reflection *00l* can be considered. If we follow the intensity variation only in the direction of $\vec{b}_3$ vector we can put $h_1 = 0$ and $h_2 = 0$ in Eq.2.21, i.e.:

$$I(h_3) = \left|A_eF_{hkl}\right|^2 N_1^{\,2}N_2^{\,2}\frac{\sin^2\pi N_3h_3}{\sin^2\pi h_3} \quad (2.23)$$

Using Eqs. 2.12, 2.13 and 2.18 the value of h_3 can be related with 2θ angle:

$$h_3 = \frac{2d_{00l}}{\lambda}\sin\theta \quad (2.24)$$

In Fig.2.4 the one dimensional function $\frac{\sin^2\pi N_3h_3}{\sin^2\pi h_3}$ vs. h_3 for *l*=1 is shown. Also, this function vs. 2θ is presented assuming $d_{00l} = \lambda$=1Å. The calculation were performed for N_3 =500 and N_3=1000 atoms (or crystallographic planes) in the direction along the scattering vector. This situation corresponds to the crystallite size of 50 nm and 100 nm along the direction of scattering vector.

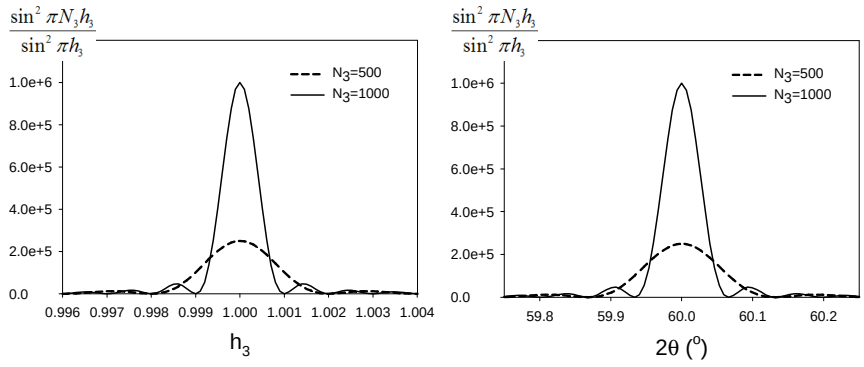

Fig. 2.4. Function $\frac{\sin^2\pi N_3h_3}{\sin^2\pi h_3}$ vs. h_3 (for *l*=1) and the same function vs. 2θ (assuming $d_{00l} = \lambda$=1A) are shown.

The following conclusion can be drawn from the above equations illustrated in Fig. 2.4:

- intensity at the point of reciprocal lattice (or for $2\theta_0$ angle which fulfill strictly Bragg low) is proportional to the square from numbers of reflecting planes being perpendicular to the scattering vector ($\lim_{h_3 \to 0} \frac{\sin^2 \pi N_3 h_3}{\sin^2 \pi h_3} = N_3^2$),

- broadening of intensity given by width of the peak is proportional to $1/N_3$, i.e. number of reflecting planes in the direction of scattering vector $\Delta\vec{k}$,

- total (integrated) intensity is proportional to N_3,

- broadening of the intensity around the point of reciprocal does not depend on the reflection order (the same profile of peak be obtained for different *l*, because the period of function defined in Eq. 2.23 with respect to h_3 is equal to1).

The above conclusions can be generalized for any *hkl* reflection.

More general derivation of the intensity distribution in the diffraction peak for crystallites with lattice distortion was given by Warren and Averbach [11]. In this case also the partial waves diffracted on scattering centres are considered but the calculations were performed for a powder sample and contributions of diffracted intensity from grains having different orientations was integrated. Moreover, the scattering centres are shifted from the points of nets. The result of calculations is given as the Fourier series (presented also for the *00l* reflection):

$$I(h_3) = \left|A_e F_{hkl}\right|^2 N \sum_n [a_n \sin(2\pi n h_3) + a'_n \cos(2\pi n h_3)] \qquad (2.25)$$

which can be also written with respect to 2θ angle substituting h_3 by relation 2.24. The coefficients of expansion are [11]:

$$a_n = a_n^B \left(1 - 2\pi^2 n^2 l^2 < \varepsilon^2 >\right) \quad (2.26\text{ a}) \qquad \text{and} \qquad a'_n = -a_n^B \left(2\pi^2 n^2 l^2 < \varepsilon >\right) \quad (2.26\text{ b})$$

where $< \varepsilon^2 >$ and $< \varepsilon >$ are the square mean and mean values of the lattice microstrains in the direction of scattering vector, inside a crystallite (those which are caused by defects

and associated with the third order stresses), and a_n^B is the factor depending on the crystallite size (also in the direction of scattering vector).

The a'_n coefficients represent nonsymmetrical distribution of strains within the crystallite. However, if we consider only effect of the third order stresses and the distribution of defects is random (or in more general case if the probability of ε and $-\varepsilon$ occurrence is equal) the a'_n coefficients vanish.

It is clear that, the a_n coefficients bring an important information about size of crystallite (a_n^B) and square mean strain of its lattice strains caused by the third order stresses. The a_n factors do not depend on the order of reflection (*00l*), and it can be shown [11] that:

$$\left.\frac{da_n^B}{dn}\right|_{n\to 0} = -\frac{1}{N_3} \tag{2.27}$$

where N_3 is an average number of reflecting plains along scattering vector.

On the other hand the function of a_n vs. $<\varepsilon^2>$ depend the order of reflection (*00l*). Therefore the analysis of size and strain by Warren-Averbach is based on the expansion of diffraction peak profile into a Fourier series and then calculation of $<\varepsilon^2>$ and N_3 (or rather $D = N_3 a_3$, i.e., size of crystallite) in direction of scattering vector from A_n coefficients. In this method two diffraction peak must be measured for two orders of reflections (usually the first and second order for example *111* and *222*).

Next step in analisis of peakprofile, after single crystal and powder sample is it the case of polycrystalline aggregate which is built from crystallites having different orientations (like in powder but often some orientations are preferred in the case of crystallographical texture). Moreover, in real structure of polycrystalline material mosaic microstructures of grains can have a significant impact on diffraction (especially after large plastic deformation). Such a crystal do not have atoms arranged in a perfectly regular network, but a large number of small blocks, each of which is slightly disoriented with respect to its neighbors [6]. Diffraction peak results from the coherent scattering of the incident beam on the so-called domains which in fact represent crystallites considered by

Warren and Averbach [11, 12]. The size of such domains is of tents or hundreds nanometres, so their effect on the peak broadening is comparable with that shown in Fig. 2.4. In the case of polycrystalline material usually the same methods of profile analysis are used as for powder sample, however, in this case such properties as crystallographic texture, complex microstructure and moreover presence of residual stresses should be considered in interpretation of the obtained results.

The polycrystalline grains are not free as in the powder sample but they interact elastically with their neighbours. Therefore, the first and second order stresses causing mean elastic deformation of the lattice which can be observed as a shift of the diffraction peak position. Using diffraction methods the mean lattice strain can be determined as the relative change of interplanar spacing and can be calculated from the relative shift of the peak:

$$< \varepsilon >_{\{hkl\}} = \frac{< d >_{\{hkl\}} - d^0_{\{hkl\}}}{d^0_{\{hkl\}}} \tag{2.28}$$

or using Bragg's relation (Eq. 2.11):

$$< \varepsilon >_{\{hkl\}} = -\cot\theta_0 \left(< \theta >_{\{hkl\}} - \theta_0 \right) \tag{2.29}$$

where $< d >_{\{hkl\}}$ is the mean interplanar spacing for *{hkl}* crystallographic planes determined in the studied sample, $d^0_{\{hkl\}}$ is interplanar spacing for these planes but in stress free crystallite, $2(< \theta >_{\{hkl\}} - \theta_0)$ is a shift of diffraction peak with respect to the position in stress free material ($2\theta_0$).

It should be underlined that the $<...>_{\{hkl\}}$ is the volume of the crystallites (in fact domains in polycrystalline grains) which take part in diffraction, i.e., they have such lattice orientations for which the scattering vector $\Delta\vec{k}$ is perpendicular to symmetrically equivalent *{hkl}* planes (or strictly: as close to the normal as diffracted intensity appears), see Fig. 2.5. Therefore, diffraction gives us information about average lattice strains for group of grains, but not directly about stress in particular grain. Further analysis is necessary to relate these strains with stress of Ist and IInd type [13, 14]. Also it should be mentioned, that the $<...>_{\{hkl\}}$ average is calculated over different grains exhibiting different strains (due to different lattice orientations or second order stresses), thus their contribution

in diffraction peak cause additional broadening (however in most cases much smaller than this produced by the third order stresses).

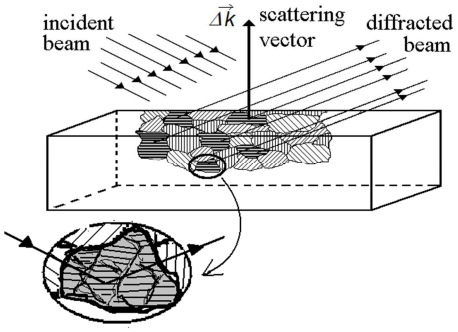

Fig. 2.5. The selective character of diffraction. Only the grains for which the scattering vector $\Delta\vec{k}$ is normal to the reflecting planes {hkl} and Bragg's law is fulfilled contribute to diffracted intensity.

Concluding it should be underlined that the peak broadening of the diffraction peak measured for polycrystalline material brings an important information about the size of so called coherent domain and mean square internal strains $<\varepsilon^2>$ (caused by defects and third order stresses), while the shift of diffraction peak can be related to mean lattice strains caused by the external or residual stresses acting on the grains embedded in polycrystalline aggregate (caused both by the first and the second order stresses). In the next chapters the method for extracting such information from experimental data will be shown.

2.3. DETERMINATION OF STRESSES FROM DIFFRACTION DATA

The residual stress state analysis is based on the diffraction measurements of the interplanar spacings in different directions of the scattering vector $\Delta\vec{k}$ [1]. In order to describe the geometry of measurements it is necessary to introduce two coordinate systems: the coordinate system connected with the specimen (***S***) and the coordinate system connected with the scattering vector. The latter frame is called the laboratory system ***L***, because scattering vector is often fixed with respect to laboratory and sample is rotated (e.g. Eulerian cradle). These systems are defined as follows (Fig. 2.6):

The specimen reference system (***S***): The S_3 axis is orientated perpendicular to the specimen surface. Axes S_1 and S_2 lie in the surface plane. If a preferred direction within the plane of the surface exists, e.g. the rolling direction, the S_1 direction is usually orientated along this preferred direction.

The laboratory reference system (***L***): L_3 axis coincides with the diffraction vector $\Delta\vec{k}$, and L_2 axis lies in the surface plane.

Then the orientations so defined ***L*** system with respect to ***S*** system can be described by two angles ψ and ϕ defined in Fig. 2.6, i.e. ψ is between S_3 and L_3 axes, while ϕ is between L_3 and its projection on the sample surface. These angles also determine orientation of the scattering vector $\Delta\vec{k} \parallel L_3$.

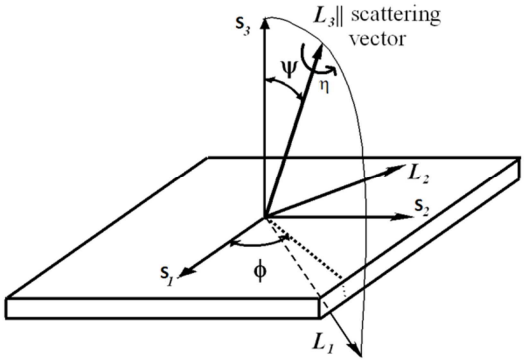

Fig.2.6. Orientation of the scattering vector with respect to the sample system ***S***. The ψ and ϕ angles define the orientation of the ***L*** system (the L_2 axis lies in the plane of the sample surface). Additionally, η – rotation of the ***L*** system around scattering vector is shown (this rotation will be used I the scattering vector method, section 3.1.3).

2.3.1. DETERMINATION OF FIRST AND SECOND ORDER STRESSES

To analyse first order stresses, the mean lattice strains has to be determined from measured shifts of the diffraction peak (Eqs. 2.28 or 2.29). Because the exact position of the diffraction peak must be determined with high accuracy it is necessary to take into account phenomena influencing the profile [1, 6] or position of the peak. To do this the following depending on 2θ factors are introduced in strain analyses:

- Lorentz-polarization factor - LP(2θ),
- absorption factor - Ab(2θ),
- refraction factor (in the case of small incidence angles) – R(2θ).

Usually, the dependence of atomic factor f_n (see Eq. 2.15) and temperature factor do not significantly influence peak profile, and they are not taken into account in corrections. The LP(2θ), Ab(2θ) factors are described in Culity [6] or Noyan [3], while the R(2θ) factor is in detail considered in this work.

Also, the asymmetry of the background may be an imortant problem in the peak position determination. In order to make the correction for the background it is necessary to apply function $I_{bcg}(2\theta)$ which can be obtained by fitting a low degree polynomial function (usually simply linear function) to the background intensities on both left and right hand sides of the diffraction peak [1]. To introduce all corrections the background must be subtracted from the measured intensities, the result must be divided by LP(2θ) and Ab(2θ) factors for every 2θ angle and next peak must be shifted by the - $2\theta_R$ angle (in the case of small angle of incident beam), i.e.:

$$I_{cor}(2\theta - 2\theta_R) = \frac{I_{\exp}(2\theta) - I_{bcg}(2\theta)}{LP(2\theta)Ab(2\theta)} \tag{2.30}$$

where the $I_{exp}(2\theta)$ and $I_{cor}(2\theta)$ are the experimental and corrected intensities, respectively.

After correction and proper preparation of data the precise position of the interference-peak can be determined calculating center of gravity of the peak or fitting theoretical functions to the intensity profile (e.g.: Gauss, Person VII, Lorentz or Pseudo-Voigt functions) [1]. Although the displacement of the diffraction peak is generally small, the fitting procedures with, e.g., Lorentz, Gauss or Voigt functions allow to determine a very precise position of the peak.

Centre-of-gravity method. In this method the intensities of $K_{\alpha 1}$-$K_{\alpha 2}$ lines are averaged out in the result. The peak position is calculated by [1]:

$$< 2\theta_{cg} >= \frac{\int I(2\theta) 2\theta d2\theta}{\int I(2\theta) d2\theta} \tag{2.31}$$

Usually the integration is performed over some threshold value assumed relatively to the maximum peak-intensity.

Fitting of the Gauss function. In this method the diffraction peak is fitted by [9]:

$$I_G(2\theta) = a_G \exp\left[-b_G(2\theta - 2\theta_{\max})^2\right] \tag{2.32}$$

where: $a_G = \frac{2}{w}\sqrt{\frac{\ln 2}{\pi}}$ and $b_G = \frac{4\ln 2}{w^2}$, w is the full width at half maximum (FWHM defined as the full angular width at half-maximum intensity of the diffraction peak [1]), related with integral breath by equation: $\beta_G = \frac{w}{2}\sqrt{\frac{\pi}{\ln 2}}$ (β is defined as the ratio of the peak area to the peak maximum [1]).

Fitting of the Lorentz function [9]:

$$I_L(2\theta) = \frac{a_L}{1 + b_L(2\theta - 2\theta_{\max})^2} \tag{2.33}$$

where: $a_L = \frac{2}{\pi w}$, $b_L = \frac{4}{w^2}$ and w can be related with β by equation: $\beta_L = \frac{\pi w}{2}$

For better resolution of determined position it is recommended to use Pearson VII-functions or Voigt-functions instead of Gaussian or Lorentz distributions. Those functions are much more flexible in describing the peak profile and fits better to the measured intensities [1].

The Pearson VII-function is given by [9]:

$$I_{P_{VII}}(2\theta) = \frac{a_{VII}}{\left[1 + b_{VII}(2\theta - 2\theta_{\max})^2\right]^m} \tag{2.34}$$

where: $a_{VII} = \frac{\Gamma(m)}{\Gamma(m) - \frac{1}{2}} \frac{2\sqrt{2^{\frac{1}{m}} - 1}}{\sqrt{\pi} w}$, $b_{VII} = \frac{4\left(2^{\frac{1}{m}} - 1\right)}{w^2}$, Γ(m)=(m-1)!, and m is the shape parameter.

The Pseudo-Voigt function [15, 16, 17] is superposition of Gaussian ($G^{'}$) and Lorentzian ($L^{'}$) functions, given by the expression [9, 17]:

$$I_{pV}(2\theta) = \eta L^{'}(2\theta - 2\theta_{\max}) + (1-\eta)G^{'}(2\theta - 2\theta_{\max}) \tag{2.35}$$

where: η is the relative contribution of Gaussian component.

If Lorentzian and Gauss components are normalized than pseudo-Voigt is also normalized.

It should be stated that from X-ray diffraction experiments performed on laboratory diffractometers (it is not the case of synchrotron radiation) the intensity of the incident beam is composed from two emission lines $K_{\alpha 1}$ and $K_{\alpha 2}$ exhibiting very similar wavelengths. The contribution of both lines cannot be experimentally separated totally and it has to be done at the stage of data analysis using one of two possible methods:

- influence of $K_{\alpha 2}$ intensity can be removed using Rachinger method [18] assuming theoretical ratios of intensities $I(K_{\alpha 1})/I(K_{\alpha 2})=0.5$ and knowing difference between wavelengths $\lambda_{K\alpha 1}$ and $\lambda_{K\alpha 1}$. Next, the center of gravity is calculated for one peak or peak profile is fitted by above defined functions,
- doublet of two measured is treated together:
    - superposition of defined above functions:

      $$I(2\theta) = I_{K\alpha 1}(2\theta) + 0.5\, I_{K\alpha 1}(2\theta - 2\theta_{K\alpha 1-K\alpha 2}) \tag{2.36}$$

      is fitted to experimental points (where $2\theta_{K\alpha 1-K\alpha 2}$ is the distance between two peaks resulting from two lines for given theoretical difference of wavelengths $2\lambda_{K\alpha 1}$ and $2\lambda_{K\alpha 1}$) ratio $I(K_{\alpha 1})/ I(K_{\alpha 2})=0.5$ is assumed,
    - or the centre of gravity is calculated for the doublet but mean next mean wavelength must be used in Bragg's law, i.e.: $\lambda_{mean}=(2\lambda_{K\alpha 1}+\lambda_{K\alpha 2})/3$

In Fig. 2.7 examples of peak position determination were presented. Peaks were measured for Al powder using K_{α} Cu radiation ($\lambda_{K\alpha 1}$=1.54056 Å and $\lambda_{K\alpha 2}$=1.54433Å) on PANalytical - X'Pert MRD diffractometer (AGH, Kraków) with Göbel mirror using

parallel beam configuration, described in Table 5.4 (chapter 5). Different peak broadenings are seen and high accuracy of measured peak position were obtained when doublet $K_{\alpha 1}$ and $K_{\alpha 2}$ (two peaks) was fitted using the pseudo-Voigt function.

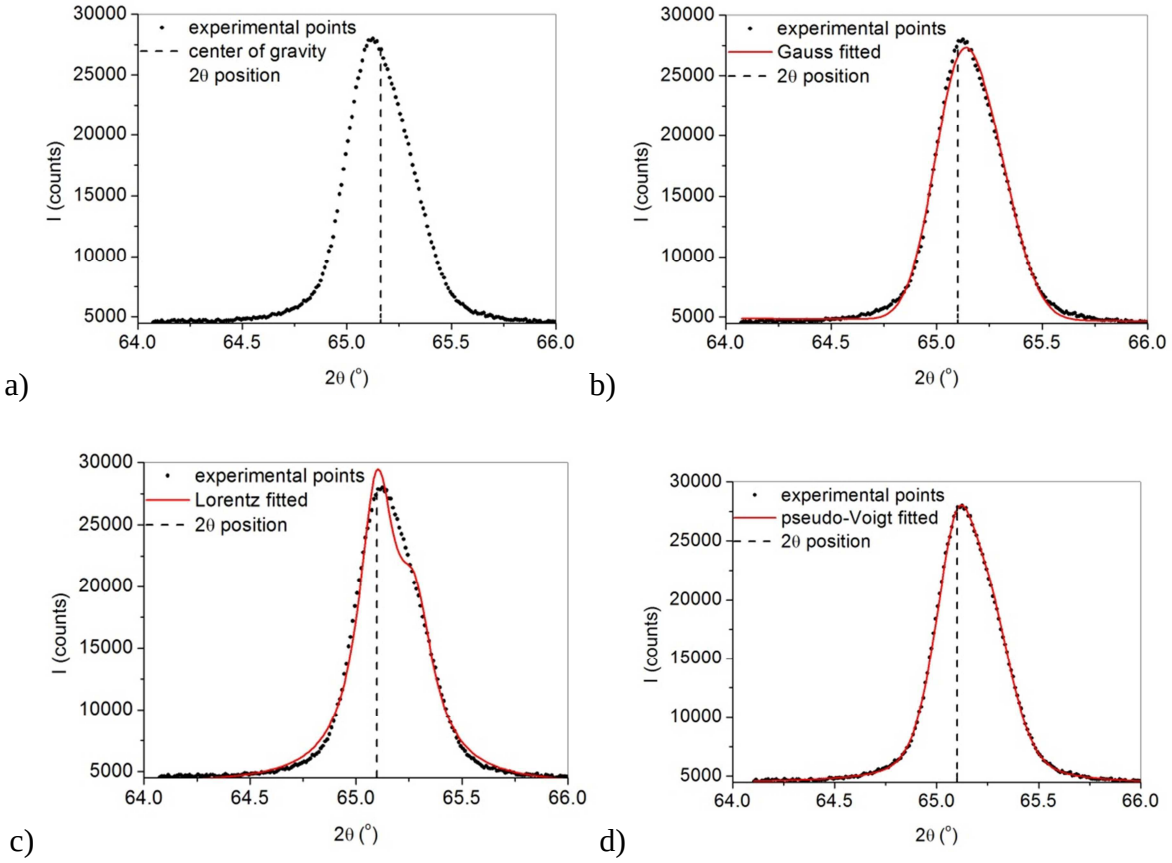

Fig. 2.7. Examples of different methods for position determination: calculation of center of gravity (a), and fitting of Gauss (b), Lorentz (c), pseudo-Voigt (d) functions. Experimental peak was measured for Al powder using PANalytical - X'Pert MRD diffractometer (AGH, Kraków - configuration given in Table 5.4.).

Table 2.1. Comparison of the determined positions for Al powder using 4 different methods.

Fitting	position 2θ (°)
Pseudo-Voigt	65.1000[a] ± 0.0003
Lorentz	65.0982[a] ± 0.0002
Gauss	65.1007[a] ± 0.0002
center of gravity	65.1023[a] (65.1620[b])

where: [a] is the position of $K_{\alpha 1}$ component, while [b] is the position of $K_{\alpha 1}$ + $K_{\alpha 2}$ dublet.

When the positions of diffraction peaks are determined the stress analysis can be performed. The diffraction strain $<\varepsilon(\phi,\psi>_{\{hkl\}}$ measured along L_3 direction (see Eq. 2.28 and Fig. 2.6) are defined as the average strain over diffracted grains volume (Fig. 2.5) which is calculated as [19, 20]:

$$<\varepsilon(\phi,\psi)>_{\{hkl\}} = \frac{\sum_{\{hkl\}} \int_0^{2\pi} \varepsilon_{33}^{L}(hkl,\xi,\phi,\psi)\, f(hkl,\xi,\phi,\psi) d\xi}{\sum_{\{hkl\}} \int_0^{2\pi} f(hkl,\xi,\phi,\psi) d\xi} \tag{2.37}$$

where $\varepsilon_{33}^{L}(hkl,\xi,\phi,\psi)$ is the strain along L_3 direction for (hkl) plane, ψ and ϕ are the angles describing the orientation of the diffraction vector (along L_3) ith the respect to the specimen reference system, ξ – the rotation around the diffraction vector (see Fig. 2.8), $f(hkl,\xi,\phi,\psi)$ is the function representing crystallographic texture, i.e. orientation distribution function ODF (defined in [21]) expressed in terms of measurement parameters and the rotation angle ξ. Summation $\sum_{\{hkl\}}$ is over all symmetrically equivalent planes *{hkl}*.

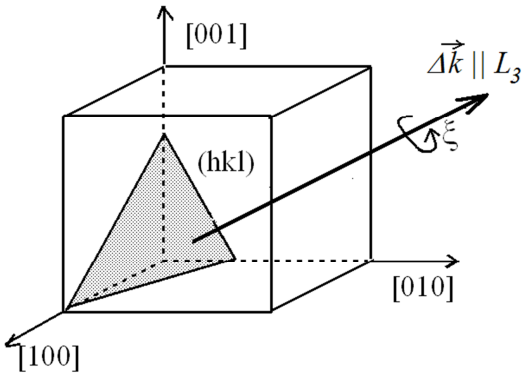

Fig. 2.8. Definition of lattice rotation around the scattering vector $\Delta\vec{k}$ normal to (hkl) plane.

In the above average only the criterion for selection of grain orientations is considered, but also the average must be calculated over the gauge volume using weight of the intensity scattered by different grains (accounting for absorption).

For polycrystal composed of elastically isotropic crystallites (for example tungsten) Hooke's law [19] can be applied to relate the macrostrains with the first order stresses:

$$\varepsilon_{ij}^{I} = S_{ijkl}\sigma_{kl}^{I} = s_{ijkl}\sigma_{kl}^{I} = \left[S_1\delta_{ij}\delta_{kl} + \frac{1}{2}S_2\frac{1}{2}(\delta_{ik}\delta_{jl} + \delta_{il}\delta_{jk}) \right]\sigma_{kl}^{I} \tag{2.38}$$

where: σ_{kl}^{I} and ε_{ij}^{I} are the first order stresses and strains (mean over whole diffraction gauge volume), S_{ijkl} and s_{ijkl} are crystal compliances (equal for isotropic material), S_1 and S_2 are the only independent components of S_{ijkl} for elastically isotropic specimen and δ_{ij} is the Kroneckers delta (all tensors are defined in ***S*** system).

In this case the elastic strain tensor is identical for all crystallites and also for diffracting group of grains [19]:

$$< \varepsilon(\phi,\psi) >_{\{hkl\}} = \varepsilon_{33}^{I,L} \tag{2.39}$$

where *L* superscript means that the strain is expressed in ***L*** system (tensor in ***S*** system have not additional superscripts as in Eq. 2.38).

Then it is possible to calculate $\varepsilon_{33}^{I,L}$ (***L*** system) strain from tensor ε_{ij}^{I} (***S*** system) [19]:

$$\begin{aligned} &< \varepsilon(\phi,\psi) >_{\{hkl\}} = \varepsilon_{33}^{I,L} = m_i\varepsilon_{ij}^{I}m_j = \varepsilon_{11}^{I}\cos^2\phi\sin^2\psi + \varepsilon_{22}^{I}\sin^2\phi\sin^2\psi \\ &+\varepsilon_{33}^{I}\cos^2\psi + \varepsilon_{12}^{I}\sin(2\phi)\sin^2\psi + \varepsilon_{13}^{I}\cos\phi\sin(2\psi) + \varepsilon_{23}^{I}\sin\phi\sin(2\psi) \end{aligned} \tag{2.40}$$

where: ε_{ij}^{I} is strain tensor in the specimen system of reference, $\vec{m}$ is the unit vector, in the direction of the scattering vector, expressed in the specimen system of reference (***S***).

$$\vec{m} = \begin{pmatrix} \sin\psi\cos\phi \\ \sin\psi\sin\phi \\ \cos\psi \end{pmatrix} \tag{2.41}$$

Taking into consideration the Hook's law (Eq. 2.1) and Eq. 2.40 it is possible to gain [19, 22]:

$$< \varepsilon(\phi,\psi) >_{\{hkl\}} = \frac{1}{2} S_2 \sin^2\psi [\sigma_{11}^I \cos^2\varphi + \sigma_{12}^I \sin(2\phi) + \sigma_{22}^I \sin^2\phi] + \\ + \frac{1}{2} S_2 [\sigma_{13}^I \cos\phi \sin(2\psi) + \sigma_{23}^I \sin\phi \sin(2\psi) + \sigma_{33}^I \cos^2\psi] + S_1(\sigma_{11}^I + \sigma_{22}^I + \sigma_{33}^I) \quad (2.42)$$

The above equation is a general expression relating first order mean stresses (full tensor) with strains measured for different directions of scattering vector described by ψ and ϕ angles and it is called $sin^2\psi$ law, because the measured strains are plotted vs. $sin^2\psi$ (with constant ϕ). If the shear stresses are equal to zero, i.e. the sample system (***S***) coincides with principal axes of stress tensor, the latter plot is a straight line and the components of the stress tensor can be extracted from the slope of the line plotted for constant ϕ.

Usually a polycrystal is composed of elastically anisotropic crystallites (anisotropic s_{ijkl}), stresses and strains vary over the differently oriented crystallites in the specimen as a result of the elastic grain interaction [19]. Even then the whole specimen can be macroscopically elastically isotropic (quasi-isotropic) when the crystallographic texture does not occur and the grain interaction is isotropic. For quasi-isotropic specimens the S_1 and $1/2S_2$ in Eq. 2.42 need to be replaced by *hkl*-dependent X-ray elastic constants (XEC) S_1^{hkl} and $1/2S_2^{hkl}$ [19], i.e.:

$$< \varepsilon(\phi,\psi) >_{\{hkl\}} = \frac{1}{2} S_2^{hkl} \sin^2\psi [\sigma_{11}^I \cos^2\phi + \sigma_{12}^I \sin(2\phi) + \sigma_{22}^I \sin^2\phi] + \\ + \frac{1}{2} S_2^{hkl} [\sigma_{13}^I \cos\phi \sin(2\psi) + \sigma_{23}^I \sin\phi \sin(2\psi) + \sigma_{33}^I \cos^2\psi] + S_1^{hkl}(\sigma_{11}^I + \sigma_{22}^I + \sigma_{33}^I) \quad (2.43)$$

In this case the XEC depends on the reflection *hkl* [23].

The most complex case is the textured polycrystalline material when macroscopic elastic anisotropy is present. For such specimen the dependence of the X-ray-averaged strains on the mean stresses is described by the X-ray stress factors (XSF) F_{ij} depending not only on *hkl* but also on texture [1, 19, 24]:

$$< \varepsilon(\phi,\psi) >_{\{hkl\}} = F_{ij}(hkl,\phi,\psi, f)\sigma_{ij}^I \quad (2.44)$$

where *f* represents ODF function.

For textured materials or in the case of direction dependent grain interaction the $sin^2\psi$ plots are generally non-linear and the X-ray analysis can be challenging. The first works on stress analysis for sample having crystallographic texture were performed by Dole & Hauk (1978, 1979) [19].

The X-ray elastic constants S_1^{hkl} and $1/2S_2^{hkl}$ and the stress factors $F_{ij}(hkl,\phi,\psi,f)$ can be evaluated experimentally by a uniaxial tension or bending test. It is also possible to calculate stress factors from single-crystal elastic constants using a model of crystallite coupling (Voigt, Reuss, Eshelby-Kröner) and the ODF as the weight function [1, 19]. Because the verification of $F_{ij}(hkl,\phi,\psi,f)$ used in grazing incident method is one of the aims of this work, the different models for calculation of these constants will be presented in next chapters.

It should be stated that using the diffraction methods, the lattice strain are not directly measured but in fact the interplanar spacings $<d(\phi,\psi)>_{\{hkl\}}$ are determined from diffraction peak positions. These positions are measured for different orientations of the scattering vector with respect to the sample, defined by the φ and ψ angles. Using Eq. 2.44, after simple transformation the interplanar spacings can be expressed by the macrostresses σ_{ij}^I and $d_{\{hkl\}}^0$ stress free interplanar spacing:

$$< d(\phi,\psi)>_{\{hkl\}} = [\ F_{ij}\ (hkl,\phi,\psi,\ f)\,\sigma_{ij}^I\ ]\ d_{\{hkl\}}^0 + \ d_{\{hkl\}}^0 \tag{2.45}$$

or in the case of quasi-isotropic material:

$$< d(\psi,\phi) >_{\{hkl\}} = \left[\begin{array}{l} \frac{1}{2} S_2^{hkl} \left\{ (\sigma_{11}^I - \sigma_{33}^I)\cos^2\phi + \sigma_{12}^I \sin 2\phi + (\sigma_{22}^I - \sigma_{33}^I) \right\} \sin^2\psi + \\ + S_1^{hkl} (\sigma_{11}^I + \sigma_{22}^I + \sigma_{33}^I) + \frac{1}{2} S_2^{hkl} \left(\sigma_{13}^I \cos\phi + \sigma_{23}^I \sin\phi \right) \sin 2\psi \end{array} \right] d_{hkl}^0 + d_{hkl}^0 \tag{2.46}$$

The calculation of the stresses using Eqs. 2.45 or 2.46 can be performed using least square method and adjusting components of stress tensor as well as $d_{\{hkl\}}^0$. However, the whole stress tensor (principal stresses) can be calculated only if $d_{\{hkl\}}^0$ (stress free parameter) is known. Fortunately, in the case of X-ray diffraction penetrating thin surface layer (due to high absorption) we can assume that the forces normal to the surface are

equal to zero and also σ_{33}^{I}=0. Because one of principal stresses is known, $d_{\{hkl\}}^{0}$ can be adjusted and its value can be also determined.

The least square procedure used in this work is based on minimising of the merit function called χ^2 which is defined as:

$$\chi^2 = \frac{1}{N-M}\sum_{n=1}^{N}\left(\frac{< d(\phi_n,\psi_n) >_{\{hkl\}}^{exp} - < d(\phi_n,\psi_n >_{\{hkl\}}^{cal}}{\delta_n}\right)^2 \tag{2.47}$$

where: $< d(\phi_n,\psi_n) >_{\{hkl\}}^{exp}$ and $< d(\phi_n,\psi_n) >_{\{hkl\}}^{cal}$ are the experimental and calculated interplanar spacings , δ_n=δ_n($< d(\phi_n,\psi_n) >_{\{hkl\}}^{exp}$) is the measurement error (standard deviation) of the determined spacing for the *n*-th measurement, *N* and *M* are the number of measured points and fitting parameters, respectively.

The value of χ^2 is a measure of goodness-of-fit, i.e. [25]:

- χ^2 = 1 means that the "good fit" was obtained (it corresponds to the fitting exactly within the limits of experimental uncertainty),
- χ^2 < 1 the uncertainties of experimental data δ_n($< d(\phi_n,\psi_n) >_{\{hkl\}}^{exp}$) are overestimated,
- χ^2 > 1 the uncertainties of experimental data are underestimated or calculated (theoretical) values $< d(\phi_n,\psi_n) >_{\{hkl\}}^{cal}$ depending on stress factors $F_{ij}(hkl,\phi,\psi)$ are not accurate enough.

An example of stress calculation for the simplest case when elastic constants are isotropic (for tungsten) will presented in the next chapter when two standard methodologies are compared (Fig.3.6).

Finally it should be mentioned, that also the methods for determination of the second order stresses were developed using the elasto-plastic models [13, 14]. From these models the theoretical values of plastic incompatibility stresses ($\sigma_{ij}^{II,\mathrm{mod}}$ - model values) and the corresponding strains $< \varepsilon(\psi,\phi) >_{\{hkl\}}^{II,\mathrm{mod}}$ can be predicted (where *mod* is used for the theoretical values). Assuming that stress variation with the ψ and ϕ angles is correctly described by models, the measured strain can be expressed by the theoretical value, i.e.:

$< \varepsilon(\psi,\phi) >^{II}_{\{hkl\}} = q < \varepsilon(\psi,\phi) >^{II,\mathrm{mod}}_{\{hkl\}}$; where: q - is a constant scaling factor. Finally, Eq. 2.45 takes form:

$$< d(\psi,\phi) >_{\{hkl\}} = \{ F_{ij}(hkl,\psi,\phi, f)\,\sigma^{I}_{ij} + q < \varepsilon(\psi,\phi) >^{II,\mathrm{mod}}_{\{hkl\}} \}\, d_{o\{hkl\}} + d_{o\{hkl\}} \qquad (2.48)$$

When the value of q parameter is determined (as additional adjusting parameter) the plastic incompatibility stresses (σ^{II}_{ij}) can be found for all grain orientations, i.e.: $\sigma^{II}_{ij} = q\sigma^{II,\mathrm{mod}}_{ij}$; where $\sigma^{II,\mathrm{mod}}_{ij}$ are the model predicted values. Thus, the macrostresses (σ^{I}_{ij}) the mismatch second order stresses (σ^{II}_{ij}) can be determined simultaneously.

2.3.2. DETERMINATION OF THIRD ORDER STRAINS AND CRYSTALLITE SIZE

One of the features that decide about physical and mechanical properties of a solid body is its microstructure, such as lattice distortion or mosaic structure of grains. Using enough resolved diffractometers it is possible to observe the broadening of the diffraction peak due to the sample microstructure. The width of the diffraction peaks is also dependent on the size of the coherently diffracting domains, faulting on certain (hkl) planes, and microstrains within the coherently diffracting domains [26]. Peak broadening is further complicated by strain anisotropy, which can be taken into account by using contrast factor [27]. Not only sample but also instrument contribution convolute into the observed diffraction peak profile. Instrumental aberrations depend on the measuring technique and geometry. This effect can be taken into account by measuring a standard powder sample.

It is possible to separate the peak broadening originated from different causes. The broadening produced by small crystallite sizes and faulting is independent of the order of reflection, whereas the strain broadening depends on the order of reflection. Two methods are usually applied to separate these effects from each other [28].

The first, Warren and Averbach method (1950), based on the Fourier expansion of the intensity function and separation of size and strain series coefficients using diffraction peaks measured for at least two orders of reflection. The second is Williamson-Hall method (1953). It allows determine the domain size and the mean squared lattice strain by the analysis based on full width half maximum values or the integral breadths [28, 26].

It should be stated that the presented methods of analysis can be applied for crystallites having the size D < 100 nm and lattice distortions $\sqrt{<\varepsilon^2>}$ grater than 10^{-3}.

Warren and Averbach method

This method is based on the expansion of peak profile into Fourier series. In the case of X-ray diffraction (on laboratory apparatus) it is necessary to remove the influence of the $K_{\alpha 2}$ line from measured intensity. It can be done numerically with Rachinger method [29] or analytically with the assumption of theoretical function describing the shape of the diffraction line [30] in which it is assumed that the intensity of line $K_{\alpha 2}$ is twice smaller than the intensity of line $K_{\alpha 1}$ and both of the lines have the same shape and the same width. Next, the effect of instrumental influence on the peak profile must be taken into account using proposed by Stokes [31] harmonic analysis of diffraction line profiles of the sample and reference sample and on the basis of them it is possible to obtain the actual intensity distribution function of the diffraction peak. The diffraction peak *G(2θ)* for reference is measured with the same conditions as this registered for the studied sample *H(2θ)*. The latter profile can be expressed as the convolution of instrumental *G(2θ)* and structural functions *I(2θ)*:

$$H(2\theta) = \int_{-\infty}^{\infty} I(\vartheta) G(2\theta - \vartheta) d\vartheta \tag{2.49}$$

If both functions *G(2θ)* and *H(2θ)* are expanded into Fourier series (the coefficients of such series are g_n, g'_n and h_n, h'_n), the coefficients of the series given by Eqs. 2.26a and 2.26b can be calculated:

$$a_n = c\frac{g_n h_n + g_n' h'_n}{(g_n)^2 + (g'_n)^2} \qquad \text{(2.50 a)} \qquad \text{and} \qquad a'_n = c\frac{g_n h_n' - g'_n h_n}{(g_n)^2 + (g'_n)^2} \qquad \text{(2.50 b)}$$

where c is a constant factor.

Finally the size of domain (D) in the direction of scattering vector and the square mean third order strain $<\varepsilon^2>$ can be calculated applying Eqs. 2.26a, 2.26b and 2.27 for peak intensities measured for two orders of reflections.

Williamson-Hall method

The crystallites size *D* along the direction perpendicular to the *{hkl}* diffracting planes can be related with the width of the diffraction peak using Scherrer formula:

$$\beta_s = \frac{K \cdot \lambda}{D \cdot \cos\theta} \tag{2.51}$$

where *K* is a constant close to unity, dependent from method of the peak width determination as well as from geometric shape of the crystallites [27].

Using the above equation the crystallite size (coherent domain) *D* can be determined from the peak width measured by X-ray diffractometer. This equation assumes that all the crystallites have the same size and the strains of the lattice are not present. In fact usually crystallites have some size distribution and additionally lattice distortion limiting application of this formula.

Broadening of the diffraction peak connected with the presence of the third order lattice distortion and can be calculated from Taylor formula:

$$\beta_T = 4\sqrt{<\varepsilon^2>}tg\theta \tag{2.52}$$

where $\sqrt{\langle \varepsilon^2 \rangle}$ is the root mean square value of the lattice distortion.

According to Hall [32] the observed total structural broadening of the diffraction line β is a superposition of the broadening caused by lattice distortion and crystallite size so it can be expressed as:

$$\beta = 4\sqrt{\langle \varepsilon^2 \rangle}tg\theta + \frac{\lambda}{D\cos\theta} \tag{2.53}$$

In order to evaluate the *D* and $\sqrt{\langle \varepsilon^2 \rangle}$ values it is necessary to approximate the diffraction profiles of the studied specimen and of the reference sample (for example strain free powder with grains having at least a few μm). There are two main methods of analysis which are in use. The first assumes that both of the profiles (specimen and reference sample) can be approximated by Cauchy function. Then the total line broadening can be expressed as:

$$\beta\cos\theta = \frac{\lambda}{D} + 4\sqrt{\langle\varepsilon^2\rangle}\sin\theta \qquad (2.54\text{ a}) \qquad \text{and} \qquad \beta = B - b \qquad (2.54\text{ b})$$

where: B and b are the peak widths of the investigated sample and of the reference sample, respectively.

After simple transformation the above formula can be written as:

$$\beta^* = \frac{1}{D} + d^*\sqrt{\langle\varepsilon^2\rangle} \qquad (2.55)$$

where: $\beta^* = \dfrac{\beta\cos\theta}{\lambda}$ and $d^* = \dfrac{4\sin\theta}{\lambda}$

The second method assumes that both of the profiles can be approximated by Gaussian function. Then the general formula can be expressed as:

$$\beta^2\cos^2\theta = \left(\frac{\lambda}{D}\right)^2 + 16\left(\sqrt{\langle\varepsilon^2\rangle}\right)^2\sin^2\theta \qquad (2.56\text{ a}) \quad \text{and} \quad \beta^2 = B^2 - b^2 \qquad (2.56\text{ b})$$

and after transformation:

$$\beta^* = \frac{1}{D^2} + d^*\left(\sqrt{\langle\varepsilon\rangle^2}\right)^2 \qquad (2.57)$$

where: $\beta^* = \dfrac{\beta^2\cos^2\theta}{\lambda^2}$ and $d^* = \dfrac{16\sin^2\theta}{\lambda^2}$

In all of this methods by plotting β^* as a function of d^* for several diffraction lines the root mean square value of the lattice distortion and the crystallite size can be determined from the slop and the intercept of the plotted curve, respectively. In this aim the linear regression is used.

The width of the diffraction peak in the above formulas may be determined as a integral breath or as the full width at half maximum (FWHM) [33].

An example of size-strain analysis using Gauss and Cauchy is presented in Fig. 2.9. The measurements were performed for mechanically polished W sample using the same experimental conditions as for peak measurement presented in Fig. 3.7. As the reference the LaB_6 powder was used. In Table 2.2 the results of analysis are shown.

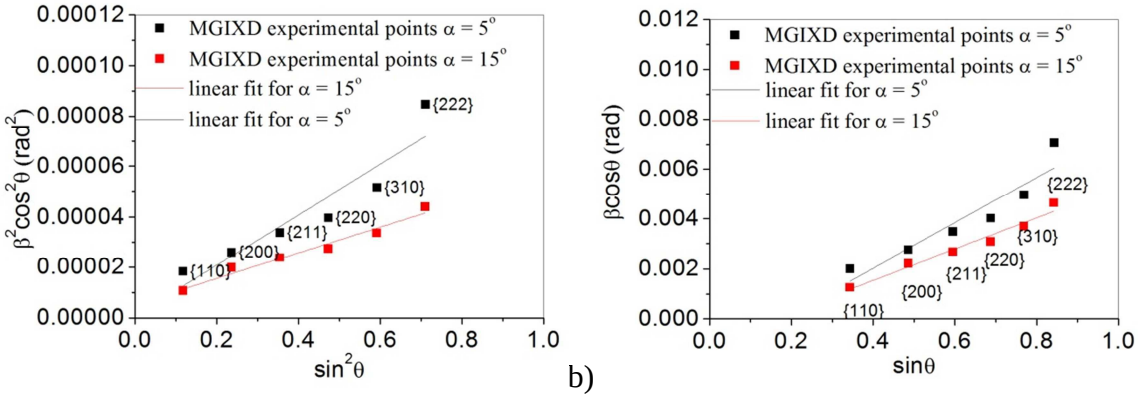

a) b)

Fig. 2.9. The linear function fitted to the experimental data in Williamson-Hall method for polished W sample using Gauss approximation (a), Cauchy approximation (b).

Table.2.2. The slope and the intercept of the fitted linear function to the experimental data for polished W sample. Calculated with Williamson-Hall method values of the root mean square of the third order strain ($\sqrt{\langle \varepsilon^2 \rangle}$) and crystallite size (D).

α (°)	function	slope [$\cdot 10^{-4}$]	intercept [$\cdot 10^{-4}$]	$\sqrt{<\varepsilon^2>}$	D (Å)
5	Gauss	1.0 ± 0.2	0.01 ± 0.09	0.0025 ± 0.0002	1678 ± 8626
15	Gauss	0.51 ± 0.05	0.05 ± 0.02	0.0018 ± 0.0001	667 ± 133
5	Cauchy	90 ± 20	-16 ± 10	0.0023 ± 0.0004	-957* ± 648
15	Cauchy	62 ± 6	-9 ± 4	0.0016 ± 0.0002	-1629* ± 653

* large negative values of D means that the intercept point is negative but it is close to zero.

If the instrumental peak width is large in comparison with the broadening due to crystallite size, than it is not possible to determine properly the coherently diffracting domain size (some values of D are negative because intercept is negative and close to zero). When the peak profile is either pure Gaussian or pure Lorentzian the simplified breadth methods work well but when the peak shape is a convolution of Gaussian and Lorentzian than these methods cannot accurately determine the crystallite size. The Williamson-Hall analysis of polished W sample showed that on the basis of MGIXD measurements with classical diffractometer (PANalytical – Empyrean diffractometer, configuration is given in Table 5.4.) it is possible to estimate the value of root mean square of third order strain but the resolution of the diffractometer is not sufficient for crystallite size determination.

3. METHODOLOGY OF STRESS MEASUREMENTS USING X-RAYS

Although the neutron diffraction methods of stress measurement were significantly developed, X-ray diffraction remains the most important tool of stress analysis which can be used in industry or in laboratory. X-ray diffraction in residual stress measurements of polycrystalline materials were applied for the first time in 1930 [34, 35, 36]. It is worth to emphasise that introduction of the $sin^2\psi$ method by Macherauch and Müller in 1961 [22, 36] was one of the greatest achievements in X-ray stress analysis (XSA).

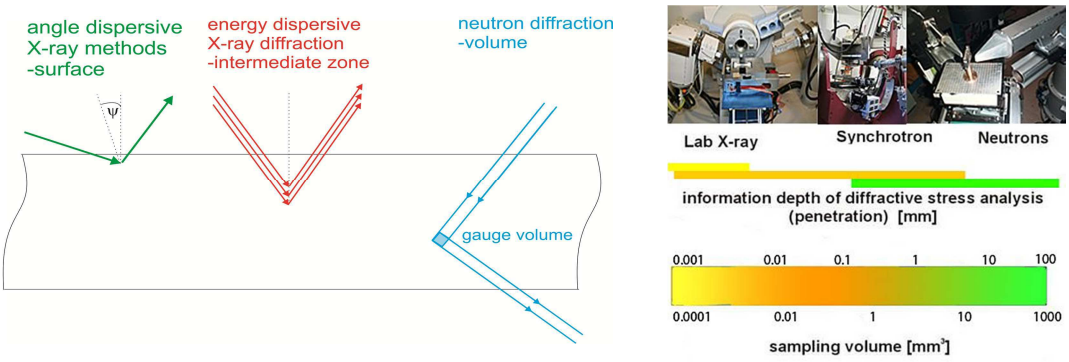

Fig. 3.1. Information depth of the diffractive stress analysis [37]

Due to high absorption of the X-rays (on laboratory diffracrometers) the stress measurements are performed using reflection method, i.e., the beam is reflected from the surface of the sample and penetrates the volume below the surface. The other methods based on the transition mode can be used only for high energy synchrotron radiation or neutron radiation. In all cases, the intensity of the beam penetrating the studied sample depends on the linear absorption of the material (μ) according to the exponential law:

$$I(x) = I_0 \exp(-\mu x) \tag{3.1}$$

where x is the length of the ray path in the material and I_0 is the intensity of the incident beam.

In the present work only the reflection mode is considered for which the information depth can be estimated using the above law. In this case, if the strain free lattice parameters $d^0_{\{hkl\}}$ as well as stress factors $F_{ij}(hkl,\phi,\psi)$ do not depend on depth [36] the mean lattice strain $<\varepsilon(\phi,\psi,\bar{z})>$ at information depth $\bar{z}$, calculated over reflecting grains (as in Eq. 2.33) must be also averaged with the weight of beam intensity over depth z under surface. It was aaumed that so calculated strain is related with the mean first order stress and also averaged with the intensity weight (see Fig. 3.5):

$$<\varepsilon(\phi,\psi,\bar{z})>_{\{hkl\}} = \frac{<d(\phi,\psi,\bar{z})>_{\{hkl\}} - d^0_{\{hkl\}}}{d^0_{\{hkl\}}} = \frac{\int_0^t <d(\phi,\psi,z)>_{\{hkl\}} e^{-z/\tau} dz}{d^0_{\{hkl\}} \int_0^t e^{-z/\tau} dz} - 1 \tag{3.2}$$

$$= F_{ij}(hkl,\phi,\psi)\sigma^I_{ij}(\bar{z})$$

$$\text{where: } \sigma^I_{ij}(\bar{z}) = \int_0^t \sigma^I_{ij}(z) e^{-z/\tau} dz \Big/ \int_0^t e^{-z/\tau} dz \tag{3.3}$$

and t is the sample thickness, τ is the "penetration depth" defined as the distance from the surface of bulk material ($t \to \infty$), for which $(1-1/e) = 0.63$ part of total intensity of the incident beam is absorbed.

The above average corresponds to so called 'information' or 'effective' depth $\bar{z}$, which can be understood as the mean value of z-depth weighted by an attenuation factor:

$$\bar{z} = \frac{\int_0^t z \exp(-z/\tau)\, dz}{\int_0^t \exp(-z/\tau)\, dz} = \begin{cases} \tau - \dfrac{t\exp(-t/\tau)}{1-\exp(-t/\tau)} & \text{for limited } t \\ \tau & \text{for } t \to \infty \end{cases} \tag{3.4}$$

A general formula for penetration depth τ in the case of bulk material or thick coatings (i.e., $t>>\tau$) is given by [38]:

$$\tau = \frac{\sin^2\theta - \sin^2\psi + \cos^2\theta \sin^2\psi \sin^2\eta}{2\mu \sin\theta \cos\psi} \tag{3.5}$$

where η is an angle of rotation of the sample around the diffraction vector i.e., L_3 axis shown in Fig. 2.6.

In the case when the incident angle of X-ray beam (α – angle between incident beam and sample surface, see Fig. 3.7) is close to the critical angle (α_{cr} – angle for which total external reflection occurs), the expression for penetration depth takes form [36]:

$$\tau(\alpha) = \frac{\lambda}{4\pi\left[\frac{\sqrt{\left(\sin^2\alpha - \sin^2\alpha_{cr}\right)^2 + 4\beta^2} + \sin^2\alpha_{cr} - \sin^2\alpha}{2}\right]} \tag{3.6}$$

where λ is the wavelength and $\beta = \frac{\mu\lambda}{4\pi}$.

In this case, as it can be seen in Fig. 3.2 small changes in α angle causes significant changes in τ.

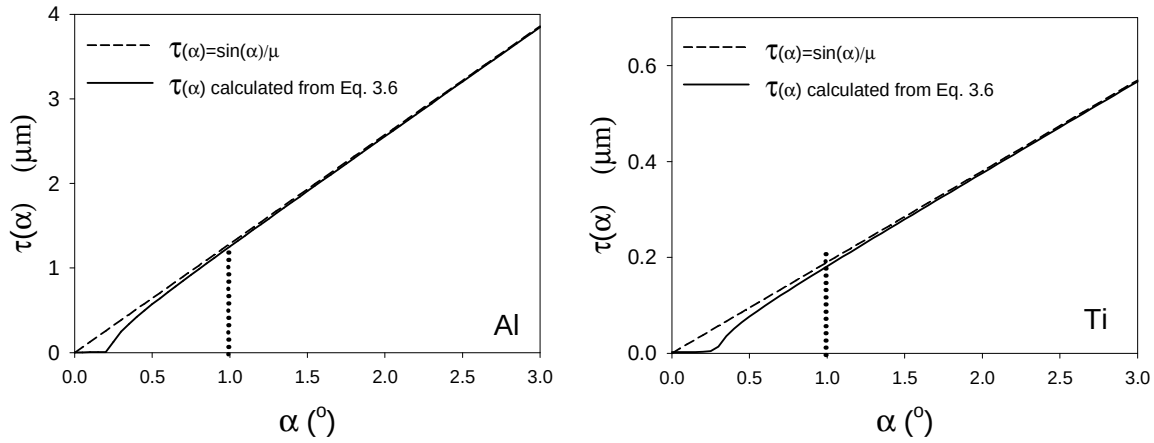

Fig. 3.2. Penetration depth as a function of incident angle for aluminum and titanium. Curves changes significantly close to the critical angle.

In should be stated that for $t \to \infty$ (bulk materials) in Eq. 3.3, the upper limit of the integral can be replaced by the infinity and the equation takes the form of the Laplace transformation with respect to 1/τ (see Eq. 3.3 in which $\bar{z}$ should be replaced by τ). In order to reveal the real depth profile of stress $\sigma_{ij}^{I}(z)$ it is necessary to perform inverse Laplace transformation for the data gained experimentally $\sigma_{ij}^{I}(\bar{z} = \tau)$ [39].

Introducing a new variable: $s = \frac{1}{\tau}$ mean stresses $\sigma_{ij}^{I}(\tau)$ determined with absorption weight can be expressed as:

$$\bar{\sigma}_{ij}^{I}(s) = \frac{\int_0^{\infty} e^{-\tau s}\sigma_{ij}(z)dz}{\int_0^{\infty} e^{-\tau s}dz} \tag{3.7}$$

where z is the real depth under the surface.

It can be noticed that the denominator of the above formula is a Laplace transform of 1, while the numerator is a Laplace transform of stress function $\sigma_{ij}^{I}(z)$. Thus, Eq. 3.7 can be rewritten as:

$$\bar{\sigma}_{ij}^{I}(s) = \frac{\mathcal{L}(s)}{1/s} = s\,\mathcal{L}(s) \tag{3.8}$$

and

$$\mathcal{L}(s) = \frac{\bar{\sigma}_{ij}^{I}(s)}{s} \tag{3.9}$$

where $\mathcal{L}(s)$ denotes Laplace transform of the macrostrain function $\sigma_{ij}^{I}(z)$.

In order to reveal the real depth profiles (z-profiles) of the macrostresses, the inverse Laplace transform of $\bar{\sigma}_{ij}^{I}(s)/s$ have to be calculated. However, it should be noted that usually only a few values of the mean stresses $\bar{\sigma}_{ij}^{I}(s)$ within limited range of τ can be determined experimentally. The fragmentary knowledge about $\mathcal{L}(s)$ function causes that the inverse Laplace transform cannot be easily determined. Thus the experimental functions $\mathcal{L}(s)$ are usually approximated by functions for which the inverse Laplace

transform can be easily designated. For example, it is possible to use the piecewise polynomials allowing dividing the Laplace space into small sections in which it is possible to describe the stress profile. Usually the polynomials of the first and second degree are used [40].

Another method for determination of the stress in depth profile $\sigma_{ij}^{I}(z)$ was proposed by Genzel et al. (1996). In this work the inverse Laplace transform is calculated numerically by the methods of orthogonal polynomials. Several sets of orthogonal function were used but the best results were achieved with use of Jacobi polynomials. It seems that this method is mostly suitable in the case of steep gradients. If necessary it is possible to divide the depth profile into intervals and then calculate inverse transforms for each interval separately [39].

To reveal the stress profile $\sigma_{ij}^{I}(z)$ Huang et al. (1997) used the constrained linear inversion of the $\mathcal{L}(s)$ profile. This analysis showed that the significant advantage of the numerical method is that there is no major restriction on the form of the penetration depth profile. What is more it is more likely to achieve the better fit to the experimental data numerically than with the inverse Laplace method [41].

In present work the *z*-profile of stress is determined using method based on expansion into Taylor series of the quested stress function $\sigma_{ij}^{I}(z)$, i.e.:

$$\sigma_{ij}^{I}(z) = \sum_{n=0}^{N} a_n z^n \tag{3.10}$$

The Laplace transform of the above function is given by equation:

$$\mathcal{L}(s) = \frac{\bar{\sigma}_{ij}^{I}(s)}{s} = \sum_{n=0}^{N} a_n \frac{n!}{s^{n+1}} \tag{3.11}$$

and the measured profile of the stresses can be expressed as:

$$\bar{\sigma}_{ij}^{I}(s) = \sum_{n=0}^{N} a_n \frac{n!}{s^{n}} \tag{3.12}$$

as $s = \frac{1}{\tau}$ it can be written:

$$\bar{\sigma}_{ij}^{I}(\tau) = \sum_{n=0}^{N} n! a_n \tau^n = \sum_{n=0}^{N} b_n \tau^n \tag{3.13}$$

where $b_n = n! a_n$.

In the above equation the function of mean macrostress $\bar{\sigma}_{ij}^{I}(s)$ gained from measurements is expressed by polynomial with variable τ. If the polynomial coefficients are determined, also the coefficients of Taylor expansion of macrostress $\sigma_{ij}^{I}(z)$ can be calculated, i.e.:

$$a_n = \frac{b_n}{n!} \tag{3.14}$$

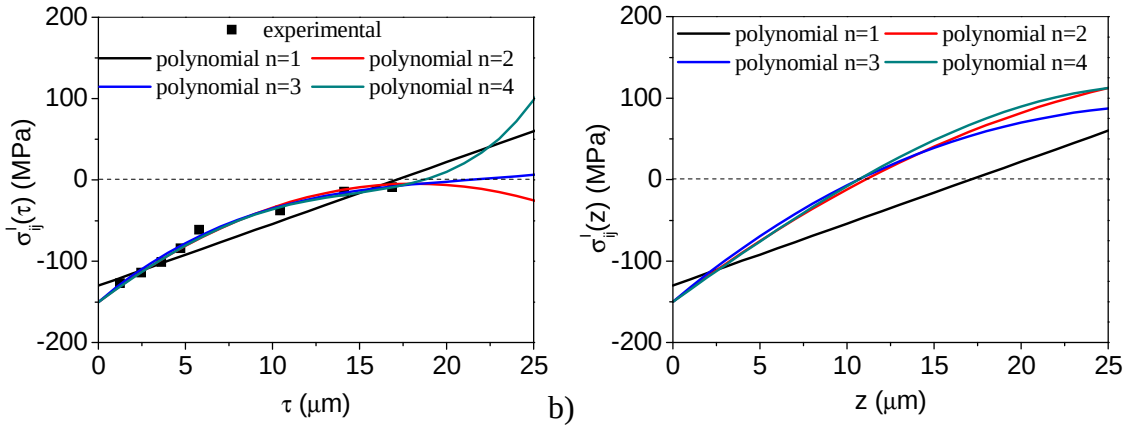

a) b)

Fig. 3.3. Experimental $\bar{\sigma}_{ij}^{I}(\tau)$ stresses for polished Al2017 alloy with polynomial fitted to the measured values (a) and corresponding profiles $\sigma_{ij}^{I}(z)$ obtained by using inverse Laplace transform (b).

At present, there are two basic types of carrying out the experiment:

- in angle dispersive diffraction mode (AD) or
- in energy-dispersive diffraction mode (ED).

In the case of the AD method one uses a monochromatic radiation, while a white X-ray beam is diffracted by a polycrystalline material in ED mode. The later method was introduced both by Giessen & Gordon (1968) and Buras et al. (1968) and it was firstly used in 1970 by Nagao & Kusumoto, 1977 [42].

AD diffraction methods with conventional X-ray tubes allow investigating the material only for the penetration depth of a few up to some tens of microns. It is also possible to get information on deeper regions below the surface of the sample in AD techniques by applying layers removal. This method, however, is a destructive method and it cannot be always used. On the other hand neutron diffraction allows getting the information for more than hundreds of microns. The high energy ED diffraction is the non-destructive method which gives the opportunity of the sample investigation for such depth (up to tents or hundreds μm) which are not reached by monochromatic radiation on laboratory diffractometers. In the ED diffraction, in reflection mode, the white radiation in the energy range from about 10 up to 150 keV with a continuous photon energy spectrum is used. In this method the scattering angle $2\theta_d$ can be chosen freely and remains constant during the measurement [2, 43]. In this case, the lattice spacing d_{hkl} expressed as a function of the diffraction line E_{hkl} on the energy scale is given by:

$$< d >_{\{hkl\}} = \frac{hc}{2\sin\theta_d} \frac{1}{< E >_{\{hkl\}}} \tag{3.15}$$

where: *h* is Planck's constant and *c* the velocity of light.

A great advantage of this method, in comparison with AD diffraction techniques, is the multitude of reflections recorded simultaneously in one energy spectrum. Each of them differ in energy so it provides additional depth information [2, 42]. The penetration depth in ED method is given by Eq. 3.5 but in this case μ denotes the linear absorption coefficient which depends on the energy E of the radiation. In the symmetrical case of diffraction (η=90°), the penetration depth for *hkl* reflection [43]:

$$\tau = \frac{\sin\theta_d}{2\mu(E)} \cos\psi \tag{3.16}$$

where $\mu \sim 1/E^3$ for absorption between the absorption edges.

In this chapter a few geometries used for stress measurement by X-rays will be shortly presented and for each the problem of information depth will be discussed. This problem is certainly very important in the case of in depth stress gradient. Also, the principles of multireflection grazing incidence X-ray diffraction (MGIXD) developed in

the present work will be introduced. The described below method will be divided in two types: methods in which the penetration depth is variable or is constants during measurement. In the first case complex analysis should be used in order to extract the stress in-depth profiles, while the latter methodologies are concentrated on designing of special geometries in which the lattice strains are measured for constant penetration of X-rays (this simplifies analysis of the data).

3.1. METHODS WITH VARIABLE PENETRATION DEPTH

3.1.1. STANDARD GEOMETRIES OF STRESS MEASUREMENT

In the standard $sin^2\psi$ method, the $<d(\phi,\psi)>_{\{hkl\}}$ vs. $sin^2\psi$ functions are measured using X-ray diffraction for a single reflection *hkl* and constant ϕ angle. As shown in Fig. 3.4, the ψ angle can be changed in two different ways, i.e. by tilting diffraction plane (ψ-geometry) or rotating both incident and diffracted beams in diffraction plane being perpendicular to the sample surface (ω-geometry). In both cases the diffraction peak for the same reflection *hkl* is measured, thus the 2θ angle remains approximately constants (excluding small shifts caused by lattice strains). The measurements of $<d(\phi,\psi)>_{\{hkl\}}$ vs. $sin^2\psi$ functions are repeated for different ϕ angles. To set desired angles ψ and ϕ the instrumental angles χ, ω and φ are varied applying conditions defined in Fig. 3.4.

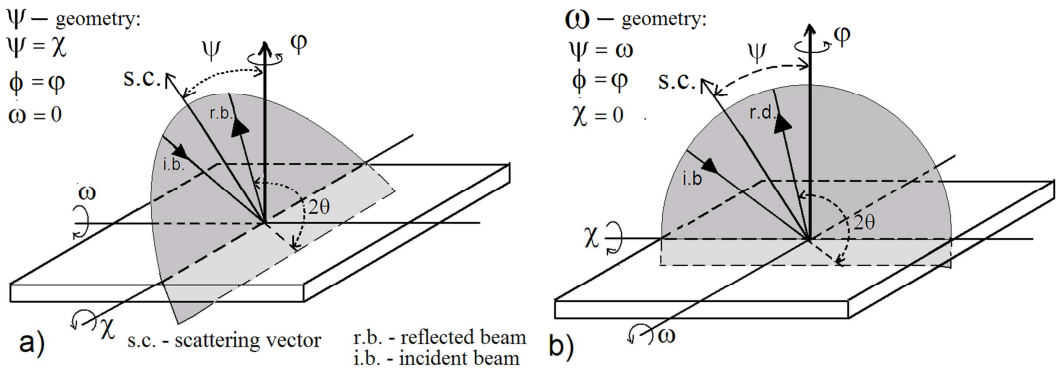

Fig. 3.4. Two different geometries used in standard measurements of residual stresses. The instrumental angles are indicated by: χ, ω and φ, while ψ and ϕ are the desired angles. Orientation of diffraction plane, scattering vector, incident (i.b.) and reflected beam (r.b) are shown.

The standard method for stress measurement is not advised for the analysis of heterogeneous stress states because the penetration depth of X-ray radiation varies significantly during measurement when both orientations of incident and reflected beams are varied (Fig. 3.5). The effective penetration depth can be calculated for the ψ and ω-geometry:

$$\psi - geometry: \quad \tau = \frac{\cos\psi \sin\theta}{2\mu} \tag{3.17}$$

$$\omega - geometry: \quad \tau = \left[\frac{\mu}{\sin(\theta - \psi)} + \frac{\mu}{\sin(\theta + \psi)} \right]^{-1} \tag{3.18}$$

where ψ , α and 2θ angles are defined in Fig. 3.4.

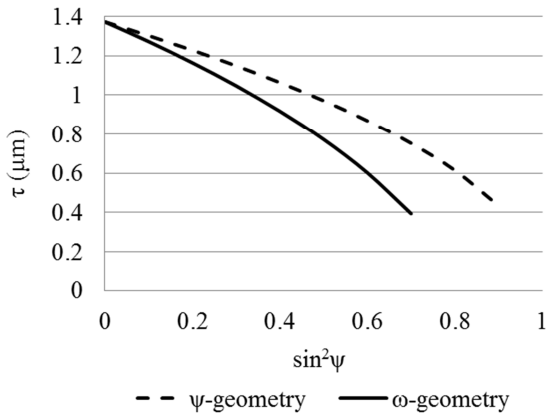

Fig. 3.5. Penetration depth calculated from Eqs. 3.17. and 3.18. for polished tungsten (τ = 3313 cm^{-1}, Cu $K_{\alpha 1}$ radiation) in function of $sin^2\psi$.

Consequently, the volume for which the measurement is performed is not well defined and the interpretation of the results is not unique. Using the standard X-ray $sin^2\psi$ method, the stress gradient can be estimated only if a special character of stress evolution is assumed (for example exponential or linear variation with depth). Moreover, this estimation is based on the curvature of the $sin^2\psi$ plot [3, 44], which can also be influenced by other effects (presence of the σ_{13}^I or σ_{23}^I shear stresses or sample anisotropy).

The example of $sin^2\psi$ plots for different ϕ angles measured using ω and ψ geometries (mechanically polished tungsten was measured for the same experimental conditions as peaks presented in Fig. 2.9, details are given in Table 5.4 for PANalytical – Empyrean diffractometer). The linear behaviour of the functions means that the stress gradient is not present in the penetration depth reached by diffraction. The results presented in Table 3.1 show the same stresses determined using both methods.

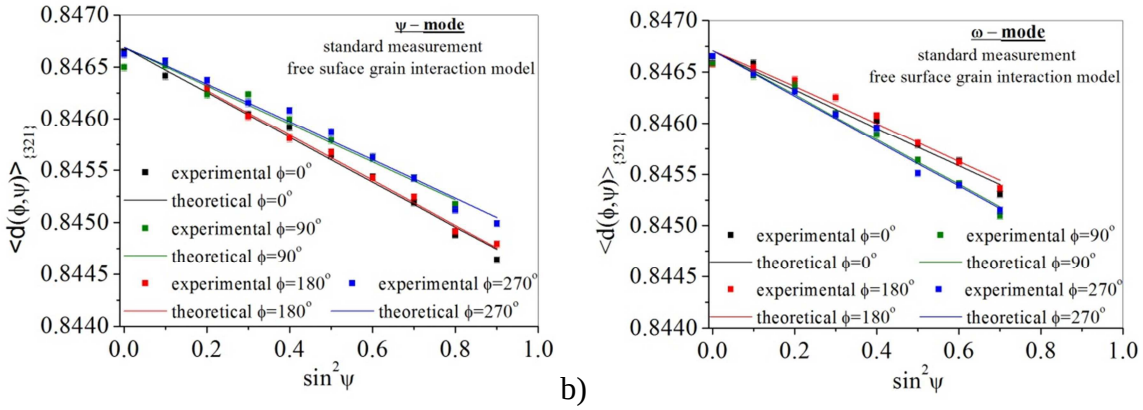

a) b)

Fig. 3.6. Interplanar spacings $<d(\phi,\psi)>_{\{hkl\}}$ vs. $sin^2\psi$ for mechanically polished tungsten sample. Results for ψ – geometry (a) and ω – geometry (b).

Table 3.1. Comparison of the results obtained for two different geometries.

geometry	σ^I_{11} (MPa)	σ^I_{22} (MPa)	χ^2	τ (μm)
ω	-660 ± 23	-787 ± 23	4.8	0.9
ψ	-657± 17	-774± 16	4.2	1.0

Finally it should be stated that the standard method can be used to measure stress gradient using ED method with synchrotron radiation. In this case the ψ-geometry is used with constant 2θ angle and the reflection are obtained for different energies $<E>_{\{hkl\}}$ corresponding to interplanar spacings $<d>_{\{hkl\}}$ according to Eq. 3.15. Because the absorption coefficient μ depends on the energy, also so measured $<d>_{\{hkl\}}$ vs. $sin^2\psi$ function will be determined for different depths (Eq.3.16). Therefore, the mean stresses obtained for different reflections will be defined also for different τ (see Eq. 3.16). The problem is that the penetration depth for each plot $<d>_{\{hkl\}}$ vs. $sin^2\psi$ (Fig. 3.5) changes significantly and in the case of significant stress gradient these functions are far from

linearity. Consequently the ED standard method can be used only in the case of small in depth variation of the stress.

3.1.2. UNIVERSAL PLOT METHOD

An interesting modification of the standard diffraction experiment introduced in order to find $\sigma_{ij}^{I}(\tau)$ in depth profile was proposed and developed by Genzel [36, 43, 45, 46]. In this method, an original treatment of standard $sin^2\psi$ plots was performed, assuming biaxial residual stress in the quasi-isotropic sample. With these assumptions the mean value from lattice strains measured for ϕ = 0^0 and ϕ = 90^0 can be related with so called in-plane residual stresses ($\sigma_{\parallel}^{I}(\tau)$) at τ depth by an equation [36]:

$$< \varepsilon(\psi,\tau) >_{\{hkl\}}^{\pm} = F_{\parallel}(hkl,\psi)\sigma_{\parallel}^{I}(\tau) \tag{3.19}$$

where: $\sigma_{\parallel}^{I}(\tau) = \frac{1}{2}\left[\sigma_{11}^{I}(\tau) + \sigma_{22}^{I}(\tau)\right]$, $F_{\parallel}(hkl,\psi) = \frac{1}{2}S_2^{hkl}\sin^2\psi + 2S_1^{hkl}$ and

$$< \varepsilon(\psi,\tau) >_{\{hkl\}}^{\pm} = \frac{1}{2}\left[< \varepsilon(\phi = 0^0,\psi,\tau) >_{\{hkl\}} \pm < \varepsilon(\phi = 90^0,\psi,\tau) >_{\{hkl\}}\right] \tag{3.19 a}$$

Then the principal stress component can be expressed by [36]:

$$\sigma_{11/22}^{I}(\tau) = \frac{< \varepsilon(\psi,\tau) >_{\{hkl\}}^{\pm}}{F_{\parallel}(hkl,\psi)} \pm \frac{< \varepsilon(\psi,\tau) >_{\{hkl\}}^{\pm}}{\Delta F_{\parallel}(hkl,\psi)} - \frac{F_{33}(hkl,\tau)}{F_{\parallel}(hkl,\psi)}\sigma_{33}^{I}(\tau) \tag{3.20}$$

where (for quasi-isotropic polycrystalline materials):

$$\Delta F_{\parallel}(hkl,\psi) = \frac{1}{2}S_2^{hkl}\sin^2\psi \text{ and } F_{33}(hkl,\psi) = \frac{1}{2}S_2^{hkl}\cos^2\psi + S_1^{hkl}(hkl)$$

Assuming a biaxial residual stress state ($\sigma_{33}^{I}(\tau)$=0) the stress free parameter $d_{\{hkl\}}^{0}$ = $< d^0(\psi^*,\tau) >_{\{hkl\}}$ can be measured in the strain-free direction ψ^* of the biaxial stress state, i.e. for $F_{\parallel}(hkl,\psi)$=0 ($\psi^* = \arcsin[-2S_2^{hkl}/S_1^{hkl}]^{1/2}$). Therefore if $d_{\{hkl\}}^{0}$ is known, the right hand side of the Eq. 3.8 contains only the experimental information and the unknown in-plane stresses is on the left hand side. As the result the profiles of biaxial stresses can be

easy determined. However, in the presence of $\sigma_{33}^{I}(\tau)$ stress fields in the eq. 3.20 the additional term occurs. It can falsify the in-plane stress depth distribution by a certain amount [43].

In this method the stress distribution vs. penetration stress can be directly computed from single standard $sin^2\psi$ plot and presented as a plot versus penetration depth [36]. Moreover, applying high energy with ED mode the universal plots for different ranges of penetration depths can be determined and shown together as an 'universal plot'.

3.1.3. SCATTERING VECTOR METHOD

Another method used for determination of in depth stress gradient is the scattering vector method [38, 43, 45]. In this method the components of the stress tensor $\sigma_{ij}^{I}(\tau)$ (in function of penetration depth τ) are determined from a series of measured $< d(\phi,\psi,\tau)>_{\{hkl\}}$ depth profiles. The interplanar spacings $< d(\phi,\psi,\tau)>_{\{hkl\}}$ are measured for constant ϕ and ψ angles, with stepwise rotation η of the sample around the scattering vector (i.e., L_3 axis in Fig. 2.6). To calculate penetration depths τ (for given ϕ and ψ) corresponding to different η angles Eq. 3.5 is applied. Using the AD diffraction, measurements are performed for at least two ψ angles. Next the self-consistent calculations of triaxial residual stress gradient are performed. In this variation procedure [45], perpendicular stress expressed by:

$$\sigma_{33}^{I}(\tau)=\frac{<\varepsilon(\psi^{*},\tau)>_{\{hkl\}}^{+}}{F_{33}(hkl,\psi)}=\frac{<d(\psi^{*},\tau)>_{\{hkl\}}^{+}-d_{\{hkl\}}^{0}}{F_{33}(hkl,\psi)} \tag{3.21}$$

(where: $<\varepsilon(\psi^{*},\tau)>_{\{hkl\}}^{+}$ is the same mean strain as in Eq. 3.19 a but in "strain-free direction of the biaxial residual stress state" defined by ψ^{*}) and the in-plane stress components $\sigma_{11/22}^{I}(\tau)$ given by Eq. 3.20 are calculated for varying value of $d_{\{hkl\}}^{0}$. The calculations are repeated for strain profiles obtained for two or more inclinations ψ receiving different profiles of triaxial stress $\sigma_{ij}^{I}(\tau)$ (or mean stress $\sigma_{\|}^{I}(\tau)$). If the procedure is convergent, the same profiles of $\sigma_{ij}^{I}(\tau)$ (or $\sigma_{\|}^{I}(\tau)$) must be gained for different ψ inclinations (the difference between such profiles determines criterion of

convergence). Finally, when the convergence is reached, the triaxial residual stress state within the accessible penetration depth and the strain-free lattice parameter are determined, without the need of some stress-free reference sample (assuming $d^0_{\{hkl\}}$ does not change with depth due to structure heterogeneity).

The above described method was also applied using ED measurements with synchrotron radiation [43]. The advantage of this improvement is certainly increased number of strain profiles measured at different penetration depths (for different energies). This provides more available input data used for stress calculations. Moreover, the stresses can be studied for significantly increased depth in comparison with laboratory apparatus (with X-ray tubes).

3.2. METHODS WITH CONSTANT PENETRATION DEPTH

The geometry based on the grazing incidence X-ray diffraction can be applied to measure gradient of residual stresses in surface layers [14, 19, 38, 45, 47, 48, 49]. The principle of this method is the use of a small incidence angle (α in Fig. 3.7) for which the path in the material of the incidence beam is much longer than the path of diffracted beam ($a>>b$ in Fig. 3.7). To perform stress measurements for constant penetration depth (τ), the orientation of scattering vector characterized by ψ angle must be varied, while small α is kept unchanged. To do this, different methods were proposed [19]: (a) multiple reflection and single wavelength – multi-reflection method [14, 47, 50, 51], (b) single reflection but multiple wavelengths – multi-wavelength method [52]; (c) single reflection and single wavelength - multiple χ method [53, 54].

3.2.1. MULTI-REFLECTION GRAZING INCIDENCE X-RAY DIFFRACTION

The multi-reflection grazing incidence X-ray diffraction (MGIXD) geometry [14], called also multiple {hkl} grazing incidence [19], is characterized by a small and constant incidence angle α and by different orientations of the scattering vector (variable $2\theta_{\{hkl\}}$ angle for a constant wavelength; see Fig. 3.7) given by the equation:

$$\psi_{\{hkl\}} = \theta_{\{hkl\}} - \alpha \tag{3.22}$$

where $2\theta_{\{hkl\}}$ are the diffraction angles corresponding to those reflections *hkl* for which diffraction peaks are measured [14, 48, 55].

In this geometry the diffraction plane (defined by incident and diffracted beam) is always perpendicular to the sample surface.

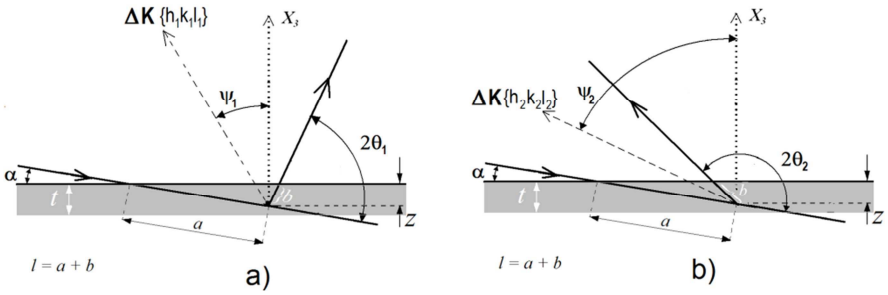

Fig. 3.7. Geometry of MGIXD-sin$^2\psi$ method. The incidence angle α is fixed during measurement while the orientation of the scattering vector is characterised by the angle $\psi_{\{hkl\}}$.

Analogically to the standard method stresses can be determined from the interplanar spacings measured in direction of the scattering vector, i.e. in this case, for different $\psi_{\{hkl\}}$ (and consequently various $\theta_{\{hkl\}}$ angles) and for constant α angle (Fig. 3.7). However, in the case of multi-reflection method instead of $<d(\phi,\psi,\bar{z})>_{\{hkl\}}$, the so called equivalent lattice parameters $<a(\phi,\psi,\bar{z})>_{\{hkl\}}$ are expressed by the macrostresses $\sigma_{ij}^{I}(\bar{z})$ and strain free a_0 lattice constant [14]:

$$<a(\phi,\psi,\bar{z})>_{\{hkl\}} = [\, F_{ij}(hkl,\phi,\psi)\,\sigma_{ij}^{I}(\bar{z})\,]\,a_0 + a_0 \qquad (3.23)$$

where:

for cubic crystal structure: $<a(\phi,\psi,\bar{z})>_{\{hkl\}} = <d(\phi,\psi,\bar{z})>_{\{hkl\}}\sqrt{h^2+k^2+l^2}$ (3.24 a)

or for hexagonal structure: $<a(\phi,\psi,\bar{z})>_{\{hkl\}} = <d(\phi,\psi,\bar{z})>_{\{hkl\}}\left\{\left[\frac{4}{3}(h^2+hk+k^2)\right]+\frac{l^2}{(c/a)^2}\right\}^{-1/2}$ (3.24 b)

where ϕ can be chosen arbitrary, while ψ depends on the diffraction angle for given reflection *hkl* (Eq. 3.22).

In the case of MGIXD method the measurements of interplanar spacings $< d(\phi,\psi,\tau) >_{\{hkl\}}$ are performed in the near surface volume, which is limited by radiation absorption. To define this volume, the path of the X-ray beam through the sample must be considered (Fig. 3.7). The measured average interplanar spacings $< d(\phi,\psi,\tau) >_{\{hkl\}}$ are equal to:

$$< d(\phi,\psi,\bar{z}) >_{\{hkl\}} = \frac{\int_0^t d(hkl,\phi,\psi,z)\exp[-\mu\, l(z)]\,dz}{\int_0^t \exp[-\mu\, l(z)]dz} \quad \text{and} \quad l(z) = z\left(\frac{1}{\sin\alpha} + \frac{1}{\sin(2\theta_{\{hkl\}} - \alpha)}\right) \qquad (3.25)$$

where the above formula can be used if $\alpha >> \alpha_{cr}$ (α_{cr} is the critical angle for total external reflection), z is a depth below the surface and the average is calculated over the volume of all reflecting grains in the beam path, i.e. from surface (z = 0) to the thickness of the coating ($z = t$). If the stresses are measured in a monolithic sample or in a thick coating $t \to \infty$.

For $\alpha >> \alpha_{cr}$, Eq. 3.25 is usually expressed in the equivalent corresponding to effective depth $\bar{z}$ given by Eq. 3.4:

$$< d(\phi,\psi,\bar{z}) >_{\{hkl\}} = \frac{\int_0^t d(hkl,\phi,\psi,z)\exp[-z/\tau]\,dz}{\int_0^t \exp[-z/\tau]dz} \quad \text{and} \quad \tau = \left(\frac{\mu}{\sin\alpha} + \frac{\mu}{\sin(2\theta_{\{hkl\}} - \alpha)}\right)^{-1} \qquad (3.26)$$

By using a long incident beam path for small α angle ($a(x) >> b(x)$ in Fig. 3.7), the above equation can be simplified, i.e.: $\tau = \frac{\sin\alpha}{\mu}$, where τ nor $\bar{z}$ does not depend on the $\theta_{\{hkl\}}$ (or $\psi_{\{hkl\}}$) angle. What is more the penetration depth can be changed by appropriate selection of α angle to investigate materials on different depths below sample surface (order of μm or even below 1 μm).

Using Eq.3.23 and assuming $\sigma_{33}^{I}(\tau) = 0$ the other parameters of stress tensor and a_0 parameter can be determined from least square fitting procedure (as described in the case of Eq. 2.45 and 2.46). On the other hand, if the value a_0 is known full stress tensor can be found for given τ or $\bar{z}$. This gives a possibility to measure a stress gradient as well

as the in-depth dependence of a_0. It should be stated, that till now, in the case of hexagonal structure the value of *c/a* was substituted from the tables [14, 47], and however in the next part of this work an original method for determination of *c/a* in depth profile will be proposed.

In Fig. 3.8 the dependence of effective penetration depth for different geometries and two materials (Al and Ti) are presented. Calculations were performed for absorption coefficients μ_{Al} = 135.6 cm^{-1} and μ_{Ti} = 918.9 cm^{-1} occurring for Cu X-ray radiation and for thick sample (i.e. for t>>τ, when $\overline{z} = \tau$). Accordingly to the above discussion strong dependence of τ on ψ angle is seen in the case of standard ω and ψ - geometries, while almost constant value of τ was determined for MGIXD method. Moreover, grazing incident geometry allows investigating much shallower depths, which can be changed by setting different α angles.

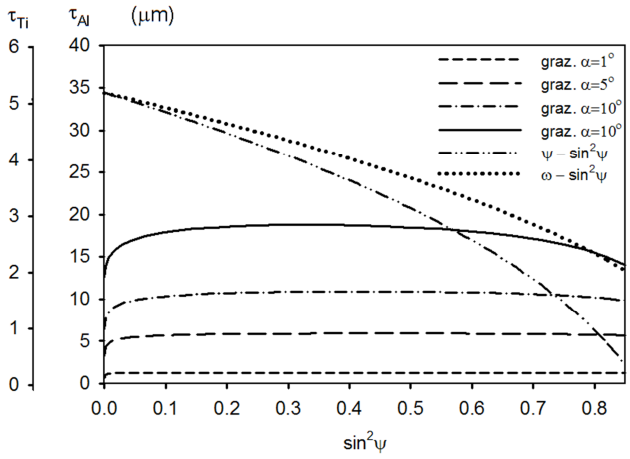

Fig. 3.8. The penetration depth (τ) vs. $sin^2\psi$ for classical ψ and ω geometries (shown for 2θ corresponding to 422 reflection in the case of Al) and for MGID-$sin^2\psi$ method (shown for four incidence angles). Two scales of τ corresponding to Al and Ti material are shown.

In present work the MGIXD method is significantly developed, tested and applied to measure in-depth profile of stresses and stress free lattice parameter as well as *c/a* parameter in the case of hexagonal crystal structure. A great advantage of this method is the possibility of using Williamson-Hall method for crystallite size and the root mean square of lattice strain determination [56, 57].

3.2.2. MULTI-WAVELENGTH METHOD

Multi-wavelength method allows to perform measurements of stresses at a constant penetration depth by applying X-rays having different energies (wavelengths) by using synchrotron radiation or different tubes at laboratory equipment [19, 52]. The experimental configuration is similar as this used in the above described multireflection method (diffraction plane is perpendicular to the sample surface as shown in Fig. 3.5) but in this case peaks for the selected single *hkl* reflection are measured. In order to gain the proper set of data, i.e. to change ψ angles (determining inclination of the scattering vector), for a given *hkl* reflection the scattering angle 2θ is varied by changing value of the wavelength. The constant penetration depth is kept unchanged adjusting additionally the incident angle α. In this method the relation between ψ, 2θ and α angles is given by Eq. 3.22.

3.2.3. MULTIPLE X - METHOD (PSEUDO-GRAZING)

Pseudo-grazing incident X-ray (p-GIXD) method, called also multiple χ [19] allows evaluation of the average level of stresses and their distribution below the surface by setting the desired penetration depth which can be done choosing the proper incident angle α (angle between incident beam and sample surface) [58]. In this method only one *hkl* reflection is used but additional rotation of the sample by χ angle (Fig. 3.4) is performed. To keep α angle constant, for different inclinations of the scattering vector (defined by ψ angle) the orientations of the sample and the angles of diffraction cannot be chosen independently. The values of these angles must be calculated from the directions of the incident beam, diffracted beam and diffraction vector as well as from the penetration depth which need to be constant when the sample is rotated. A combination of ω and χ tilting angles (see Fig. 3.4 a) allows to achieve the constant penetration depth of X-rays.

In this method the penetration depth can be expressed as [53]:

$$\tau = \frac{\sin\omega\sin(2\theta-\omega)\cos\psi}{\mu[\sin\omega+\sin(2\theta-\omega)]\cos(\omega-\theta)} \tag{3.27}$$

where: $\psi = \arccos[\cos\chi\cos(\omega-\theta)]$ and $\cos\chi = \frac{\cos\psi}{\cos(\omega-\theta)}$.

For each value of desired ψ angle and given penetration depth τ it is necessary to select proper values of the instrumental angles ω and χ according to Eq. 3.27. Next, in order to set desired angle ϕ, the sample must be rotated around normal to the surface by instrumental angle φ which can be calculated from the following relation (see Fig. 3.4):

$$\varphi = \phi + \arctan\left[\frac{-\sin\chi}{\tan(\omega-\theta)}\right] \tag{3.28}$$

The main disadvantage of this method is the limitation of the accessible range of specimen tilt angles ψ for reflections having large 2θ angles (over 100°). This limits are define by the limit of both ω (lower limit) and χ (upper limit) geometries. Table 3.2 summarizes the example of the results for polished Al2017 and Ti6Al4V samples showing the possible range of the ψ angle in p-GIXD. Furthermore, this method can be applied only on the diffractometers with the Euler cradle.

Table 3.2. Possible range of the ψ angle in p-GIXD method for Cu K_α radiation.

hkl	2θ (°)	ψ range (°)	$\sin^2\psi$
Ti6Al4V			
{103}	71	26-65	0.2-0.8
{014}	93	37-68	0.4-0.9
{114}	115	48-71	0.6-0.9
Al2017			
{220}	64	23-64	0.2-0.8
{311}	77	29-66	0.2-0.8
{331}	111	46-71	0.5-0.9

3.3. X-RAY DIFFRACTION ELASTIC CONSTANTS AND STRESS FACTORS

To study the stress state in a polycrystalline material the stresses must be related to the measured lattice strains using the X-ray elastic constants or stress factors, as shown in Eqs. 2.43 and 2.44. In the present work X-ray diffraction methods are applied to measure residual stresses in materials and the problem of X-ray stress factors (XSF) used for the interpretation of results will be studied in chapter 5. To show the influence of the X-ray stress factors on the interpretation of MGIDX results, polycrystalline materials having low (W, Ti alloy) and high elastic anisotropy of crystallites (Ni alloy, CrN coating) are investigated. The information about elastic anisotropy of a monocrystal is given by so-called Zener anisotropy factor *A*, defined as [59]:

$$A = \frac{2c_{44}}{(c_{11} - c_{12})} \tag{3.29}$$

where: c_{44} and $(c_{11}-c_{12})/2$ represent the shear stiffness in a [100] direction on a (100) plane an in a [110] direction on a (110) plane, respectively (c_{ij} are single crystal stiffnesses written using matrix convention). For perfectly isotropic crystal A=1. Values of single crystal elastic constants and Zener factor for materials studied in this work are given in Table 3.3.

Table 3.3. Single crystal elastic constants (c_{ij}) and Zener factors (A) for studied materials [60, 61, 62, 63, 64, 65, 66].

C_{ij} (GPa) or A / material	c_{11}	c_{12}	c_{13}	c_{33}	c_{44}	c_{66}	A
W	501	198	198	501	151	151	1.01
Ti	162	92	69	180	47	35	1.34
Ni	245	148	148	245	134	134	2.76
CrN	542	27	27	542	88	88	0.34
Austenite stainless steel	197	122	122	197	124	124	3.3

X-ray as well as macroscopic elastic constants can be calculated from single-crystal elastic constants by adopting a grain-interaction model [19, 67]. The commonly used

methods for calculation of the diffraction elastic constants are Voigt [68], Reuss [69] and Kröner [70] models or so called direction dependent Vook–Witt [19] or recently proposed free- surface models [71, 72]. The difference between the models is the type of assumed intergranular elastic interaction.

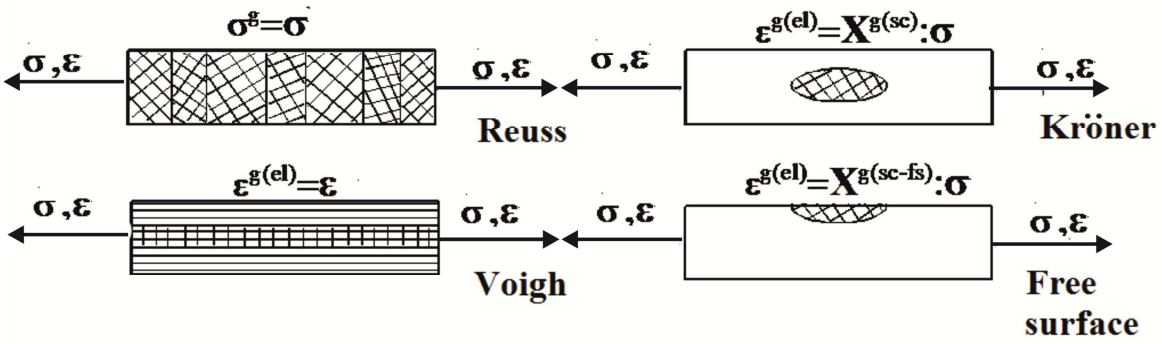

Fig. 3.9. Scheme of interaction between grains for four different models: a) Reuss - homogeneous stress, b) Voigt -homogeneous strain and c) Kröner – (sc – self consistent) ellipsoidal inclusion within homogeneous medium and d) free surface – (sc-fs – self consistent free surface) ellipsoidal inclusion placed near the surface of the homogeneous medium [20].

The Voigt model

In the Voigt [68] model the uniform grain elastic strain is assumed to be equal to the elastic macro-strain value [73]. The strain distribution is homogenous in the sample so there is a continuity of the strain at the grain boundaries. Stress tensor for each differently orientated crystallite will not be the same [19].

The X-ray stress factors (independent from *hkl*) can be calculated from [73]:

$$F_{ij}(\phi,\psi,f) = m_k m_l \left[\boldsymbol{C}^S\right]^{-1}_{klij} \tag{3.30}$$

where $\boldsymbol{C}^S$ is the macroscopic stiffness tensor expressed in the sample coordinate system **S** (Fig. 2.6) and versor $\vec{m}$ is defined in Eq. 2.41.

The macroscopic stiffness tensor $\boldsymbol{C}^S$ is calculate from single crystal stiffnesses $c_{ijkl}^S(\varphi_1,\Phi,\varphi_2)$ having orientations φ_1, Φ, φ_2 expressed in S system, using orientation distribution function $f(\varphi_1,\Phi,\varphi_2)$:

$$C_{ijkl}^S = \frac{1}{8\pi^2}\int_0^{2\pi} d\varphi_1 \int_0^{2\pi} d\varphi_2 \int_0^{\pi} c_{ijkl}^S(\varphi_1,\Phi,\varphi_2)\, f(\varphi_1,\Phi,\varphi_2)\sin\Phi\, d\Phi \tag{3.31}$$

where φ_1,Φ,φ_2 are the Euler angles describing lattice orientation of polycrystalline grain [74].

In the absence of texture, i.e. for $f(\varphi_1,\Phi,\varphi_2)$=1, the polycrystal is macroscopically isotropic, and X-ray elastic constants S_1^{hkl} and $1/2S_2^{hkl}$ can be used instead of the stress factors. The XECs, according to the Voigt model do not depend on *hkl* and thus are equal to the mechanical constants. Following Welzel [19], the X-ray elastic constants S_1 and $1/2S_2$ can be calculated from the components of the single-crystal compliances defined with respect to the lattice (s_{ij} – two indexes convention). For cubic crystals:

$$S_1 = \frac{2s_0(s_{11}+2s_{12})+5s_{12}s_{44}}{6s_0+5s_{44}}; \qquad \frac{1}{2}S_2 = \frac{5(s_{11}-s_{12})s_{44}}{6s_0+5s_{44}} \quad \text{and} \quad s_0=s_{11}-s_{12}-s_{44}/2 \tag{3.32}$$

The Reuss model

In Reuss model [73, 75] the stress is assumed to be uniform across the sample for all polycrystalline grains. For each crystallite the strain tensor is different so at the grain boundaries the strain mismatch will occur [19].

The X-ray stress factors can be calculated [1, 19]:

$$F_{ij}(hkl,\phi,\psi,f) = m_k m_l \frac{\sum_{\{hkl\}}\int_0^{2\pi} s_{klij}^S(hkl,\xi,\phi,\psi)\, f(hkl,\xi,\phi,\psi)d\xi}{\sum_{\{hkl\}}\int_0^{2\pi} f(hkl,\xi,\phi,\psi)d\xi} \tag{3.33}$$

where the same mean value as in Eq. 2.28 is calculated for $\boldsymbol{s}^S$ – single crystal elastic compliance tensor expressed in **S** system, i.e., average over volume of diffracting grains.

Both $s^{S}_{klij}(hkl,\xi,\phi,\psi)$ and $f(hkl,\xi,\phi,\psi)$ values for given reflection *hkl* are expressed as functions of orientation angles defined in Fig. 2.8.

In the absence of texture i.e. when *f(hkl,ξ,φ,ψ)*=1, the S_1^{hkl} and $1/2S_2^{hkl}$ can be used instead stress factors. For cubic crystal, the X-ray elastic constants S_1^{hkl} and $1/2S_2^{hkl}$ can be calculated from the components of the single-crystal compliances [19]:

$$S_1^{hkl} = s_{12} + s_0\Gamma(hkl)\,, \qquad \frac{1}{2}S_2^{hkl} = s_{11} - s_{12} - 3s_0\Gamma(hkl) \tag{3.34}$$

where $\Gamma(hkl)=(h^2k^2+h^2l^2+k^2l^2)/(h^2+k^2+l^2)$ is the orientation factor for cubic materials.

XECs according to the Reuss model are *hkl* - dependent.

The Eshelby – Kröner model

In the self-consistent [70] method the grain is approximated by an ellipsoidal inclusion [76], which is embedded into a homogenous and isotropic medium with the elastic properties of the entire polycrystal. In this model the inclusion has an elastic property of cubic symmetry [77]. Kneer (1965) [78] extended the model for textured specimens [19].

Following Welzel [19] the elastic strain of a single-crystalline inclusion is given by:

$$\varepsilon_{ij} = [S_{ijkl} + t_{ijkl}]\sigma^{I}_{kl} \tag{3.35}$$

where t_{ijkl} is the tensor which describes the deviation of the elastic properties of an individual grain from the average elastic properties of the entire polycrystal/surrounding matrix. It depends on the shape of the inclusion, the single-crystal elastic constants and the macroscopic mechanical compliance tensor S_{ijkl} of the aggregate. Usually, spherical inclusions are considered.

The X-ray stress factors can be calculated from:

$$F_{ij}(hkl,\phi,\psi,f) = m_k m_l \frac{\int_0^{2\pi} [S^S_{klij}(hkl,\xi,\phi,\psi) + t^S_{klij}(hkl,\xi,\phi,\psi)]\, f(hkl,\xi,\phi,\psi) d\xi}{\int_0^{2\pi} f(hkl,\xi,\phi,\psi) d\xi} \tag{3.36}$$

In the absence of texture the $f(hkl,\xi,\phi,\psi)=1$, the X-ray elastic constants S_1^{hkl} and $1/2S_2^{hkl}$ can be defined. For cubic crystallites the XEC's can be calculated from [19, 79]:

$$S_1^{hkl} = S_{12} + T_{12} + T_0\, \Gamma(hkl) \quad \text{and} \quad \frac{1}{2} S_2^{hkl} = S_{11} - S_{12} + T_{11} - T_{12} - 3T_0\, \Gamma(hkl) \tag{3.37}$$

where $T_0=T_{11}-T_{12}-2T_{44}$, $T_{11} - T_{12} = \dfrac{(G-\nu)(3K+6G)}{G[8G^2 + G(9K+12\nu) + 6\nu K]}$,

$2T_{44} = \dfrac{(G-\mu)(3K+6G)}{G[8G^2 + G(9K+12\mu) + 6\mu K]}$, $3K=1/(S_{11}+2S_{12})$, $\mu=1/S_{44}$, $2\nu=1/(S_{11}-S_{12})$ and

K is the bulk modulus, G is the shear modulus and S_{ij} are the macroscopic compliances (two indexes convention).

Free surface model

Free surface model [71, 72] treats grain as an ellipsoidal inclusion placed near the surface of the homogeneous medium. This is direction dependent model in which the interaction between grains is changing with the direction with respect to the sample.

In this model the grains close to the surface interact differently for the forces normal and parallel to the surface. For the direction perpendicular to the surface the grains exhibit a Reuss type of interaction behaviour and for the in surface plane they follow Kröner model. This idea is similar to that used in Vook-Witt model in which combination of Reuss and Voigt approaches is applied [19]. Therefore the elastic interaction between grains is neglected in the direction normal to the surface. Grains on the surface can freely deform in normal direction.

The X-ray stress factors can be calculated from:

$$F_{ij}(hkl,\phi,\psi,f) = m_k m_l \frac{\int_0^{2\pi} X^S_{klij}(hkl,\xi,\phi,\psi)\, f(hkl,\xi,\phi,\psi) d\xi}{\int_0^{2\pi} f(hkl,\xi,\phi,\psi) d\xi} \tag{3.38}$$

where:

$$X^S_{klij}(hkl,\xi,\phi,\psi) = \begin{cases} S^s_{klij}(hkl,\xi,\phi,\psi) \text{ for } k=3 \text{ or } l=3 \text{ as in Reuss model} \\ S^s_{klij}(hkl,\xi,\phi,\psi) + t^s_{klij}(hkl,\xi,\phi,\psi) \text{ for } k\neq 3 \text{ and } l\neq 3 \text{ as in Kröner model} \end{cases}$$

It should be underlined that the presented above models approximates real polycrystalline aggregate and in fact, the grain to grain interactions depend on the grain size distribution, grain boundary misorientation distribution and a Zener anisotropy factor. It is well known that the high crystal anisotropy together with crystallographic texture leads to nonlinearity of the $sin^2\psi$ plots obtained from standard methods of stress measurement [14, 19, 73]. One of the aims of this work is a verification of XEF calculated by different models and their application for interpretation of the results obtained using MGIXD method. In this case the difference between XEF calculated for different reflection *hkl* is very important especially for high single crystal anisotropy.

4. AIMS OF THE THESIS

The aim of this work is to develop one of the methodologies for stress measurements based on the grazing incidence X-ray diffraction, namely: multireflection grazing incidence method. On the basis of present knowledge and due to numerous advantages of this method it seems that it is a valuable tool for in-depth stress analysis, especially important for samples having stress gradient. That is why this method will be considerably developed and applied for coatings and surface layers of the materials subjected to different processes. Moreover one of the main purposes of the thesis is to investigate the mechanical properties of the polycrystals such as: elastic constants and their elastic anisotropy. Different theoretical grain elasto-plastic interaction models will be considered and applied in X-ray stress analysis in the thesis.

Till now the multireflection grazing incidence diffraction is not commonly used method for X-ray stress analysis. The commercial companies applied this method in their software but without taking into account the elastic anisotropy. What is more the systematic verification of this method with synchrotron radiation was not presented as well the precise limits of application were not summarized in the literature. That is why the main interests in the thesis will be concentrated on method development. Firstly, physical and geometrical effects influencing X-ray stress analysis will be taken into consideration. Secondly, elastic anisotropy and proper choice of the grain interaction models will be analysed in order to perform the valuable in-depth stress analysis. Thirdly, MGIXD method will be compared with standard methods, in effect new possibilities of this method will be highlighted. What is more method will be verified with synchrotron radiation. For the first time MGIXD method will be applied for EDDI (energy dispersive diffraction) experiment. Finally method will be applied to measure in-depth profile of stresses in materials subjected to different kinds of surface treatment.

At the end of the thesis the conclusions and practical recommendations for the users of this method will formulated.

5. TESTS, LIMITS AND EXPERIMENTAL DEVELOPMENTS OF THE MGIXD METHOD

The MGIXD method, proposed and developed by Skrzypek et al. [14, 48, 80], is an indispensable tool for non-destructive analysis of the heterogeneous stresses for different (well defined) volumes below the surface of the sample. There are important benefits in using different reflections to measure residual stresses. The most important is the wide range of scattering vector inclinations enabling sufficient range of measured $<a(\phi,\psi)>_{\{hkl\}}$ vs. $sin^2\psi$ plot which is used to calculate stress tensor from linear regression or least square method. The main disadvantage of multi-reflection method is that the interplanar spacings must be measured using also the low 2θ reflections (for example about 40^o-50^o). In this case the resolution of the strain obtained from measured peak shift is low (see Eq. 2.29) and this is why the peak position must be precisely determined. Precise measurement is possible due to simple experimental geometry in which the orientation of the scattering vector is changed in diffraction plane being perpendicular to the sample surface (like in ω geometry presented in Fig. 3.4). This configuration enables to use linear focus of the X-ray tube and application of the parallel beam geometry in which the parallel plate collimator (soller collimator) is used in the reflected beam optics (Fig. 5.13). Moreover, the incident beam can be collimated for example by Göbel mirror or multi-capillary collimator. The advantage of parallel beam is its high resolution in determination of peak position and minimisation of the error caused by sample displacement in z-direction (see Fig. 5.13). Till now, the parallel beam geometry used in MGIXD method was realised without collimation of the incident beam which was limited by slits [14, 48]. In the present work the geometry with Göbel mirror will be applied for stress measurements using MGIXD method. This experimental setup will be described and tested. The reproducibility of the results of XSA will be tested for different diffractometes on the powder sample [81].

In this chapter also some new developments of the methodology, most important corrections of experimental data and tests will be presented.

5.1. CORRECTIONS OF DETERMINED PEAK POSITION

In the case of stress measurement, it is of the highest importance to know the exact position of the diffraction peak. To do this a few factors [1, 6] should be taken into account [82]. Hence, these factors for MGIXD are discussed below.

5.1.1. INTENSITY CORRECTIONS

As mentioned in section 2.4 there are different reasons of peak asymmetry which should be corrected before determination of peak position. The appropriate correction factor used for standard and MGIXD methods are summarised in Table 5.1. These factors, depending on 2θ angle, should be used to correct each peak accordingly to Eq. 2.30, after background subtraction. The $LP(2\theta)$ correction is the same for all methods, $Ab(2\theta)$ correction is not necessary for ψ – geometry, while the absorption correction is the same for ω – geometry and MGIXD methods. However, in the latter case different angles are kept constant during peak scanning (i.e. ψ and α for ω – geometry and MGIXD method, respectively).

Table 5.1. The intensity correction factors for different methods of stress measurements [3, 6], where the angles: ψ, α and 2θ are defined in Fig. 3.7.

	ψ – geometry	ω – geometry	MGIXD
Lorentz-polarization: LP(2θ)		$\frac{1+\cos^2 2\theta}{\sin^2 \theta}$	
Absorption: Ab(2θ)	1	$(1+\tan\psi\cot\theta)/2$ $\psi = const.$	$(1+\tan(\theta-\alpha)\cot\theta)/2$ $\alpha = const.$

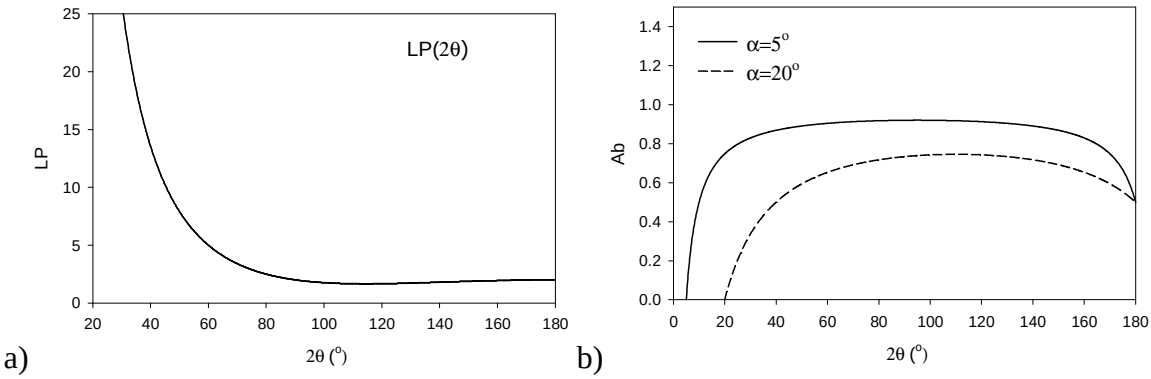

a) b)

Fig. 5.1. Dependence of LP(*2θ)* (a) factor and Ab(*2θ)* (b) factors on the scattering angle *2θ.*

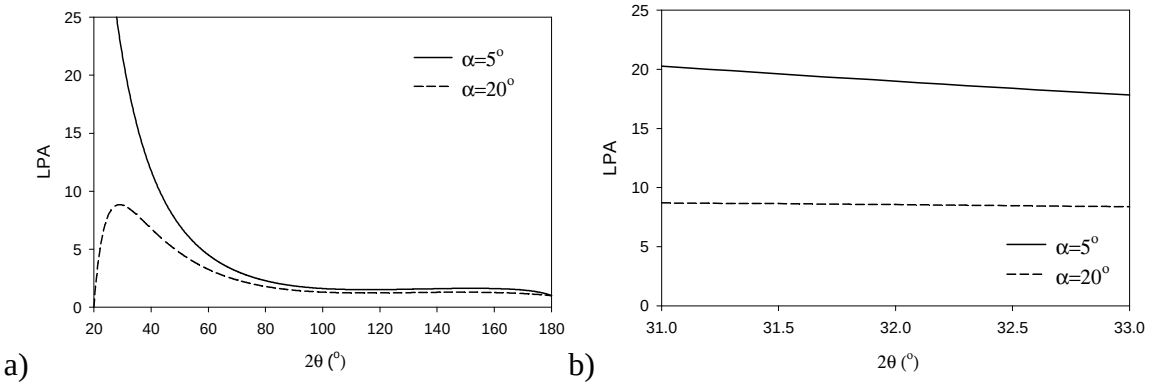

a) b)

Fig. 5.2. Dependence of LPA= LP * Ab factor on the scattering angle *2θ.* A small range of variation for relatively low *2θ* (about 30°) is shown in figure b.

As seen on Figs. 5.1 and 5.2 the most important variation of intensity (LPA = LP*Ab) factor occurs for small *2θ* angles. However, even in this range the relative changes of intensity are very small for the range of about 1 degree corresponding to the width of the measured peak (in the case of high density of defects).

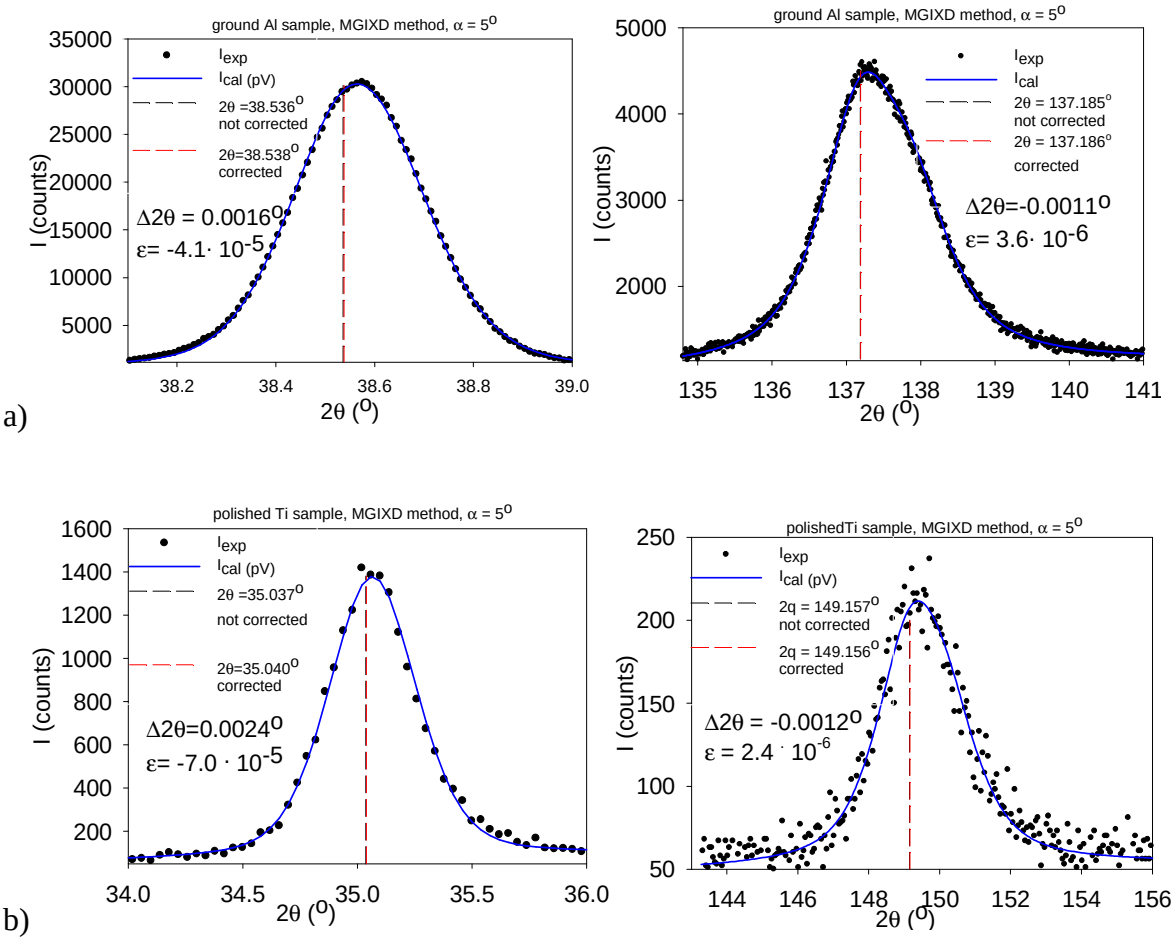

Fig. 5.3. The influence of LPA correction on the peak position for Al 2017 (a) and Ti grade 2 (b) polished sample. The peak position without and with correction for $K_{\alpha 1Cu}$ lines are indicated by dashed lines (in same cases the lines overlap). The PANalytical - X'Pert MRD (AGH, Kraków) diffractometer was used for ground Al2017 measurements while the PANalytical - X'Pert MRD (ENSAM, Paris) was used for polished Ti measurements. The configuration of both diffractometers is given in Table 5.4.

Examples of the diffraction peak shifts *(Δ2θ)* and corresponding strains (ε) calculated from Eq. 2.29 caused by the LPA correction are shown in Fig. 5.3. The peaks at low and high *2θ* angles for ground Al and Ti samples having significant structural peak broadening were chosen. Also, the values of stresses and lattice parameters determined with and without corrections for the studied samples are presented in Table 5.2. It can be concluded that even in the case of relatively broad diffraction peaks the influence of LPA correction on the measured peak position, corresponding strain and consequently value of determined stress or strain free lattice constants is very small.

Table 5.2. The stresses (σ) and lattice constants (a_0) determined for ground Al2017 and polished Ti grade 2 samples from the experimental data with and without LPA correction.

	calculation without LPA correction	calculation with LPA correction	difference
	ground Al 2017 (cubic)		
σ_{11}(MPa)	204.2 ± 4.8	206.9 ± 5.7	2.7
σ_{22}(MPa)	126.4 ± 4.8	129.4 ± 5.7	3.0
a_0 (Å)	4.04697 ± 0.00008	4.04698 ± 0.00010	0.00001
	polished Ti grade 2 (hexagonal)		
σ_{11}(MPa)	-411±11	-405.4 ±12.2	5.6
σ_{22}(MPa)	-405±11	-397.7 ±12.1	7.3
a_0 (Å)	2.9506 ±0.0001	2.9506 ± 0.0001	-
c/a	1.5881 ± 0.0003	1.5881 ± 0.0003	-

5.1.2. PEAK SHIFT DUE TO REFRACTIVE INDEX SMALLER THAN 1

The refraction of the X-rays on the boundary between two different media can significantly influence the position of the diffraction peak. The deviation of wave direction, described by Snell–Descartes law, causes a change in the value of the diffraction angle $\Delta 2\theta$ and additionally a small inclination $\Delta\psi$ of the scattering vector orientation. So far the only solutions for a refraction correction are given in the case of a smooth surface.

In this section the change of diffraction angle caused due to refractive index $n < 1$ is considered. The derived formulas are compared with those found in literature. Assuming a perfectly smooth surface, the influence of the refraction on the position of the diffraction peak can be studied by taking into account:

- the change of the wavelength value inside the studied material and its influence on the Bragg's law, Eq. 2.11,
- the refraction of the beam on the boundary between two different media described by Snell–Descartes law.

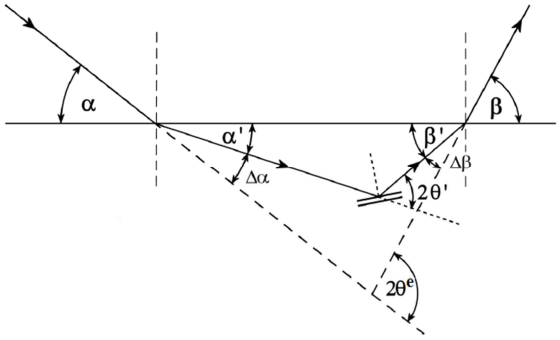

Fig. 5.4. Influence of refraction on the value of diffraction angle 2θ (where $2\theta^e$ is the measured diffraction angle).

The complex value of refractive index is defined as: $n=1-\delta+i\kappa$. The imaginary part κ indicates the amount of absorption loss when the electromagnetic wave propagates through the material, while the real part determining the refraction of the rays is slightly smaller than unity. The refractive index can be expressed by [83, 84]:

$$n=1-\delta, \quad \text{where:} \quad \delta=\frac{r_0\lambda^2}{2\pi}N_{at}f_{re}, \tag{5.1}$$

where: N_{at} – number of atoms per volume, r_0 – classical electron radius ($2.82\cdot10^{-15}$ m), f_{re} – real part of atomic scattering factor and λ – wavelength of X-ray radiation.

When the wave propagates from vacuum to the medium its length is changing:

$$\lambda'=\frac{\lambda}{n}=\frac{\lambda}{1-\delta} \tag{5.2}$$

where: λ and λ' are the wavelength values in the vacuum and in the material, respectively.

Inside the considered material, the Bragg's law (Eq. 2.11) can be written for λ' wavelength:

$$m\lambda'=\frac{m\lambda}{1-\delta}=2d\sin\theta' \tag{5.3}$$

where: $2\theta_B^{'}$ is the diffraction angle inside the material defined in Fig. 5.4 and m is the reflection order .

By simple comparison of the above formula with that written for the wavelength λ in the vacuum (i.e.: $m\lambda = 2d\sin\theta$), we get:

$$1-\delta = \frac{\sin\theta}{\sin\theta'} = \frac{\sin(\theta'-\Delta\theta_1)}{\sin\theta'} \tag{5.4}$$

where: $\Delta\theta_1 = \theta'-\theta$.

When assuming small value of $\Delta\theta_1$ angle the above formula can be transformed:

$$1-\delta = \frac{\sin\theta'\cos\Delta\theta_1 - \cos\theta'\sin\Delta\theta_1}{\sin\theta'} \approx 1-\cot\theta'\cdot\Delta\theta_1 \tag{5.5}$$

Finally, the correction of diffraction angle due to change of wavelength in Bragg law is given by:

$$\Delta 2\theta_1 = 2\delta\tan\theta' \tag{5.6}$$

The second correction can be calculated from Snell–Descartes law. For refractive index *n* less than 1, the relation between directions of the incident and diffracted beams is described by equations:

$$\frac{\sin(90^o-\alpha)}{\sin(90^o-\alpha')} = \frac{\cos\alpha}{\cos\alpha'} = 1-\delta \qquad \text{(5.7 a)} \qquad \frac{\sin(90^o-\beta)}{\sin(90^o-\beta')} = \frac{\cos\beta}{\cos\beta'} = 1-\delta \qquad \text{(5.7 b)}$$

where the angles are defined in Fig 5.4.

Next, the deviations of the incident and diffracted beams $\Delta\alpha = \alpha'-\alpha$ and $\Delta\beta = \beta'-\beta$ can be determined using two approximations:

$$\text{a)}\ \begin{matrix}\alpha\to 0\\ \beta\to 0\end{matrix} \quad \text{or} \quad \text{b)}\ \begin{matrix}\Delta\alpha\to 0 \ \ \textit{and} \ \ \Delta\alpha << \alpha'\\ \Delta\beta\to 0 \ \ \textit{and} \ \ \Delta\beta << \beta'\end{matrix} \tag{5.8}$$

In the first case (a), which will be applied for $\alpha' < 5^o$ or/and $\beta' < 5^o$, we can write (calculations are presented for α angle, but the same transformations could be done for small β) :

$$(1-\delta)\cos\alpha' = \cos\alpha \ \Rightarrow\ (1-\delta)\left(1-\frac{\alpha'^2}{2}\right) \approx \left(1-\frac{\alpha^2}{2}\right) \ \Rightarrow 1-\delta-\frac{\alpha'^2}{2} \approx 1-\frac{\alpha^2}{2} \tag{5.9}$$

and

$$\Delta\alpha = \alpha - \sqrt{\alpha - 2\delta} \qquad \text{or/and} \qquad \Delta\beta = \beta - \sqrt{\beta - 2\delta} \tag{5.10}$$

where $\alpha_{cr} = \sqrt{2\delta}$ is an critical incident angle for total external reflection (below this angle, i.e. when $\alpha < \alpha_{cr}$ only the reflected beam exists and $\Delta\alpha = 2\alpha_{cr}$).

The second approximation (b) is used for angles $\alpha' > 3^o$ or/and $\beta' > 3^o$:

$$1-\delta = \frac{\cos\alpha}{\cos\alpha'} = \frac{\cos(\alpha' + \Delta\alpha)}{\cos\alpha'} = \frac{\cos\alpha'\cos\Delta\alpha - \sin\alpha'\sin\Delta\alpha}{\cos\alpha'} \approx 1 - \tan\alpha' \cdot \Delta\alpha \approx 1 - \tan\alpha \cdot \Delta\alpha$$

and consequently

$$\Delta\alpha = \delta\cot\alpha \qquad \text{or/and} \qquad \Delta\beta = \delta\cot\beta \tag{5.11}$$

The change $\Delta 2\theta_2$ of the scattering angle caused by refraction is equal to the sum of $\Delta\alpha$ and $\Delta\beta$ deviations (see Fig. 5.4), i.e.: $\Delta 2\theta_2 = \Delta\alpha + \Delta\beta$.

Finally, the total shift of the diffraction peak $\Delta 2\theta = \Delta 2\theta_1 + \Delta 2\theta_2$ caused by the passing of the wave through a boundary between two different media and change of the wavelength, can be expressed by:

$$\begin{cases} \Delta 2\theta = \alpha - \sqrt{\alpha - 2\delta} + \delta\cot\beta + 2\delta\tan\theta & \text{for} \quad \alpha < 5^o \\ \Delta 2\theta = \delta\cot\alpha + \delta\cot\beta + 2\delta\tan\theta & \text{for} \quad \alpha > 3^o \end{cases} \tag{5.12}$$

where: $2\theta^e = 2\theta + \Delta 2\theta$, $2\theta^e$ is the measured diffraction angle and 2θ is the value which should be used in Bragg's relation written for the vacuum (Eq. 2.11). The value 2θ was used in the above equation instead of θ' because in good approximation $\theta \approx \theta' \approx \theta^e$ (angles defined in Fig. 5.4). In the above formula $\beta > 5^o$ was considered (to keep constant information depth for MGIXD method the condition $\beta >> \alpha$ must be fulfilled) and in the intermediate range $3^o < \alpha < 5^o$ both functions are convergent having practically the same value.

It should be underlined that the choice of the boundary angles 3^o and 5^o is not very strict and it was checked that for all studied materials the range of functions convergence is much wider. This choice has been suggested by Genzel [36] and it can be applied for any other material analyzed by conventional X-rays and also synchrotron radiation.

The above derived formulas can be compared with that given by James (1993) and applied for grazing incidence geometry by Hart [85]:

$$\Delta 2\theta = \frac{\delta}{\sin 2\theta}\left[2 + \frac{\sin\alpha}{\sin(2\theta-\alpha)} + \frac{\sin(2\theta-\alpha)}{\sin\alpha}\right] \tag{5.13}$$

and another one derived by Genzel [36]:

$$\Delta 2\theta = \arccos\left[\frac{\cos(\alpha-\Delta\alpha)\cos(\beta-\Delta\beta)}{\cos\alpha\cos\beta}(\cos 2\theta + \sin\alpha\sin\beta) - \right. \\ \left. -\sin(\alpha-\Delta\alpha)\sin(\beta-\Delta\beta)\right] - 2\theta \tag{5.14 a}$$

where:

$$\begin{cases} \Delta\alpha = \alpha - \sqrt{\alpha - 2\delta} & for \quad \alpha < 5^o \\ \Delta\alpha = \delta\cot\alpha & for \quad \alpha > 3^o \end{cases} \quad and\ /\ or \quad \begin{cases} \Delta\beta = \beta - \sqrt{\beta - 2\beta} & for \quad \beta < 5^o \\ \Delta\beta = \delta\cot\beta & for \quad \beta > 3^o \end{cases} \tag{5.14 b}$$

After elementary transformations it can be shown that the first formula (5.13., given by Hart) is equivalent to the derivation done in the present work but only for higher range of deformation (indicated by α > 3^o in Eq. 5.12). To demonstrate graphically this equivalence the shift of peak position predicted by different approaches are shown in Fig. 5.5a, where the wavelength for Cu radiation and Al sample where considered (values of δ and α_{cr} are given in Table 5.3). The results obtained with the second part of Eq. 5.12 but applied for high and low ranges of α perfectly coincide with that obtained from Hart equation but they do not agree with the results obtained from Genzel approach.

On the other hand comparing Genzel approach (Eq. 5.14) with the incomplete Eq. 5.12 (i.e. setting $2\delta\tan\theta = 0$) we get perfect convergence as shown in Fig. 5.5b. This means that in the case of Genzel approach the effect of wavelength change in Bragg's law is not taken into account (as seen also in Eq. 5.14a). Finally, the complete formula derived

in the present work (Eq. 5.12) is compared with Hart (Eq. 5.13) and Genzel (Eq. 5.14) approaches in Fig. 5.6. It can be concluded that Eq. 5.13 is accurate for higher α angles where $2\delta\tan\theta$ term is relatively more important but fails for angles close to α_{cr}. In the case of Eq. 5.14 the shift of peak position is underestimated for all range of α (this effect is not well visible for low α because the shift caused by refraction is relatively large).

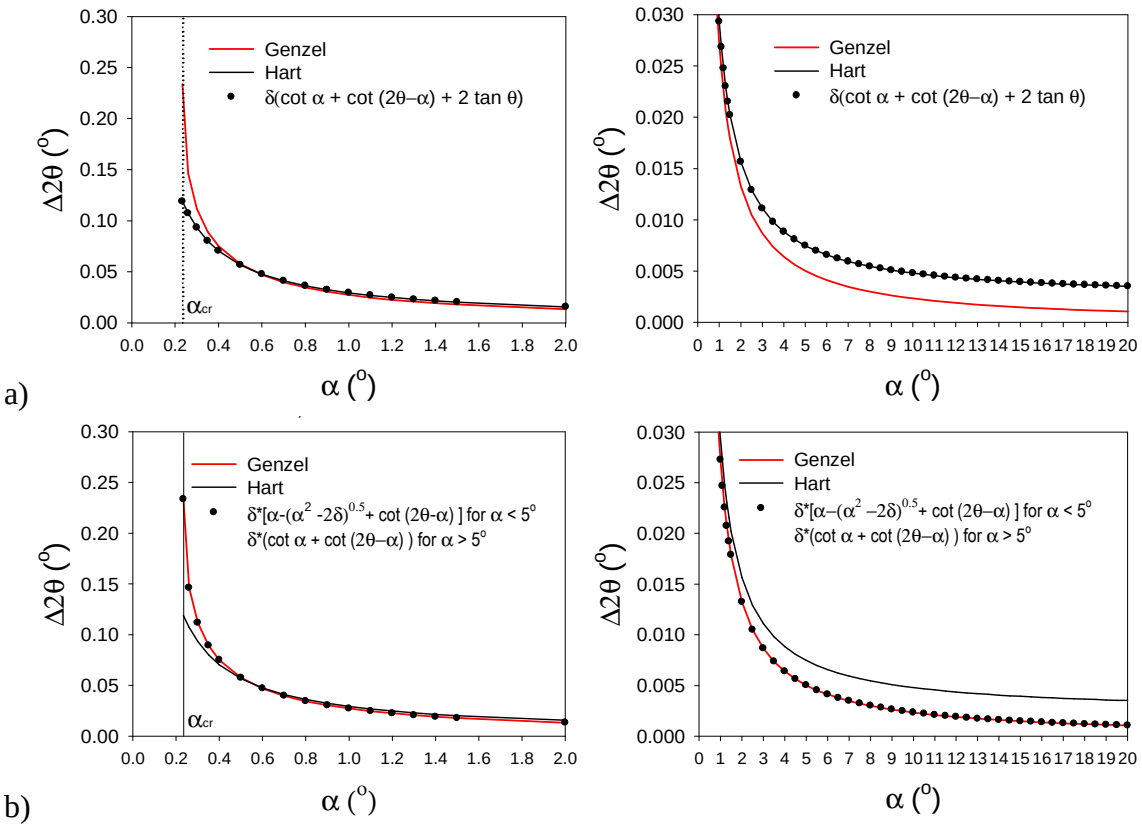

Fig. 5.5. Peak shift caused by refractive factor $n=1-\delta$ for $\delta=0.85$ and $\alpha_{cr}=0.24^{o}$ and $2\theta=132.5^{o}$ (Al sample and Cu radiation). Genzel and Hart approaches compared with the formula 5.12, i.e. assuming (a) $\Delta 2\theta=\delta(\cot\alpha+\cot\beta+2\tan\theta)$ for whole range of α and (b) $2\delta\tan\theta=0$.

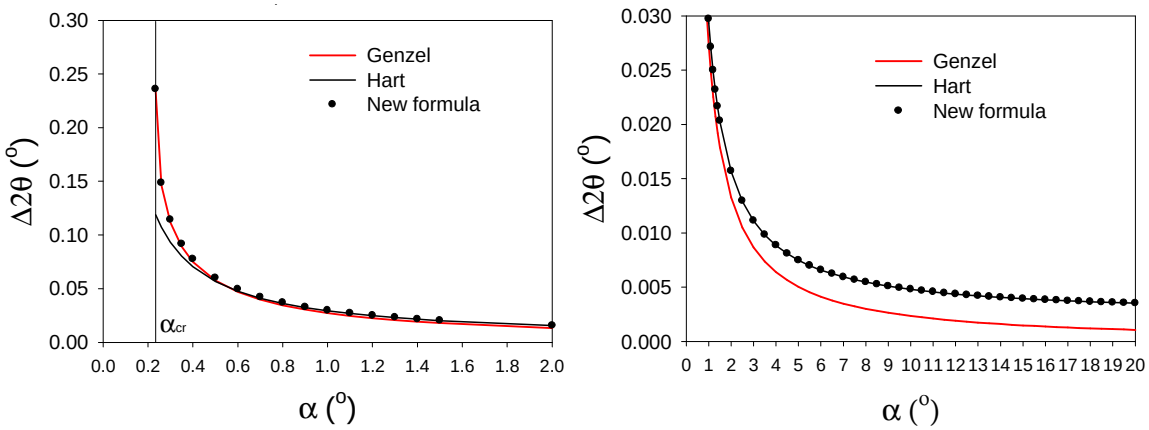

Fig. 5.6. Peak shift caused by refractive factor $n=1-\delta$ for the same parameters as in Fig. 5.5 compared for Genzel, Hart approaches and complete formula 5.12 ('New formula').

Although in Figs. 5.5 and 5.6 the shift of peak position is shown, the most important for stress analysis is to estimate the lattice strain corresponding to that shift. Therefore in Fig. 5.7 the pseudo-strain (i.e. fictitious strain which would be measured if the refraction effect is not corrected) calculated as $\varepsilon=-\cot\theta\cdot\Delta\theta$ (see Eq. 2.29) is shown for the same conditions as in previous Figs. 5.5 and 5.6 Moreover, the peak shift $\Delta 2\theta$ and strain ε calculated for other materials and wavelengths given in Table 5.3 are presented in Fig. 5.8.

Interesting conclusions can be drawn from the comparisons done in Figs. 5.7 and 5.8. The use of the MGIXD method is limited for small values of α angle due to significant shift of peak position (important pseudo-strain ε) caused by the refractive index $n<1$. This is especially important for low 2θ angles. The effect of wavelength change (term $\Delta\theta_1=2\delta\tan\theta$) is significant for large diffraction angle (2θ) and decreases for smaller 2θ. However, in the case of strain we can write: $\varepsilon_1=(-\cot\theta)(2\delta\tan\theta)/2=-\delta$, i.e. the wavelength change causes constant (for all angles α, β and 2θ) and not significant negative pseudo-strain equal $-\delta$ (compare Genzel approach and 'New formula' in Fig. 5.7). Thus the most important influence on the measured strain is caused by the refraction effect, i.e. $\varepsilon_2=-\cot\theta\cdot\Delta\theta_2$ (where $\Delta 2\theta_2=\Delta\alpha+\Delta\beta$, see Eqs. 5.10 and 5.11). Because $\Delta\theta_2$ is positive and does not depend on the 2θ angle, the pseudo-strain ε_2 is

negative and its absolute value strongly increases for low diffraction angle (see Figs. 5.7 and 5.8).

It should be emphasized that effect of the refractive index $n<1$ on the strain measurement depends strongly on value of the δ parameter, i.e. in the case of Al the pseudo-strain is about $\varepsilon_2 \approx -1.5\cdot 10^{-4}$ for $\alpha = 5^o$ and for low diffraction angle $2\theta = 35.5^o$, while $\varepsilon_2 \approx -1\cdot 10^{-3}$ for $\alpha = 5^o$ and $2\theta = 40.2^o$ in the case of tungsten (see Fig. 5.8). Moreover the pseudo-strains varies for different 2θ angles what leads to pseudo-stress (because $\psi = \theta - \alpha$), depending also on the value of X-ray diffraction constants. The pseudo-strains will cause also an erroneous value of determined stress free lattice parameter. Therefore the correction should be done for the experimentally determined peak position $2\theta^e$ according to the equation: $2\theta = 2\theta^e - \Delta 2\theta$.

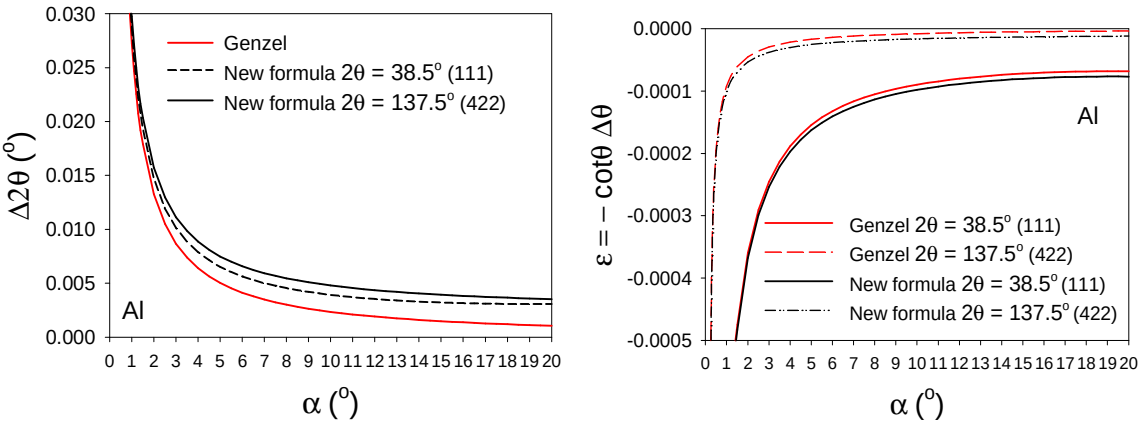

Fig. 5.7. Peak shift $\Delta 2\theta$ and pseudo-strain ε caused by refractive factor $n = 1 - \delta$ for Al sample and Cu radiation (the same parameters as in Fig. 5.5 and 5.6; also given in Table 5.3) compared for Genzel approach (and $\Delta\theta_1 = 2\delta \tan\theta = 0$) and the 'New formula' with different 2θ angles.

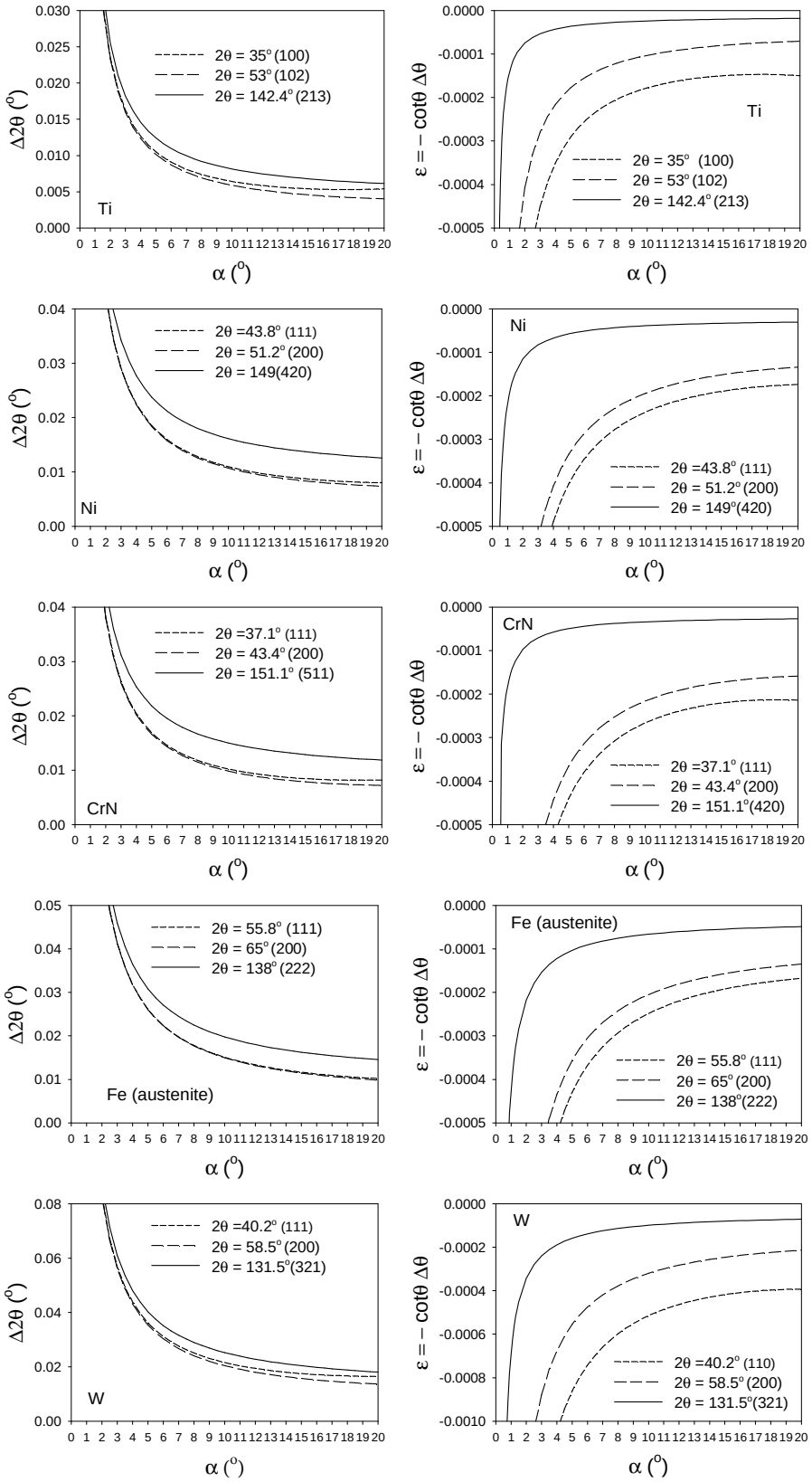

Fig. 5.8. Peak shift $\Delta 2\theta$ and pseudo-strain ε caused by refractive factor $n = 1 - \delta$ for different materials and chosen wavelengths (see Table 5.3). Calculations were performed by the 'New formula' applied for low and high 2θ angles corresponding to available *hkl* reflections.

Table 5.3. The α_{cr} and δ values calculated for the studied materials and used wavelengths using X-ray database of Lawrence Berkeley National Laboratory's Center for X-Ray Optics [86].

Material	Al	Ti	Ni	CrN	Fe	W
Wavelength (Å)	1.54	1.54	1.54	1.54	1.94	1.54
X-ray tube	Cu	Cu	Cu	Cu	Fe	Cu
$\delta \cdot 10^{5}$	0.85	1.35	2.73	2.15	3.42	4.63
α_{cr} (^{o})	0.24	0.30	0.40	0.38	0.47	0.55

It was already mentioned above, that the refraction of the X-rays not only shifts the diffraction angle *2θ*, but also leads to a change of the orientation of the diffraction vector *Δψ*. This deviation is relatively small and practically does not influence the values stress determined from $sin^2\psi$ plot. The value of $\Delta\psi = \psi^e - \psi$ (where ψ^e and ψ the correct values respectively) can be calculated from formula given by Genzel [36]:

$$\Delta\psi = \psi^e - \arccos[\sin(\beta - \Delta\beta)\sin\theta - \cos(\beta - \Delta\beta)\cos\theta\cos\xi] \tag{5.15}$$

where:

$$\cos\xi = 2\left\{\frac{\sin\left[\frac{1}{2}(\pi - \theta - \beta + \psi)\right]\sin\left[\frac{1}{2}(\pi - \theta - \beta - \psi\right]}{\cos\theta\cos\beta}\right\} - 1$$

or simply (see Fig. 5.4):

$$\Delta\psi = (\Delta\alpha - \Delta\beta)/2 \tag{5.16}$$

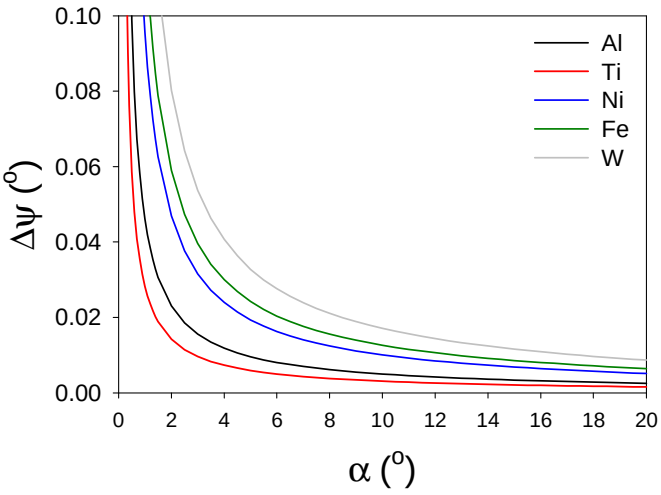

Fig. 5.9. Deviation $\Delta\psi$ caused by refraction for different materials and chosen wavelengths (see Table 5.3) according to Eq. 5.15.

Because the deviation $\Delta\psi$ is smaller than 0.1^{o} for all considered ranges of α and all materials given in Table 5.3, the influence of refraction on the value of determined stress is negligible (such small deviation practically has not influence on the slope of $sin^2\psi$ plot).

The above derived formulas for correction of experimental data were derived for the case of perfectly smooth surface. The main difficulty of the application of such correction is that the surface roughness can significantly reduce value of the peak shift ($\Delta 2\theta$) calculated for perfectly flat sample. A first model for an explanation of how surface roughness could influence the refraction effect was given by Ely et al. [87]. Ott M.H and Löhe D [88], showed that for smooth surface theoretical corrections agree very well with experiment and what is more Snell's law describes this effect with good accuracy at least down to incidence angles of 0.8°. It was also proven that with increasing surface roughness the refraction correction effect decreases.

To take into account that refractive index is smaller than unity, the analysis of the experimental data should be performed twice (i.e. with and without correction), to see the boundary values of stresses and determined strain free lattice constant a_0. The example results of such calculations are shown in Figs. 5.7, 5.8 and 5.9, and such comparison will be later done for each sample studied in this work. The example of the results (Figs. 5.7 and 5.8) were obtained using Kröner model and applying fitting procedure based on

Eq. 3.23 (the *c/a* parameter for hexagonal Ti samples was determined using a new self-consistent method described in the next chapter). When the calculations are performed without correction, the value of a_0 decreases for decreasing α incident angle, while the correction for smaller than unity refractive index leads to higher values of a_0, and the increase is more significant close to the sample surface. After correction the lattice parameter is approximately constant in function of the incident angle α and such result was expected for the powder and mechanically polished samples in which the crystal structure should not change in function of the depth below the surface (and consequently on α angle). The stress values determined with and without correction are also different and this difference is certainly larger for Ti in comparison with Al, as expected comparing δ values in Table 5.3. As we see in Fig. 5.10, in the case of powder sample, the refraction effect influences significantly stress determined for small incidence angle (see $\alpha = 1^o$), i.e. compressive pseudo-stress is obtained without correction (this value is fictitious because zero stress is expected in the powder sample). However, applying correction we change the calculated stress to significant positive value. This would suggest that the assumption of smooth samples can be not exactly fulfilled and the correction of peak position is overestimated. Finally, we can see that refraction does not influence value of determined *c/a* parameter (Fig. 5.18). This is due to the fact that variation of *c/a* will cause the shifts of relative peaks positions depending on *hkl* reflections which is not monotonic in function of 2θ. Therefore, the determined in fitting procedure *c/a* value is not influenced significantly by the monotonic with respect to 2θ shifts of the diffraction peaks caused by smaller than unity refractive index. In the contrary, both strain free lattice constant a_0 and stresses determined using MGIXD method depend (indirectly) on the monotonic variation of the peak position in function of 2θ angle, what leads to sensitivity of these values on the value of refractive index.

Summarizing, it should be stated that the influence of non-unit refractive index on the on the determined a_0 parameter and residual stresses depends on the type of material, wavelength of X-rays, incident angle and moreover on the roughness of the surface. It is known that roughness reduces the refraction effect [88]. Therefore the interpretation of the experimental results performed with correction for flat surface and without correction establishes limits for the values of the stresses and a_0 parameter in the studied sample. Such calculations must be always compared in order to see the range of incident angle for

which the correction is not significant (as for the samples presented in Figs. 5.8 and 5.9). If we want to analyze data for the range where the influence of refraction is significant we will know only the limits of the determined values. To verify the obtained results for mechanically machined surface it is important to follow changes of determined a_0 parameter, which should not change significantly with incidence angle. In the case of presented results we can say that after correction we obtained reasonable values of stresses and a_0 parameter for the incidence angles $\alpha \geq 3^o$ (for both Al and Ti samples using Cu K_α X-ray radiation).

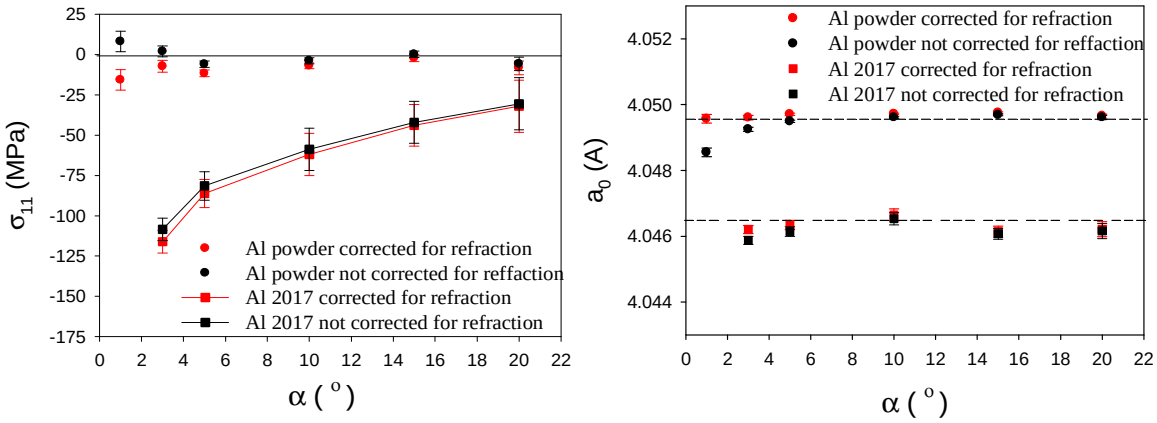

Fig. 5.10. Residual stress and strain free lattice parameter a_o in function of the incidence angle α determined with and without correction for smaller than unity refractive index. The MGIXD method was applied for mechanically polished aluminium alloy (Al 2017) and for Al powder, using -PANalytical - X'Pert diffractometer (configuration described in Table 5.4) with Cu K_α X-ray radiation. In calculations the Kröner XEC calculated from single crystal elastic constants given in Table 3.3 were used.

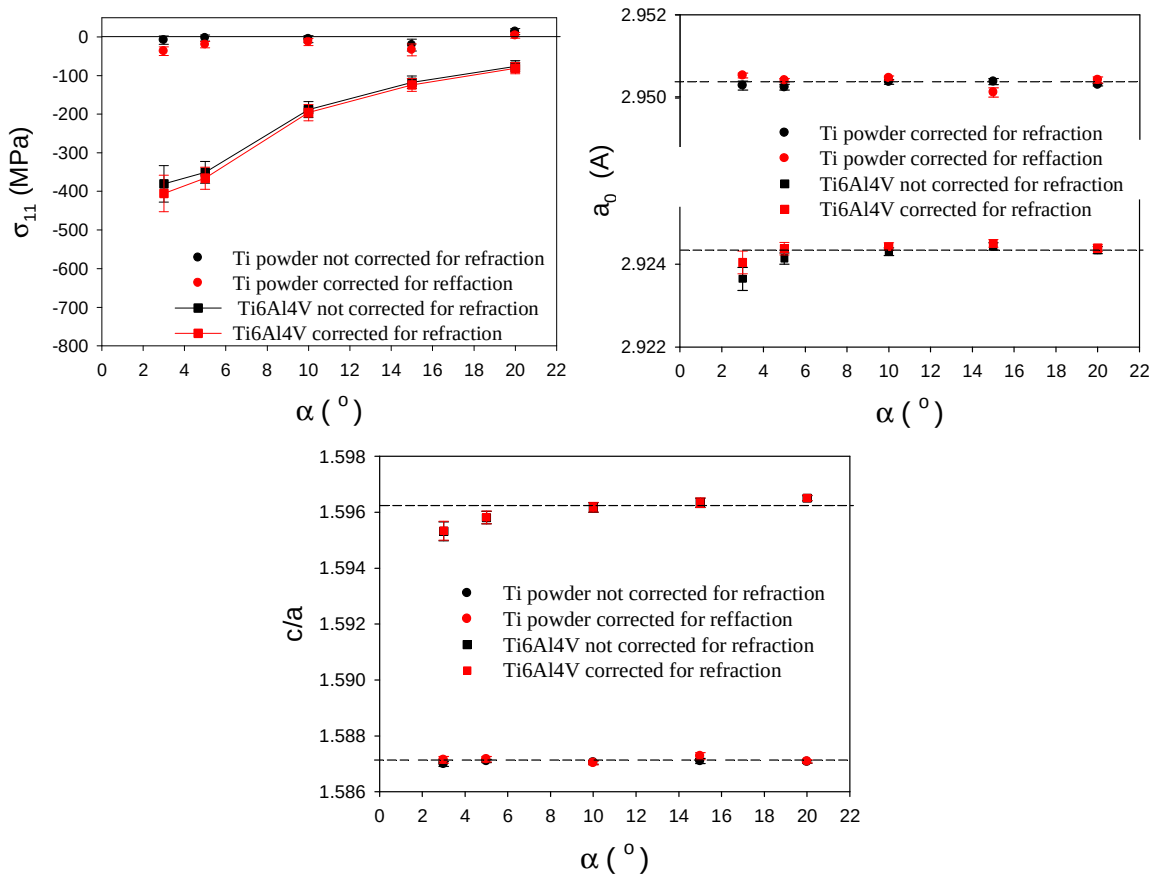

Fig. 5.11. Residual stress, *c/a* and a_o parameters in function of the incidence angle α determined with and without correction for smaller than unity refractive index. The same experiment as described in caption of Fig 5.10 was used for mechanically polished titanium alloy (Ti6Al4V) and for Ti powder.

5.2. TESTS OF THE EXPERIMENTAL CONFIGURATION

In diffractometry, both peak shape and angular resolution are influenced by the optical properties of the devices in the primary and reflected beam optics [89]. The main disadvantage of MGIXD method is its low accuracy in stress determination (about ±50 MPa for steel sample) when the classical line focus (with slit in incident beam optics) and parallel plate collimator (soller collimator) in the reflected beam optics were used [49].

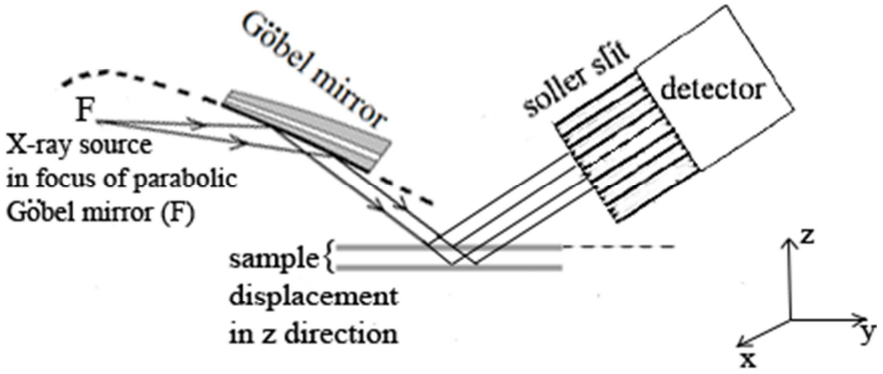

Fig. 5.12. Parallel beam configuration with Göbel mirror (incident beam optics) and soller collimator (diffracted beam optics). Shift of the sample in z direction moves the diffracted beam across the soller slits collimator, but the rays always reach the detector for the same value of 2θ position [90]. The X-ray source is located in the focus of the mirror.

The accuracy of measurements can be considerably improved by using collimating X-ray optics realized by parabolically bent graded multilayer mirrors [89]. The multilayer is bent to parallelize the divergent beam of an X-ray tube and monochromatize the radiation to its K_α-contents [90]. The graded multilayer monochromators (Göbel mirrors) are composed as a combination of layers made of two materials having different atomic number (Z), which allows gaining high total reflectivity [91]. The distance of layers from each other as well as their slope depends on the wavelength and on the localization of the mirror in relation with the position of the source.

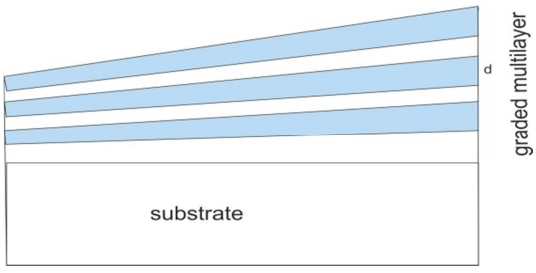

Fig. 5.13. Göbel mirror composed from the layers having different atomic numbers.

Typically used Göbel mirrors are composed from tungsten and silicon (W/Si). Göbel mirror W/Si is composed from the layers having low atomic number (silicon, Z_{Si}=14) and layers having high Z (tungsten, Z_W=74) which are arranged alternately. Both elements have similar linear coefficient of thermal expansion. Using this kind of mirrors

reduces influence of sample misalignment and surface topography on the reflex positions. If Göbel mirror is located on the parabola in such a way that the X-ray beam incidence on it from the source located at the focal point of the parabola (with the accuracy of 1°), then the divergence radiation of the source is converted to monochromatic and parallel beam with an accuracy of about 0.8°-0.05°.

In parallel-beam geometry the angle of the diffraction must be measured directly. The soller slit (collimator) with blades perpendicular to the diffraction plane and a divergence of about 0.15° prevents radiation penetrating under a different angle from reaching the detector (Fig. 5.12) [90].

Although Göbel mirror and the plate collimator parallelizes the primary beam in direction of diffraction plane it is still divergent in direction perpendicular to the diffraction plane. It can cause the asymmetry of the diffraction peak which is dependent on the value of primary beam divergence. In order to reduce the asymmetry, the second soller slit, in the primary beam or/and in the front of the other soller slit, may be used. It reduces the divergence perpendicular to the diffraction plane [90].

In diffraction methods it is very important to be able to perform measurements in-depth of the sample with a very good accuracy. Gross M. et al. [90] showed that the parallel-beam geometry achieved by a Göbel mirror allows measurements with varying angle of incidence in high accuracy.

In the present work the X-ray measurements were performed on four diffractometers described in Table 5.4 using parallel beam configuration.

Table 5.4. Configurations of the laboratory X-ray diffractometers used in preset work.

Diffractometer	PANalytical - X'Pert MRD (AGH, Kraków)	PANalytical – Empyrean (AGH, Kraków)	PANalytical – X'Pert MRD (ENSAM, Paris)	Seifert - PTS MZ VI (ENSAM, Paris)
Divergence of Göbel mirror (^{o})	0.02	0.02	> 0.05	no mirror
Type and size of slit forming incident beam	rectangular ($1/2^o$ x 4 mm)	rectangular ($1/2^o$ x 4 mm)	rectangular ($1/2^o$ x 4 mm	slits width : 0.5mm vertical limitation : 1.5
Divergence of Soller collimator in reflected beam optics – plates perpendicular to diffraction plane (^{o})	0.18	0.18	0.27	0.30
Soller collimators – plates perpendicular to diffraction plane	present	present	not present	not present
X-ray tube focus	line	line	point (1.2x0.4 mm²)	point (1x1 mm²)
Type of radiation used	Cu K_α	Cu K_α	Cu K_α	Fe K_α
Monochromator	not present	not present	for the reflected beam: graphite (cut the K_β)	not present : not necessary thanks to the type of detector (energy resolution)
Type of detector	proportional	semiconductor	proportional	solid detector

The first three diffractometers presented in Table 5.4 gave very similar results (it has been tested on powder samples), and the third configuration was used to measure stresses in austenitic steel (in this case Cu K_α radiation is not convenient due to high fluorescence causing high background and absorption). The reproducibility of the experimental setup with the Göbel mirror was tested repeating measurements for different powder specimens. It was found that the difference between the stresses measured using the MGIXD method was about 10 MPa for the Al powder [92, 55] (Table 5.5).

Table 5.5. Comparison of results for Al powder for three different diffractometers.

diffractometer	α (°)	σ (MPa)	a_0 (Å)	χ^2
PANalytical - X'Pert MRD (AGH, Kraków)	5	-0.7 ± 7.3	4.0493 ± 0.0002	0.06
	15	-6.9 ± 13.3	4.0493 ± 0.0001	0.7
PANalytical – Empyrean	5	-0.2 ± 4.9	4.04904 ± 0.00008	0.5
	15	-2.3 ± 7.5	4.04935 ± 0.00009	1.0
PANalytical – X'Pert MRD (ENSAM, Paris)	5	-10.2 ± 2.0	4.04949 ± 0.0001	0.2
	15	-1.4 ± 2.0	4.04969 ± 0.0001	0.2

One of the aims of this work is testing of the parallel configuration of the diffractometer containing Göbel mirror in the incidence beam optics. The test were performed on Al – powder sample having low elastic crystal anisotropy (Zenner factor A= 1.2) and relatively low absorption ($\mu_{\lambda=1.54\ Å}$ = 136 cm^{-1}) enabling measurements at different depths shown in Fig. 3.8. The results of the tests and the analysis of experimental uncertainty used in the MGIXD method are described below.

5.2.1. UNCERTAINTY OF PEAK POSITION

In the analysis of experimental data it is important to take the different sensitivity of the measured lattice strain on the value of scattering angle 2θ into account. In this work the fitting procedure is based on Eq. 3.23, in which the uncertainties of equivalent lattice parameters $\delta_n(<a(\phi,\psi)>_{\{hkl\}})$ are treated as the weight in the calculation of the χ^2 value (compare Eq. 2.47):

$$\chi^2 = \frac{1}{N-M}\sum_{n=1}^{N}\left(\frac{<a(\phi_n,\psi_n)>_{\{hkl\}}^{exp} - <a(\phi_n,\psi_n)>_{\{hkl\}}^{cal}}{\delta(<a(\phi_n,\psi_n)>_{\{hkl\}})}\right)^2 \tag{5.17}$$

where $<a(\phi_n,\psi_n)>_{\{hkl\}}^{exp}$ and $<a(\phi_n,\psi_n)>_{\{hkl\}}^{cal}$ are the experimental and calculated lattice parameters and the $\delta(<a(\phi_n,\psi_n)>_{\{hkl\}})$ uncertainty is calculated directly from the uncertainty of peak position $\delta_n(2\theta_{\{hkl\}})$, i.e.:

$$\delta(<a(\varphi_n,\psi_n)>_{\{hkl\}}) = <a(\varphi_n,\psi_n)>^{exp}_{\{hkl\}} \cot(2\theta_{\{hkl\}})\,\delta_n(2\theta_{\{hkl\}}) \quad (5.18)$$

In the data analysis it can be assumed that that the $\delta_n(2\theta_{\{hkl\}})$ uncertainty is equal to the standard deviation of the peak position obtained from procedure of peak adjustment. However, these values are very small (smaller than 0.01^o) and other experimental errors play a more significant role, for example those due to the misfit of the sample position, defocusing or misalignment errors. Errors having different reasons are in fact unknown; therefore it was decided (if the standard deviation from peak adjustment is smaller than 0.01°) to assume a reasonable value of peak position uncertainty, the same for all reflections. As shown in Fig. 5.14 (see error bars) the values of $\delta(<a(\phi_n,\psi_n)>_{\{hkl\}})$, calculated using Eq. 5.18 with $\delta_n(2\theta_{\{hkl\}}) = 0.01^o$, are different for different $2\theta_{\{hkl\}}$. This ensures different influences of measured equivalent parameters $<a(\phi_n,\psi_n>^{exp}_{\{hkl\}}$ on the fitting quality criterion (Eq. 5.17) and consequently on the values of the determined stresses. As seen in Fig. 5.14 the uncertainties $\delta(<a(\phi_n,\psi_n)>_{\{hkl\}})$ are larger for lower a value of $2\theta_{\{hkl\}}$ scattering angle, i.e., the low $2\theta_{\{hkl\}}$ angle reflections affect the fitting results less than those for which $2\theta_{\{hkl\}}$ is higher (cf. Eq. 5.18). It is also important to estimate the uncertainty of the determined stresses in the case of unknown the $\delta_n(2\theta_{\{hkl\}})$ value. Therefore, regardless of the reasons of the experimental errors or inaccuracy of the data treatment the stress uncertainties were calculated assuming a ‘good fit’ for which $\chi^2 = 1$ [25].

5.2.2. TESTING INCIDENT BEAM OPTICS

MGIXD method and standard method (with 422 reflection) were applied to determine stress in Al powder sample. The measurements were performed on the PANalytical X'Pert MRD (AGH, Kraków) diffractometer in parallel beam mode (configuration in Table 5.4) [92]. The tests for Al powder were repeated twice, i.e., using the Göbel mirror or slit with divergence of 1/2° for the primary optic. Moreover, the data treatment for XGIXD method was repeated applying two different conditions, i.e., using all measured reflections presented in Fig. 5.15 or excluding two low 2θ reflections (111) and (200), for which $< a(\phi_n, \psi_n >_{\{hkl\}}^{exp}$ deviate significantly from the theoretical values.

Table 5.6. Residual stress component σ_{11} determined for Al powder using two optics of incidence beam: Göbel mirror or slit (stresses calculated excluding 111 and 200 reflections compared with results obtained from all reflections). In calculations the free surface XEC calculated from single crystal elastic constants given in Table 3.3 were used.

method	α (°) or *hkl*	$\bar{z}$ (μm)	primary beam config.	σ_{11} (MPa) all reflections	reflections 111, 200 excluded		
					σ_{11} (MPa)	a_0 (Å)	χ^2
MGIXD	α=5°	5.8	Göbel mirror	-5.0 ± 3.0	-1.6 ± 1.5	4.04936 ± 0.00003	0.05
			Slit	-22.1 ± 5.3	-16.0 ± 5.3	4.04973 ± 0.00009	0.55
	α=10°	10.8	Göbel mirror	-3.1 ± 3.2	-0.4 ± 1.1	4.04948 ± 0.00002	0.02
			Slit	-28.1 ± 6.4	-33.3 ± 5.6	4.04995 ± 0.00008	0.64
	α=15°	14.9	Göbel mirror	-3.0 ± 4.4	0.4 ± 3.8	4.04945 ± 0.00006	0.29
			Slit	-7.3 ± 6.1	-8.6 ± 7.3	4.04914 ± 0.00011	1.07
Standard	422	12-34	Göbel mirror	-2.1 ± 0.5		4.04946 ± 0.00001	0.65
			Slit	-0.5 ± 1.4		4.04903 ± 0.00004	3.08

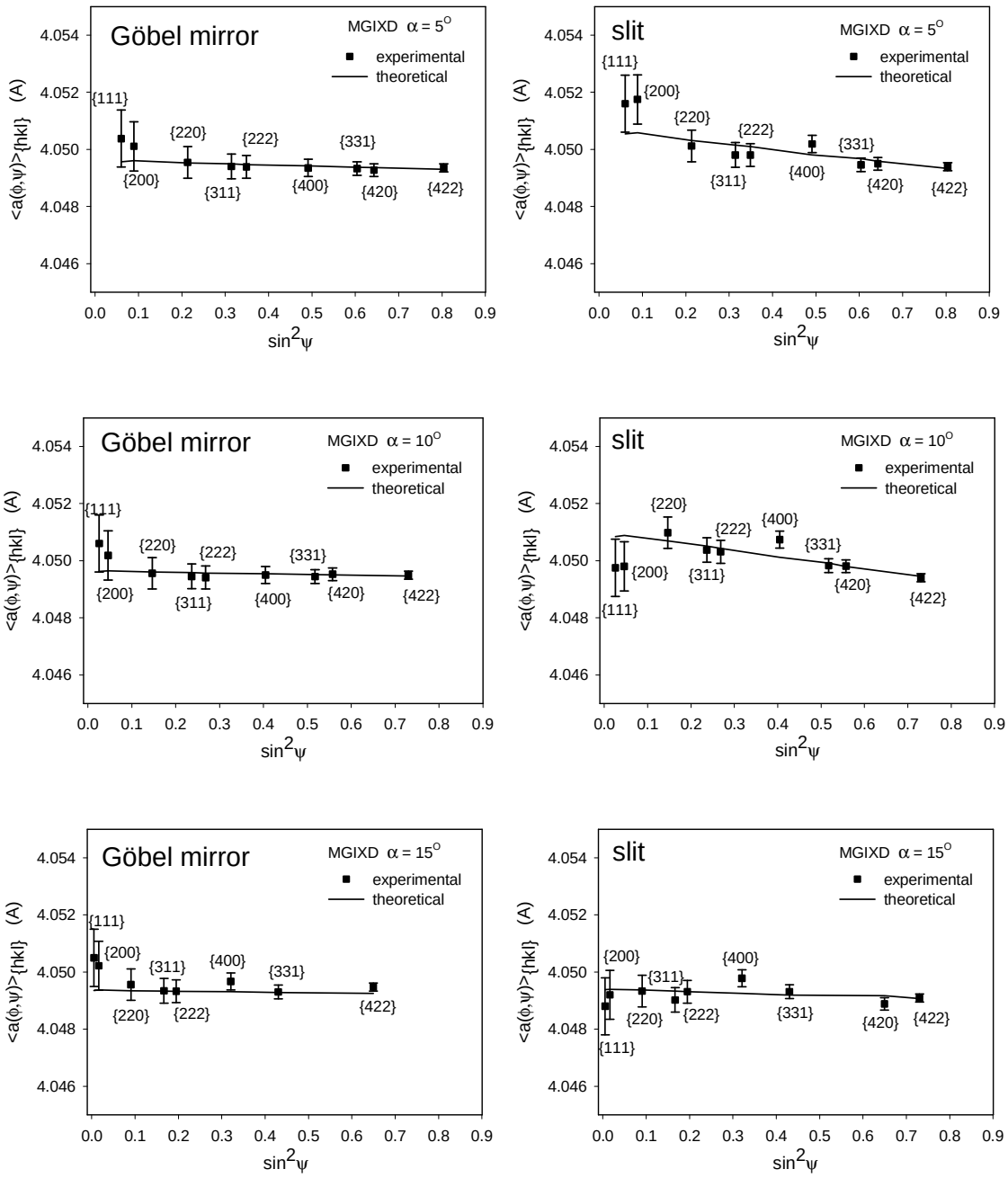

Fig. 5.14. Measured lattice parameters (points) and theoretical results of fitting (continuous lines) vs. $sin^2\psi$ for Al powder sample. Results of grazing incidence method for three angles α and for two different beam geometries are shown.

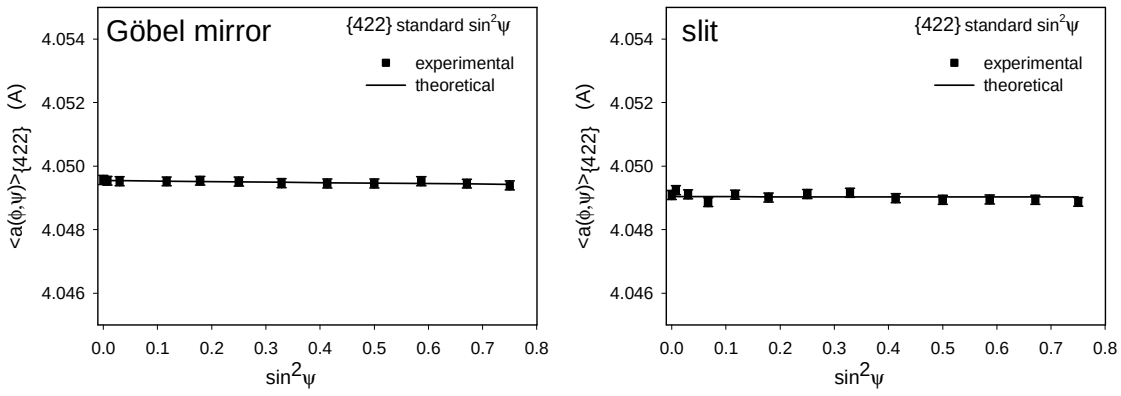

Fig. 5.15. Similar comparison as in Fig. 5.14 but for standard method (ω – method).

Results of stress analysis in Al powder are shown in Table 5.6. and the $sin^2\psi$ plots for grazing incidence method (MGIXD) and standard method are shown in Figs. 5.14 and 5.15, respectively. All calculations were performed with assumption $\delta(2\theta_{\{hkl\}}) = 0.01°$. Comparing the results obtained using MGIXD method with and without two low 2θ reflections (i.e. 111 and 200) it can be stated that a small improvement of the results (lower fictitious stress and its uncertainty) was obtained when the latter reflections were excluded. As seen in Table 5.6 the values of χ^2 are much lower when the Göbel mirror was used (for both MGIXD and standard methods). Small, but significant, values of fictitious stresses (between -8 and -33 MPa) were found, when the slit was used. As the real stress for the powder sample is equal to zero, the determined non-zero stresses can be treated as the values of systematic uncertainty caused by the diffractometer or sample misalignments. The latter uncertainties can be minimized using parallel optics of the incident beam. The near zero values of stresses measured in the Al powder (values lower than -5 MPa, see Table 5.6) show that the experimental errors were significantly reduced by use of the Göbel mirror. In the case of standard method almost zero stress was determined for both used configuration of the incident beam optics.

Finally it should be stated that using MGIXD method (especially with) a good accuracy of a_0 determination was achieved. When the Göbel mirror is applied, the differences between a_0 measured at different depths is in the order of about 10^{-4} Å.

5.2.3. INFLUENCE OF 2Θ - ZERO POSITION ON THE MEASURED STRESS

In order to precisely designate the stress value it is necessary to take into account the 2θ-zero position. MGIXD method was applied to determine stress in Al powder sample and to verify the influence of the 2θ-zero position on the measured stresses and lattice parameter. The measurements were performed on the PANalytical – X'Pert MRD (configuration in Table 5.4) in parallel beam mode (Göbel mirror). In calculations the Kröner XEC calculated from single crystal elastic constants given in Table 3.3 were used. The tests of the 2θ direct beam position on the measured stresses and lattice parameter for Al powder are presented on Fig. 5.16. To investigate the effect of 2θ-zero position on measured quantities different values of deviation from 2θ - zero position were assumed (Fig. 5.16).

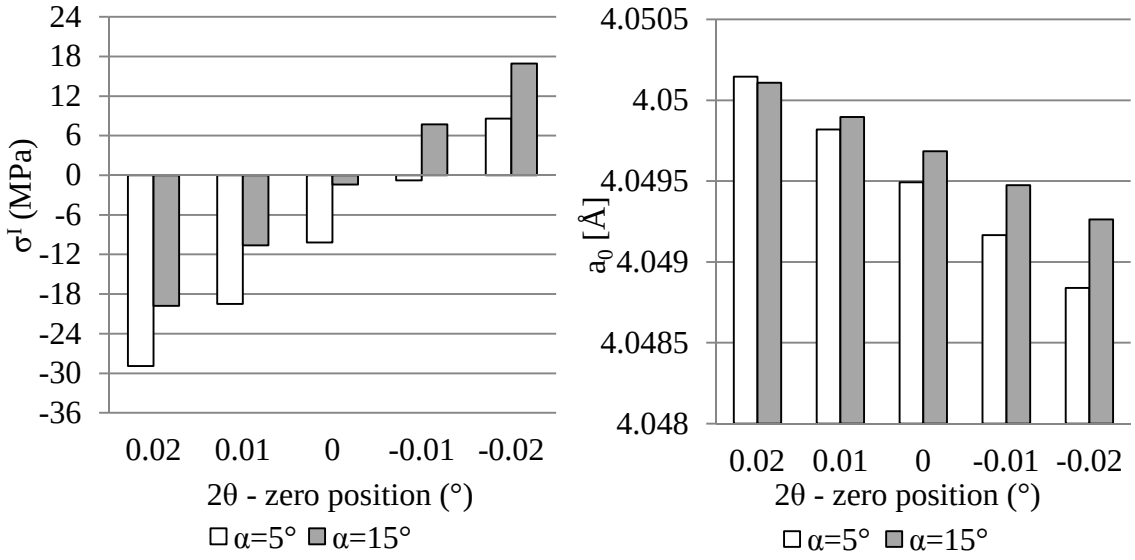

Fig. 5.16. Influence of *2θ* – zero position on the measured stress for powder sample.

In the light of presented results it can be concluded that deviation from *2θ* - zero position equal to 0.01° causes about 10 MPa deviations of the measured stress value (for Al sample) and about 0.0003 Å deviation for a_0 lattice parameter.

5.2.4. INFLUENCE OF Z- POSITION ON THE MEASURED STRESS

Precise determination of the stresses is also dependent on the z - position of the sample. In order to investigate this effect for MGIXD method the measurements were performed on the PANalytical - X'Pert MRD (ENSAM, Paris - configuration in Table 5.4) in parallel beam mode (Göbel mirror). In calculations the Kröner XEC calculated from single crystal elastic constants given in Table 3.3 were used. Different deviations from z - zero position (in direction normal to the surface) were introduced and the values of stresses and lattice parameter for each z -position deviation were determined and compared. Results of the test are presented on Fig. 5.17.

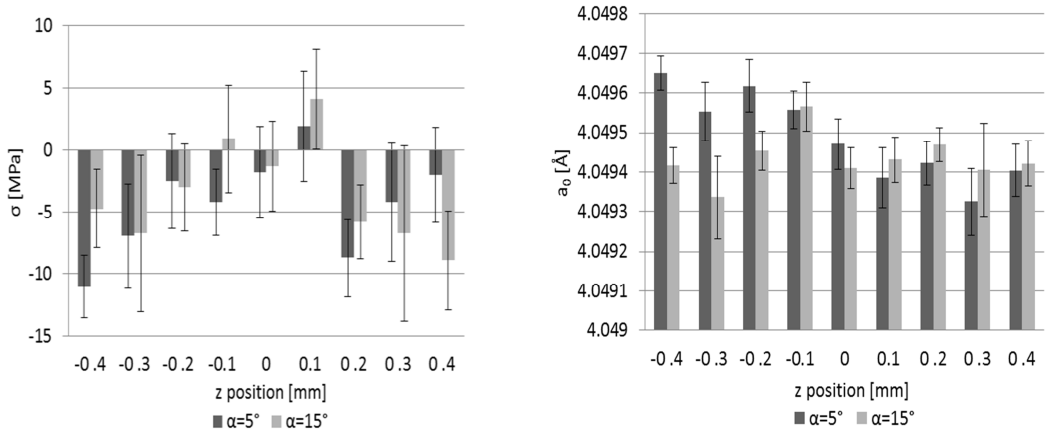

Fig. 5.17. Influence of z – zero position on the measured stress for powder sample

On the basis of the presented results it can be concluded that the deviation from z-zero position equal to 0.01 mm causes about 5 MPa deviation of calculated value of stresses and less than 0.0002 Å for a_0 lattice parameter.

Summarizing results obtained in section 5.2, it can be concluded that application of Göbel mirror collimating incident beam decreases uncertainty of the determined peak position and it is possible to achieve accuracy even of a few MPa for the stresses in Al sample (the accuracy in of the stress determination in another materials can be easily estimated comparing Young modulus of Al and this of the studied material). The accuracy of determined strain free lattice parameter a_0 is in order of 10^{-4} Å. Moreover it was shown that using parallel optics minimises errors connected with displacement of the sample in the z direction (normal to sample surface). Experimental error of about 5 MPa for stress and less than 0.0002 Å for lattice parameter a_0 corresponds to shift of 0.1 mm. It was also found that the more important source of systematic error is caused by the shift of 2θ - zero value. The misalignment of the diffractometer equal $\Delta 2\theta = 0.01^o$ leads to the fictitious stress of about 10 MPa and change of 0.0002 Å for lattice parameter a_0 determined for the Al stress-free powder. This error can be minimised by the careful alignment of the diffractometer or the results obtained for the studied sample can be corrected by using the powder diffraction data. Concerning the statistical uncertainty it will depend on the quality of measured peak, and for the studied samples it was about 1.5-5 MPa for stress and less than 10^{-4} Å for a_0, and the latter value is significantly smaller than the errors caused by misalignment of the sample position and diffractometer alignment.

The performed tests confirmed that we can expect the reproducibility of measurements for different experimental setups containing the Göbel mirror is about 10 MPa and a 0.0005 Å for lattice parameter a_0 in the case of Al elastic constants. These values were confirmed in the performed experiments. Also, it is reasonable to assume that the position of peak is determined with accuracy not better $\Delta 2\theta = 0.01^o$ (see the error bars corresponding to this value in Fig. 5.14). Finally, it should be stated that the above values of expected systematic and statistical errors are calculated for particular sample and they can be different for another set of measured reflection. However, the presented results give a view on the accuracy of the experimental setup and the applied methodology.

5.3. CONCLUSIONS

In the light of presented results the LPA correction does not influence the XSA significantly. Even in the case of relatively broad diffraction peak the influence of LPA correction on the measured peak position, corresponding strain and consequently value of determined stress or strain free lattice constants is relatively small. On the other hand the refraction correction can significantly influence the results of the XSA. Comparing the 'New formula' developed in the thesis with the approaches proposed by Genzel and Hart it can be concluded that for high incident angles the 'new approach' is consistent with the one proposed by Hart, but it differs in comparison with Genzel's (in which the effect of wavelength change was neglected). For small incident angles the Genzel's approach and the one proposed in thesis are consistent but the Hart's formula do not reflect the effect properly. It is caused by not precise approximation for small incident angles. The effect of refractive index $n<1$ on the stress measurement strongly depends on value of the δ parameter (and thereby the type of material), wavelength, incident angle and surface roughness. On the basis of considered results, if MGIXD method is used, it is advised to perform the stress analysis with and without refraction correction and when the difference of obtained results is significant for designated parameter than these results should be rejected. This effect is the limitation of MGIXD method.

Results presented in this chapter confirmed that both statistical error and the misalignment error can be significantly reduced when the Göbel mirror is used in the primary optic of the diffractometer. In the case of parallel beam geometry used for MGIXD method the z-position imprecisions do not significantly influence the obtained results of XSA, however the 2θ-zero position should be precisely adjusted.

6. NEW INTERPRETATIONS OF MGIXD MEASUREMENTS AND VERIFICATION OF X-RAY STRESS FACTORS (XSFS)

In this chapter two important theoretical developments of the MGIXD method are presented. The first one enabling determination of *c/a* parameter and significantly improving quality of experimental data analysis for hexagonal structure has been proposed and tested. The second one in which density of stacking faults is taken into account (originally proposed by Baczmański [20]) will be applied to the case of tensile and compressive stresses in austenitic sample. Second part of the chapter concerns verification of different type of XSF, which can be applied to interpret the experimental data obtained using MGIXD method. Finally, examples of determination of stresses in surface layer for materials having high and low single crystal elastic constants anisotropy are presented.

6.1. SELF - CONSISTENT FITTING OF C/A PARAMETER

In the case of cubic crystal structure the experimental $<a(\phi,\psi)>_{\{hkl\}}$ lattice parameters are calculated directly from measured $<d(\phi,\psi)>_{\{hkl\}}$ spacings (Eq. 3.24a). Subsequently, the σ_{ij}^{I} and a_0 fitting parameters can be found by adjusting the $<a(\phi,\psi)>_{\{hkl\}}$ values obtained from Eq. 3.24a to the measured ones (Eq. 3.23), as in the standard method. However, more complex procedure of experimental data must be applied for hexagonal structure since the value of *c/a* parameter must be known a priori to calculate the experimental $<a(\phi,\psi)>_{\{hkl\}}$ from Eq. 3.24a. To overcome this difficulty the iteration method can be applied. In the first step of this procedure we substitute the theoretical value of *c/a* into Eq. 3.24b and the least square method is used to find out σ_{ij}^{I} and a_0 from Eq. 3.23. The result of the first adjustment is usually poor because the

experimental $<a(\phi,\psi)>_{\{hkl\}}$ are not correctly calculated using approximate value of *c/a*. Consequently the experimental $<a(\phi,\psi)>_{\{hkl\}}$ do not agree with those obtained from Eq. 3.23 for optimized σ_{ij}^{I} and a_0 fitting parameters. Thus the procedure must be developed in order to correct the value of *c/a* for the studied material, taking into account the macrostresses present in the sample. In this aim Eq. 3.24b can be rewritten in the following form:

$$y = p\,x \tag{6.1}$$

where: $y = \left[\frac{<a(\phi,\psi)>_{\{hkl\}}}{<d(\phi,\psi)>_{\{hkl\}}}\right]^2 - \left[\frac{4}{3}(h^2+hk+k^2)\right]$, $x = l^2$ and $p = \frac{1}{(c/a)^2}$.

The above linear equation vs. l^2 allows us to determine *p* and consequently *c/a* parameters using simple linear regression method. In calculations the measured $<d(\phi,\psi)>_{\{hkl\}}$ spacings and values of $<a(\phi,\psi)>_{\{hkl\}}$ calculated from Eq. 3.23 (for σ_{ij}^{I} and a_0 optimized in the first step for approximate value of *c/a*) are substituted. It should be stated that the so obtained *c/a* parameter is still approximate, but it can be applied in the second step of iteration to calculate $<a(\phi,\psi)>_{\{hkl\}}$ used in the least square procedure based on Eq. 3.24b. As the result the new values of σ_{ij}^{I} and a_0 are determined. It will be shown that two iteratively applied simple fitting procedure leads to convergence allowing determination of macrostresses σ_{ij}^{I}, strain free lattice parameter a_0 and moreover more accurate value of *c/a*. Finally, if the self-consistent iterative calculations are convergent a very good agreement between theoretical values of $<a(\phi,\psi)>_{\{hkl\}}$ (obtained from Eq. 3.23) and experimental ones (determined from Eq. 3.24b) can be reached.

As an example the results obtained with the new method for ground and polished samples are presented. These samples were chosen due to different sign of stresses generated in surface region. Measurements were performed in two directions (i.e. for ϕ=0^o and ϕ=90^o) and for two incidence angles (i.e. for α = 5^o and α = 15^o), with Cu X-ray tube and Göbel mirror in the incidence beam optics. The PANalytical - X'Pert and PANalytical - X'Pert MRD diffractometers were used for ground and polished samples, respectively (see Table 5.4). The diffraction peaks having 2θ higher than 40^o were taken into analysis.

At first the calculation of the stresses in polished and ground Ti (grade 2) was performed using assumed values of *c/a* parameter indicated in Figs 6.1a, b and Fig. 6.2a, b, respectively. In this case the value of *c/a* was not varied during data treatment. It can be noticed that the experimental points are spread far from the lines obtained by fitting Eq. 3.23 with the XSF calculated using Kröner model (see $<a(\phi,\psi)>_{\{hkl\}}$ vs. $sin^2\psi$ plots in Figs. 6.1a, b and Figs. 6.2a, b from single crystal elastic constant given in Table 3.3 and orientation distribution functions (ODFs) given in Fig. 7.1 (in the next chapter when these sample are described). The correction for beam refraction was taken into account, however, this effect is reliable (smaller than uncertainly) for $\alpha = 5^o$ and $\alpha = 10^o$, as it was shown in Fig. 5.11, where the results with and without refraction corrections were compared.

Next, the self-consistent procedure was used and the value *c/a* was also adjusted. The resulting $<a(\phi,\psi)>_{\{hkl\}}$ vs. $sin^2\psi$ plots exhibit significantly better agreement between theoretical and experimental points (Figs. 6.1c and 6.2c). The values of *c/a* parameter and goodness of fitting χ^2 determined using the presented above procedure are given in these figures. It can be seen that value of χ^2 decreases significantly when experimental points approach the theoretical curves.

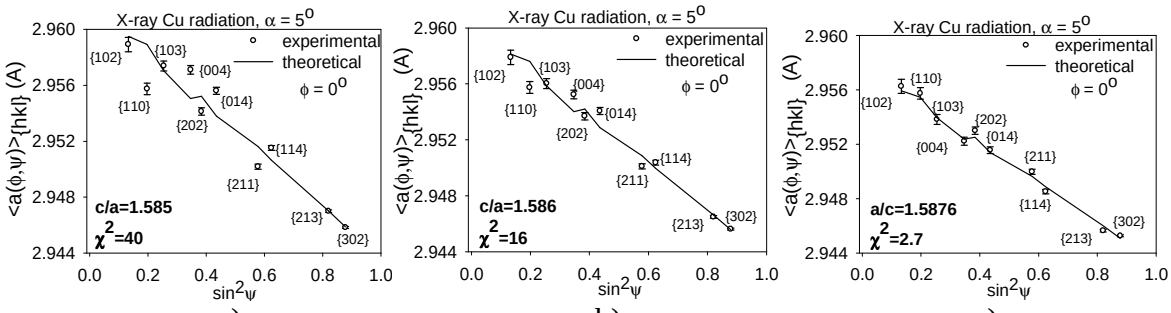

Fig. 6.1. The $<a(\phi,\psi)>_{\{hkl\}}$ vs. $sin^2\psi$ plots for mechanically polished Ti sample (under pressure of 5 N), measured with $\alpha = 5^o$. In figures (a) and (b) the theoretical plots were fitted to experimental points determined with assumed *c/a* values, while in the case of figure (c) the *c/a* parameter was adjusted. Uncertainty of peak position $\delta(2\theta) = 0.01^o$ was assumed.

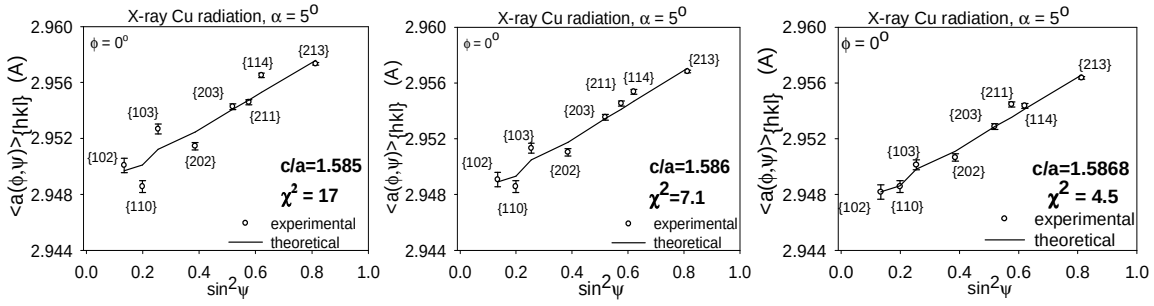

a) b) c)

Fig. 6.2. Similar results as in Fig. 6.1 but for ground Ti sample.

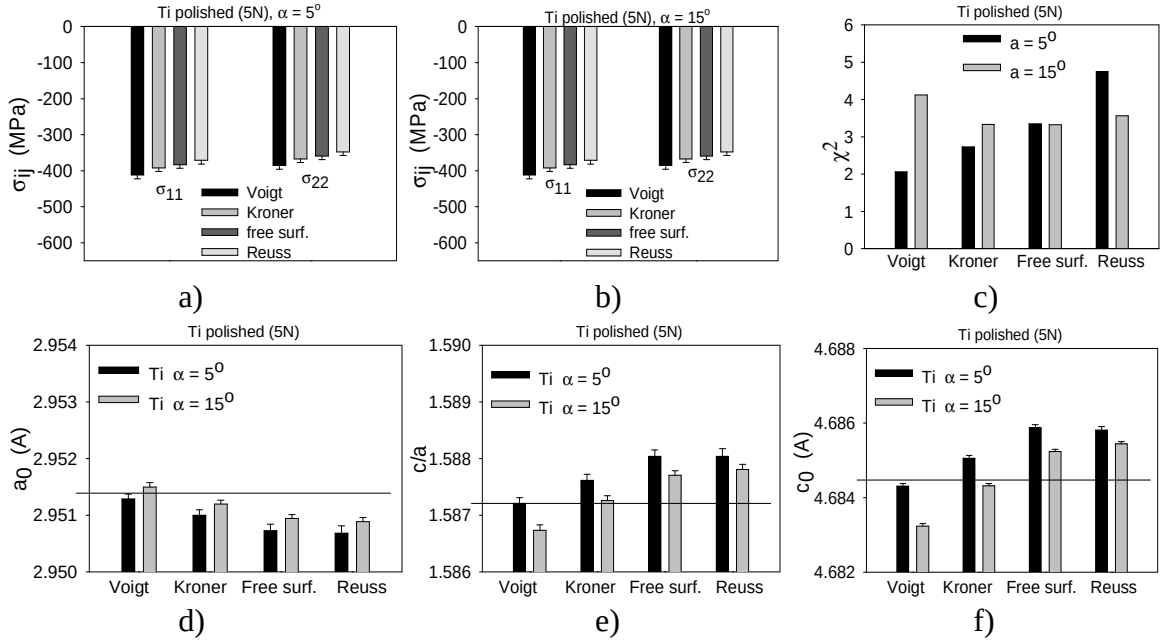

a) b) c)

d) e) f)

Fig. 6.3. The results of self-consistent fitting for mechanically polished Ti sample, measured with $\alpha = 5^o$ and $\alpha = 15^o$. The following values are presented: a) and b) - stresses in two directions, c) χ^2 - goodness of fitting as defined in Eq. 4.17, d-e) lattice parameters. The horizontal lines indicates mean value calculated over all models for both samples (polished and ground).

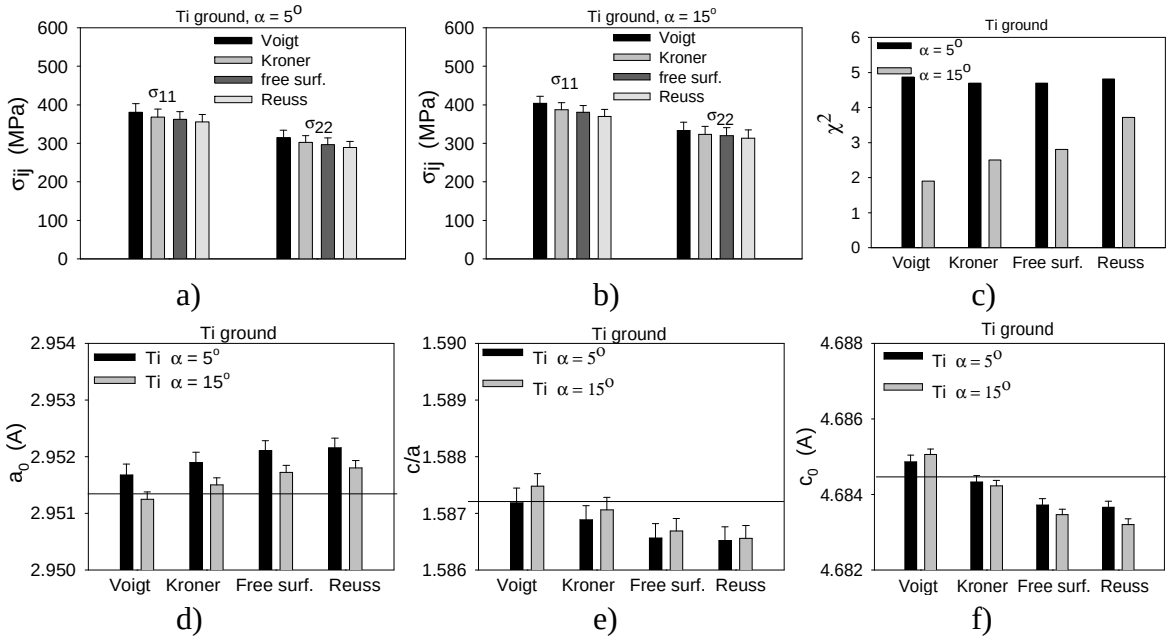

Fig. 6.4. Similar results as in Fig. 6.3 but for ground Ti sample.

The quantitative results of fitting using different XSF models are presented in Figs. 6.3 and 6.4 for polished and ground samples, respectively. It can be concluded that the biaxial stress was found for the both studied samples (compression after polishing and tensile after grinding as shown in Figs. 6.3a, b and 6.4a, b) and the stress values calculated using different models of diffraction elastic constants are not significantly different. Small difference between models is expected because the elastic anisotropy of Ti single crystal is low (Zener anisotropy factor A= 1.34). Also, there is no large difference between goodness parameter χ^2 for different models and all results fit well to almost linear measured functions $<a(\phi,\psi)>_{\{hkl\}}$ vs. $sin^2\psi$. The determined lattice parameters show some regular differences between models. In Figs. 6.3 d, e, f and 6.4 d, e, f the values of determined a_0, c/a and c_0 (where the two first parameters are obtained from fitting, while the third one is calculated as $c_0 = \left(c/a\right) \cdot a_0$ are compared with mean parameters calculated for both samples and both incidence angles ($\alpha = 5^o$ and $\alpha = 15^o$). These averages: $a_0 = 2.9514 \pm 0.0008$ Å, $c/a = 1.5872 \pm 0.0008$ and $c_0 = 5.6845 \pm 0.0014$ Å, can be calculated because samples are made from the same material (Ti grade 2) and different mechanical treatment should not influence strain free lattice parameters. It should be underlined that the obtained lattice parameters are very close to the accurate values for high purity Ti [93]: $a_0 = 2.95111 \pm 0.00006$ Å, and $c_0 = 4.68433 \pm 0.0001$ Å and

c/a = 1.5873 (similar values can be found in [94]). It can be also noticed that when the Kröner and Voigt XSF were used the determined lattice parameters were similar for the ground and polished sample. Moreover they are very close to the average values and these which are found in literature. On the other hand the a_0, c/a parameters obtained with XSF calculated by free surface or Reuss model are slightly overestimated for polished sample and underestimated for ground sample (opposite tendency occurs for c_0).

It can be concluded that the elastic properties of the studied titanium sample are almost isotropic and this is why fitting results obtained with XSF calculated by all models give very similar results. The most accurate values are obtained when Kröner or Voigt method were applied. Finally it should be stated that the new methodology of experimental data treatment enables determination not only strain free a_0 constant but also the c/a parameter. This method is unambiguous for materials having low elastic anisotropy, however in the case of anisotropic materials the determined lattice parameters depend on the model used for calculation of XSF. Thus the problem of verification of XSF is a crucial one, not only for correct determination of the stresses but also to find out correct strain free value lattice parameters for hexagonal structure (XSF will be tested in this chapter).

6.2. PEAK DISPLACEMENT CAUSED BY STACKING FAULTS

Not only residual stresses are the reason of diffraction peak shift with respect to the position corresponding to the perfect lattice. The diffraction lines can be influenced by stacking faults in the material. Two types of stacking faults can be distinguished: deformation stacking faults and twin stacking faults. Both of them may cause the peak shift [1]. Typically the twin stacking faults occurs during the growth of a crystal. Wagner [95] showed that that when the peak shift originates from high twin stacking fault density the shift of the peak is negligibly small. Deformation stacking faults may cause shift of the different diffraction lines in different directions. First work concerning this effect was done by Paterson [96], Warren et al [97] and Wagner [95]. Wagner and Velterop et al. showed [4, 98] that stacking faults can significantly change the position of the diffraction lines. This effect is especially important for the fcc crystals having low stacking fault energy (e.g. austenitic steels) [20]. In this case the magnitude of the displacement depends on the

probability of finding the stacking fault and on the reflection *hkl* used in the experiment. In the absence of the second order incompatibility stresses [20, 99]:

$$< a(\phi,\psi) >_{\{hkl\}} = [F_{ij}(hkl,\phi,\psi, f)\sigma_{ij}^{I} + \rho\, G(hkl)]\, a_0 + a_0 \tag{6.2}$$

$$\text{with} \quad G(hkl) \cong -\frac{\sqrt{3}}{4\pi(u+b)} \sum_{b} \frac{\pm(h+k+l)}{h^2+k^2+l^2}$$

where $\rho = \rho_s - \rho_d$, ρ_s and ρ_d are the probabilities of finding the single and the double layer stacking fault, respectively, between neighboring planes {111}, $G(hkl)$ is the coefficient the reflecting relative change of the interplanar spacings caused by stacking faults for the diffracting *{hkl}* planes, while *b* and *u* are the numbers of peak components which are affected and not affected, respectively, by the stacking faults, respectively [20].

For a quasi-isotropic sample the above equation can be written as:

$$\begin{aligned} < a(\phi,\psi) >_{\{hkl\}} = [& S_1^{hkl}\left(\sigma_{11}^{I} + \sigma_{22}^{I} + \sigma_{33}^{I}\right) + \frac{1}{2} S_2^{hkl}\left(\sigma_{11}^{I}\cos^2\phi + \sigma_{22}^{I}\sin^2\phi + \sigma_{12}^{I}\sin 2\phi\right)\sin^2 \\ & + \frac{1}{2} S_2^{hkl}\sigma_{33}^{I}\cos^2\psi + \frac{1}{2} S_2^{hkl}\left(\sigma_{13}^{I}\cos\phi + \sigma_{23}^{I}\sin\varphi\right)\sin 2\psi + \rho G(hkl)]a_0 + a_0 \end{aligned} \tag{6.3}$$

As it can be seen in a Fig. 6.5 both the macrostress (Fig. 6.5a) and stacking faults (Fig. 6.5b) cause the nonlinearities of the $<a(\phi,\psi)>_{\{hkl\}}$ vs. $sin^2\psi_{\{hkl\}}$ plots. Macrostresses (500 MPa) influence the slope as well as the nonlinearites of the curve. In contrast the stacking faults increase only the nonlinearities of these plots. This fact allows to separate the effect originated from the stresses from the one connected to the stacking faults [20] and perform the calculation of stresses values and the probability of stacking faults in polycrystal. The idea of fitting is similar to that used by Baczmanski [20] in the case of determination of second order stresses, when *q* scaling factor was used in Eq. 6.2 as additional adjusting parameter. In the case of Eqs. 6.2 and 6.3 value of ρ is varied in fitting procedure in order to receive the best agreement of theoretic and experimental results. The optimized ρ parameter has meaning of probability of finding stacking fault between neighboring planes {111}.

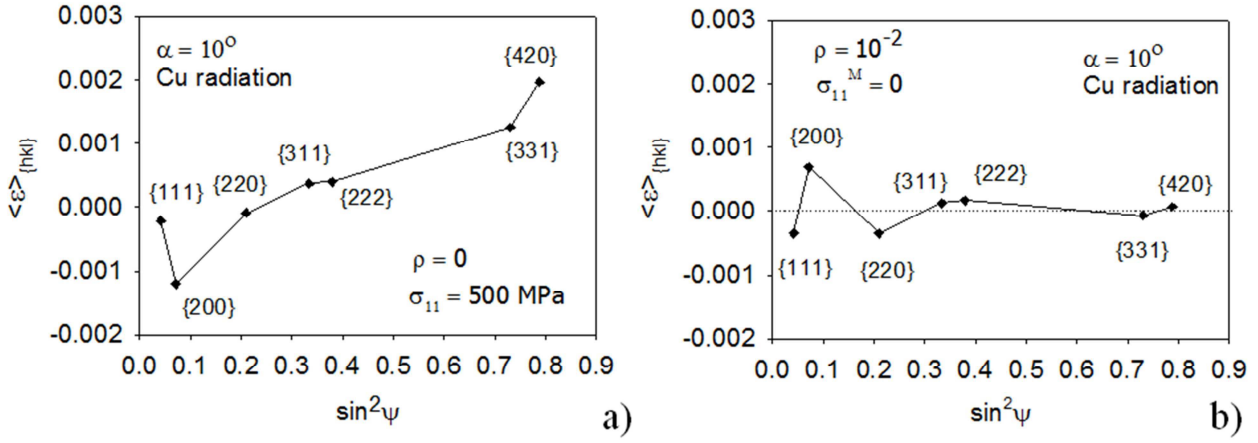

Fig.6.5. Lattice strains calculated for different *hkl* reflections as the effect of (a) uniaxial stress and (b) presence of stacking faults on the planes {111} for austenitic sample (XSF were calculated using free surface model with elastic constants given in Table 3.3 and assuming random texture [20]).

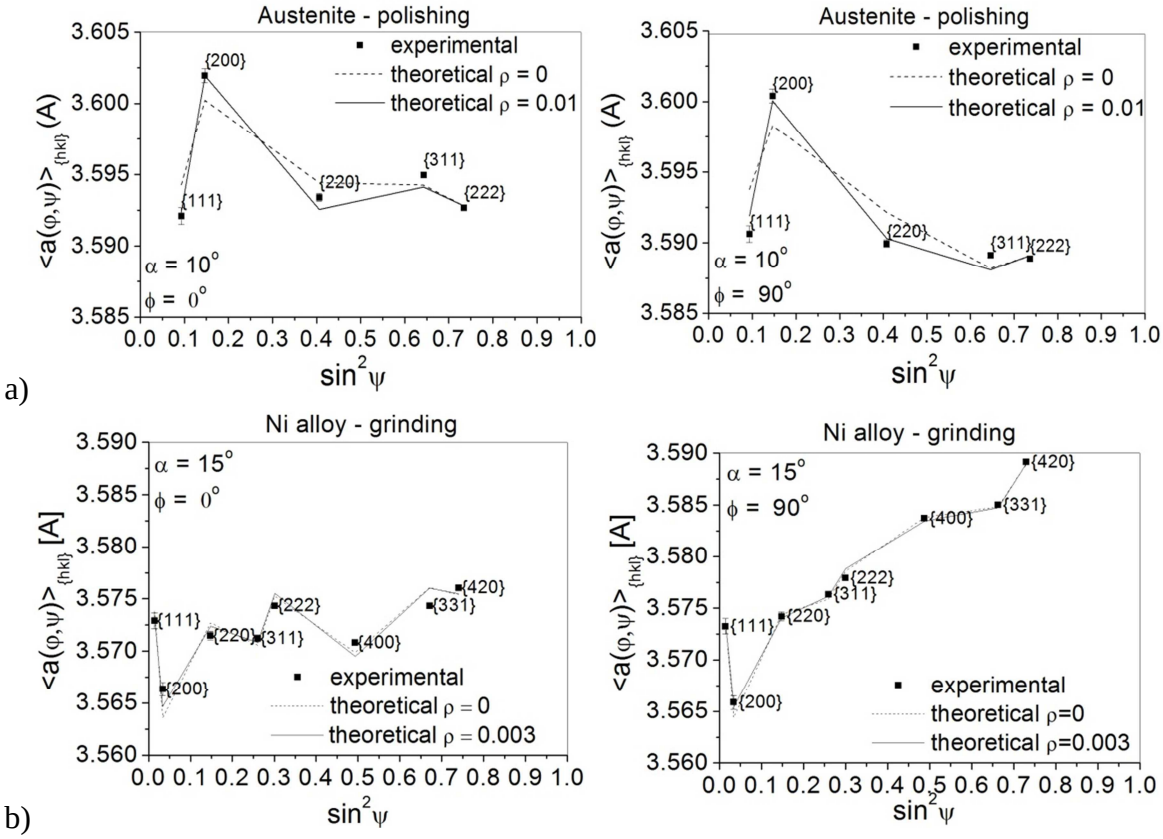

Fig. 6.6. The $\langle a(\phi,\psi)\rangle_{\{hkl\}}$ lattice parameters fitted to the experimental points using Eq. 6.3 (assuming $\rho \neq 0$ - continuous line or $\rho = 0$ - dashed line) for polished austenitic stainless steel (AISI 316L, Table 6.1) and ground Ni alloy (Inconel 690, Table 6.1). XSF were calculated with free surface model using texture functions given in Fig. 6.19.

In light of these results it appears that for Ni alloy it is not necessary to take into consideration the presence of stacking faults in stress analysis. The value of the ρ parameter is in the margin of error equal to 0. On the contrary for austenite stainless steel having low energy of stacking faults it would appear likely that taking into account the presence of stacking faults in stress analysis can be beneficial. Admittedly the stacking fault effect improves the fit of the theoretical curve (calculated from the chosen grain interaction model) to experimental points but it seems possible that this effect causes the change in XSF values, which now may differ from the real ones. On the other hand it is worth to emphasize that the ρ parameter determined for austenitic samples always have a positive value regardless whether the sample is in tensile (Fig. 6.7) or in compression (Fig. 6.6b). It means that the deviation of the experimental points from theoretical values is always in the same direction independently from the applied load.

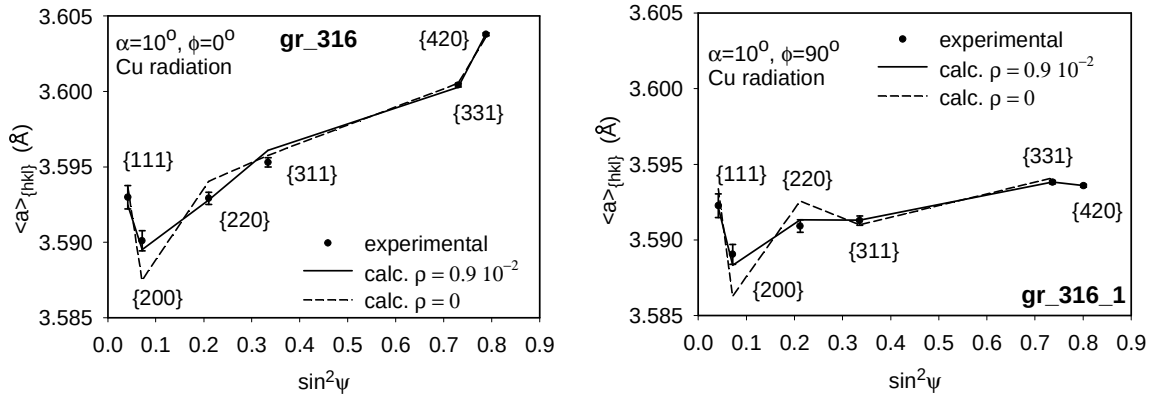

Fig. 6.7. The $<a(\phi,\psi)>_{\{hkl\}}$ lattice parameters fitted to the experimental points using Eq. 6.3 (assuming $\rho \neq 0$ - continuous line or $\rho = 0$ - dashed line) for the ground austenitic steel - AISI 316L, Table 5.1 XSF were calculated with free surface model. This result is taken from [20].

6.3. VERIFICATION OF XSF USED IN MGIXD

A correct choice of model for calculation of XSFs is significant for materials exhibiting high elastic anisotropy. In order to select the proper model of XSF it is valuable to evaluate an agreement of theoretical $< a(\phi,\psi) >_{\{hkl\}}$ vs. $sin^2\psi$ curve with experimental results [100].

To show the influence of the diffraction elastic constants on the interpretation of XSF results, polycrystalline materials having low (Ti, W) and high elastic anisotropy of crystallites (Ni, CrN, austenite stainless steel) were investigated. Zener factors for listed samples are gathered in Table 3.3. Compositions of the studied samples are given in Table 6.1. The orientation distribution functions were taken into account in XSF calculations for all investigated samples (Figs. 6.9 and 6.19).

Two samples exhibiting low (Ti) and high (austenite stainless steel) elastic anisotropy were investigated during tensile test, for other samples: polished W, ground Ni alloy, CrN coating and polished austenite stainless steel the residual stresses after surface treatment or coating deposition were measured.

Table 6.1. Composition of the materials used in thesis (wt.%).

Material	Components									
Ti grade 2	Ti	O	Fe	Ni	C	N				
	bal.	0.131	0.109	0.020	0.010	0.010				
Ni alloy Inconel 690 (sample prepared by AREVA)	Ni	Cr	Fe	Si	Ti	Mn	C	Cu	P	S
	bal.	29.91	10.61	0.38	0.33	0.29	0.022	0.01	0.009	0.002
Austenite stainless steel AISI316L	Fe	Cr	Ni	Mo	Mn	Cu	Si	P	S	C
	bal.	17.24	11.14	1.96	1.67	0.35	0.056	0.04	0.04	0.02
Al 2017	Al	Si	Fe	Cu	Mn	Mg	Cr	Zn	Ti	
	bal.	0.5	0.7	4.0	0.65	0.6	0.1	0.25	0.15	
Ti6Al4V	Ti	Fe	C	O	N	Al	V			
	bal.	0.25	0.008	0.2	0.05	6.0	4.0			

6.3.1. TENSILE TEST

The lattice strains were measured 'in situ' during tensile test in elastic range of deformation for austenite stainless steel (AISI316L) and titanium (grade 2) samples. The MGIXD method and standard method (ψ-mode for austenite and ω-mode for titanium) were used to determine stress in the sample under applied known stress (sample orientation with respect to incident and reflected beams is shown in Fig. 6.8. Measurements for Ti sample were performed on the PANalytical - X'Pert MRD (AGH, Kraków) and for austenite stainless steel on the Seifert - PTS MZ VI. The configuration of both diffractometers is given in Table 5.4. To prepare the sample the surface layer of 200 μm was removed by electropolishing. In order to avoid the influence of unknown residual stresses or/and systematic errors of determined peak positions, the measurements were performed for the non-loaded sample and a sample under uniaxial stress. The relative differences between interplanar spacings for loaded sample (i.e. $< d(\phi,\psi) >_{\{hkl\}}^{load}$) and non-loaded specimen (i.e. initial: $< d(\phi,\psi) >_{\{hkl\}}^{init}$) were calculated.

$$< \varepsilon(\phi,\psi) >_{\{hkl\}}^{rel} = \frac{< d(\phi,\psi) >_{\{hkl\}}^{load} - < d(\phi,\psi) >_{\{hkl\}}^{init}}{< d(\phi,\psi) >_{\{hkl\}}^{init}} \tag{6.3}$$

In the above equation the exact value of interplanar spacing for a stress free material is not needed and the strain $< \varepsilon(\phi,\psi) >_{\{hkl\}}^{rel}$ corresponding directly to the applied stress Σ_{11} is calculated and the effect of residual stresses or/and systematic errors of determined peak positions is avoided. The main challenge of this part of work is to verify if the value of applied stress Σ_{11} can be recalculated from diffraction data and what type of XSF allows determining the stress accurately. Moreover, it will be tested which model of XSF calculation properly describes grains interaction, especially for elastically anisotropic crystallites.

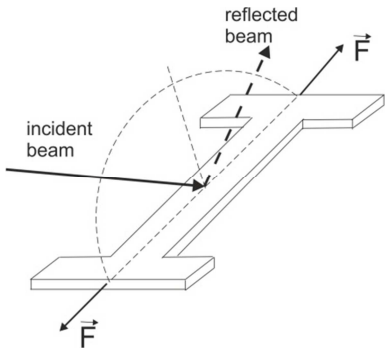

Fig. 6.8. Orientation of the sample during tensile test. The uniaxial stress Σ_{11} was applied along ϕ= 0° direction.

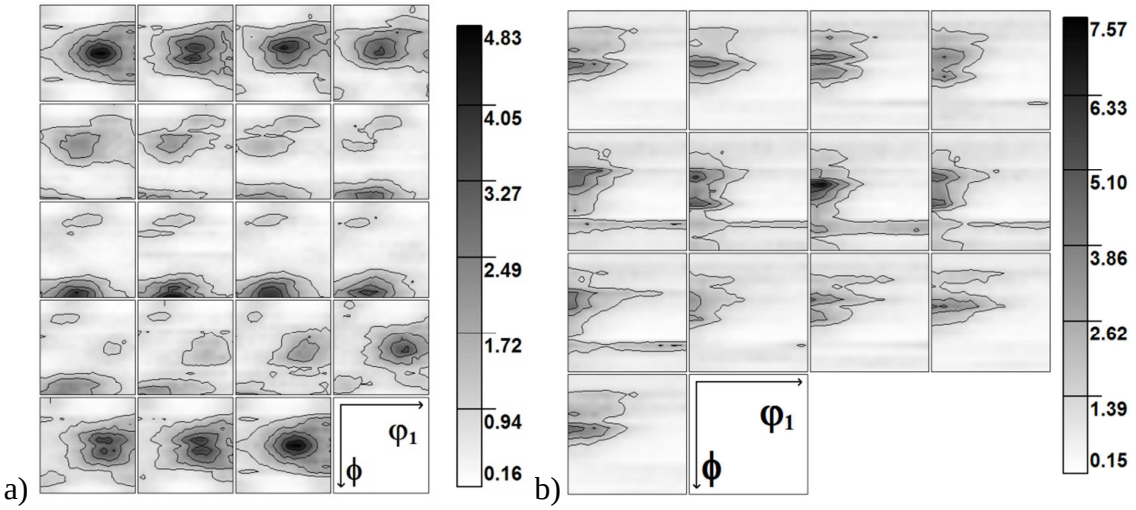

Fig. 6.9. Orientation distribution function (ODF) determined using Mn radiation for austenitic (a) and Cu radiation for Ti (b) samples (these samples were used in tensile tests). The sections through Euler space [74] with the step of 5° are presented along ϕ_2 axis: a) $0^o \leq \varphi_1, \Phi, \varphi_2 \leq 90^o$ for austenite stainless steel and b) $0^o \leq \varphi_1, \Phi \leq 90^o$ and $0^o \leq \phi_2 \leq 60^o$ for Ti (grade 2).

High anisotropy – austenitic sample

In order to investigate the influence of the grain interaction model on the values of calculated stresses austenite stainless steel (Table 6.1) having high elastic anisotropy (A=3.3, see Table 3.3) was subjected to a controlled tension (Σ_{11} = 50 MPa, 180 MPa and 300 MPa) during loading and unloading in the tensile test. For each value of given load the stress measured by X-ray diffraction was determined using the XSF calculated by four models with ODF function presented in Fig. 6.9a. In the case of MGIXD method the

measurements were performed for α=20° (corresponding to penetration depth τ =2.9 μm). Initial value of calculated stresses and lattice parameters for non-loaded sample are gathered in Table 6.2. The $<a(\phi,\psi)>^{init}_{\{hkl\}}$ vs. $sin^2\psi$ plots for initial sample are presented in Fig. 6.10. Small compressive and tensile stresses (comparable with their uncertainties) were found for ϕ = 0° and ϕ = 90°, respectively. In calculation least square fitting procedure was applied using Eq. 3.23.

Table 6.2. The initial values of stresses and lattice parameters for non-loaded austenite stainless steel.

model	α [°]	σ_{11} (MPa)	σ_{22} (MPa)	a_0 (Å)	χ^2
free surface	20	-29± 18	27± 18	3.5937 ± 0.0001	1.5
Kröner		-27 ± 24	25 ± 23	3.5937 ± 0.0001	1.7
Reuss		-26 ± 16	25 ± 17	3.5937 ± 0.0001	1.5
Voigt		-26 ± 33	24 ± 31	3.5937 ± 0.0001	1.9

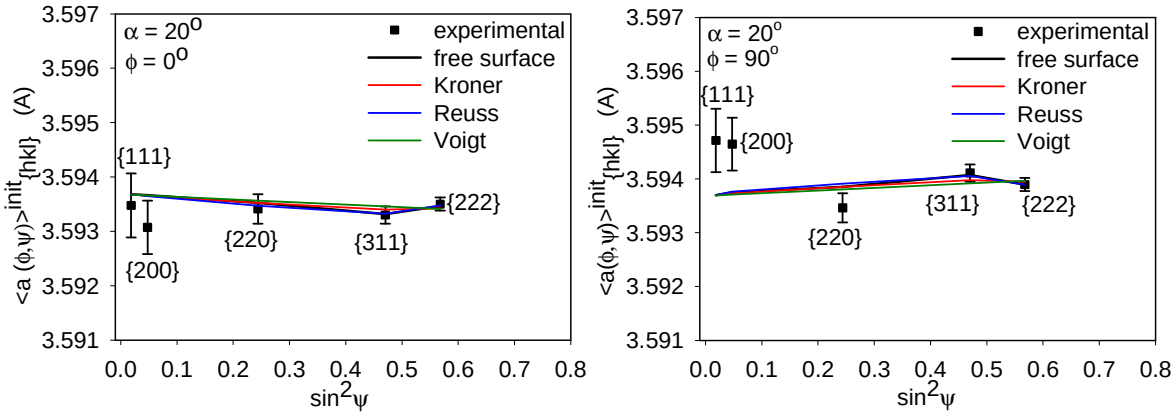

Fig. 6.10. The $<a(\phi,\psi)>^{init}_{\{hkl\}}$ vs. $sin^2\psi$ plots for initial non-loaded austenite stainless steel (uncertainty of peak position $\delta(2\theta)=0.01^o$ was assumed).

The relative lattice strains $<\varepsilon(\phi,\psi)>^{rel}_{\{hkl\}}$ vs. $sin^2\psi$ (for α=20°) calculated according to Eq. 6.3 for each load and four grains interaction models during loading and unloading are shown in Figs. 6.11 and 6.12, respectively. In these figures the experimental data are compared with the results of least square fitting based directly on the relation:

$$<\varepsilon(\phi,\psi)>^{rel}_{\{hkl\}} = F_{11}(hkl,\phi,\psi,f)\sigma^I_{11} + F_{22}(hkl,\phi,\psi,f)\sigma^I_{22} \tag{6.4}$$

where the adjusted values of σ^I_{11} and σ^I_{22} stresses can be compared with the values of applied stress Σ_{11} and $\Sigma_{22} = 0$ MPa, respectively.

The non-linearity of the $sin^2\psi$ plots in Figs. 6.11 and 6.12 is associated with a strong elastic anisotropy of the sample. As it can be deduced from these plots the lattice strains are smallest in direction <111> and largest in direction <200> for loaded the austenitic sample. This result qualitatively agrees with evolution of $½s_2$ and s_1 values for different reflections *hkl* (in the approach of quasi-isotropic material), which explains the observed tendency. If the interaction between grains is well predicted the nonlinearities of the theoretical curves should reflect this dependence.

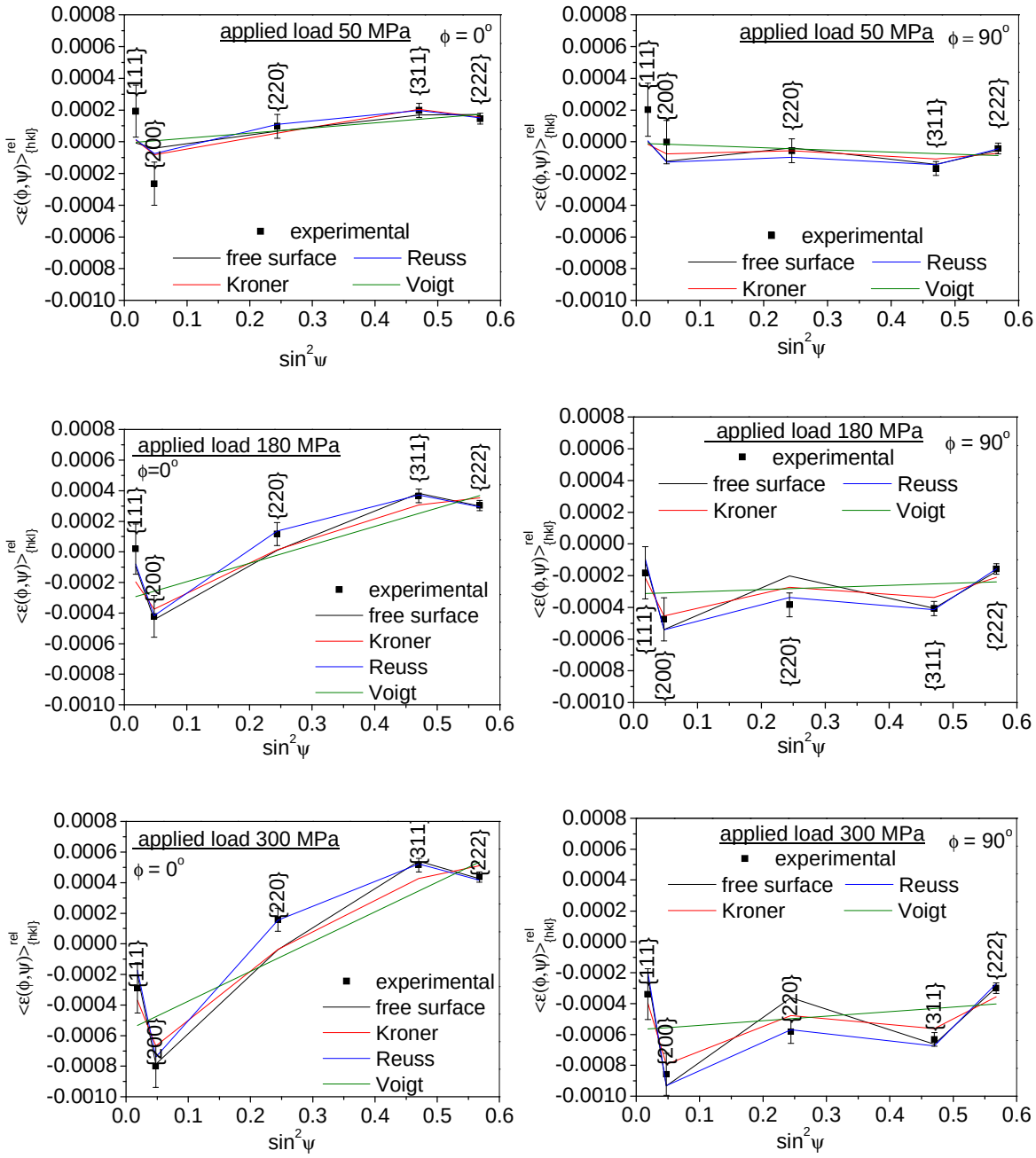

Fig. 6.11. Relative lattice strains $<\varepsilon(\phi,\psi)>^{rel}_{\{hkl\}}$ vs. $sin^2\psi$ (for α=20°) during loading of the austenitic sample. Experimental results are fitted using Eq. 6.3 with XSF calculated by four tested models.

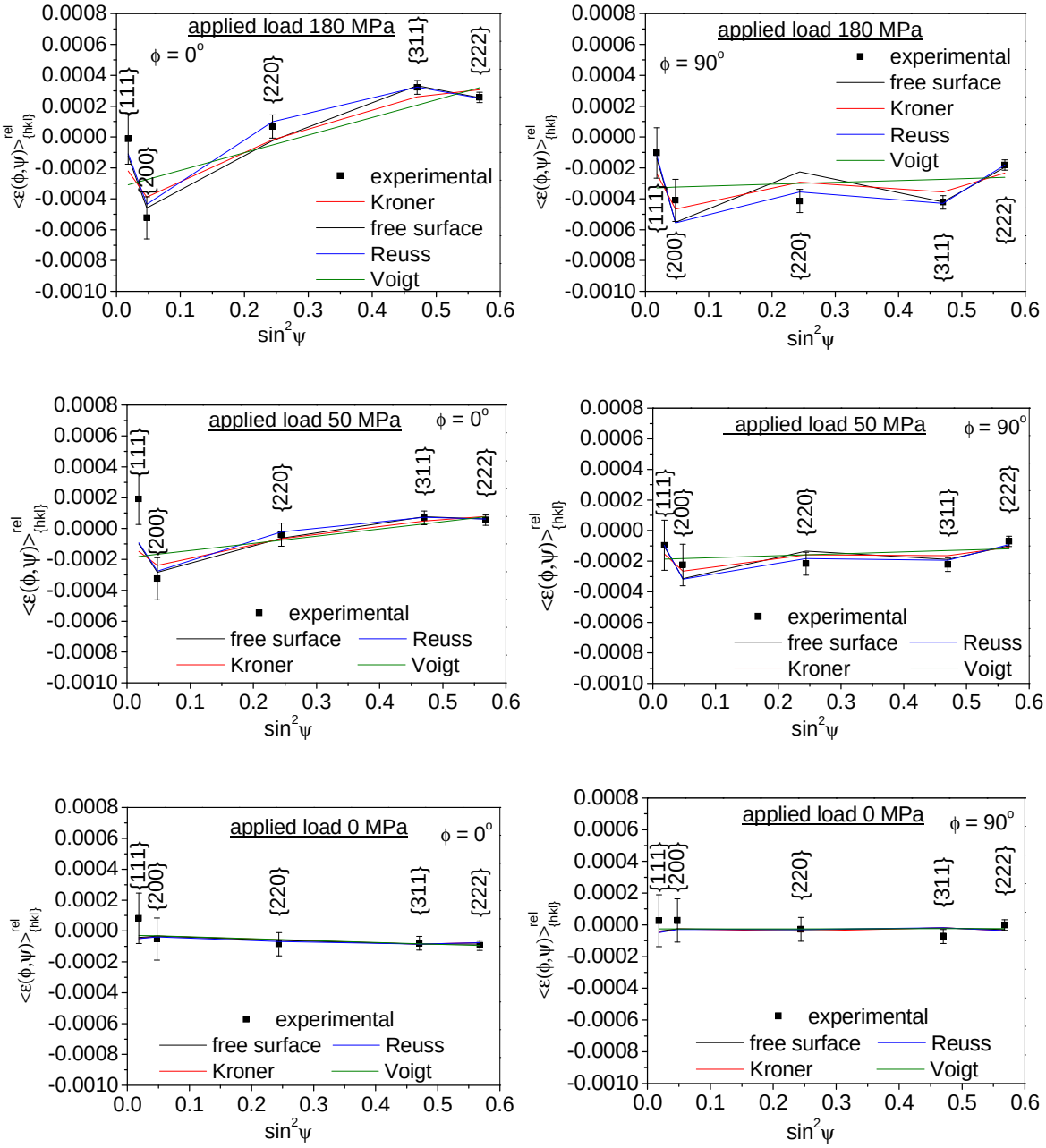

Fig. 6.12. Similar comparison as in Fig. 6.12 but for unloading of the austenitic sample.

From the *sin²ψ* plots in Figs. 6.11 and 6.12 it is seen that the experimental values and thereby the elastic anisotropy are well approached by Reuss, Kröner and free surface model. The linear dependence of lattice strains vs. *sin²ψ* predicted by Voigt model cannot be applied for austenite stainless steel having strong elastic anisotropy. Quantitative comparison of fitting quality is given by goodness parameter χ^2 which value is compared in Fig. 6.13 for all applied loads and four tested models. Analysing Eq. 2.47 it can be stated that χ^2 must increase if the differences between experimental values and theoretical results

increases. If a given model perfectly predicts XSF, the χ^2 value is determined only by experimental uncertainties and it should not increase for larger applied stresses (the lattice strain due to stress increases by the same value as the theoretically predicted strain and consequently distance between them does not change). However, if the XSF values are not correctly calculated by model (even for some orientations) the difference between theoretical and experimental interplanar spacings enlarges with increasing applied load causing significant increase of the χ^2 value (due to squaring in definition of χ^2).

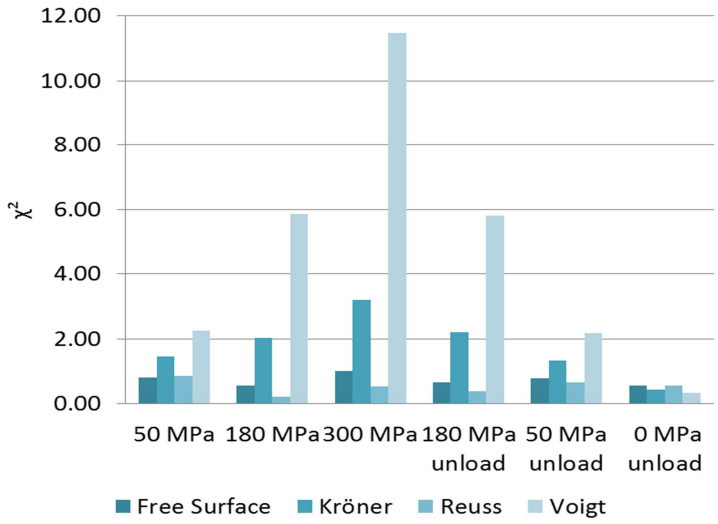

Fig. 6.13. Comparison of the values of χ^2 for four different grain interaction models during tensile of austenitic sample (loading and unloading).

Comparing values χ^2 and its dependence on the applied load it can be concluded that Reuss and free surface model correctly predict elastic anisotropy of XSFs (Fig. 6.13). For these models χ^2 is small and constant for all applied external stresses. In contrast χ^2 obtained with Kröner and Voigt models are larger and rise with applied stress. This effect is especially significant for linear dependence of lattice strains vs. $sin^2\psi$ predicted by Voigt model and it is also evidence that any models giving linear $sin^2\psi$ plot should not be used to interpret results of MGIXD measurements.

In order to determine which of these models is the best the comparison of the stresses re-calculated from diffraction data (Eq. 6.4) with the values of applied load is presented in a Fig. 6.14, for loading and unloading sample. The measurements were done using two methods: MGIXD (α=20° shown in Fig. 6.14a) and standard ψ -geometry

(Fig. 6.14b). It can be seen that the loading and unloading processes are exactly reversible (points for the same applied stress overlap for both experimental methods), i.e., the measurements were performed within elastic range of deformation. Also the stress after unloading is very close to zero value (within the uncertainty range). The stresses state in the sample was successfully determined from diffraction data i.e. the re-calculated stress σ_{11}^{I} approaches applied stress Σ_{11}, while σ_{22}^{I} is close to zero value, especially for larger loads (180 MPa and 300 MPa). It must be underline that good agreement between results obtained with both standard and MGIXD methods and values of applied stress Σ_{11} was found in the case of Reuss and free surface models, while σ_{11}^{I} obtained with Kröner and Voigt models deviate from the value of applied stress Σ_{11}. For the latter models especially large deviation between applied and re-calculated stresses is seen in the case of standard measurements (Fig. 6.14b). The worst results i.e., the largest deviation between applied and recalculated stress was obtained when the Voigt model was used.

Summarizing the presented results concerning quality of strain fitting (Figs. 6.11-6.13), as well as from the comparison of the calculated stresses and applied loads (Fig. 6.14) it appears that the Reuss and free surface models fit the best the experimental data in the case of anisotropic austenite stainless steel.

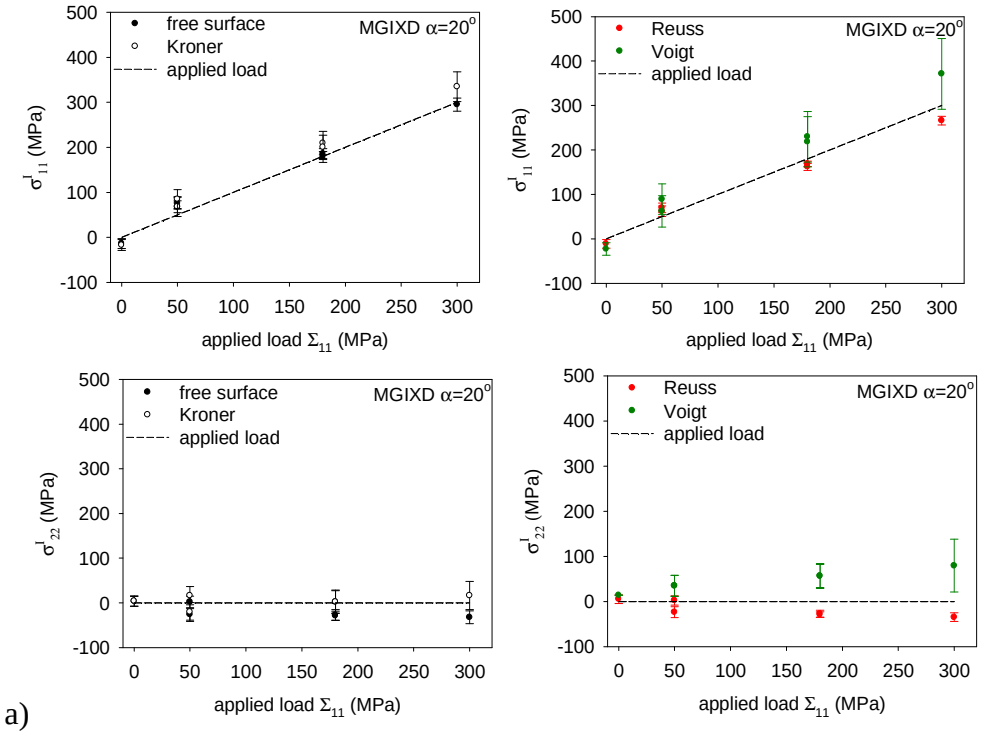

a)

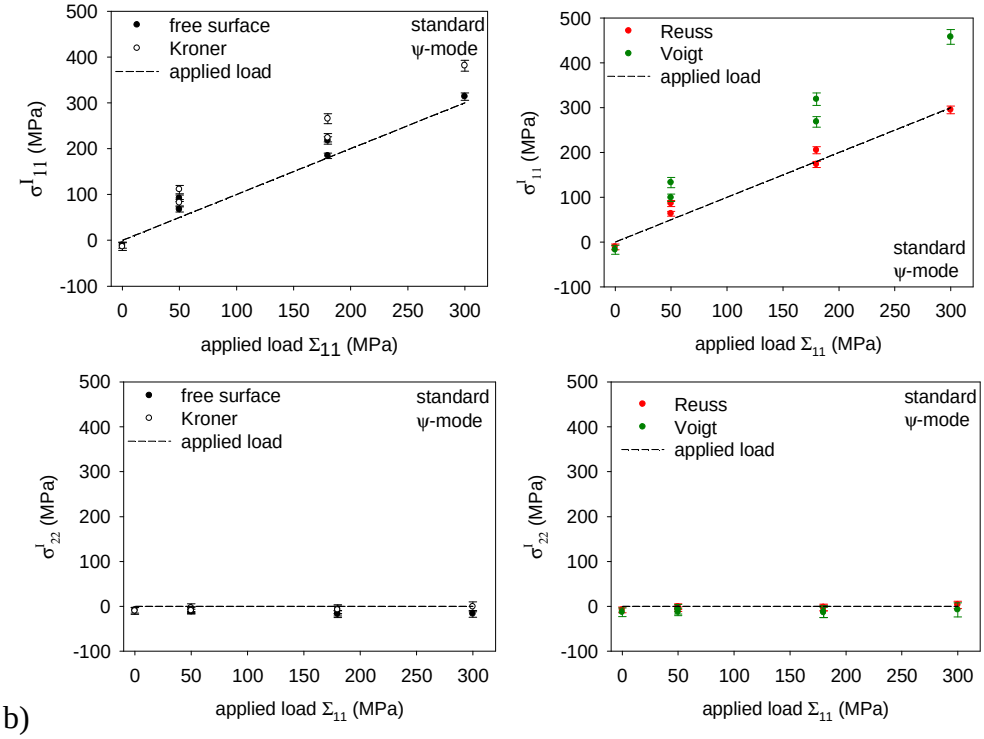

b)

Fig. 6.14. Comparison of the values of σ_{11}^{I} and σ_{22}^{I} re-calculated stresses compared with the applied stress Σ_{11} and $\Sigma_{22} = 0$ MPa, respectively (dashed line indicates value of the stress $\sigma_{11}^{I} = \Sigma_{11}$ or $\sigma_{22}^{I} = \Sigma_{22} = 0$ MPa). Results of loading and unloading are shown and the point for $\Sigma_{11} = 0$ MPa corresponds to the state after unloading. The MGIXD method (a) and standard method - ψ mode (311 reflection) (b) were used.

Low anisotropy – Ti sample

Second investigated sample was Ti (grade 2; see Table 5.1) sample having low elastic anisotropy (A=1.34, see Table 3.3). Ti was subjected to a controlled tension (50 MPa, 150 MPa, 210 MPa) during loading in the tensile test. For each value of given load the stress measured by X-ray diffraction was determined using the XSF calculated by four models with ODF function presented in Fig. 6.9b. In the case of MGIXD method the measurements were performed for α = 10° and α = 20° (corresponding to penetration depths: τ = 1.6 μm and τ = 2.5 μm), while the ω-geometry was used for standard measurements. Initial value of calculated stresses and lattice parameters for non-loaded sample are gathered in Table 6.3, while the $< a(\phi,\psi) >_{\{hkl\}}^{init}$ vs. $sin^2\psi$ plots for initial sample are presented in Fig. 6.15 (MGIXD method). Compressive stresses of about minus 30 MPa was found for ϕ = 0° and almost zero stress for ϕ = 90°, respectively. In calculation least square fitting procedure was applied using self-consistent method described in section 6.1.

Table 6.3. The initial values of stresses, strain free lattice constants and c/a parameters for non-loaded Ti (grade 2) sample - MGIXD method.

model	σ_{11} (MPa)	σ_{22} (MPa)	a_0 (Å)	c/a	χ^2
			α = 10°		
free surface	-30.9 ± 5.4	-4.7 ± 5.6	2.9511 ± 0.0001	1.5872 ± 0.0001	1.3
Kröner	-31.9 ± 5.4	-4.9 ± 5.6	2.9511 ± 0.0001	1.5872 ± 0.0001	1.3
Reuss	-30.2 ± 5.3	-4.4 ± 5.5	2.9511 ± 0.0001	1.5872 ± 0.0001	1.3
Voigt	-33.5 ± 5.6	-5.3 ± 5.7	2.9511 ± 0.0001	1.5872 ± 0.0001	1.4
			α = 20°		
free surface	-33.1 ± 8.2	10.7 ± 8.6	2.9514 ± 0.0001	1.5869 ± 0.0001	2.9
Kröner	-35.3 ± 8.2	10.4 ± 8.6	2.9514 ± 0.0001	1.5869 ± 0.0001	2.9
Reuss	-32.3 ± 8.0	11.4 ± 8.4	2.9514 ± 0.0001	1.5869 ± 0.0001	2.9
Voigt	-38.2 ± 8.4	9.4 ± 8.8	2.9514 ± 0.0001	1.5869 ± 0.0001	3.0

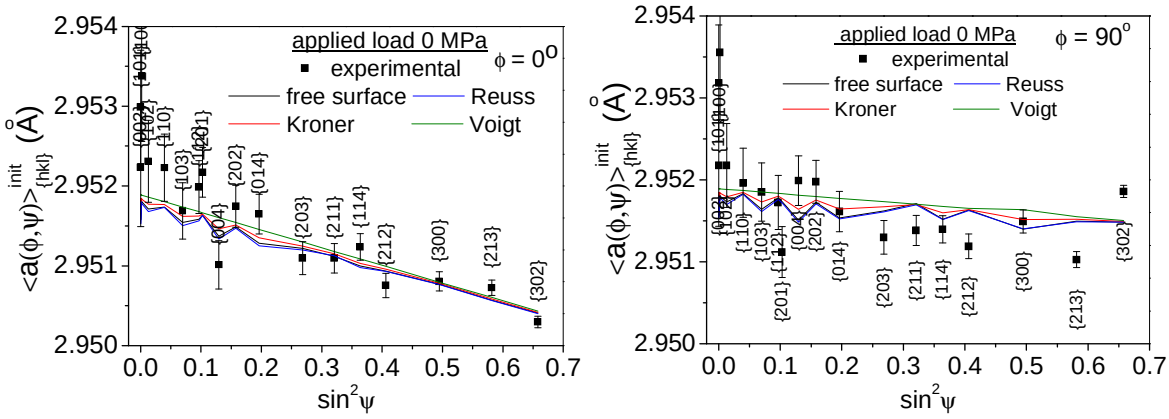

Fig. 6.15. The $<a(\phi,\psi)>^{init}_{\{hkl\}}$ vs. $sin^2\psi$ plots for initial non-loaded Ti (grade 2) sample measured measured using MGIXD with α = 20° (uncertainty of peak position $\delta(2\theta) = 0.01^o$ was assumed).

The results obtained for tensile test are presented in the following figures:

- Fig. 6.16 - the relative experimental lattice strains $<\varepsilon(\phi,\psi)>^{rel}_{\{hkl\}}$ vs. $sin^2\psi$ for α=20° (MGIXD method),
- Fig. 6.17 - values of goodness parameter χ^2 for α=10° and α=20° (MGIXD method);
- Fig. 6.18 - values of re-calculated stresses compared with applied ones.

As it is sheen in Fig. 6.16, in the case of Ti sample having low elastic anisotropy the nonlinearities of the $<\varepsilon(\phi,\psi)>^{rel}_{\{hkl\}}$ vs. $sin^2\psi$ plots are very small in comparison with austenitic sample. However, for the largest applied stress Σ_{11} = 210 MPa we can see that the experimental points are approached by theoretical lines when Reuss and free surface methods are used and slightly worse result was obtained for Kröner model. Again, the linear $<\varepsilon(\phi,\psi)>^{rel}_{\{hkl\}}$ vs. $sin^2\psi$ plots obtained with Voigt XSF do not match the experimental points. The same conclusions can be drawn from Fig. 6.17 where values of χ^2 are compared. It should be also stated that the goodness parameter slightly increases

with increasing value of applied stress (of course the effect is strongest in the case of Voigt model). Thus, the XFS are not as well predicted as in the case of Reuss or free surface model applied for austenite stainless steel.

Finally, comparing the re-calculated stress σ_{11}^{I} with applied stress Σ_{11} and the σ_{11}^{I} stress with zero value, it can be concluded that a very good agreement was obtained for the largest stress Σ_{11} = 210 MPa. If smaller load is applied the re-calculated value σ_{11}^{I} is overestimated, especially for Σ_{11} = 150 MPa. It should be underlined that exactly the same values of the recalculated stress were obtained for both incident angles α = 10° and α = 20° (MGIXD method) and for standard method (ω-mode). Hence, we can conclude that MGIXD method gives reasonable results (comparable with standard method) and the disagreement between recalculated σ_{11}^{I} and applied Σ_{11} stresses can be caused by sample heterogeneity or non-uniaxiality of the stress in the sample. Finally, it should be stated, that the stresses obtained with different models for calculation of XSFs are almost identical. This is evidence that the elastic anisotropy plays a minor role in interpretation and any model can be applied to calculate XSFs.

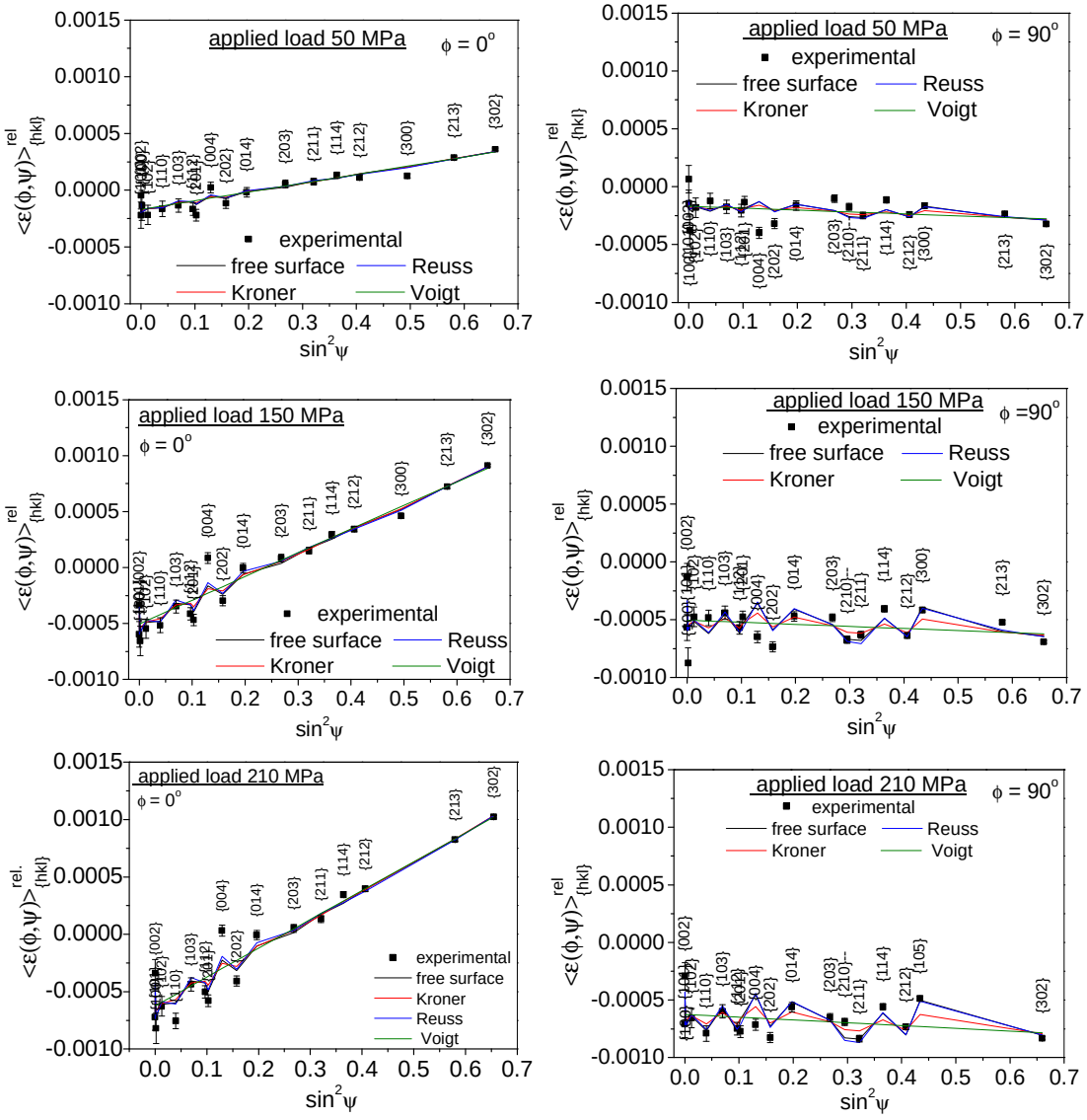

Fig. 6.16. Relative lattice strains $<\varepsilon(\phi,\psi)>^{rel}_{\{hkl\}}$ vs. $sin^2\psi$ (for α=20°) during loading of the Ti sample. Experimental results are fitted using Eq. 6.3 with XSF calculated by four tested models.

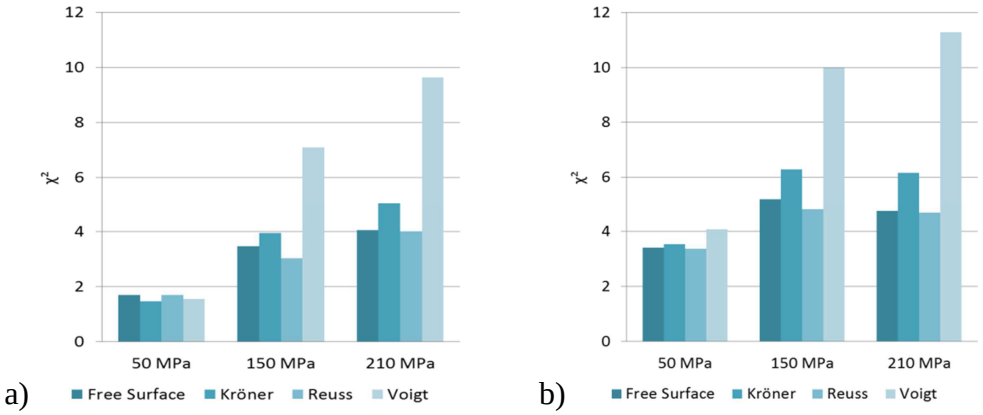

Fig. 6.17. Comparison of the values of χ^2 for four different grain interaction models during tensile of Ti sample for α=10° (a) and α=20° (b) – MGIXD method.

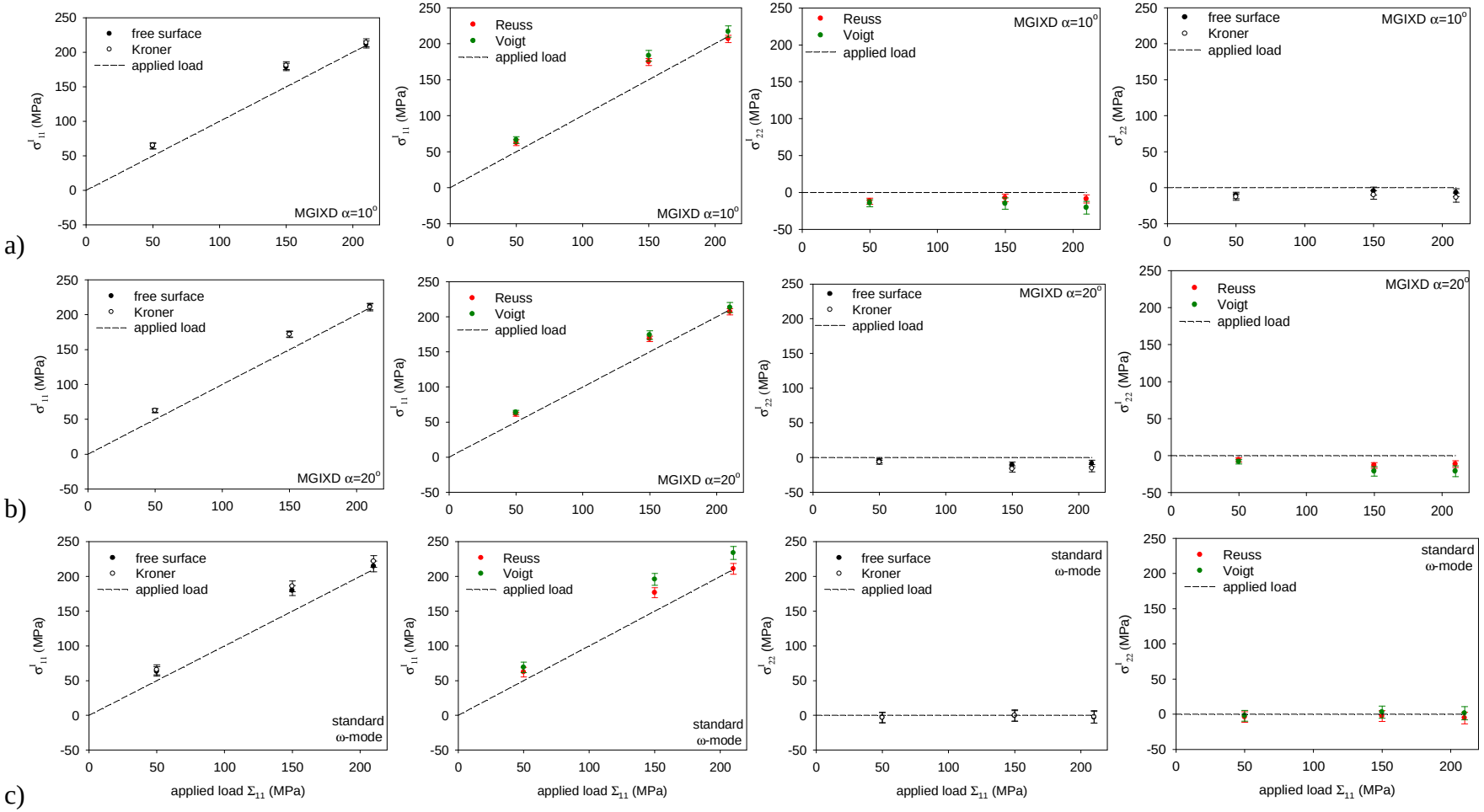

Fig. 6.18. Comparison of the values of σ_{11}^{I} and σ_{22}^{I} re-calculated stresses compared with the applied stress Σ_{11} and $\Sigma_{22} = 0$ MPa, respectively (dashed line indicates value of the stress $\sigma_{11}^{I} = \Sigma_{11}$ or $\sigma_{22}^{I} = \Sigma_{22} = 0$ MPa). The MGIXD method for α=10° (a), α=20° (b) and standard method with ω-mode (213 reflection) (c) were used to measure stresses in loaded Ti sample.

6.3.2. MEASUREMENTS OF RESIDUAL STRESSES

Next samples having significant surface residual stresses and not subjected to the external load were investigated. The pole figures were measured for polished W (high-purity), CrN coating and ground Ni alloy, and the determined ODF functions are presented in Fig. 5.19. In the case of polished W sample and deposited CrN coating the fiber type of texture was found, while ground sample does not exhibit significant sample symmetry. These textures were used in calculations of XSF from single crystal elastic constants given in Table 3.3.

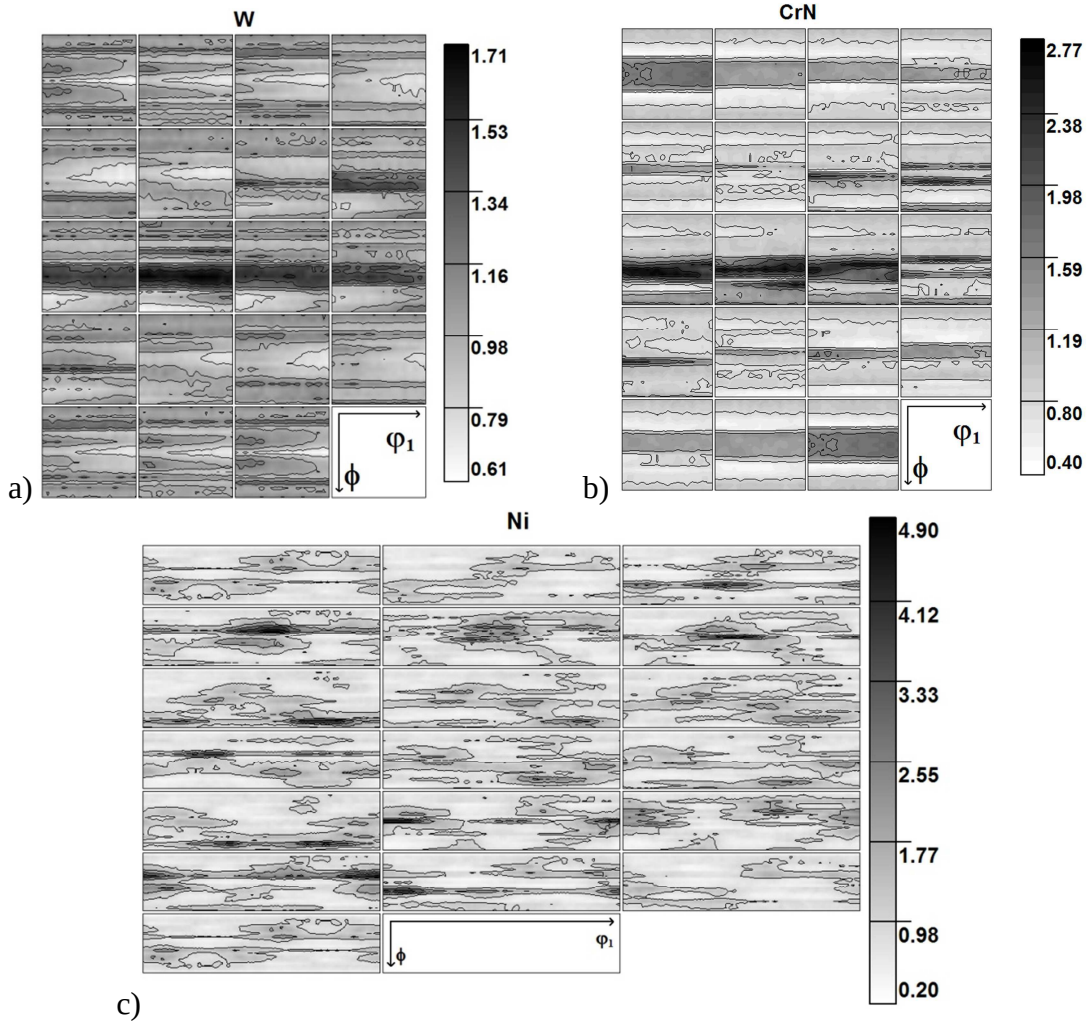

6.19. Orientation distribution function (ODF) determined using Cu radiation for polished W (a), CrN coating (b) and ground Ni alloy (c) samples for which residual stresses were measured. The sections through Euler space [74] with the step of 5° are presented along ϕ_2 axis and ranges $0^o \leq \varphi_1, \Phi, \varphi_2 \leq 90^o$ for W and CrN (a, b) and $0^o \leq \Phi, \varphi_2 \leq 90^o$, $0^o \leq \varphi_1, \leq 360^o$ for ground Ni alloy.

Firstly, elastically isotropic sample (A=1, see Table 3.3) tungsten (W) was investigated. To generate stress in surface layer sample surface was manually polished (paper 2000 grit, non-directional polishing) causing roughness equal R_a=0.16 μm. The MGIXD method for different incident α angles as well the standard method (ω and ψ geometries with 321 reflection) were applied to measure lattice strains. In order to calculate stresses the fitting procedure based on Eq. 3.23 and two components σ_{11} and σ_{22} of biaxial stress were determined. Comparison of stresses determined using different XSFs (calculated using single crystal elastic constants from Table 3.3 and texture shown in Fig. 6.19 a) and the values of χ^2 parameter obtained in this analysis are presented in Fig. 6.19. The $< a(\phi,\psi) >_{\{hkl\}}$ vs. $sin^2\psi$ plots for an example incident angle α = 5° (MGIXD method) and for standard methods are shown in Fig. 6.20, while the comparison of the $sin^2\psi$ plots for different incident angles α is shown in Fig. 6.21 (XSFs given by free surface model were applied in calculations).

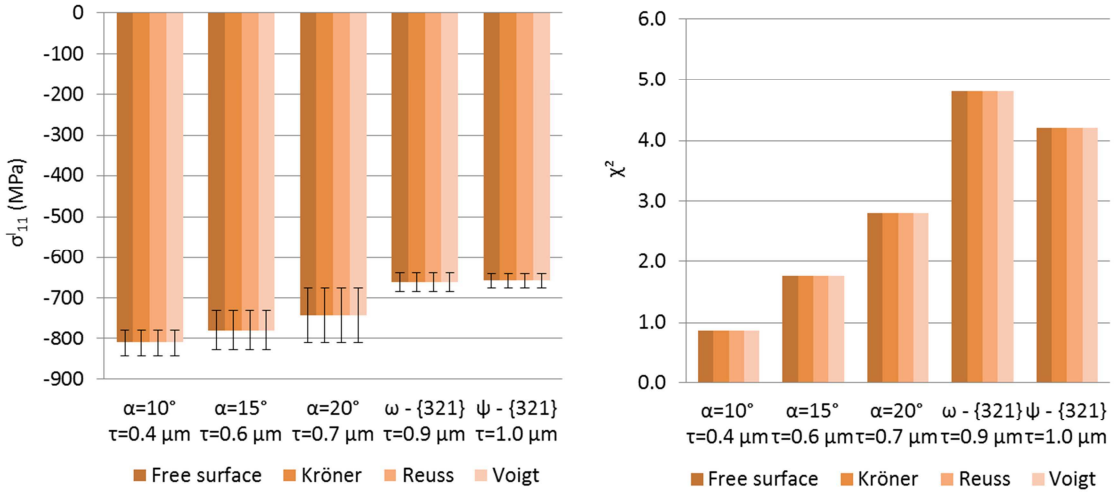

Fig. 6.19. Values of determined stresses in polished W sample using MGIXD method and standard method (a) and comparison of χ^2 parameter values (b) for four grain interaction models (refraction correction was not introduced).

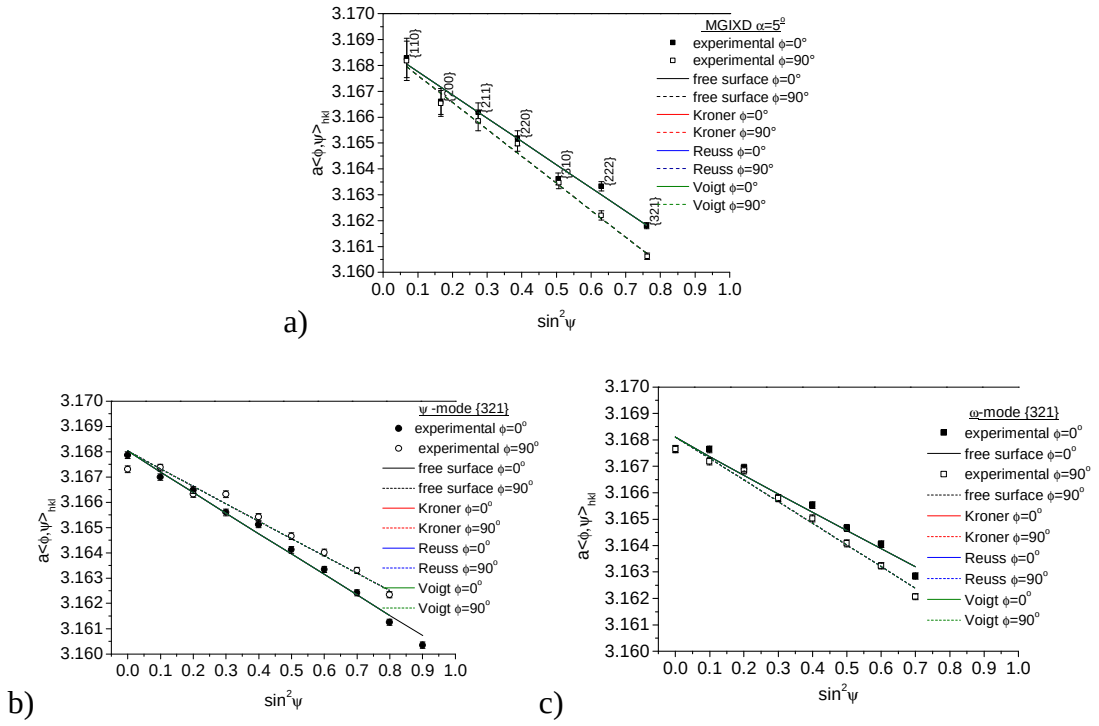

Fig. 6.20. Experimental points and theoretical $<a(\phi,\psi)>_{\{hkl\}}$ vs. $sin^2\psi$ for polished W sample. Measurements presented for MGIXD (α=5°) (a) and standard ψ-mode (b) and ω-mode (c) methods (uncertainty of peak position $\delta(2\theta)=0.01^o$ was assumed).

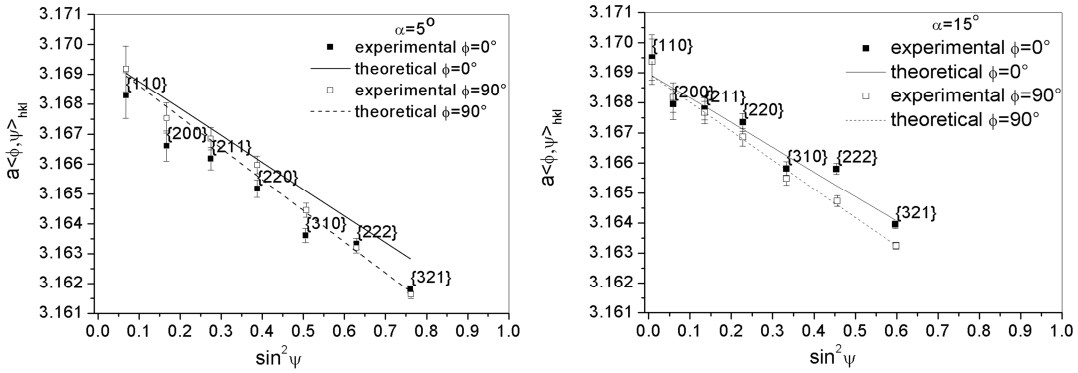

Fig. 6.21. Example of the $<a(\phi,\psi)>_{\{hkl\}}$ vs. $sin^2\psi$ plots for polished W sample. Results presented for MGIXD method for incident angles α=5° and α=15°.

In the light of these results it is clearly seen that in the case of elastically isotropic sample there is no any difference in the values of calculated stresses, for MGIXD and standard method, for any of chosen grain interaction models. In the case of isotropic W sample the $<a(\phi,\psi)>_{\{hkl\}}$ vs. $sin^2\psi$ plots are straight-lines for each of considered models. This is certainly due to perfect elastic isotropy of W crystals and consequently equal values of XSF for all reflections.

Presenting the stresses determined by MGIXD method (Fig. 6.22), it is also important to define the range of information depths $\bar{z} = \tau$ (or α angles) for which the results of analysis are reasonable. In the case of studied sample we can assume that real values of the stresses as well as strain free lattice parameter are between those obtained with and without refraction correction. We can see that the uncertainty of the obtained results increase significantly for incident angle $\alpha \leq 10^{o}$ ($\tau \leq 0.4$ μm), because the difference between results with and without correction increases. As shown in Fig. 6.22, the value of strain free parameter does not change significantly with the information depth. The stress in the mechanically polished W is compressive, biaxial and approximately fulfils relation $\sigma_{11} \approx \sigma_{22}$. The stress value determined by MGIXD method is almost constant for the studied penetration depth (slowly decreasing with depth), and perfectly agree with the results of both standard methods. The stresses obtained with the latter method were presented for an average value of penetration depth for all ψ-inclination angles.

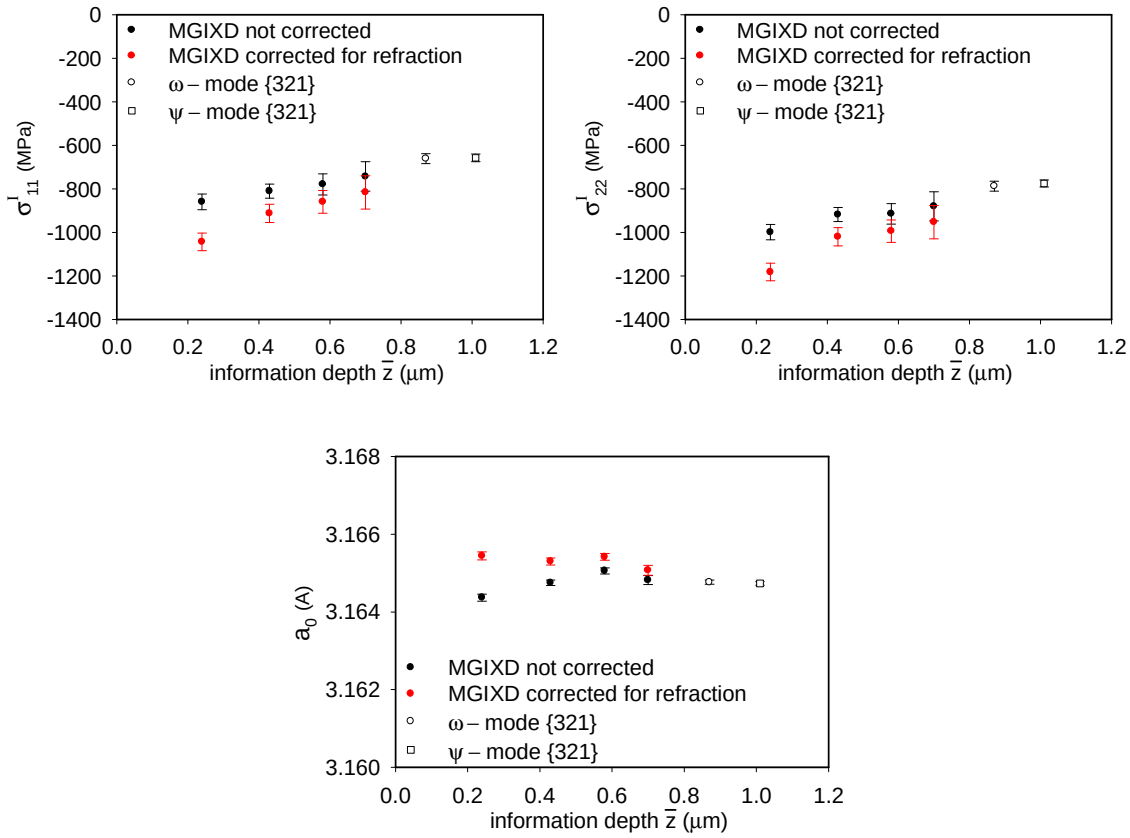

Fig. 6.22. Residual stresses and strain free lattice parameter in function of the information depth $\bar{z}$ (equal to τ, see Eq. 3.4) determined with and without correction refraction effect for polished W sample.

Secondly, samples having high elastic anisotropy were investigated: ground Ni alloy (A=2.76), polished austenite stainless steel (A=3.3) and CrN coating (A=0.34). The Ni alloy (composition given in Table 6.1) was ground manually in one direction (angle 5°; effort 80N and advance 88 mm/s). Such surface treatment cause rough surface (R_a = 3.3 μm) having topography presented in Fig. 6.23, showing regular 'ridges and furrows' with amplitude of 10 μm distributed with the period of about 100 μm. It was found that after crystallographic texture after grinding does not exhibit sample symmetry (the ODF is shown grinding). The stress measurements were performed using Cu radiation on PANalytical - X'Pert MRD (ENSAM, Paris) diffractometer having configuration given in Table 4.4.

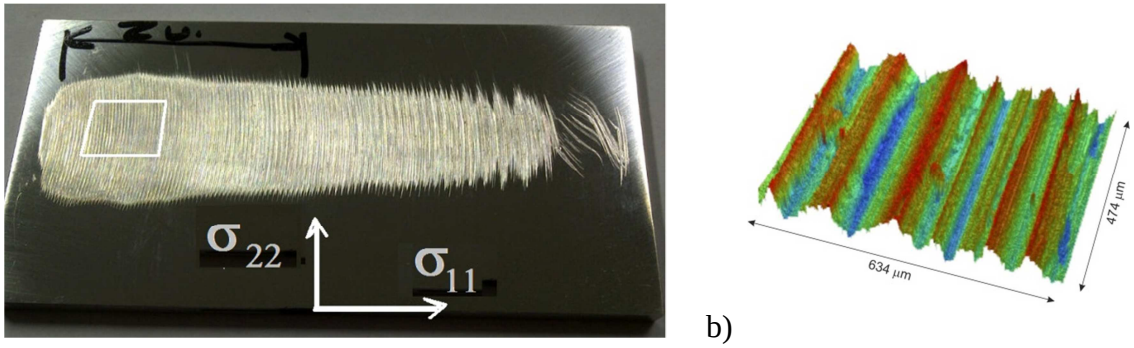

a) b)

Fig. 6.23. Surface topography of ground Ni alloy sample with orientations of measured stresses (a) and roughness characterisation in the direction perpendicular to direction of grinding (b). The measuring area is indicated in figure (a).

The CrN coating (6 μm thickness) was deposited at high temperature on a 4H13 steel substrate deposited on the 4H13 steel substrate. The coating was obtained by means of the arc-vacuum method in a nitrogen atmosphere at the pressure of N_2 equal to $3.5x10^{-2}$ mbar and the temperature of 450° C [101, 102]. The average speed of deposition was 60 nm/min. As a result, the coating exhibiting the average surface roughness R_a = 0.33 μm and fibre crystallographic texture (Fig. 6.19 c) was produced. The stresses were measured using Cu radiation on PANalytical - X'Pert diffractometer MRD (AGH, Kraków) with configuration given in Table 5.4.

In the case of austenite stainless steel (the same material as used in tensile test - AISI316L with composition given in Table 6.1) the sample surface was mechanically (manually) polished in all two directions, changing orientations of the sample during polishing. In this case average roughness equal R_a = 0.13 μm was obtained. The stress measurements were performed on Seifert - PTS MZ VI using Fe radiation (Table 5.4).

The MGIXD method and standard method were applied to determine stresses in aforementioned samples. Fitting procedure based on Eq. 6.2 showed that only in the case of austenitic sample the determined probabilities of finding stacking fault between neighbouring planes (ρ value) has significant influence on the results and its value exceeds the uncertainty. Therefore ρ parameter was adjusted in the case of polished austenite stainless steel, while for the other samples $\rho = 0$ was assumed. The result of stress analysis for different considered grain interaction models and for all samples is presented in a Fig. 6.24 while the values of χ^2 test are shown in Fig. 6.25. The example of $< a(\phi,\psi) >_{\{hkl\}}$ vs. $sin^2\psi$ plots, compared all for analysed samples are presented in Fig. 6.26 (for different grains interaction models) and in Figs. 6.26 – 6.29 (for different α incident angles).

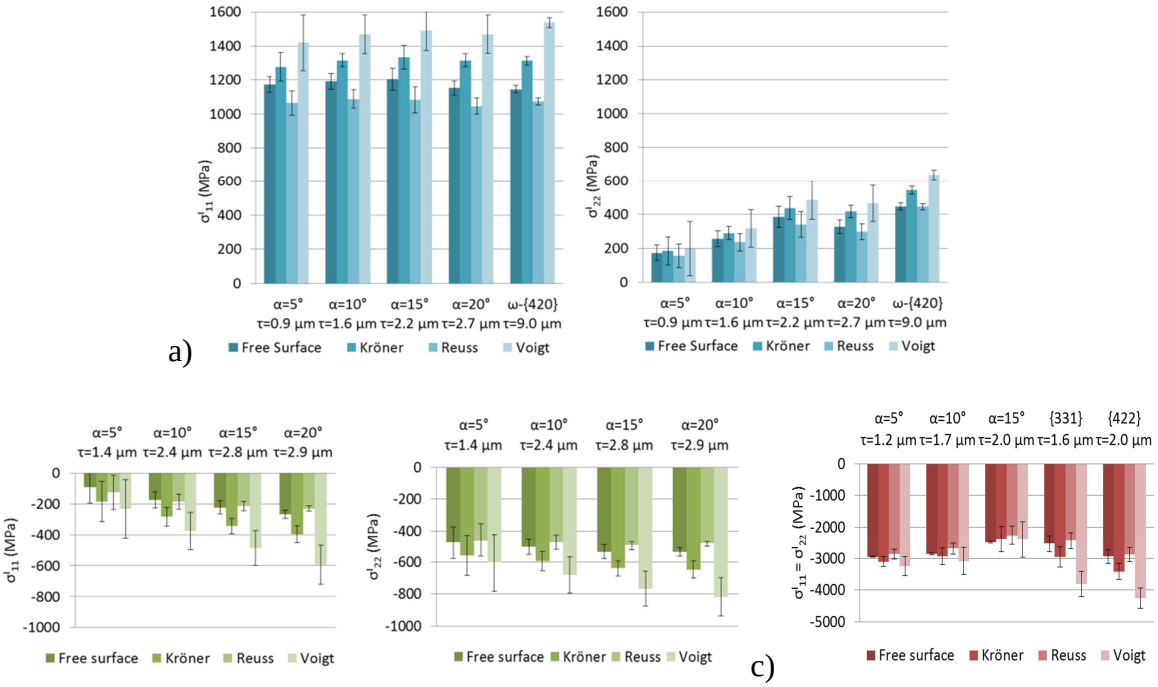

Fig. 6.24. Comparison of influence of four models of the grain interaction model on the results of X-ray stress analysis for ground Ni alloy (a), polished austenite stainless steel (b), and CrN coating (c). The results for different incident angle α are compared with standard method for hkl reflections.

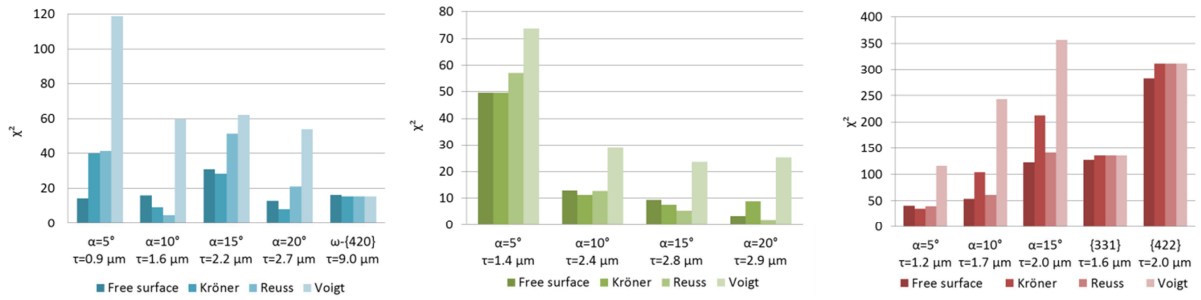

Fig. 6.25. Comparison of the values of χ^2 parameter for different grain interaction model for ground Ni alloy (a), polished austenite stainless steel (b), CrN coating (c). The results for different incident angle α are compared with standard method for hkl reflections.

The results presented for all considered samples show that the theoretical curves do not matches experimental points when Voigt model is used to calculate XSF. Comparing values of stresses determined using different models of XSF calculation we can notice large discrepancies, especially for Ni alloy and austenitic stainless steel (Fig. 6.24). On the basis of the values of χ^2 parameter (Fig. 6.25), it can be concluded that for Ni alloy as well as polished austenite stainless steel we cannot decide which of those three: Reuss, Kröner and free surface models is the best one. In such a case we must accept larger uncertainty of measured stress values due to difference between these three models if the XSF are not verified in tensile test as for Ni alloy. Certainly, in the case of austenite stainless steel the results presented in Fig. 6.25 confirms conclusion drawn previously from tensile tests, that the Reuss and stress free models correctly predict XSFs. For CrN sample it would appear that free surface model fit the best the experimental data. It is worth to emphasize that the considered uncertainty of determined peak position $\delta(2\theta) = 0.01^o$ is much too small, relative to the actual value, also for the models which seems to correctly fit the experimental points. This is due to the fact that even slight misalignment of the model to the experimental values will increase with increasing stress value. For example, if goodness of fit caused by model discrepancy is on the level χ^2 =1-2 for 300 MPa (as for austenite stainless steel or Ti the tensile tests) it will increase proportionally to squared stress, reaching value χ^2 =16-32 for 1200 MPa (as in the case of ground Ni alloy, excluding Voigt method), χ^2 =4-8 for 600 MPa (as for polished austenite stainless steel, excluding Voigt method and all methods for α = 5^o) and χ^2 =100-200 for 3000 MPa (as for CrN coating, excluding Voigt method and standard method for 422 reflection). Therefore, in spite of large values of χ^2 the discrepancy of the models (excluding Voigt) is on the same level for the tensile tests as well as for samples with residual stresses almost for all measurements.

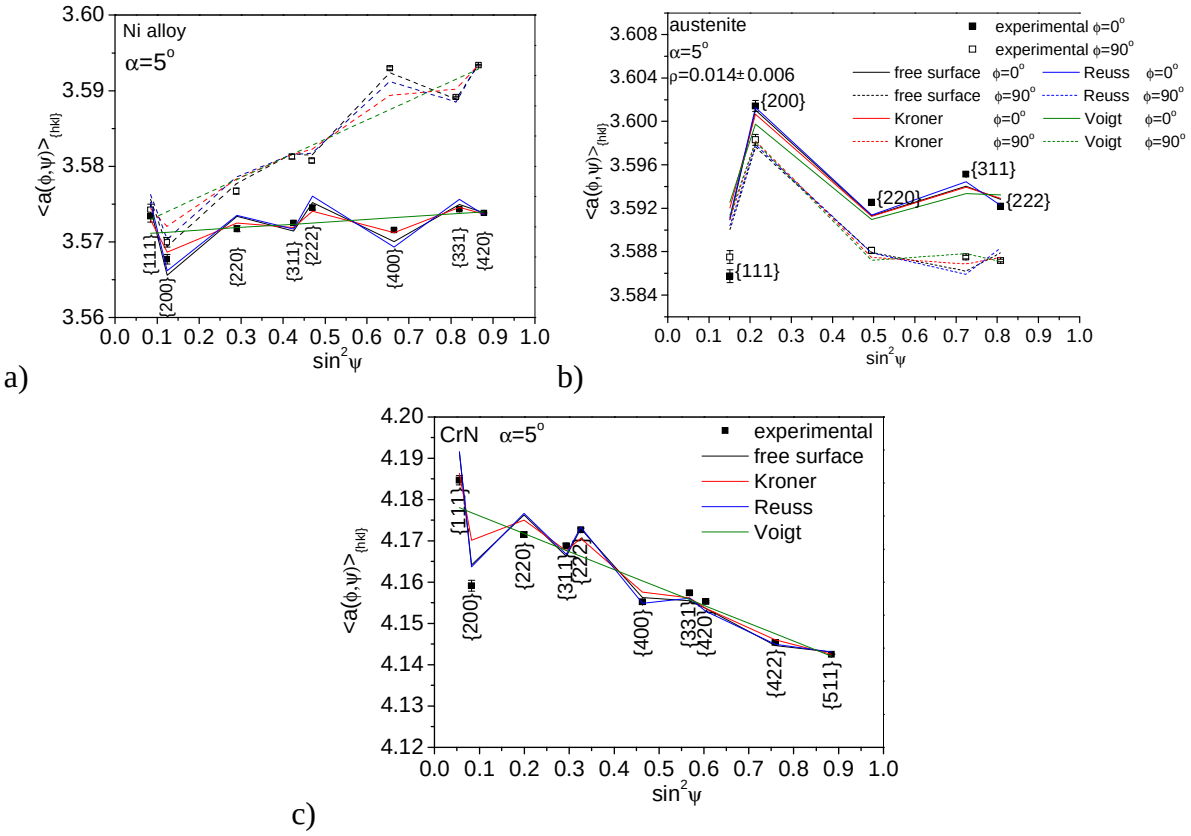

Fig. 6.26. The $<a(\phi,\psi)>_{\{hkl\}}$ vs. $sin^2\psi$ plots, compared for different grain interaction models, for MGIXD α=5° for ground Ni alloy (a), polished austenite stainless steel (b), CrN coating (c). Only in the case of austenitic sample ρ parameter was fitted and determined (ρ =0.014±0.006).

In the sight of presented results it seems that free surface as Reuss model are in a very good agreement with experimental results in comparison with other models (see Fig. 6.26). In particular the Voigt model cannot be taken into account stress analysis because it does not reflect the anisotropy of XSF, which is seen as the nonlinearities $<a(\phi,\psi)>_{\{hkl\}}$ vs. $sin^2\psi$ plots. In the case of polished austenite stainless steel (A=3.3) and ground Ni (A=2.76) alloy the lattice strains in direction <111> are relatively smaller than in the direction <200>, while opposite tendency occur for CrN coating (A=0.34). It can be deduced form Figs. 6.26 -6.29 analysing shift of the experimental points from straight line and considering the sign of stress (compressive for austenite stainless steel and CrN coatingand, tensile for Ni alloy). This confirm opposite type of single crystal anisotropy for crystal having A >1 and A<1 (Young modulus is smaller in <200> direction in comparison with <111> for A>1 and the opposite tendency occurs for A<1). The latter results can be compared with elastically isotropic

(W) sample for which the $<a(\phi,\psi)>_{\{hkl\}}$ vs. $sin^2\psi$ experimental plots are linear and the experimental point lie (in a margin of error) on the straight line.

For more precise analysis of the influence of the chosen model for investigated stresses the $<a(\phi,\psi)>_{\{hkl\}}$ vs. $sin^2\psi$ plots are presented in Figs. 6.26 - 6.28 for different incident angle α in MGIXD method for free surface model, which is in the best agreement with experimental results, and for Kröner model which does not reflect fully the experimental results.

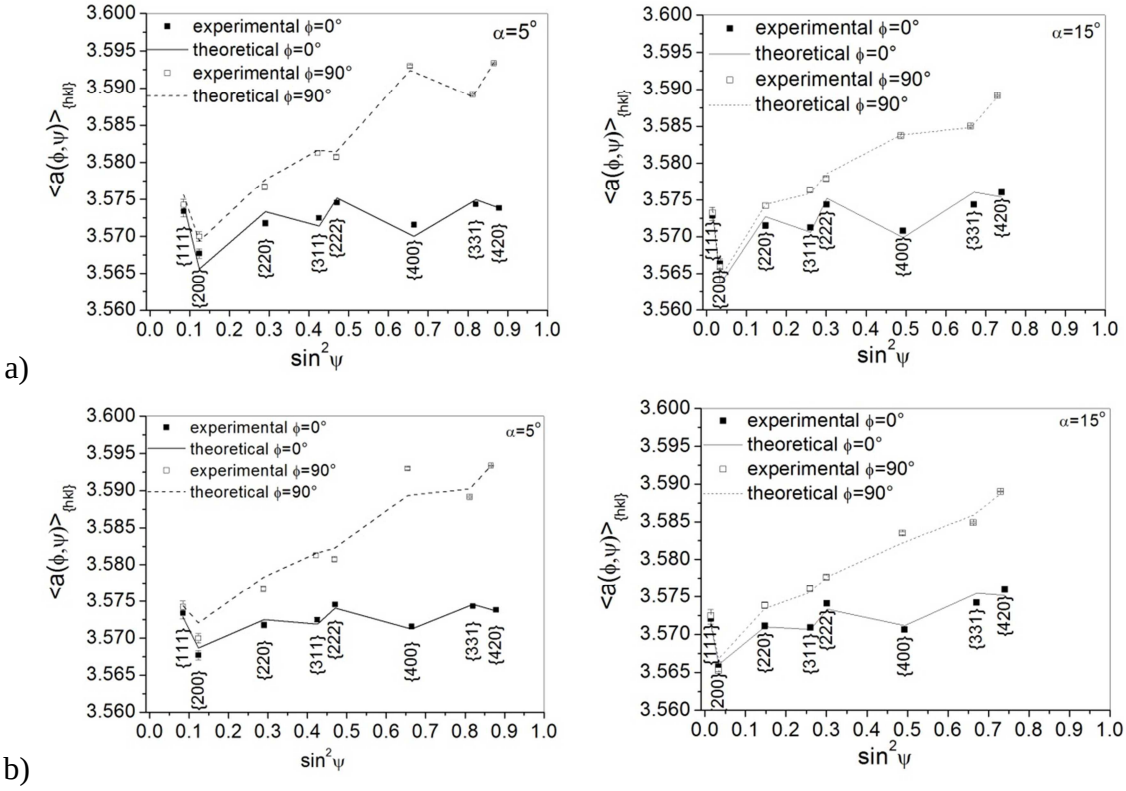

Fig. 6.27. Example of the $<a(\phi,\psi)>_{\{hkl\}}$ vs. $sin^2\psi$ plots for ground Ni alloy. Measurements presented for incident angles: 5°, 15° (MGIXD). The theoretical curve obtained using XSF calculated from single crystal data using free surface (a) and Kröner (b) models.

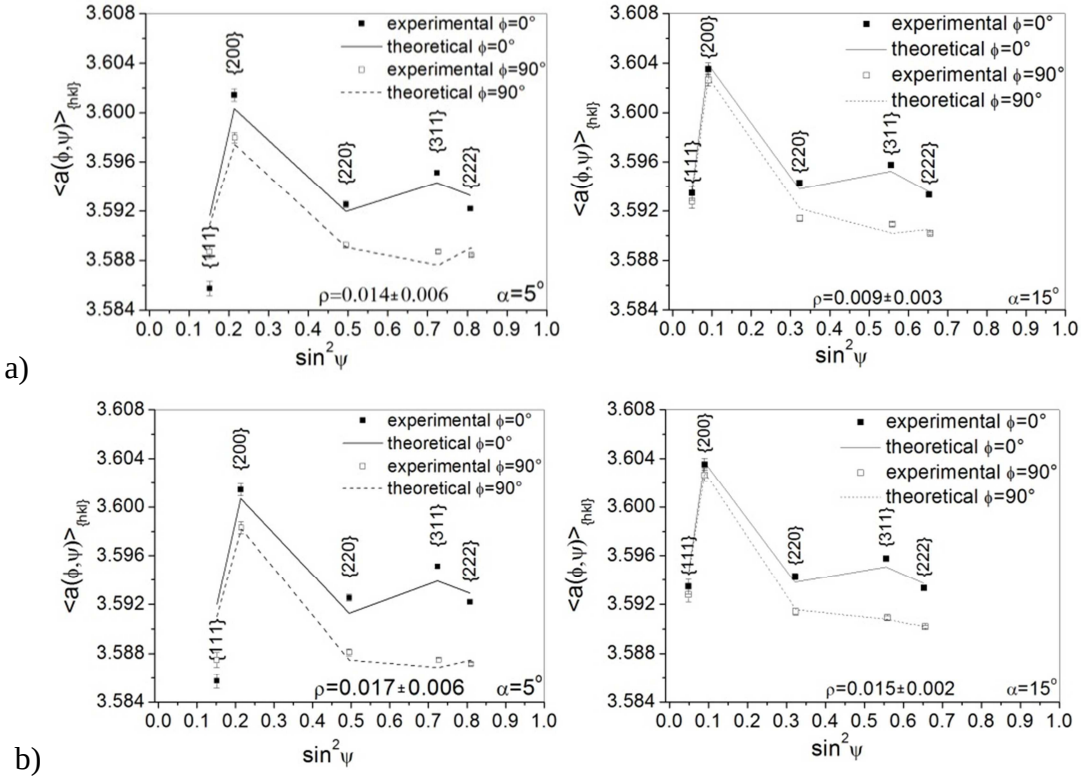

Fig. 6.28. Example of the $<a(\phi,\psi)>_{\{hkl\}}$ vs. $sin^2\psi$ plots for polished austenite stainless steel. Measurements performed by MGIXD for incident angles: 5°, 15°. The theoretical curve obtained using XSF calculated from single crystal data using free surface (a) and Kröner (b) models.

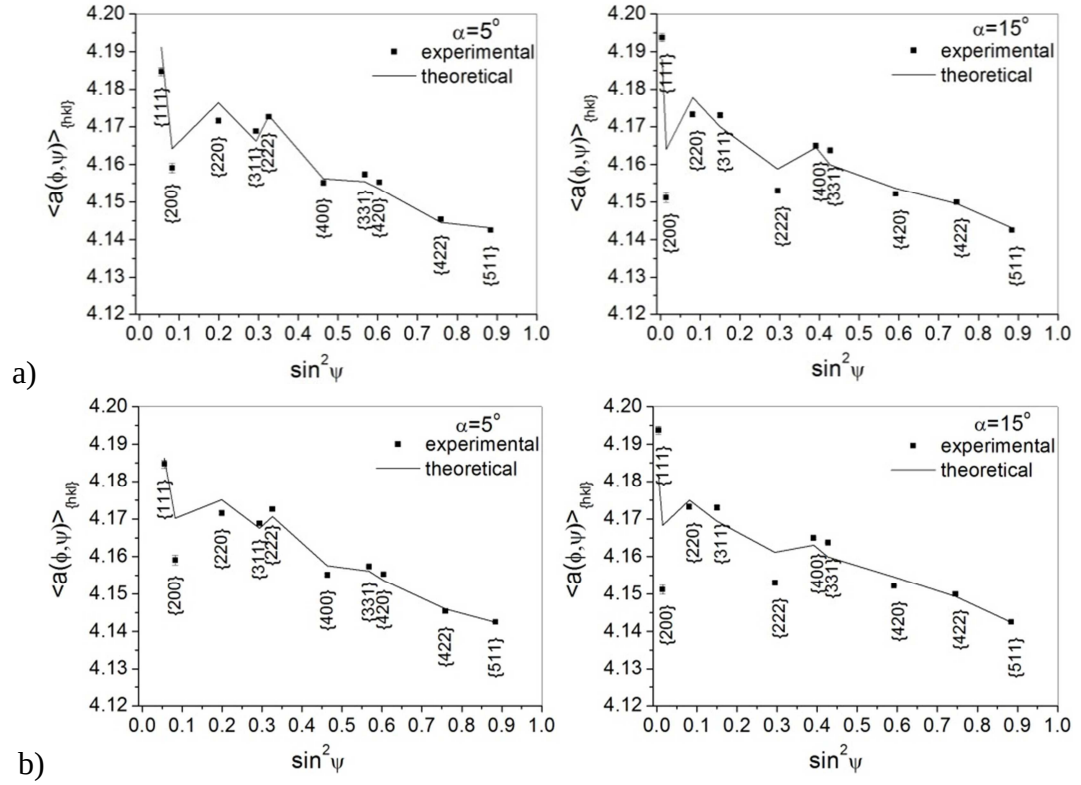

Fig. 6.29. Example of the $<a(\phi,\psi)>_{\{hkl\}}$ vs. $sin^2\psi$ plots for CrN coating. Measurements performed by MGIXD for incident angles: 5°, 15°. The theoretical curve obtained using XSF calculated from single crystal data using free surface (a) and Kröner (b) models.

Finally, the results of residual stress analysis in anisotropic samples are presented in Fig. 6.30 where the dependence of stresses and strain free parameters vs. information depth is shown (Eq. 3.4). Analysis was performed applying XSF calculated by the free surface model with refraction correction or without this correction.

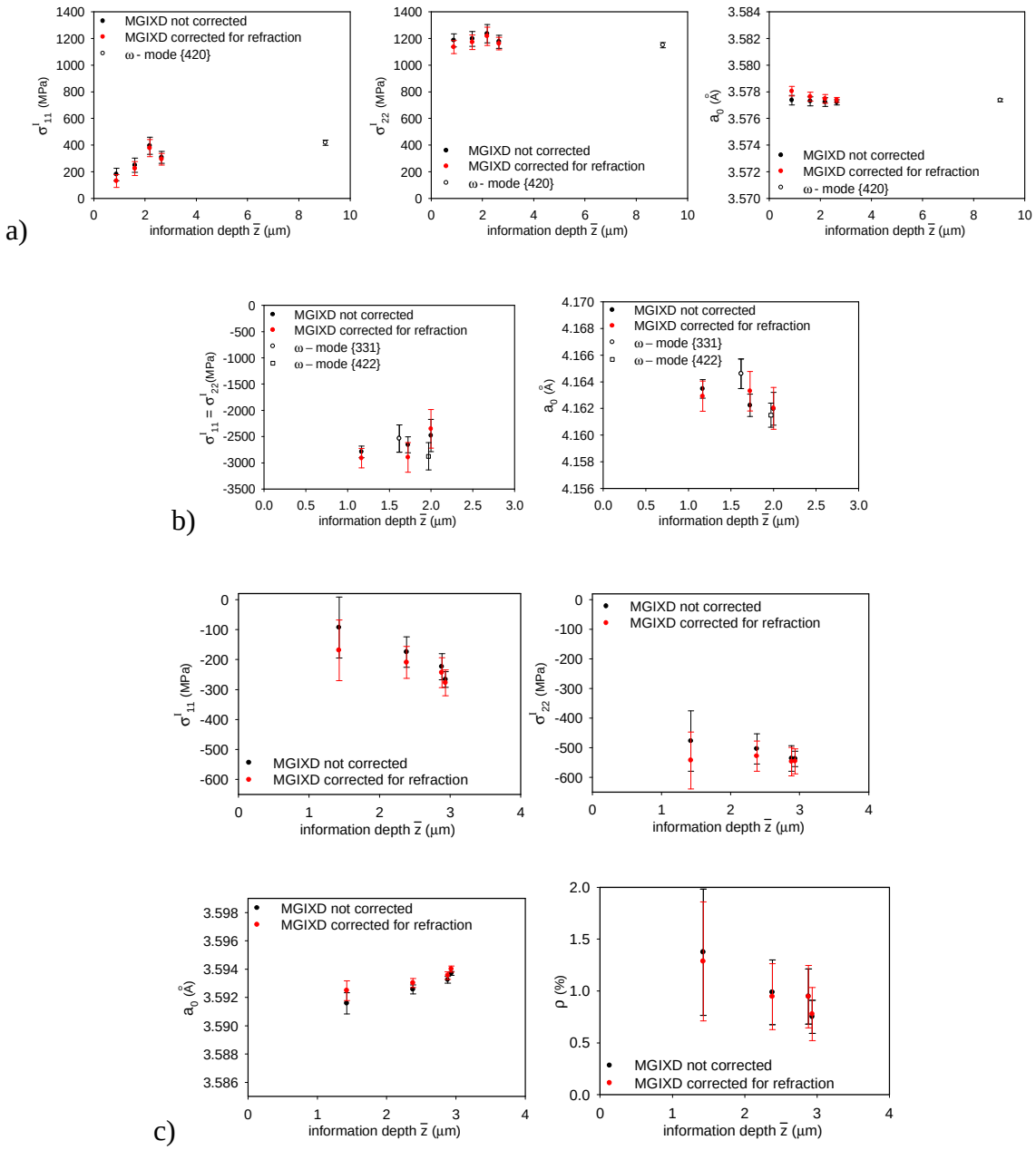

Fig. 6.30. Residual stresses, strain free lattice parameter and ρ parameter (in the case of austenitic sample) in function of the information depth $\bar{z}$ (see Eq. 3.4) determined with and without correction refraction effect index for ground Ni alloy (a), CrN coating (b) and polished austenite stainless steel (c).

Analysing the results from Fig. 6.30 it can be conclude:

- Tension stresses were found in the ground Ni alloy sample (such stress is generated due to temperature gradient during grinding). Residual stresses are large and constant for different incident angles in the direction of grinding (σ_{22}^{I} - along ridges and furrows), while it is much smaller and decreasing to zero value at surface for perpendicular direction (σ_{11}^{I}), see Fig. 6.23. This effect can be easily explained due to shadows for the X-ray beam causing from the ridges which are important when the measurement is performed in transfers direction (σ_{11}^{I} are measured for the top ridge where its relaxation close to the surface is very large). The stress σ_{22}^{I} is measured for the ridges and furrows as well (no shadow) and it does not relax significantly at the top of ridge (in direction of grinding). The standard measurements confirm tendency of stress evolution in larger depth. It should be also emphasised that no significant difference was observed for the stresses determined taking into account refraction correction and without correction. This is because the shift of the diffraction peak is very small in comparison large shift caused by large stress (strain). However, we can see influence of refraction on the value of strain free lattice parameter a_0. It should be underlined that determined value of a_0 is constant for different depths (even for so large stresses) if the refraction correction is not applied and the correction causes unexpected variation of a_0. It means that refraction should not be taken into account due to very rough surface (R_a=3.3 μm).

- Compressive very large stress was found in CrN coating ($\sigma_{11}^{I} = \sigma_{22}^{I}$ was assumed because of fibre sample and process symmetry). It results from different shrinking amplitudes of the CrN layer and the steel substrate during cooling (their thermal expansion coefficients are, respectively 6 x 10^{-6} K [103] and 11-12 x 10^{-6} K [104, 105]). It should be noted that the observed important compressive stress is caused not only by the temperature effect but also due to the peening of the growing coating by accelerated atoms, interdiffusion and the reactions with the substrate [105, 106]. A similar level of the stresses in the CrN coating deposited on the steel base was previously observed in [101, 105, 106]. For this sample the stresses are so large that the effect of refraction correction is relatively small (Fig. 6.30b).

- Compressive stress was determined in polished austenitic sample. Higher value of compressive stress was found in the direction in which the last polishing was applied (i.e. $|\sigma_{22}^{I}| > |\sigma_{11}^{I}|$) and the stress in transverse direction (σ_{11}^{I}) relaxes close to the surface.

This effect is very similar to this observed in ground Ni alloy taking into account that ridges and furrows were created in austenitic sample (with small roughness R_a=0.13 μm) along direction of the last polishing. The dependence of a_0 vs. depth is not constant but the variation is rather small. Concerning probability of stacking fault finding it can be seen that it decreases with penetration depth. Fitting or not fitting of the ρ parameter does not change the results of calculated stresses and a_0 (but quality of fitting is better, see Fig. 6.31). This is because ρ influence only deviation of points from the straight line in $<a(\phi,\psi)>_{\{hkl\}}$ vs. $sin^2\psi$ plot but does not change its slope. Finally, it can be concluded that results difference between results corrected and not corrected for reflection effect increase significantly for incident angle $\alpha \leq 10^o$ ($\tau \leq 2.4$ μm).

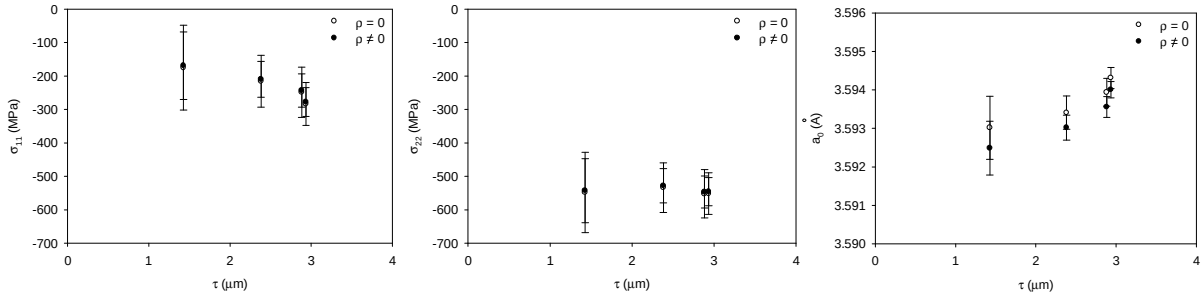

Fig. 6.31. The influence of fitting or not fitting of the ρ parameter on the results of calculated stresses and a_0 parameter.

6.4. CONCLUSIONS

In this chapter the interpretation of the MGIXD was significantly developed in order to determine *c/a* parameter in hexagonal materials and the probabilities of finding stacking fault ρ between neighboring planes {111}. The method of *c/a* determination was tested on polished Ti (grade 2) sample showing that for the material having low elastic anisotropy the stresses, strain free parameter a_0 as well as *c/a* value can be determined using presented in this work self-consistent iteration method (the experimental values determined in the case of tensile as well compressive stresses were compared with literature). Significantly better fitting of the theoretical values to experimental ones was obtained when *c/a* was adjusted. It should be underlined the *c/a* value can be estimated in good approximation for elastically isotropic material (as Ti) or if the XSF are known (measured or verified). The second case was not considered in the present work but this test is an important issue for further development of MGIXD method (using for example elastically anisotropic Zr alloy sample).

Probability of finding stacking fault ρ was determined for polished austenitic stainless steel (alloy having low stacking fault energy). Reasonable values were of ρ was determined in the case compressive stress in the polished sample. Similar calculation has been done previously for ground sample (the same austenitic steel) by Baczmanski [20] receiving similar value of ρ. This methodology also requires knowledge of XSF for anisotropic material (like austenite stainless steel). This is why it is important to verify different models of XSF calculations what has been done in the second part of this chapter.

The best verification of the XSF can be done measuring lattice relative strains during tensile test (we avoid influence of initial residual stresses, stacking faults, systematic errors due to misalignments, refraction and other effects). From the performed tests it is evident that both the experimental and the calculated $<\varepsilon(\phi,\psi)>^{rel}_{\{hkl\}}$ vs. $sin^2\psi$ functions based on different *hkl* reflections exhibit nonlinerities in the case of sample having elastic anisotropy (austenite stainless steel), in contrary for elastically isotropic sample (like Ti) this dependence is almost linear. Anisotropy of XSF was also observed on the $\{hkl\} < a(\phi,\psi) >$ vs. $sin^2\psi$ plots obtained when the residual stresses were measured in Ni alloy, austenite stainless steel and CrN samples. In view of the nature of presented results obtained using MGIXD and standard method, it can be concluded that Reuss and free surface grain interaction models are in the best agreement with the experimental results. These models reflect in the best way the elastic anisotropy of the studied samples. This conclusion does not agree with the previous studies [1] in which the Kroner type XEC/XSFs were positively verified for quasi-isotropic materials (without texture) or in some cases for textured samples [1]. However, it was also shown that in the case of textured samples the anisotropy of XSF is better predicted by Reuss or free surface models than by the Kroner approach [1,100]. The coupling of the grains in the measured sample depends on the material but also on the depth above the sample surface. Indeed in the case of MGIXD method the penetration depth is usually lower than in the case of standard measurement, thus the conditions of free surface are better fulfilled for the measured volume.

Concluding, reliable diffraction stress analysis is only possible when an appropriate grain interaction model is applied for anisotropic sample. Therefore the free surface model (having physical explanation in contrast to Reuss model) was applied to determine probability of finding stacking fault (ρ) in polished austenite stainless steel. In this chapter the examples of stress analysis for isotropic (W) as well anisotropic samples samples (Ni alloy, austenite stainless steel, CrN) were performed taking into accounts uncertainty due to refraction effect.

7. MGIXD METHOD USING DIFFERENT WAVELENGTHS OF SYNCHROTRON RADIATION

In the previous chapter the role of XSF, refraction and other effect influencing results of MGIXD measurements were considered. In this part the attention will be paid on the possibility of measuring stress evolution vs. depth below the sample surface. Moreover the methodology of data interpretation is developed in order to treat data obtained not only for different incident angles but also using simultaneously different wavelengths. Finally, it will be shown that using our software also the results of energy dispersion diffraction measurements can be successfully treated. Therefore, the new elaborated method is not only 'multi-reflection' but also 'multi-wavelength'. The advantage of the method is that more experimental data are available to calculate the stresses. Moreover, application of different wavelengths enables verification of the MGIXD measurements.

The preliminary experiments were performed for two samples exhibiting low crystal anisotropy: Al – fcc structure and Ti – hcp structure, using X-Pert Philips X-ray diffractometer (Cu K_α radiation) equipped with a Göbel mirror in incidence beam optic (Table 5.4). The results obtained using classical X-ray diffraction were verified by synchrotron radiation in order to test the MGIXD method and to precisely designate the variation of stresses in function of depth. Measurements were performed at G3 beamline at the DORIS III (HASYLAB) storage ring. For selected samples, MGIXD geometry was used to measure stresses at different depths below the surface.

Secondly, selected samples which did not exhibit the stress gradient when measured on the classical diffractometer, were investigated using EDDI method with the synchrotron radiation at BESSY (EDDI beamline). This method was used to perform the measurements in the deeper regions of the sample in order to reveal if the stress gradient occurs.

7.1. X-RAY MEASUREMENTS

At first measurements were performed using MGIXD method on a PANalytical – X'Pert MRD (AGH, Kraków) and PANalytical - X'Pert MRD (ENSAM, Paris) both equipped with a Göbel mirror in incidence beam optic (configuration given in Table 5.4). The Al2107 alloy and Ti samples were ground or polished. In the case of grinding the speed of rotation of the grinding wheel (external diameter equal to 300 mm, internal diameter equal to 127 mm and width equal to 40 mm) was 2000 rpm while the work speed was 9 m/min. Several passes were carried and in each pass the layer of 20 μm was removed. Such treatments were applied for Al2017 alloy and Ti (grade 2) samples (compositions are given in Table 6.1). Two types of mechanical two-directional manual polishing were applied for other samples:

I) with 5 steps using emery papers: 800, 1200, 2000, 2500, 4000 grit and the last treatment was performed with pressing force of 5 N, next polishing paste was used for final treatment (size of the polished surface: 1.5 mm per 1.5 mm);

II) one polishing with emery paper 2000 grit and without any pressing.

Polishing type I was applied for the Al2017 and Ti (grade 2) samples, while polishing II was performed for Al2017 and Ti6Al4V alloys (composition given in Table 5.1). The surface roughness R_a parameter for all mechanically treated samples was gathered in Table 7.1.

Table 7.1. Values of surface roughness parameter (R_a) for investigated sample.

Surface treatment	R_a (μm)
Al2017	
Polishing type I (5 N)	0.13
Polishing type II	0.27
Grinding	1.18
Ti (grade 2)	
Polishing type I (5 N)	0.04
Grinding	1.87
Ti6Al4V	
polishing type II	0.29

The orientation distribution functions were determined using Cu radiation for all mechanically treated samples (Fig. 7.1). It can be seen that grinding process change texture significantly for both Al 2017 and Ti (grade 2) samples. Initial texture (before grinding) for Ti sample is given in Fig. 6.9, while the initial texture of Al2017 was almost random. These texture has not sample symmetry and the ODFs are presented for $0^o \leq \phi_1 \leq 360^o$. Polishing also modifies texture but the changes are smaller, i.e. the texture of Al 2017 remains almost isotropic after both types of polishing, while the preferred texture orientations in Ti (grade2)

are shifted with respect to the initial after polishing type I. Polished Ti and Ti6Al4V samples exhibit orthorhombic sample symmetry, and the range $0^o \leq \phi_1 \leq 90^o$ was shown.

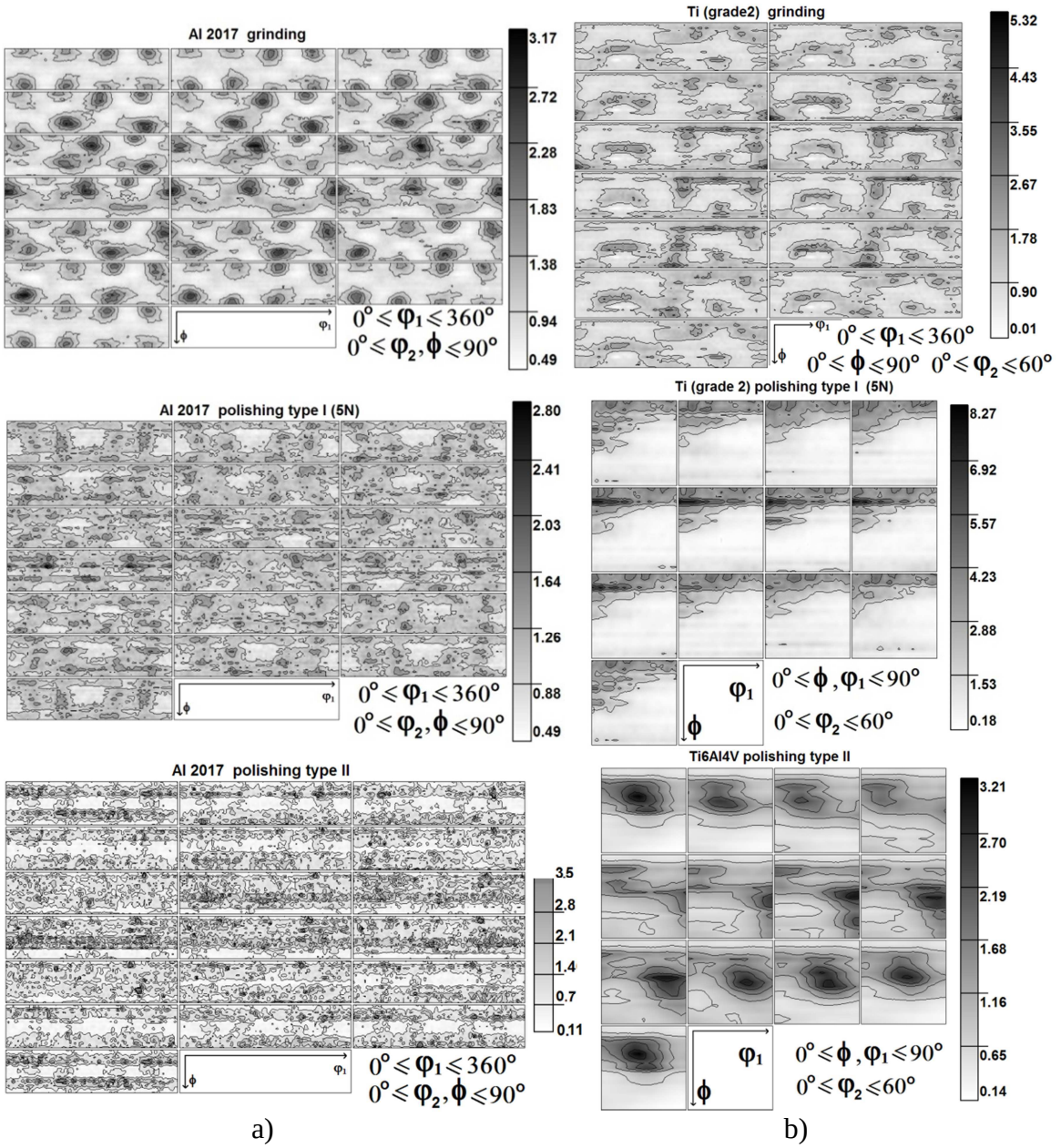

a) b)

Fig. 7.1. Orientation distribution functions (ODF) determined using Cu radiation for ground and polished Ti, Ti6Al4V and Al2017 samples. The ranges of Euler angles depending on sample and crystal symmetry are given.

Al samples

The example peak profiles for powder Al, polished (type II) and ground aluminum alloy obtained using pseudo-Voigt function, are presented in Fig.7.2 while the example $<a(\phi,\psi)>_{\{hkl\}}$ vs. $sin^2\psi$ plots are shown in Figs. 7.3 for polished (type II) and ground Al2017, respectively.

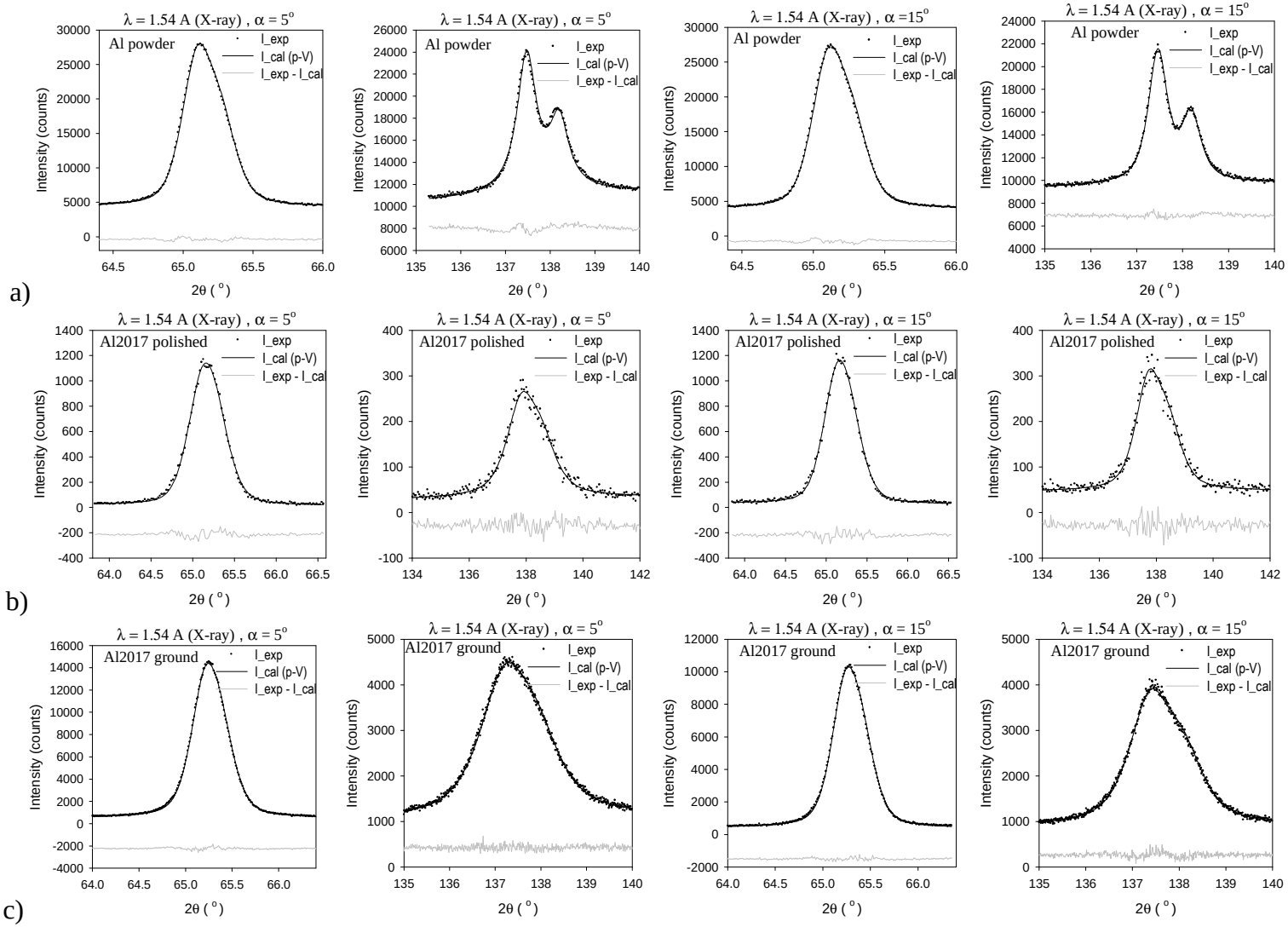

Fig. 7.2 Example of the peak profiles for ground Al powder (a), Al2017 polished type II (b) and ground (c) samples, fitted by pseudo-Voigt function.

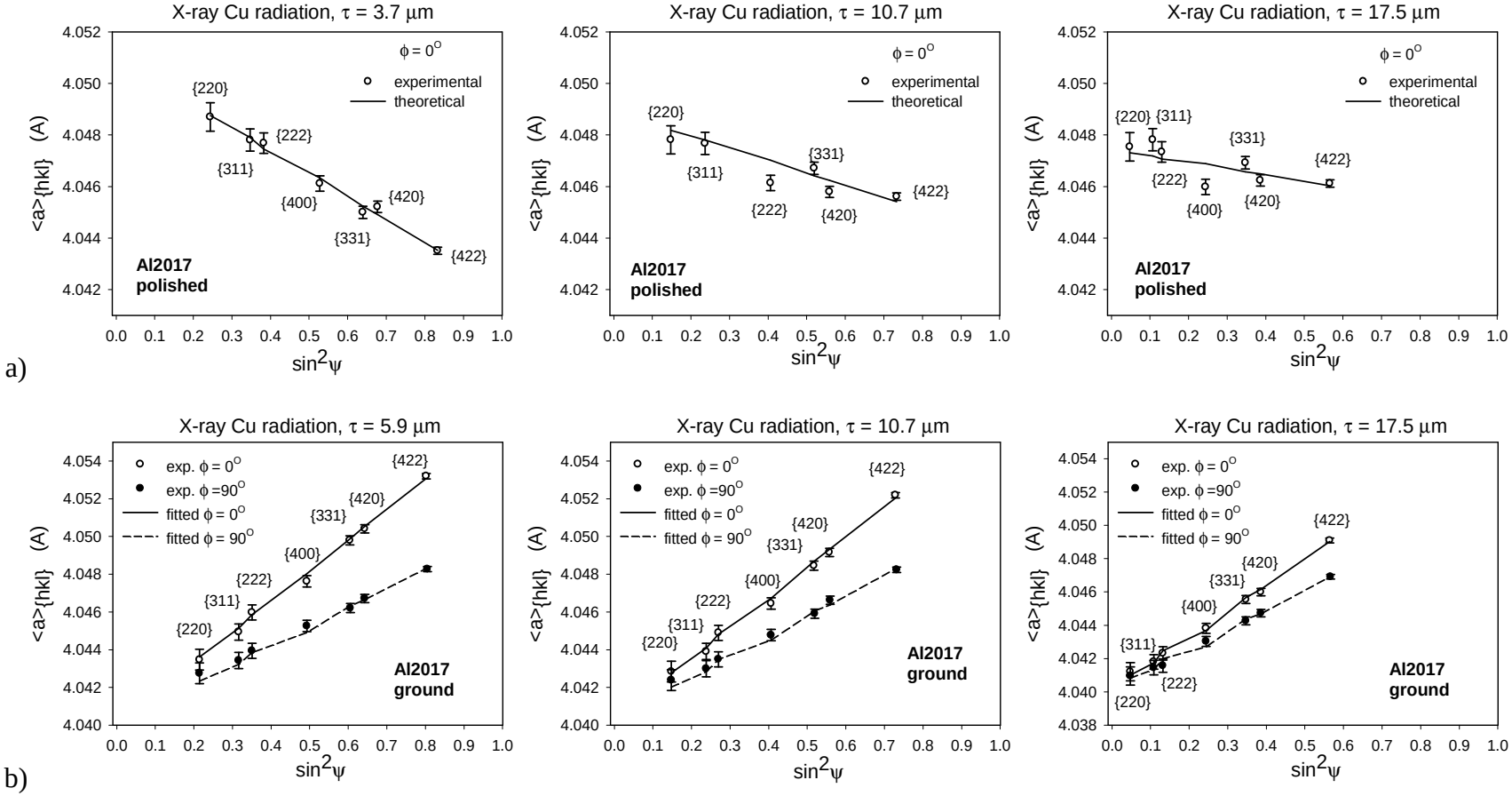

Fig. 7.3. Example of the $<a(\phi,\psi)>_{\{hkl\}}$ vs. $sin^2\psi$ plots for polishing type II (a) and grinding (b) Al2017 samples, for different penetration depths. Significant difference between plots for $\phi = 0^0$ and $\phi = 90^0$ is shown in the case of ground sample.

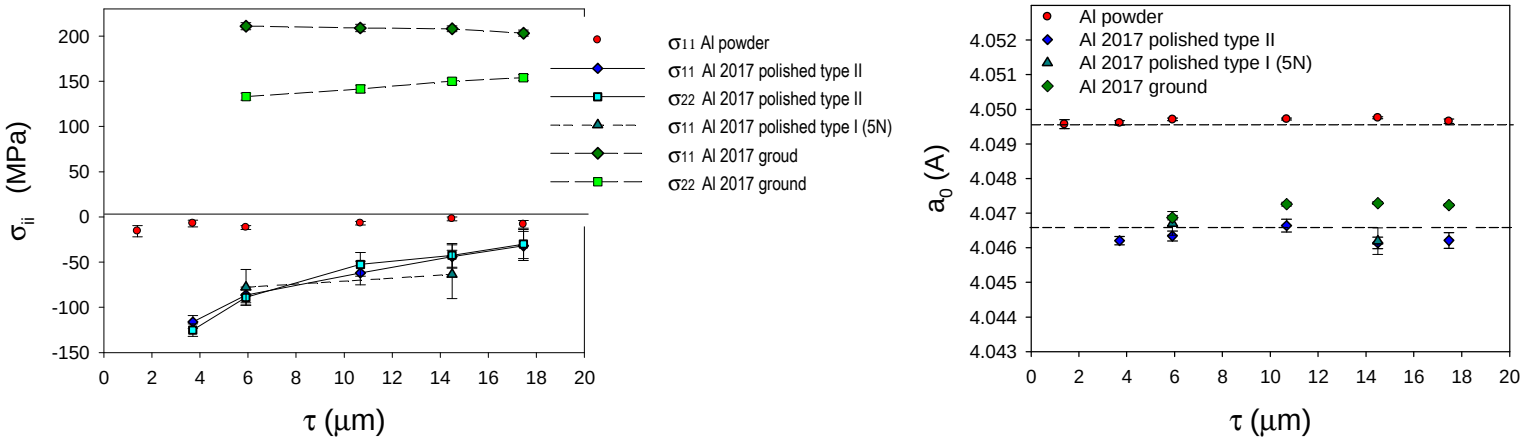

Fig. 7.4. The in-depth profile of stress and a_0 parameter for mechanically polished (type I and II) and ground Al2017 samples, as well as the reference powder sample, obtained by MGIXD method (Cu K_α radiation).

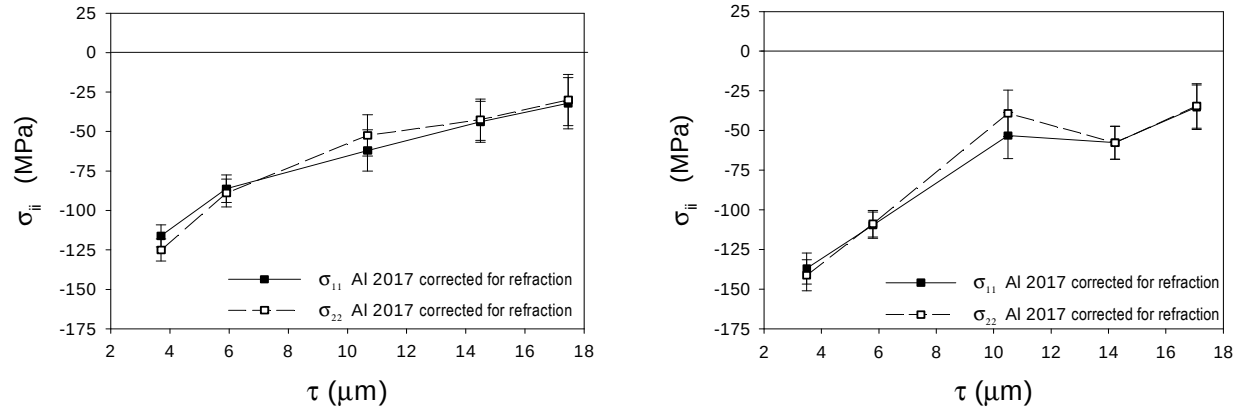

a) b)

Fig. 7.5. The stress in-depth profile for mechanically polished Al2017 sample (type II) measured by MGIXD method. The peak position determined a) by fitting of pseudo-Voigt function and b) using center of gravity method.

Analyzing peak profile it can be concluded that the polished as well as ground samples exhibit significant broadening of diffraction peaks in comparison with those obtained for recrystallized Al powder. The peak profiles can be successfully fitted by two pseudo-Voigt functions corresponding to $K_{\alpha 1}$ and $K_{\alpha 2}$ lines. The $<a(\phi,\psi)>_{\{hkl\}}$ vs. $sin^2\psi$ plots were fitted using procedure based on Eq. 3.23, in which the XSF calculated by Kröner method from single crystal elastic constants given in Table 3.3. Because of low crystal anisotropy for Al samples all methods of XSF calculation give almost the same results, moreover effect of texture is also not significant. As shown in Fig. 7.3 significant difference between $\phi = 0^0$ and $\phi = 90^0$ was found, while no such difference was observed in the case of polished samples.

The in-depth stress and a_0 lattice parameter profiles as a function of penetration depth (τ) determined for different incident angles (α) for all studied Al2017 samples are compared with measurements performed for Al powder sample (Fig. 7.4). Refraction correction was taken into account; however it is not significant for the studied range of incident angles as shown in Fig 5.10. Moreover, the stresses obtained using two methods for determination of peak positions were compared in the case of sample for which stress gradient occurs (polishing type II), i.e., fitting by pseudo-Voigt function (Fig. 7.5a) and center of gravity method (Fig.7.5b). Analyzing Figs. 7.4 and 7.5, it can be concluded that:

- Stresses close to zero were measured in Al powder.
- Tensile stresses were generated after grinding. This is caused due to temperature gradient effect because of interaction between sample body and the heated surface layer (this layer contracts during cooling). The stress along direction of grinding σ_{11} is higher than in the transverse direction (σ_{22}). No significant evolution of stresses occurs in the depth penetrated by X-rays.
- Compressive stresses $\sigma_{11} \approx \sigma_{22}$ were found in the polished samples. No significant in-depth evolution was found for polishing type I (5N pressing force), while stress gradient occurs after type II of polishing.
- No significant in-depth evolution was found for a_0 lattice parameter. Large difference was found between a_0 determined for Al powder and Al2017 alloy.
- Approximately the same stresses were obtained using both method for determining of peak position (fitting with pseudo-Voigt and center of gravity - CG).

Finally, the Williamson-Hall method was used for investigation of the in- depth evolution of root mean square of the third order strain and crystallite size (coherent domain). The fitted linear functions to the experimental points in Williamson-Hall method for both polished and ground Al2017 are presented on Figs. 7.6. The calculated results are summarized in Table 7.2. As the reference the LaB_6 powder was used.

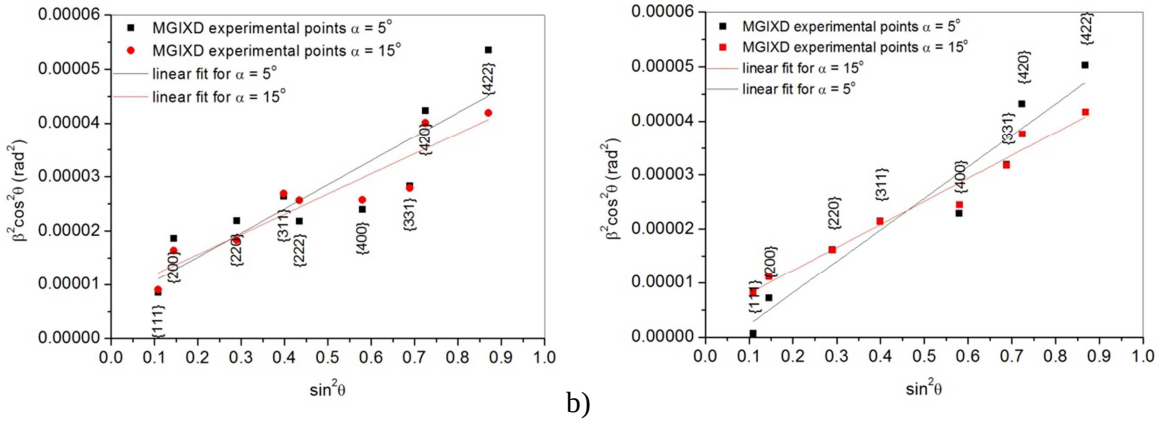

a) b)

Fig. 7.6. The linear function fitted to the experimental data in Williamson-Hall method for polished – type II (a) and ground (b) Al2017 samples (analysis with Gaussian approximation, see chapter 2.3.1).

Table 7.2. The root mean square of the third order strain ($\sqrt{\langle \varepsilon^2 \rangle}$) and crystallite size ($D$) calculated with Williamson-Hall method for Al 2017 ground and polished (type II) samples.

α (°)	τ (μm)	$\sqrt{<\varepsilon^2>}$		D (Å)	
Al2017 polished (type II)					
5	5.8	0.0017	±0.0002	619	±231
15	14	0.0015	±0.0001	540	± 94
Al2017 ground					
5	5.8	0.0019	±0.0001	---	----
15	14	0.0016	±0.0001	791	±168

It can be concluded that similar values of the third order strains ($\sqrt{\langle \varepsilon^2 \rangle}$) were found for polished (type II) and ground samples. The strain $\sqrt{\langle \varepsilon^2 \rangle}$ decreases with depth. Large uncertainties of the determined crystallite size (D) unable study of D evolution with depth.

Measurement of *D* is close to the limit of method sensibility, i.e. only *D* smaller than about 500 Å can be measured using applied configuration of the diffractometer (instrumental broadening is about $FWHM_{2\theta=90^\circ} \approx 0.3^\circ$ verified using LaB_6 powder).

Ti samples

As it was mentioned the second series of samples was prepared from Ti and Ti alloy. The example of peak profiles for all investigated samples and Ti powder, obtained with pseudo-Voigt fitting function are presented in Figs. 7.7 and 7.8. The example $\langle a(\phi,\psi)\rangle_{\{hkl\}}$ vs. $sin^2\psi$ plots for polished (type I) Ti6Al4V alloy are shown in Figs. 7.9, while similar plots for Ti (grade 2) sample were already presented in Figs. 6.1 and 6.2 (chapter 6).

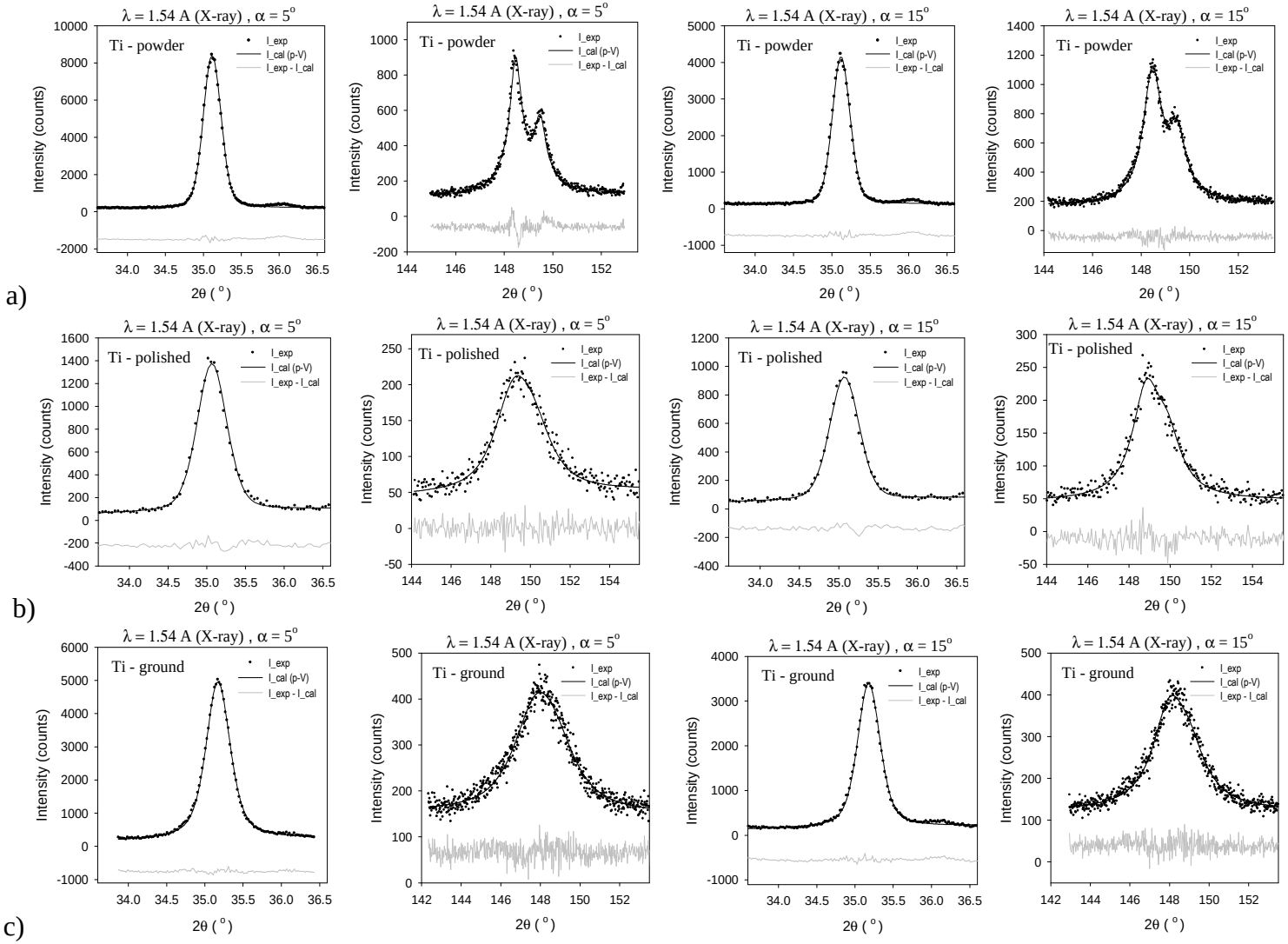

Fig. 7.7. Example of the peak profiles for ground Ti powder (a); and Ti (grade2) polished type I (b) and ground (c), fitted by pseudo-Voigt function.

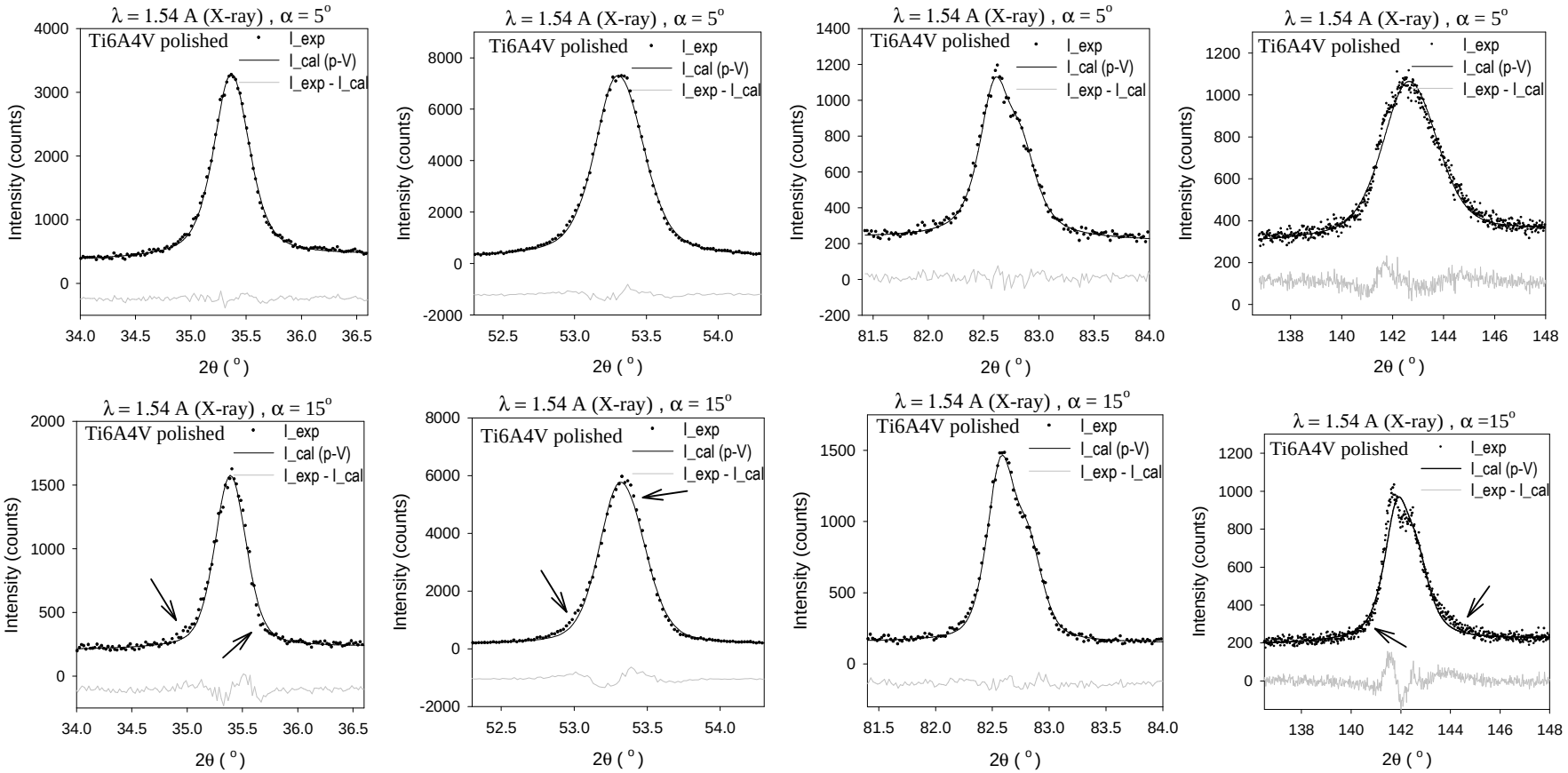

Fig. 7.8. Example of the peak profiles for polished (type 2) titanium alloy (Ti6Al4V), fitted by pseudo-Voigt function.

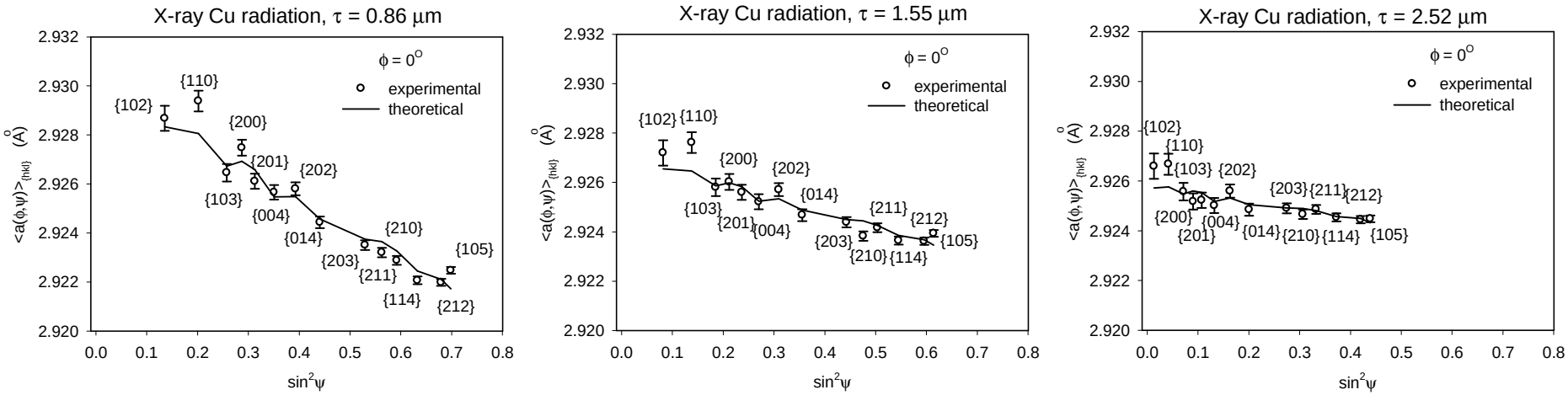

Fig. 7.9. Example of the $<a(\phi,\psi)>_{\{hkl\}}$ vs. $sin^2\psi$ plots for polished (type II) titanium alloy (Ti6Al4V), for different penetration depths.

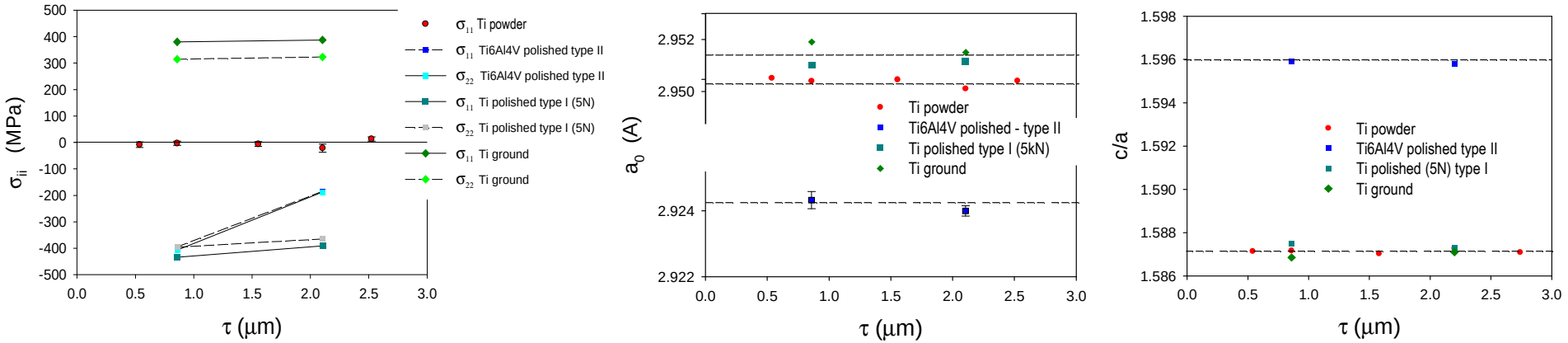

Fig. 7.10. The in-depth profiles of stress, a_0 and c/a parameters for mechanically polished (type I) and ground Ti- grade 2 samples and polished (type II) Ti6Al4V alloy, as well as the reference powder sample, obtained by MGIXD method (Cu K_α radiation and pseudo-Voigt profile used for fitting).

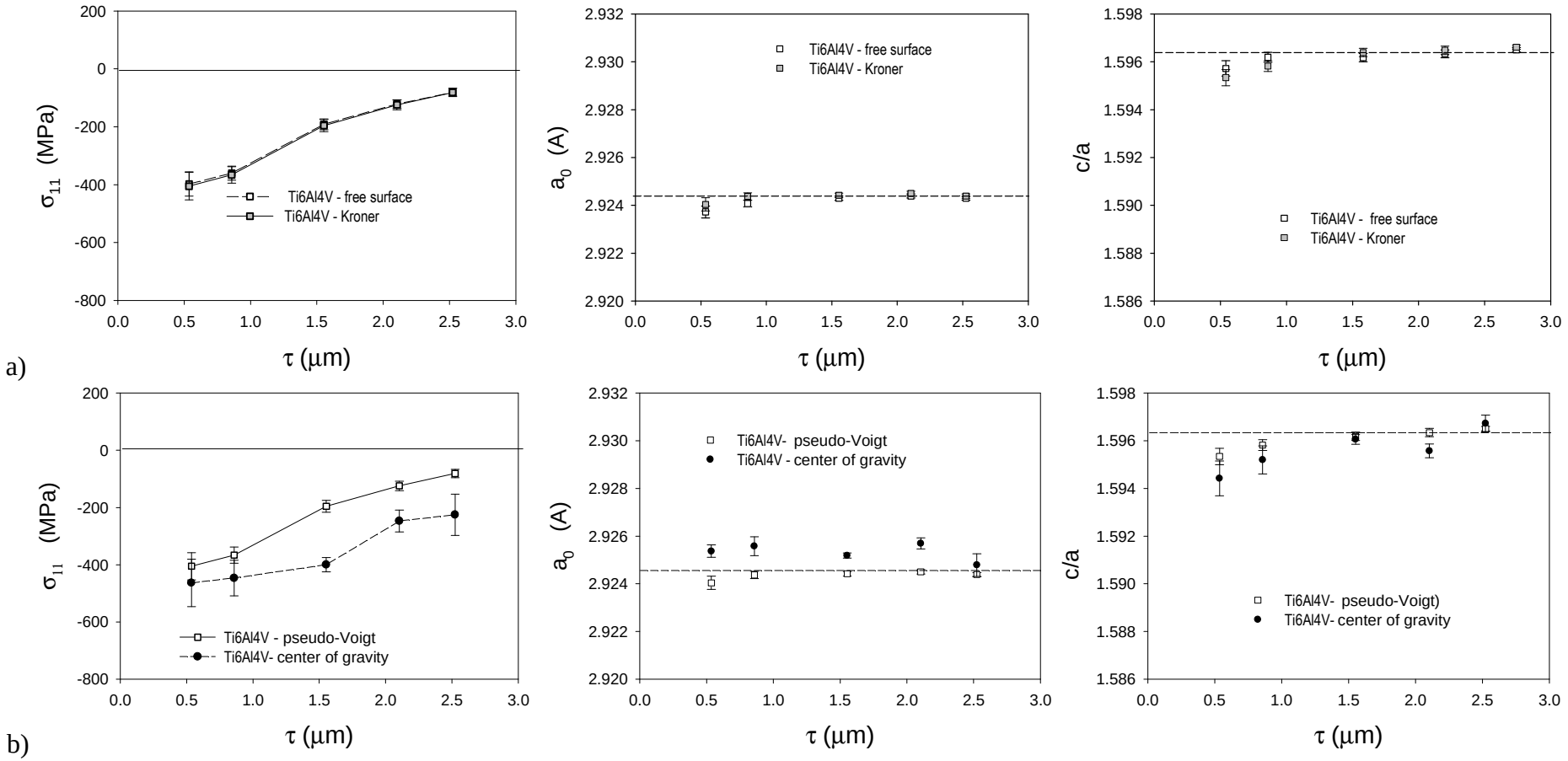

Fig. 7.11. The stress in-depth profiles (stress, a_0 and c/a parameters) for mechanically polished Ti6Al4V alloy (type II) measured by MGIXD method. Comparison of the results obtained: a) using Kröner and stress free XSF (peaks are fitted by) pseudo-Voigt function and b) the peak position determined by fitting of pseudo-Voigt function and using center of gravity method (are compared for XSF calculated with Kröner method).

Similarly like for Al2017 samples, the polished and ground Ti samples exhibit significant broadening of diffraction peaks in comparison with recrystallized powder. The pseudo-Voigt functions fit correctly the experimental peaks measured for ground or polished (with pressing force equal 5 N - type I) Ti (grade 2) sample while disagreement between theoretical and experimental profiles was found in the case of polished Ti6Al4V alloy (type II); see asymmetries indicated by arrows in Fig. 7.8. The disagreement is particularly evident for high 2θ angles. The $<a(\phi,\psi)>_{\{hkl\}}$ vs. $sin^2\psi$ plots were fitted using procedure based on Eqs. 6.1 and 3.23, in which the XSF are calculated by Kröner method from single crystal elastic constants given in Table 3.3 and c/a parameter was adjusted. Similarly, as in the case of Al sample low crystal anisotropy causes that the choice of XSF model and crystallographic texture is not significant. It should be stated that the $a(\phi,\psi)>_{\{hkl\}}$ vs. $sin^2\psi$ plots were limited to the range of $sin^2\psi$ for which acceptable fitting of pseudo-Voigt function was obtained (Fig. 7.9).

The in-depth stress and lattice parameters (a_0 and c/a) profiles as a function of penetration depth (τ) were determined from measurements performed for different incident angles (α), and compared with analogical measurements performed for the Ti powder sample (Fig. 7.10). Refraction correction (taken into account) is not significant for the studied range of incident as shown in Fig. 5.11. The stresses obtained using two methods (fitting by pseudo-Voigt function and center of gravity) for determination of peak positions were compared in the case of polished Ti6Al4V alloy (type II) exhibiting significant stress gradient (Fig. 7.11). Analyzing the presented above results concerning residual stresses for Ti and Ti alloy samples, it can be concluded that (see Figs. 7.10 and 7.11):

- Stresses close to zero were measured in Ti powder.
- Different types of stresses were generated after application both surface treatments, i.e. tensile stresses after grinding (higher stress along direction of grinding) and compressive stress after polishing. No significant evolution of stresses occurs in the depth penetrated by X-rays for ground and polished (with pressing force) samples, while the significant gradient of stresses occurs for polished Ti alloy in accessible on the classical diffractometer range of penetration depth.
- No significant in-depth evolution was found for a_0 and c/a parameters for all measured samples. The values of a_0 lattice parameters for Ti (grade 2) polished and ground samples are comparable with each other and are close to the lattice parameters of powder sample (similar to the values characterizing pure material:

a_0 = 2.95111 ± 0.00006Å, and c/a = 1.5873 [93]). On the other hand the value of the lattice parameters of Ti6Al4V alloy, as it was expected, is significantly different from those obtained for Ti (grade 2) sample (Ti6Al4V parameters are close to a_0 = 2.9323 Å and *c/a* = 1.5957, obtained by Bernier et al. [107] for similar alloy, using synchrotron radiation).

- The determined *c/a* parameter does not depend on depth if stress gradient does not occur, thus for Ti powder and polished or ground Ti (grade 2). However, in the case of stress gradient in polished Ti6Al4V alloy, *c/a* exhibits small monotonic in depth dependence which is slightly more significant in the case of XSF given by Kröner than in the case of free surface model (Fig. 7.11a). On the other hand, also a_0 shows small deviation close to the surface, which in turn, is smaller for Kröner model (Fig. 7.11a). Because the deviations of a_0 are *c/a* are small and could be caused by another reasons, it is not possible to decide which model better describes grain interactions in the studied sample. However, the hypothesis that stress relaxation close to the surface causes different grains interaction at different depths should be in future verified.
- Different values of stresses and a_0 and *c/a* parameters were obtained depending if the peak positions were determined by fitting pseudo-Voigt function or calculating the center of gravity (Fig. 7.11b). This important problem will be considered in this work and it is expected that such difference is due to asymmetry of peak caused by stress gradient (the measured peak is integrated from different depths exhibiting different lattice strains).

Williamson-Hall analysis was used for investigation of the in- depth evolution of root mean square of the third order strain and crystallite size (coherent domain). The fitted linear functions to the experimental points in Williamson-Hall method for investigated Ti samples are presented in Fig. 7.12 (as the reference the LaB_6 powder was used). The calculated results are summarized in Table 7.3.

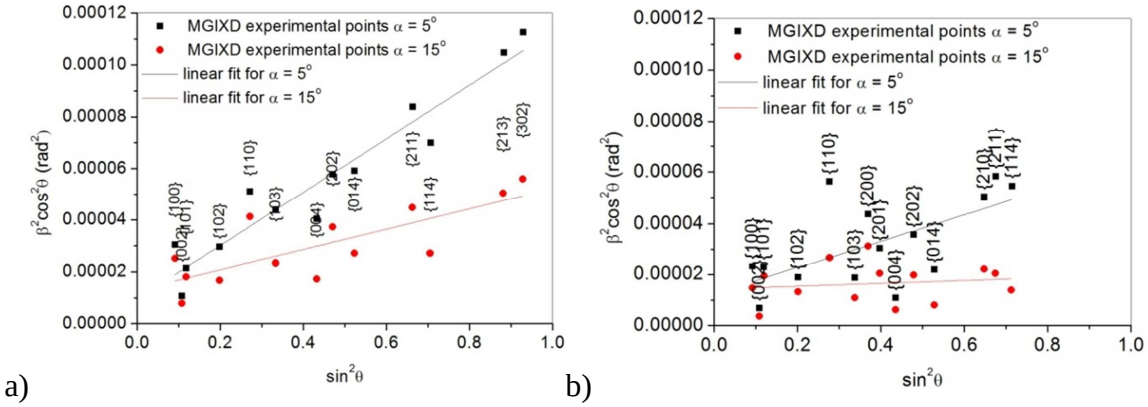

a) b)

Fig. 7.12. The linear function fitted to the experimental data in Williamson-Hall method for Ti (grade 2) polished – type I (a) and for polished (type II) Ti6Al4V alloy (b) - Gaussian approximation.

Table 7.3. The root mean square of the third order strain ($\sqrt{\langle \varepsilon^2 \rangle}$) and crystallite size ($D$) calculated with Williamson-Hall method for Ti and Ti6Al4 samples.

α (°)	τ (μm)	$\sqrt{<\varepsilon^2>}$		D (Å)	
Ti6Al4V polished – Type II					
5	0.9	0.0018	± 0.0003	438	± 143
15	2.1	0.0006	± 0.0006	408	± 66
Ti (grade 2) polished – type I					
5	0.9	0.0025	± 0.0001	501	± 123
15	2.1	0.0016	± 0.0002	430	± 83
Ti (grade 2) ground					
5	0.9	0.0039	± 0.0008	238	± 152
15	2.1	0.0020	± 0.0002	474	± 163

The values of the third order strains ($\sqrt{\langle \varepsilon^2 \rangle}$) in polished (type I) and ground Ti (grade 2) samples are higher than in Ti6Al4 alloy, for which polishing type II was applied. In all samples the strain $\sqrt{\langle \varepsilon^2 \rangle}$ decreases with depth. In the case of slightly polished Ti6Al4 alloy very small value of strain $\sqrt{\langle \varepsilon^2 \rangle}$ was measured in the depth τ = 2.1 μm where material is not deformed plastically. Similarly as for Al sample due to large uncertainty of the determined crystallite size the study of D evolution is not possible.

As mentioned before, the clasicall X-ray measurements were an introduction to the study performed with synchrotron diffraction. X-ray measurements enabled to choose appropriate samples, i.e. the samples having important in-depth gradients (Al2017 and Ti6Al4 - type II of polishing). Next these samples were studied using similar wavelengths (energies), as used on the laboratory diffractometers, with synchrotron radiation. Additionally for the ground and polished (with pressing force) Ti (grade 2) samples much higher energies was used (EDDI – energy dispersion diffraction) to study stress behavior in deeper layers.

7.2. SYNCHROTRON MEASUREMENTS USING MGIXD WITH DIFFERENT WAVELENGTHS AND INCIDENT ANGLES.

The results for samples exhibiting a high in-depth stress gradient (the results obtained using classical X-ray diffraction) were verified using synchrotron radiation. The experiment was performed at HASYLAB, DORIS III storage ring, on beamline G3 spectrometer, using soller collimator (with divergence 0.15°) and scintillation detector. The double-crystal germanium monochromator was used. The beam dimension at monochromator was about 5 mm per 10 mm. All monochromator movements were driven by stepper motors. The tilted gold mirror was used for suppression of the higher harmonics. The advantages of synchrotron radiation are its perfect collimation, monochromatization, high intensity and possibility of wavelength variation. Moreover, very valuable advantage is that penetration depth can be change for the same incident angle by changing wavelength. In Fig. 7.13 the penetration depths for different wavelengths are shown. Three different wavelengths (λ=1.2527 Å, λ =1.5419 Å and λ =1.7512 Å) were chosen and the incidence angles (α), for which the penetration depth is the same, were calculated. The important question verifying the methodology was if the same stresses will be determined for such combination of wavelengths and incident angles. The sets of incident angles and wavelengths corresponding to the same penetration depths were determined drawing horizontal lines in Fig. 7.13.

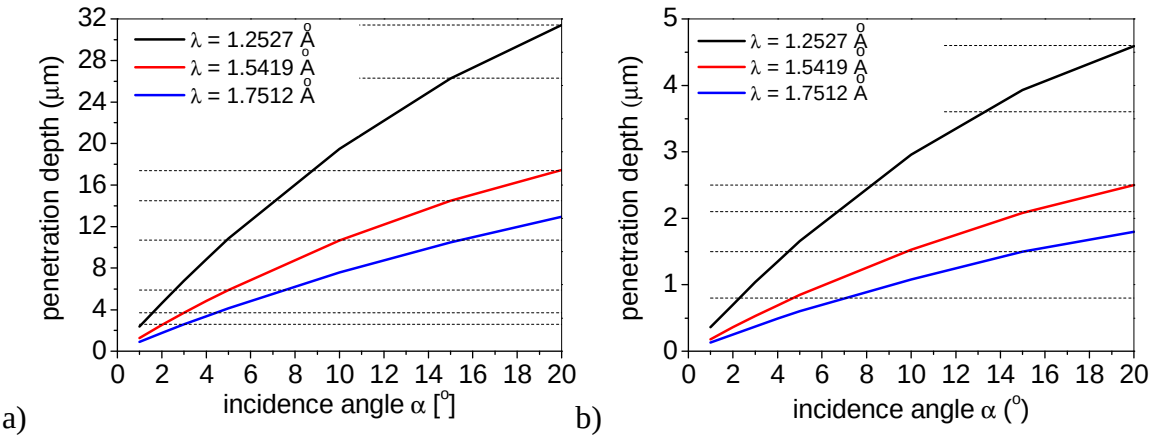

Fig. 7.13. The penetration depth vs. incidence angle α for Al (a) and Ti (b) samples. Curves for three, different, selected wavelengths are shown. Horizontal lines are drawn for constant penetration depths.

Al2017 sample

Fist studied sample was mechanically polished (type II) Al 2017 alloy for which the significant gradient of stresses was determined using classical X-ray diffractometer. The MGIXD method with radiations having three different wavelengths: λ=1.2527 Å, λ =1.5419 Å and λ =1.7512 Å were applied. Synchrotron radiation enabled to extend the penetration depth (τ) for which the stresses are determined. The measured peaks were fitted by the pseudo-Voigt function. The example of peak profiles are presented in a Fig. 7.14.

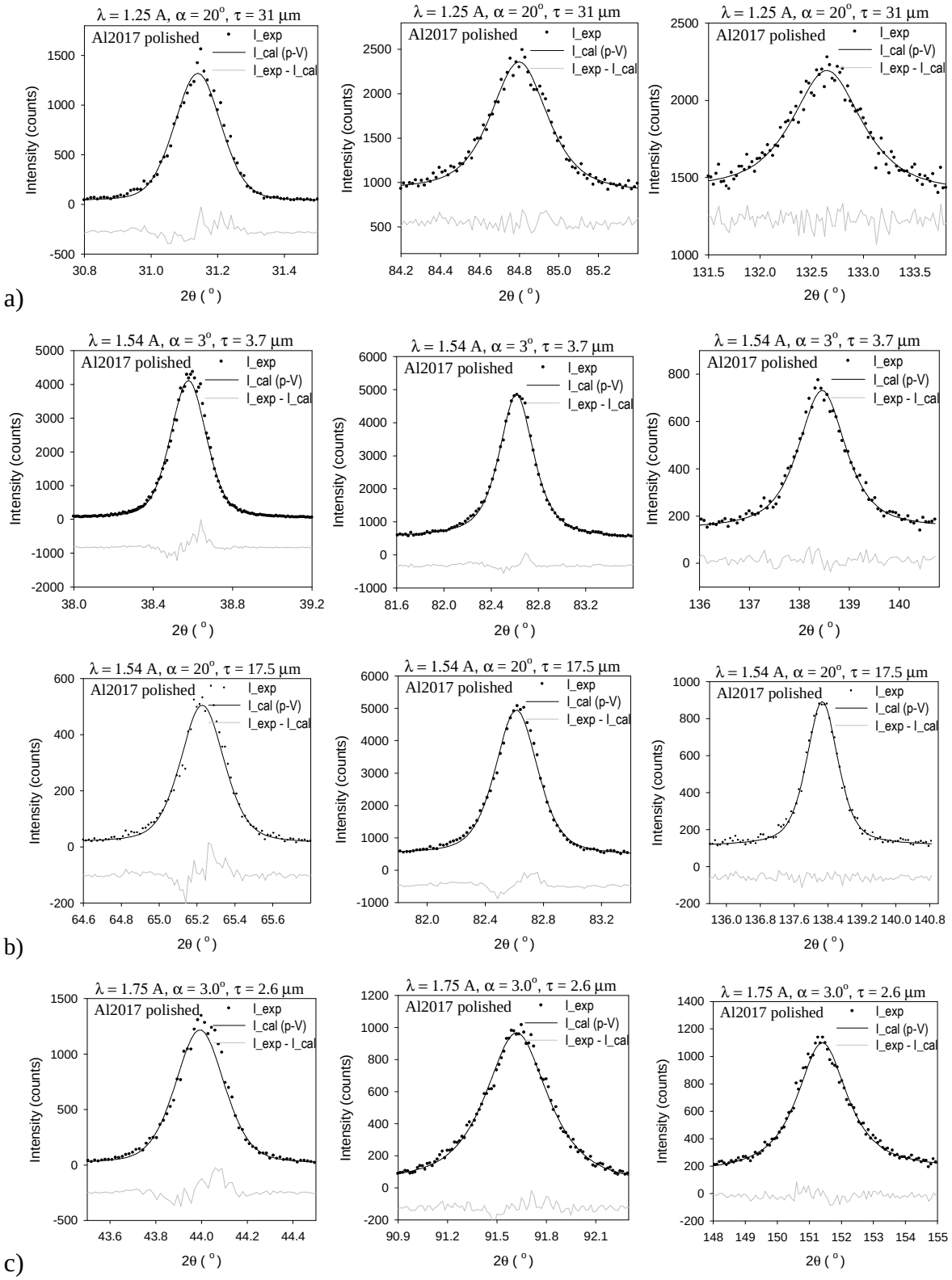

Fig. 7.14. Example peak profiles fitted with the pseudo-Voigt function presented for different incident angle and different wavelengths: a) λ=1.2527 Å, b) λ =1.5419 Å and c) λ =1.7512 Å.

In the case of synchrotron radiation having better resolution ($FWHM_{2\theta=90^\circ} \approx 0.1°$) in comparison with X'Pert PANalitical diffractometer ($FWHM_{2\theta=90^\circ} \approx 0.3°$) the diffraction data measured at G3 spectrometer shows more accurate peak profiles. Consequently peak asymmetry occurs when peaks are fitted by pseudo-Voigt function and the physical reason of this asymmetry will be discussed later (Fig. 7.14).

In order to check agreement of the in-depth profiles obtained for different absorption of synchrotron radiation (depending on energy), the stresses and a_0 parameter as the functions of penetration depth (τ), were determined for each wavelength independently. The positions of peaks were found by fitting of pseudo-Voigt function (Fig. 7.15a) or calculating the center of gravity (Fig. 7.15b), and next the fitting procedure based on Eq. 3.23, with Kröner, XSF was applied to calculate the values of stresses $\sigma_{11}^{\ I} = \sigma_{22}^{\ I}$ (this assumption was previously confirmed by X-ray measurements) and a_0 parameter. When peaks were fitted by pseudo-Voigt function, a very good agreement was achieved between data obtained using synchrotron radiation (for three different wavelengths) as well as classical diffractometer (preliminary measurements on PANalytical – X'Pert MRD (ENSAM, Paris)). If the peak positions are calculated as center of gravity (Fig. 7.15b) the agreement is worse but the stresses are still equal, in the margin of uncertainty, for different wavelengths and classical diffractometer. Both methods (pseudo-Voigt and center of gravity) give very similar results. To confirm that the determined stresses really depend on the penetration depth and not on the geometrical conditions also the stresses as the function of incident angle α were drawn in Fig. 7.16. As expected, due to different absorption significant difference of stresses measured with different wavelengths are seen for the same value of α angle.

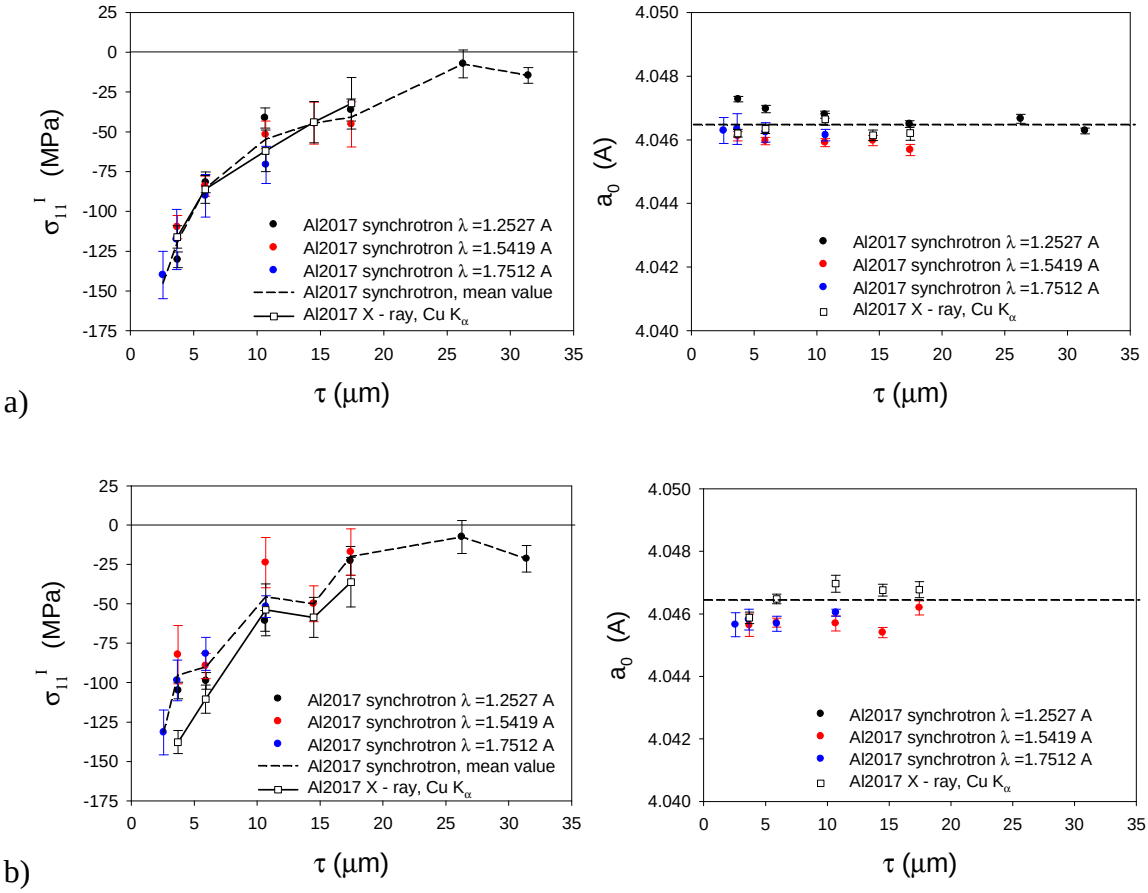

Fig. 7.15. The in-depth profiles of stresses and a_0 lattice parameter for polished Al2017 sample. Comparison for different peak position determination between pseudo-Voigt function (a) and center of gravity (b). The results for different wavelengths of synchrotron radiation and for laboratory diffractometer are shown.

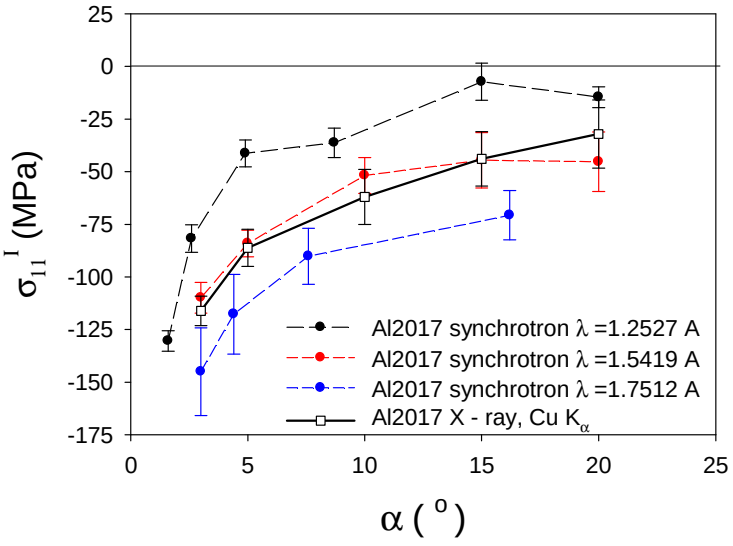

Fig. 7.16. Stress values for polished Al2017 sample as a function of incident angle (α) for different wavelengths using synchrotron radiation and for laboratory X-rays.

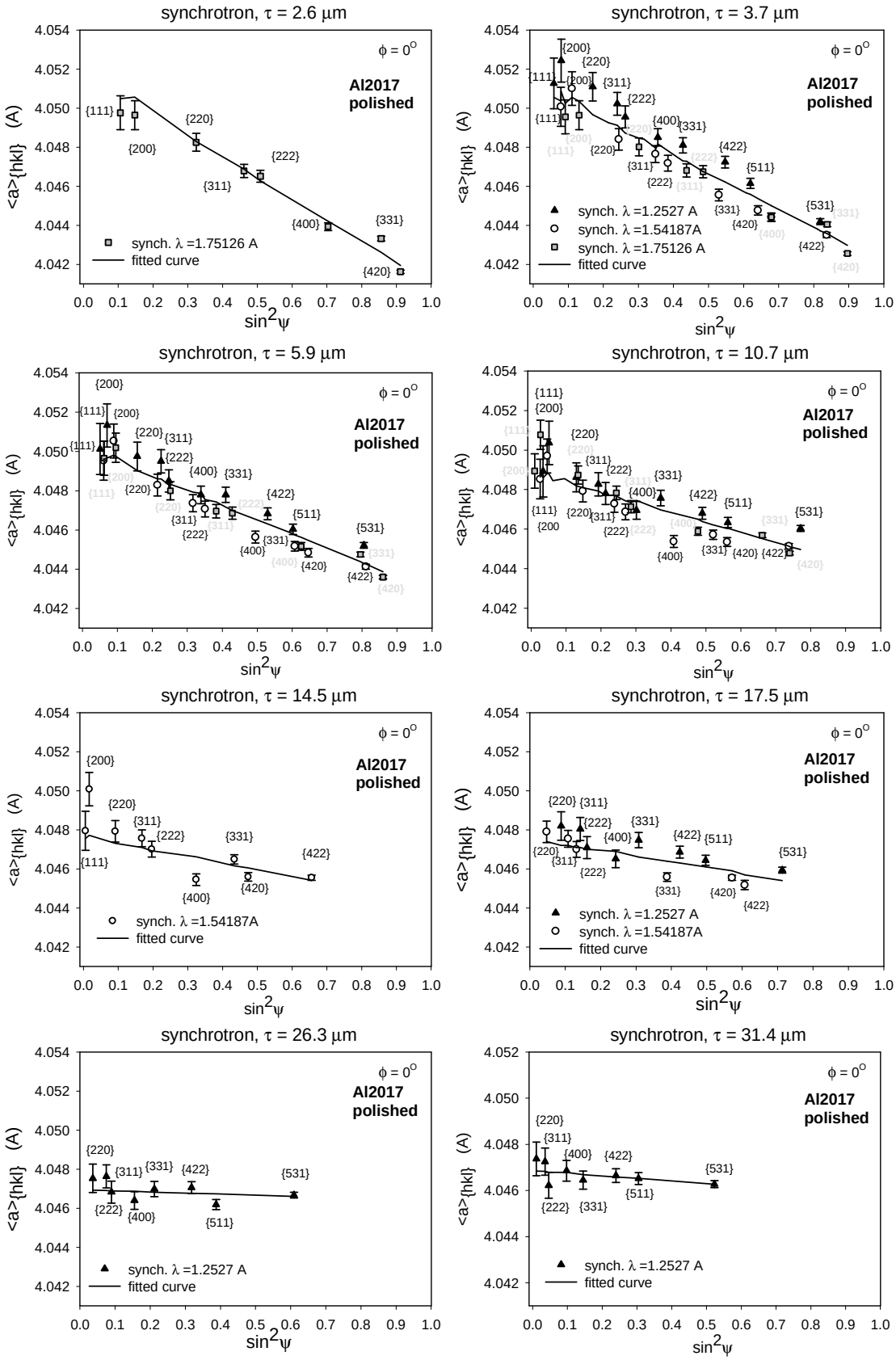

Fig. 7.17. The $<a(\phi,\psi)>_{\{hkl\}}$ vs. $sin^2\psi$ plots for polished Al2017 sample obtained with three wavelengths and different incident angle (α). In each figure experimental data corresponding to the same penetration depth are shown together with fitted theoretical line.

The agreement between results obtained with different wavelengths allows developing the MGIXD. The idea is to collect $<a(\phi,\psi)>_{\{hkl\}}$ values corresponding to the same penetration depth τ on the same $sin^2\psi$ plot. Therefore $<a(\phi,\psi)>_{\{hkl\}}$ vs. $sin^2\psi$ curves (containing information obtained using different wavelengths) are presented on separate plots corresponding to chosen penetration depths (Fig. 7.17). Subsequently, for the first time the MGIXD method based on Eq. 3.23 was simultaneously applied for all $<a(\phi,\psi)>_{\{hkl\}}$ values measured at the same penetration depth and being combination of chosen wavelength and incident angle (XSF calculated by Kröner method). As seen in Fig. 7.17 the experimental points are close to the fitted lines and systematic decrease of the negative slope of the $<a(\phi,\psi)>_{\{hkl\}}$ vs. $sin^2\psi$ plot (representing compressive stress) with penetration depth is seen for both experimental and fitted results. The stress in-depth profile obtained with the developed method is presented in Fig. 7.18a. The advantage of this approach is that each point on the in depth dependence was obtained not only with different reflections *hkl* corresponding to different incident angles (multi-reflection) but also with different wavelengths (multi-wavelengths).

Having values of mean stress vs. penetration depth τ the variation of stress vs. z – 'real depth' can be calculated using the inverse Laplace transform applied to polynomial function (see chapter 3). It was found that the solutions ($\sigma_{11}^{I}(z)$) are similar for polynomial of 2nd and 3rd degree as presented in Fig. 7.18b.

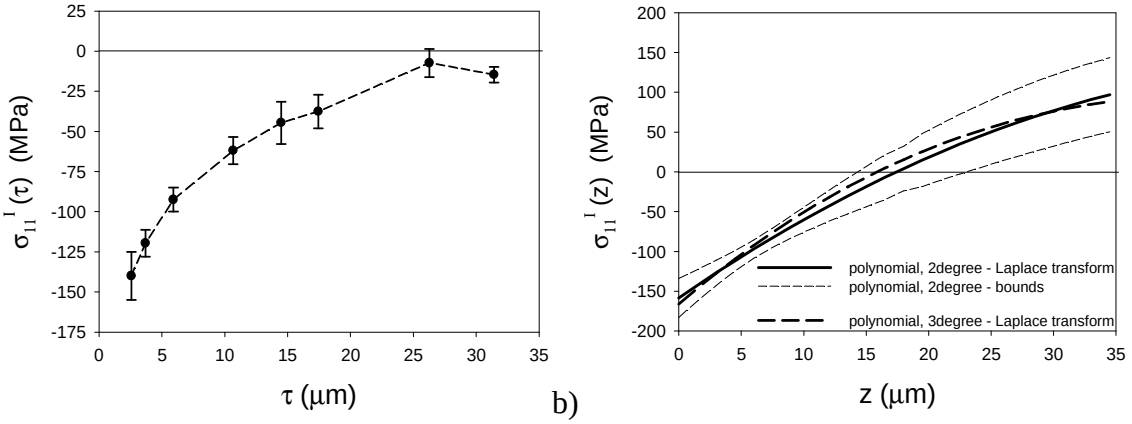

Fig. 7.18. The stress profile for polished Al2017 sample for all experimental points obtained for three different wavelengths as a function of τ - penetration depth (a) and z - real depth in sample (b). The uncertainty bounds are given for polynomial of 2nd degree.

Although the stress profile was found and presented in Fig. 7.18b two important questions must be answered, i.e.:

a) for which maximum *z*- depth the presented approximation can be applied, and
b) does the determined stress gradient explains asymmetry of diffraction peak measured using synchrotron radiation?

To answer the above question the inverse analysis was performed, i.e., assuming the determined stress distribution $\sigma_{11}^{I}(z)$ the experimental results were simulated.

a) The mean stress denoted by $\sigma_{11}^{I}(\tau)$ and calculated using equation:

$$\sigma_{ij}^{I}(\tau) = \int_0^x \sigma_{ij}^{I}(z) e^{-z/\tau} dz \Big/ \int_0^x e^{-z/\tau} dz \tag{7.1}$$

up to different limits x, instead of $x \to \infty$ as in the real thick sample (where $\sigma_{11}^{I}(z)$ is the dependence of stress vs. real depth *z*). The results were compared with the measured mean stresses which should correspond to the recalculated $\sigma_{11}^{I}(\tau)$ values. It was found that the recalculated profiles does not change significantly and agree with experiment if the integration is performed at least up to x = 40 μm, i.e. the stresses over 40 μm does not influence significantly measured values. Therefore, the distribution of stresses $\sigma_{11}^{I}(z)$ up to the depth of 40 μm was correctly determined, however it was not proved that the solution is unique.

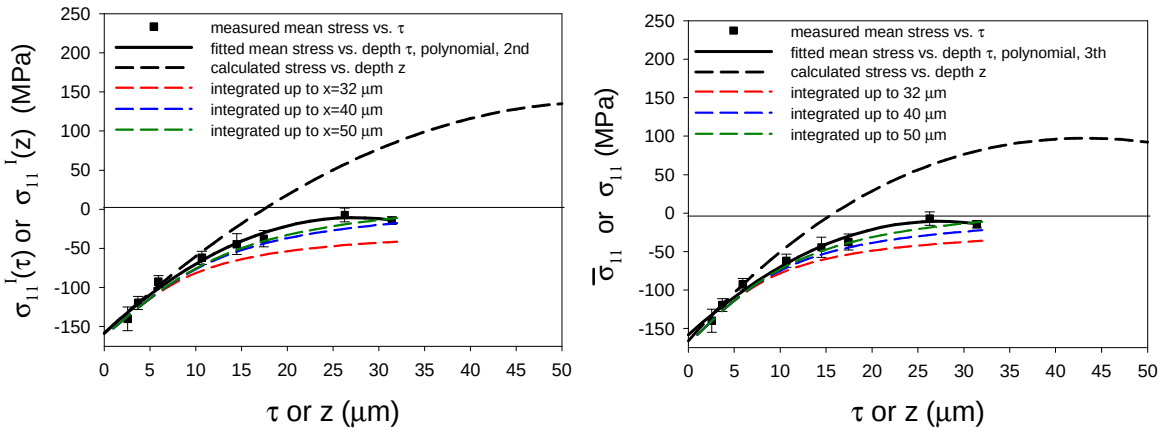

Fig. 7.19. The stress profiles for polished Al2017 sample: $\sigma_{11}^{I}(z)$ calculated from inverse Laplace transform, $\sigma_{11}^{I}(\tau)$ measured or recalculated from $\sigma_{11}^{I}(z)$ using Eq. 7.1. Polynomial of 2nd (a) and 3rd (b) degree were applied to fit the $\sigma_{11}^{I}(\tau)$ experimental values.

b) The experimental diffraction peak profiles were simulated. Each peak was modeled as superposition of pseudo-Voigt functions having positions corresponding to the interplanar spacing modified by different stresses $\sigma_{11}^{I}(z)$ at different depths *z*. In calculation of lattice strains the XSF (Kröner method) were used. The main problem of such modeling is that both FWHM and η (contribution of Lorentz component) are unknown and they can depend on the depth *z*. Only the dependence of peak intensity is known and described by absorption law. In this work the η parameter was assumed constant for different depths and it was determined by fitting pseudo-Voigt function to experimental peak for given *hkl* reflection (and corresponding 2θ). In the simulation, the superposed pseudo-Voigt profiles were weighted by intensity depending on absorption (corresponding to the depth *z*) and different dependences of FWHM on the depth were assumed in order to reproduce one of the most asymmetric peaks (λ =1.5419 Å, $2\theta \approx 38.6^{o}$ and $\alpha = 15^{o}$). The following in-depth profile of FWHM = *b* was assumed:

$$b = b_0 + b_1 \exp(-z/\xi) \tag{7.2}$$

where b_0 is the FWHM for $z \to \infty$ and ξ, b_1 describes the evolution of FWHM for decreasing depth *z*, caused by microstructure variation due to polishing.

The evolution of FWHM described by Eq. 7.2 and arbitrarily assuming $b_0 = b_1$ with different ξ parameters is shown in Fig. 7.20. It was found that the experimental asymmetrical peak (λ =1.5419 Å, $2\theta \approx 38.6^{o}$ and $\alpha = 15^{o}$) is correctly modeled for ξ=10 μm and $b_0 = b_1$. In calculations the determined $\sigma_{11}^{I}(z)$ dependence was used and the model peak profiles were compared with experimental points as well as with calculations assuming zero stress (see Fig. 7.21a). In Fig. 7.21b similar comparison but assuming constant FWHM is shown. Important question is if the other peaks (at different α, 2θ and for different λ) are also correctly reproduced for the FWHM evolution described by ξ=10 μm. In this aim different peaks were modeled assuming the same variation of microstructure (described by ξ=10 μm) and stress dependence $\sigma_{11}^{I}(z)$. Only the values of b_0 (assuming $b_0 = b_1$) was adjusted for different reflections *hkl* (see Table 7.4). In Fig. 7.22 the experimental profiles were compared with the modeled ones assuming stress variation $\sigma_{11}^{I}(z)$ or stress equal to zero. Very good agreement between experimental and theoretical peaks confirms that the $\sigma_{11}^{I}(z)$

function correctly describes in-depth stress dependence. Moreover, it can be also seen that the stress gradient differently influences the diffraction peaks measured for different penetration depth. If penetration depth τ is relatively small (in comparison with stress variation distance), compressive stress causes significant shift of the diffraction peak (τ = 3.7 μm, τ = 5.9 μm in Fig. 7.22 and τ = 2.6 μm in Fig. 7.23), while for deeper penetration depth (τ = 14.5 μm, τ = 17.5 μm in Fig. 7.22 and τ = 31 μm in Fig. 7.23) the peak is not much shifted but significant asymmetry appears due to superposition of the intensities from regions where compressive stress decreases and next change to tensile one.

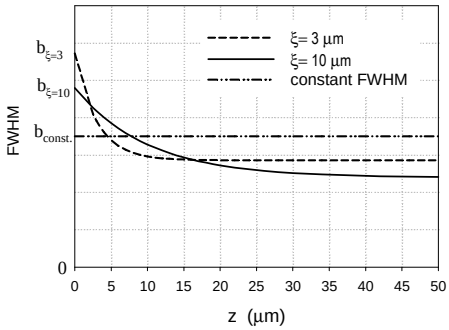

Fig. 7.20. Variation of FWHM described by Eq. 7.2 with different values of ξ parameter (assuming $b_0 = b_1$).

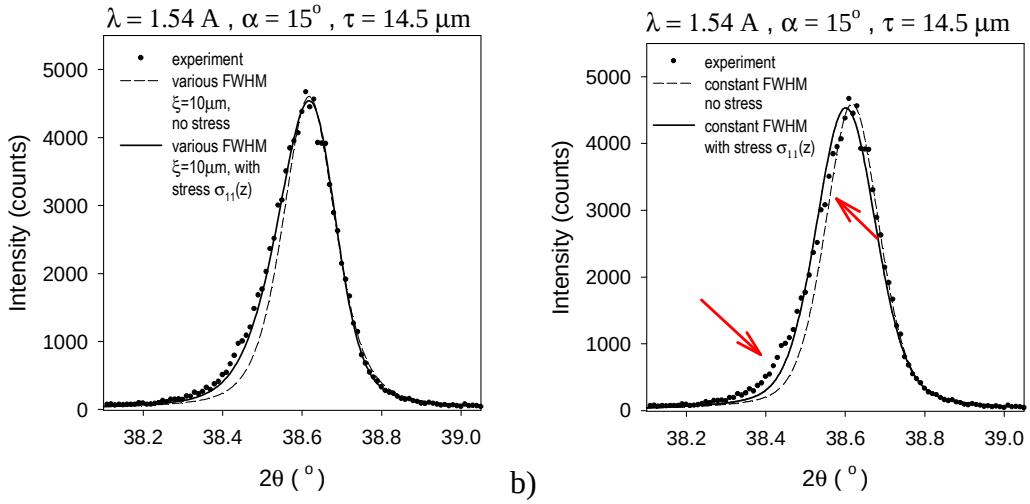

a) b)

Fig. 7.21. Comparison of diffraction peak profiles: experimental, simulated for $\sigma_{11}^{I}(z)$ stress function and assuming zero stress (λ=1.5419 Å, 2 $\theta \approx 38.6^{o}$ and $\alpha = 15^{o}$). Results for FWHM variation described by Eq. 7.2 with ξ=10 μm (a) and for constant FWHM (b) are shown.

It can be concluded that inverse analysis (integration of stress $\sigma_{11}^{I}(z)$ with intensity weight) allowed to determine range of the depth from which the stresses influence diffraction results (about 40 μm), i.e., for which the $\sigma_{11}^{I}(z)$ was determined. Moreover, the inverse analysis applied for peak profiles confirmed the stress distribution given by $\sigma_{11}^{I}(z)$. In the latter calculation increase of FWHM for the peaks coming from the regions closer to the surface was assumed. This effect is due to microstructure change caused by mechanical polishing (increase of number of defects and decrease of crystallite in deformed material). It should be mentioned that similar simulation of peak profile was also done by Genzel et al. [36] in order to explain influence of stress gradient on the profile asymmetry. However, calculations were performed for one peak in the case of the deposited coating, i.e. when constant FWHM can be assumed.

Table 7.4. Values of b_0 (assuming $b_0 = b_1$) used in modeling of the peaks for different 2θ angles and wavelengths.

	λ=1.5419 Å			λ=1.7512Å			λ=1.2527Å		
2θ (^{o})	38.6	82.7	138.2	44.0	91.6	151.5	31.15	84.8	132.7
b_0 (^{o})	0.12	0.20	0.75	0.12	0.26	0.90	0.115	0.22	0.65

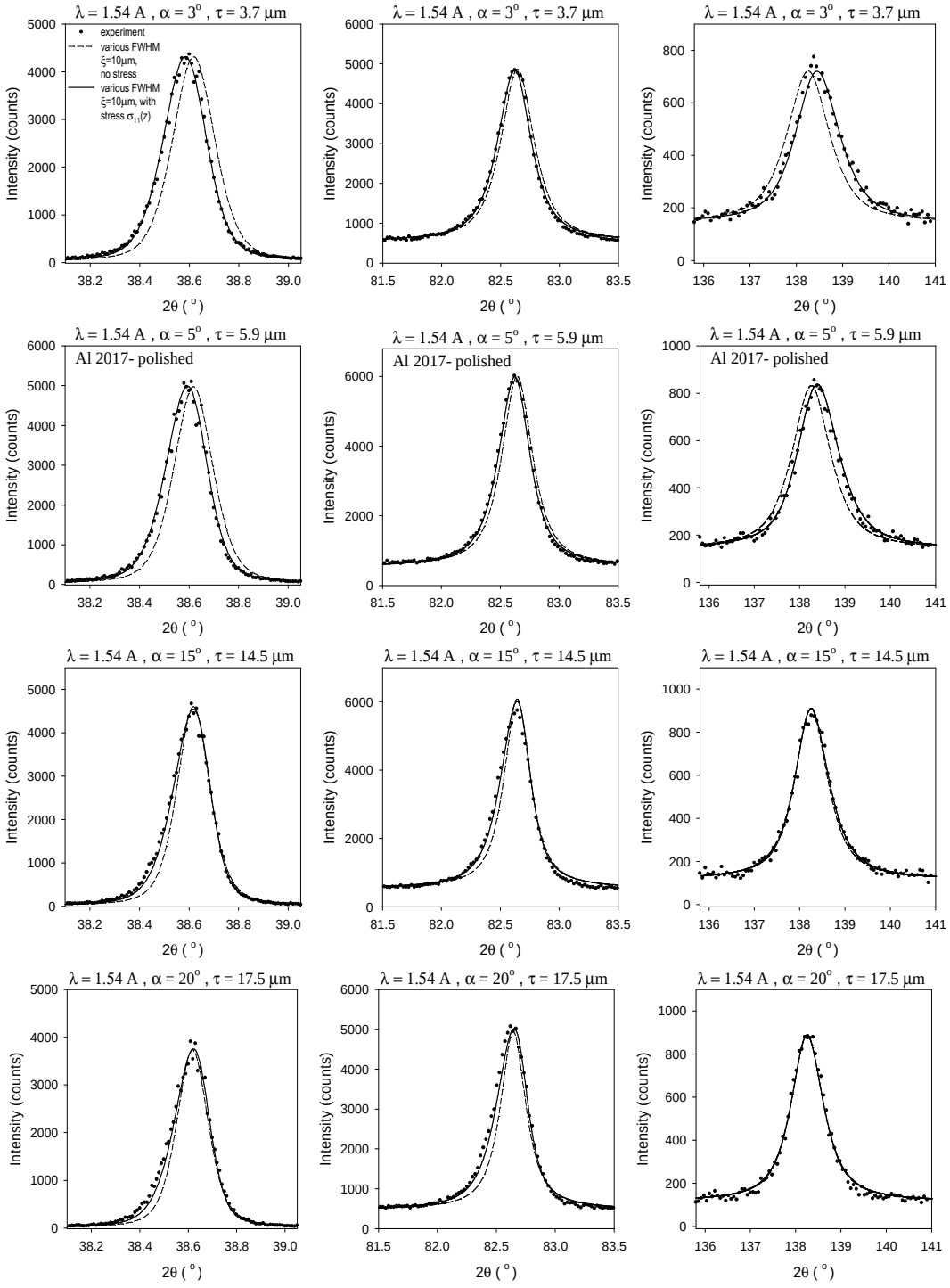

Fig. 7.22. Comparison of diffraction peak profiles: experimental, simulated for $\sigma_{11}^{I}(z)$ stress function and assuming zero stress. For all peaks (λ=1.5419 Å) the same variation of FWHM described by Eq. 7.2 with ξ=10 μm was used in calculations ($b_0 = b_1$ is given in Table 7.4).

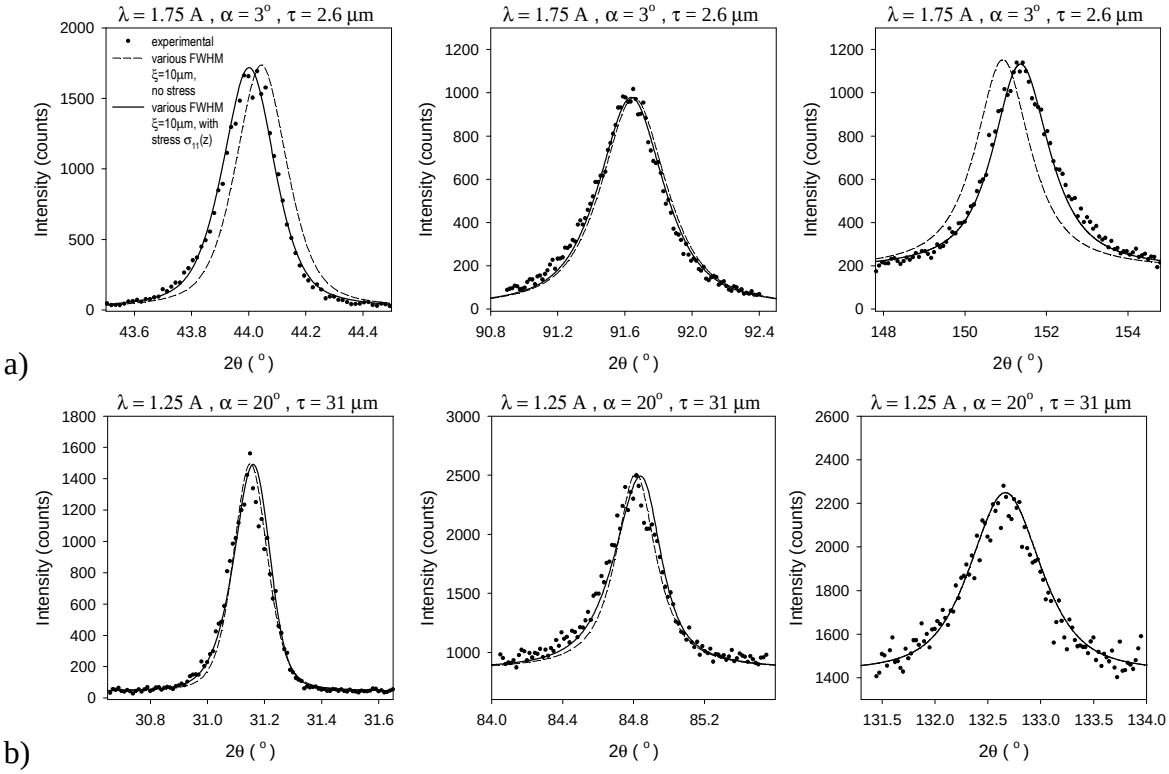

Fig. 7.23. Similar comparison as in Fig 7.18 but for example peaks measured with λ =1.7512Å (a) and λ=1.2527Å (the same variation of FWHM as in Fig. 7.18, described by Eq. 7.2 with ξ=10 μm was used in calculations and $b_0 = b_1$ given in Table 7.4).

Finally the root mean square strains $\sqrt{<\varepsilon^2>}$ corresponding to density of dislocations but also influenced by stress gradient $\sigma_{11}^{I}(z)$ were calculated using Williamson-Hall method for polished Al2017 sample. Fitted linear function to experimental data is shown in Fig. 7.24. The results of calculation are summarized in Table 7.5. As the reference the LaB_6 powder was used.

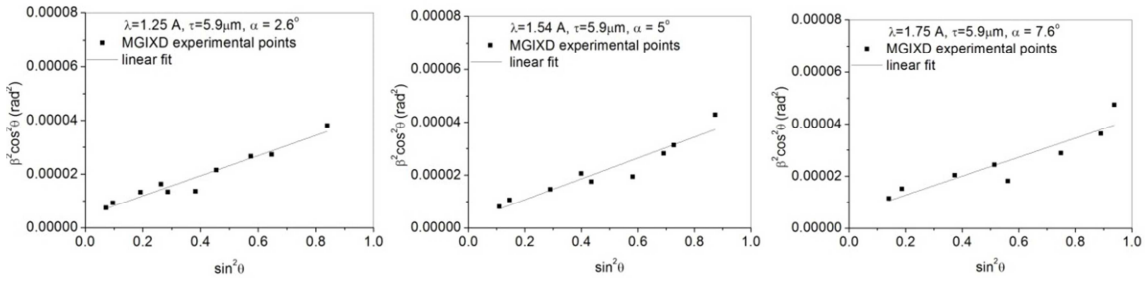

a)

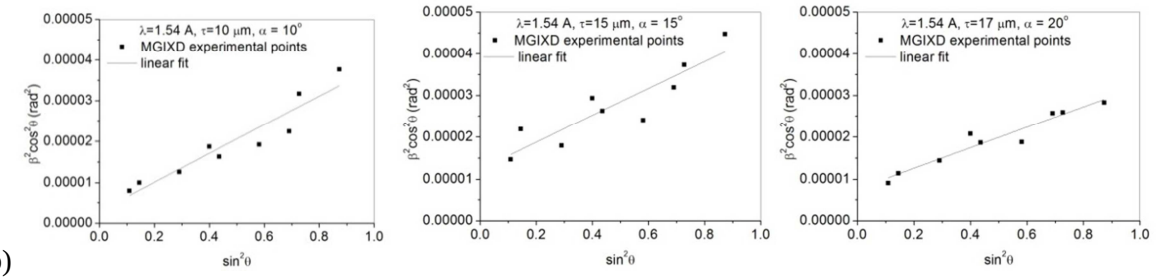

b)

Fig. 7.24. The linear function fitted to the experimental data using Williamson-Hall method for polished Al2017 (Gauss approximation). Results compered for different wavelengths but for the same penetration depth (a) and for the same wavelength but different incidence angle α (different penetration depth) (b).

Table 7.5. The root mean square of the third order strain ($\sqrt{\langle \varepsilon^2 \rangle}$) and crystallite size ($D$) calculated with Williamson-Hall method for Al 2017 polished samples (different wavelengths and incident angles).

λ(Å)	α (°)	τ (μm)	$\sqrt{<\varepsilon^2>}$	D (Å)
1.2527	2.6	5.9	0.0015 ± 0.0001	596 ± 96
1.7512	7.6	5.9	0.0015 ± 0.0001	747 ± 261
1.5419	5	5.9	0.0016 ± 0.0001	915 ± 413
1.5419	10	10	0.0015 ± 0.0001	868 ± 330
1.5419	15	15	0.0014 ± 0.0001	438 ± 55
1.5419	20	17	0.0012 ± 0.0001	553 ± 48

It can be concluded that results obtained using Williamson-Hall analysis are in a good agreement for the data collected with different wavelengths and comparable with

those obtained using classical diffractometer (in the margin of uncertainty). As expected the third order strain systematically decreases with the depth in the sample (this supports the above analysis concerning simulation of peak profiles), however the uncertainty of *D* is too large to determine the variation of the coherently diffracting domain size with depth. The results of Wiliamson-Hall analysis have rather qualitative character, showing tendency of variation, because it should be underlined that the $\sqrt{<\varepsilon^2>}$ strain is influenced not only by the defects (third order stresses) but also by the gradient of stress $\sigma_{11}^{I}(z)$ integrated over diffracting volume.

Ti6Al4V sample

Second studied sample was polished Ti6Al4V alloy (polishing type II) for which the gradient of stresses was observed for data obtained from classical diffractometer (Fig. 7.11). The example peak profiles obtained using synchrotron radiation is presented in Figs. 7.25-7.27 (for the comparison the diffraction peak profile from classical difractometer is presented on a Fig. 7.28). In this case strong asymmetry of diffraction peak suggest that two irradiated regions of the sample have different microstructure, i.e. layer of about 0.5-1 μm which has been severely plastically deformed (region of high density of dislocations) and the base material, under this layer, having much lower density of dislocations (smaller plastic deformation). Indeed the diffraction peaks can be easily separated into two pseudo-Voigt functions having different integral widths and position (Figs. 7.25-7.27). This effect was not clearly visible for diffraction peak from the classical diffractometer because of larger divergence of the beam and the presence of $Cu_{K\alpha 2}$ line. But still it is possible to separate two peaks for chosen profiles as shown in Fig. 7.28 (compare also the same peak measured by synchrotron radiation, shown in Fig. 7.25b). It should be underlined that in this case the separated peaks represent different regions in the sample and they can be treated independently. The broad peak (representing 'hard' deformed material in the layer) shifts relatively to the narrow one (coming from 'soft' base material), i.e. when $\psi=\theta-\alpha$ angle increases (together with 2θ, for constant α) the broad peak shifts from the left to the right site of the narrow one (see Fig. 7.25). It was also found that the relative contribution of the narrow peak increases for deeper penetration depths when

larger volume under the layer is irradiated. This effect is presented for chosen measurements, showing:

- almost constant intensity ratio for different 2θ, but constant λ and α (Fig. 7.25a and b), as well as for combinations of λ and α giving the same τ (Fig. 7.27);
- increase of the severely deformed ('hard') layer contribution when penetration depth decreases, i.e. when α decreases for constant λ (compare Fig. 7.25a with 7.25b) or when λ increases for approximately the same α (Fig. 7.26).

The above qualitative analysis shows that upper layer is more deformed ('hard') than the deeper base material.

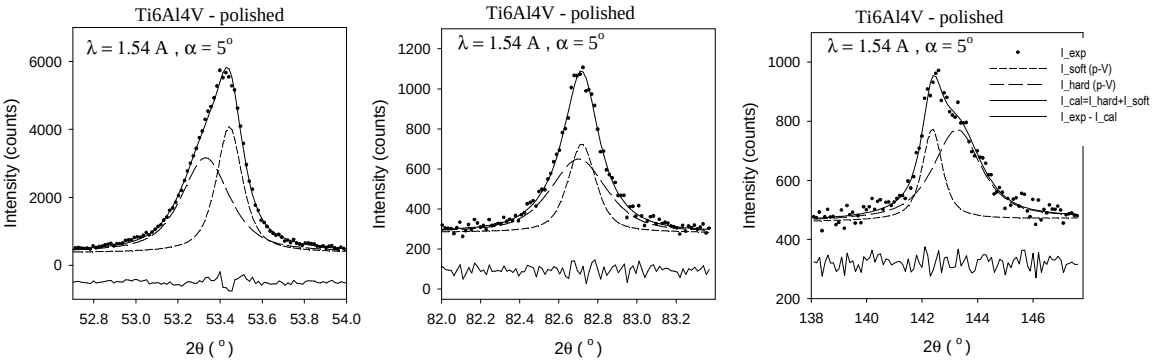

a)

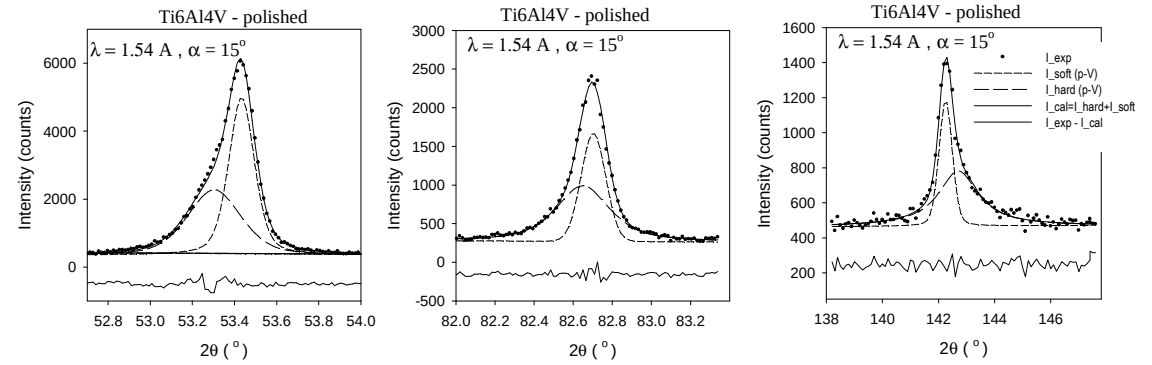

b)

Fig. 7.25. Comparison of fitted with pseudo-Voigt function peak profiles for λ=1.5419 Å and for two incident angles: 5° (a) and 15° (b).

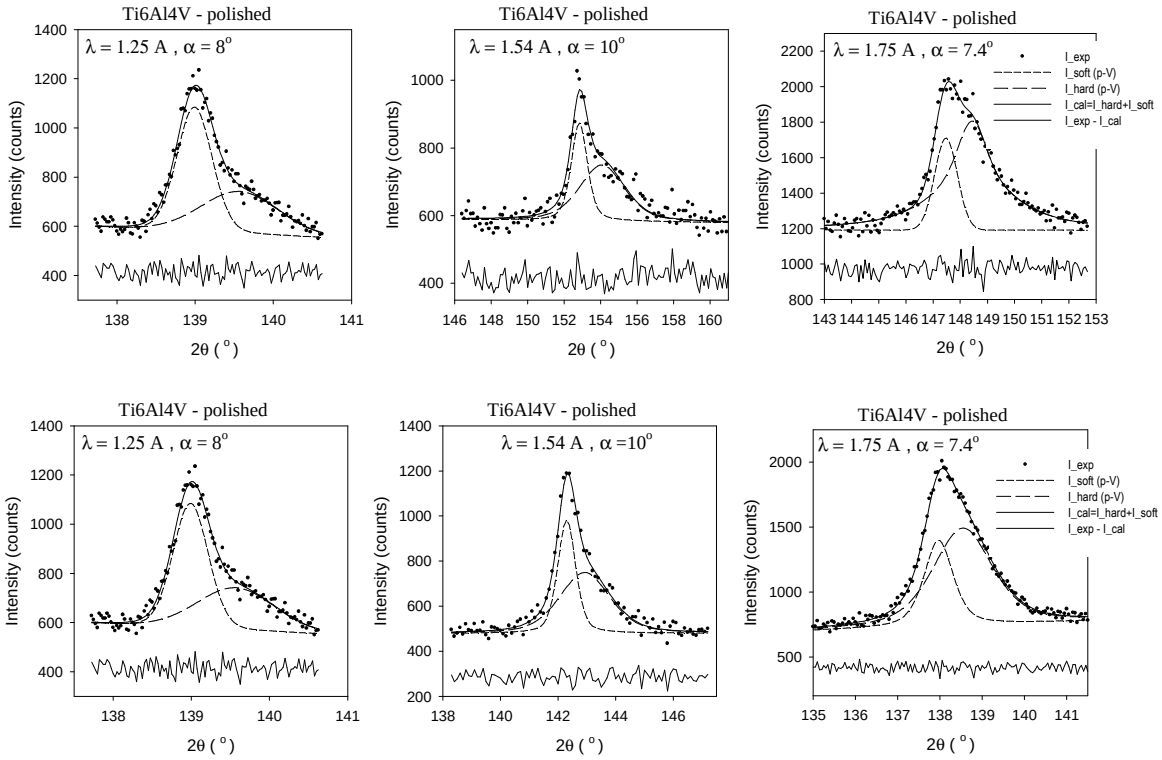

Fig. 7.26. The example peak profiles for more less the same incident angle α but for different wavelengths and penetration depths. Two pseudo-Voigt functions were fitted to the experimental data.

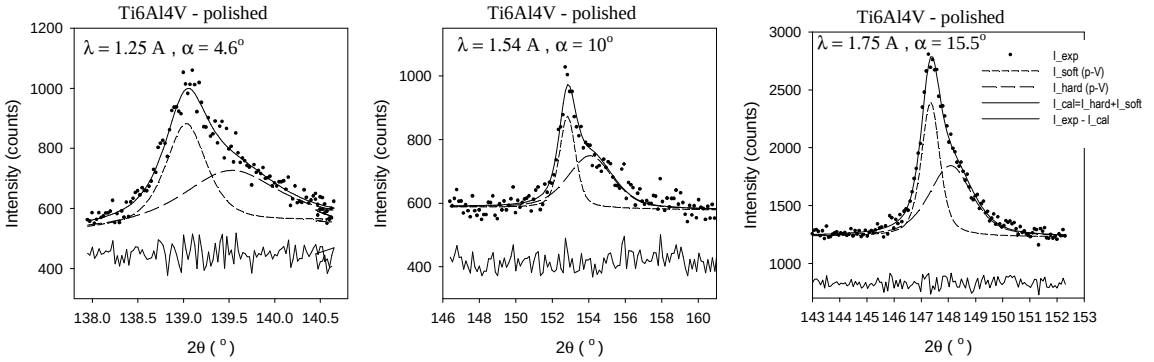

Fig. 7.27. The example peak profiles for the same penetration depth τ = 1.5 μm.

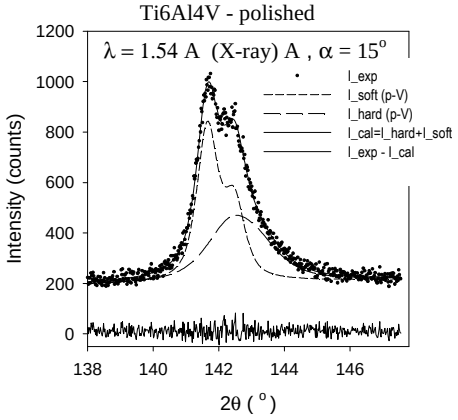

Fig. 7.28. The example peak profile obtained using classical diffractometer and fitted by two peaks.

At first, the residual stresses were determined using lattice parameters $<a(\phi,\psi)>_{\{hkl\}}$ vs. $sin^2\psi$ measured by three different wavelengths. Due to the presence of heterogeneity of the layers in sample the peak position was determined by centre of gravity method (one pseudo-Voigt function cannot be fitted to the measured peaks). The in-depth profiles of the determined stresses $\sigma_{11}^I(z)$, lattice stress free a_0 and c/a parameters are compared with those obtained using laboratory diffractometer (Fig. 7.29). The Kröner XSF was used in procedure based on Eqs. 6.1 and 3.23)

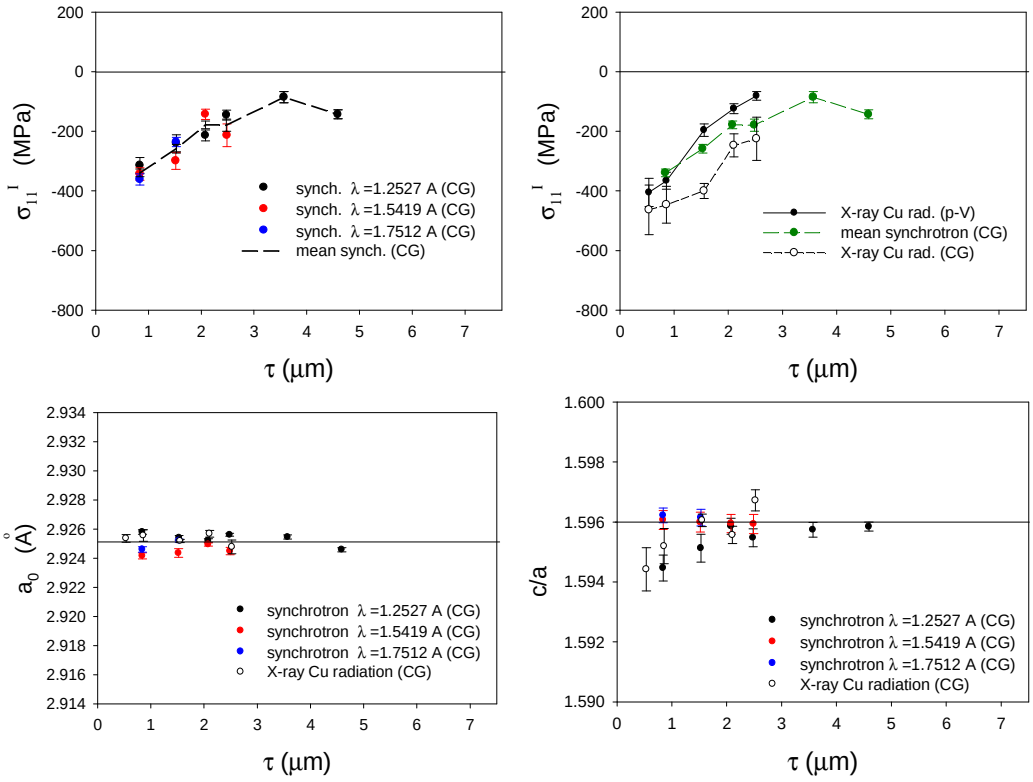

Fig. 7.29. The in-depth profiles of the stresses $\sigma_{11}^I(z)$, a_0 and c/a parameters, for Ti6Al4V sample. Comparison for three different wavelengths (synchrotron) and laboratory diffractometer using pseudo-Voigt fitting (p-V) and centre of gravity method (CG) for determining of peak position.

The in-depth profile of stresses presented on Fig. 7.29 is similar for the three different wavelengths used in experiment. Furthermore the results obtained from synchrotron measurements are not far from those obtained on classical diffractometer. The largest uncertainty and significant shift disagreement of the results (with other data) was obtained when centre of gravity method was used to determine peak position measured on laboratory diffractometer.

The above results represent an average values weighted by absorption, but more superior analysis can be performed for synchrotron data. As it was mentioned before the diffraction peaks can be easily separated into two pseudo-Voigt functions and the calculation of stresses can be performed for both of the regions in sample. To do this $< a(\phi,\psi) >_{\{hkl\}}$ vs. $sin^2\psi$ functions were determined independently from the positions of broad ('hard' region) and narrow ('soft' region) peaks. The $sin^2\psi$ plots are almost linear (Fig. 7.30) and they allow to determine stresses $\sigma_{11}^{I}(z)$, a_0 and c/a parameters for each region, independently. Significant negative slope of the curves suggests large compressive stress in the 'hard' region and almost horizontal lines correspond to small stress in the 'soft' region.

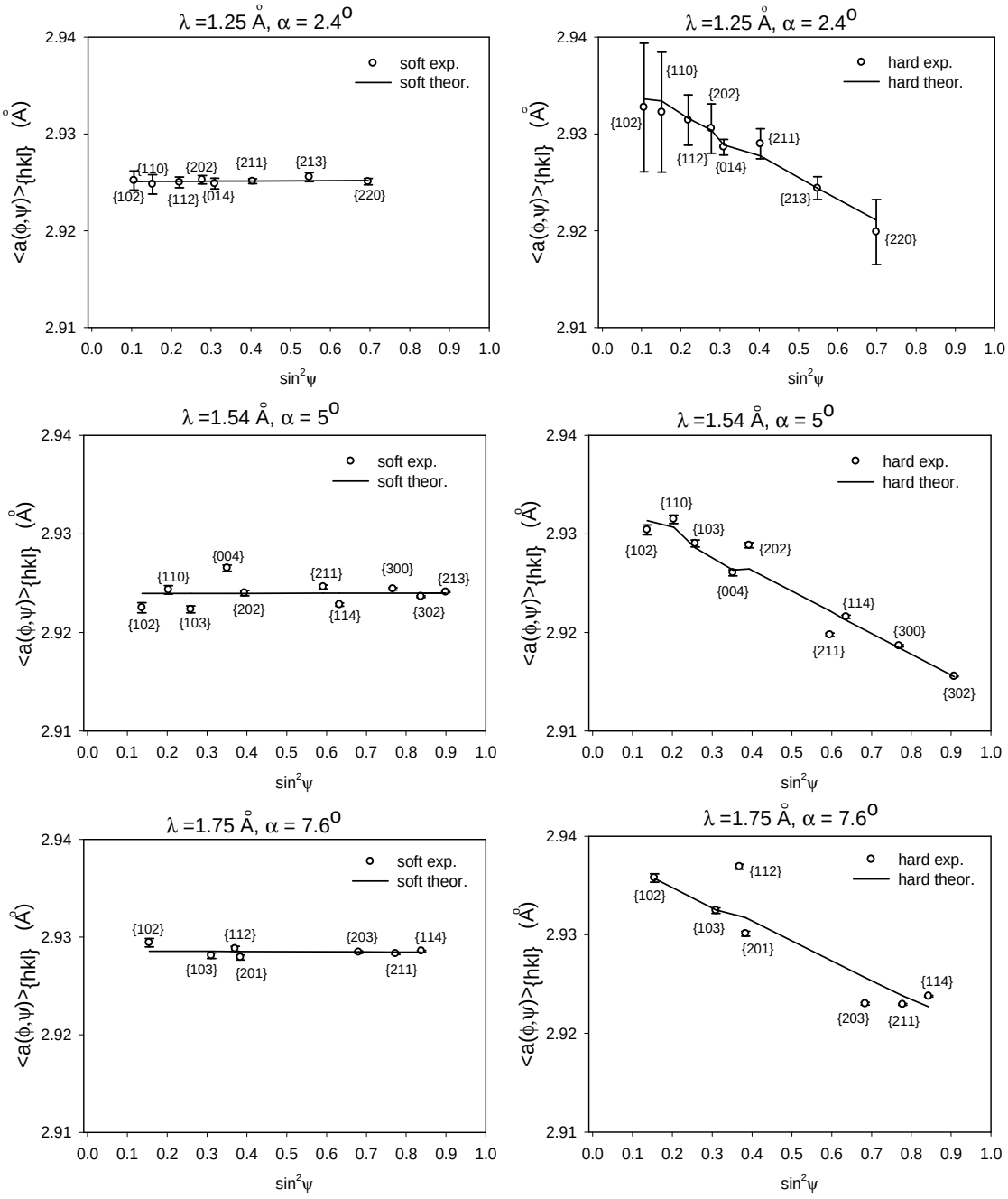

a) b)

Fig. 7.30. The example $<a(\phi,\psi)>_{\{hkl\}}$ vs. $sin^2\psi$ plots for polished Ti6Al4V sample obtained with three wavelengths and different incident angle (α) (the same penetration depth τ=0.84 μm). The plots for the 'soft' (a) and 'hard' (b) regions are separated. In each figure experimental data are shown together with fitted theoretical lines.

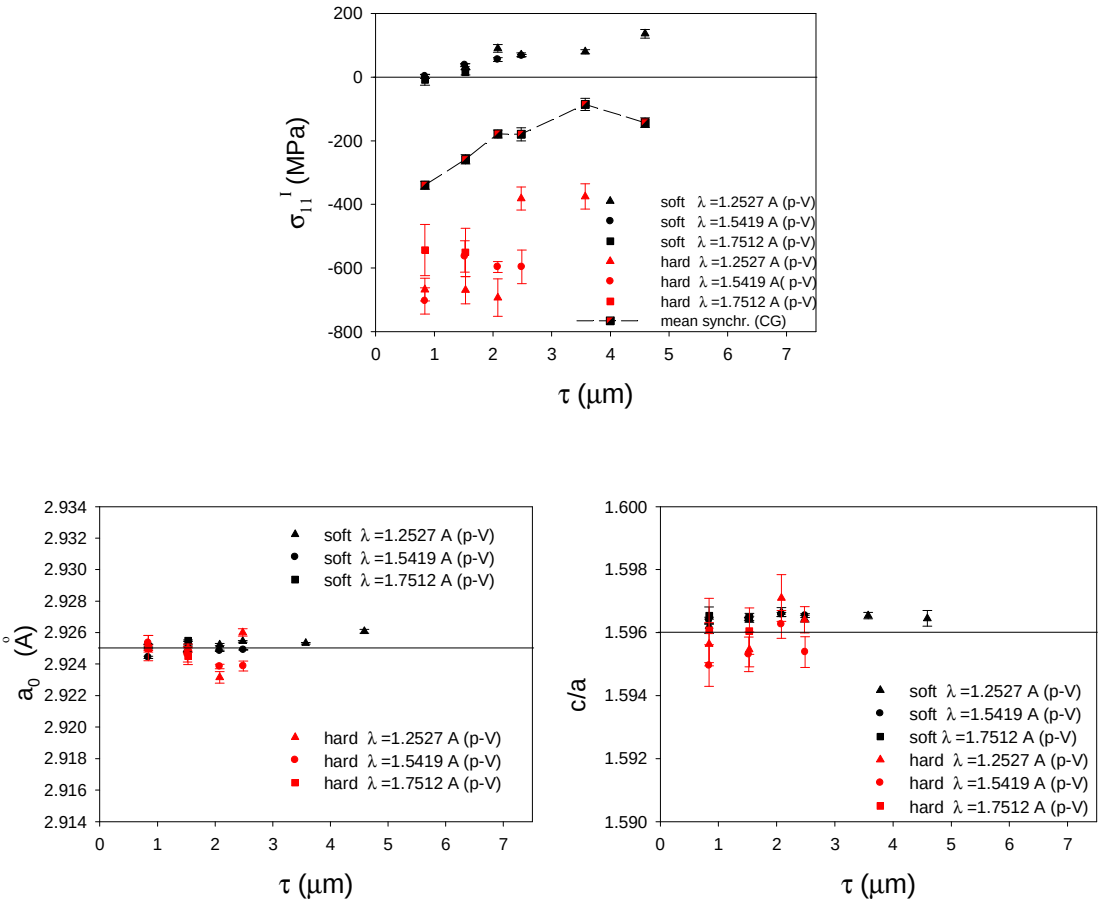

Fig. 7.31. The in-depth profiles of the stresses $\sigma_{11}^{I}(z)$, a_0 and *c/a* parameters, for Ti6Al4V sample. Results after peak separation are plotted as the function of penetration depth τ. The results are compared with those obtained using center of gravity method for peak position.

In-depth profiles of the measured values for ‘hard’ and ‘soft’ regions of the sample are presented in Fig. 7.31. High compressive stress of about 500-700 MPa has been found in the layer (irradiated for all wavelengths and geometrical conditions), while in the base material a small tensile stress increases with penetration depth within the range of about 0-120 MPa. The stress determined using centre of gravity method is approximately equal to the average from the values measured in the layer and base material, weighted by the intensity of reflected beam. For smaller penetration depth contribution of the layer causes relatively higher value of the measured stress, while for deeper penetration stress value approaches to this measured in the base material. It should be also noted that using synchrotron radiation (λ=1.2527 Å) the stress was determined for much deeper regions in

comparison with classical X-ray results (in this case stresses in the layer cannot be determined because of very low contribution of the broad peaks). It should be underline that almost the same values of a_0 and c/a parameters were obtained both for 'soft' and 'hard' regions (after separation of two peaks), as well as for the mean results calculated using centre of gravity method. These parameters do not vary with penetration depth.

Now, it is possible to evaluate the thickness of the deformed layer. As it was mentioned before, the information gained from the diffraction experiment is weighted by the absorption of X-ray in the material. On the basis of the exponential attenuation law it is possible to find the thickness of the layer from the relative intensities of the diffraction peaks. The intensities of the separated pseudo-Voigt profiles corresponding to the 'hard' (I_{hard}) and 'soft' (I_{soft}) regions of the sample, respectively can be expressed as:

$$I_{hard} = I_0 \int_0^t e^{-\frac{z}{\tau}} dz \Big/ \int_0^\infty e^{-\frac{z}{\tau}} dz = I_0 \left(1 - e^{-\frac{t}{\tau}} \right) \tag{7.3}$$

$$I_{soft} = I_0 \int_t^\infty e^{-\frac{z}{\tau}} dz \Big/ \int_0^\infty e^{-\frac{z}{\tau}} dz = I_0 e^{-\frac{t}{\tau}} \tag{7.4}$$

where t is the thickness of the severely deformed ('hard') layer and I_0 is the total peak intensity.

By dividing both sides of above equations by each other and after simple transformation the thickness of the layer is given by:

$$t = \tau \ln \left(\frac{I_{hard}}{I_{soft}} + 1 \right). \tag{7.5}$$

Using Eq. 7.5 the values of *t*- thickness were determined from $\frac{I_{hard}}{I_{soft}}$ for all peaks for which separation of two peaks is possible (for some peaks the position of both peaks is the same and separation cannot be done, however the positions of both peaks can be determined). The results presented in Fig. 7.32 show that the uncertainty of *t* thickness increases for low 2θ as well as for decreasing wavelength λ and not all peaks can be used to determine thickness of the 'hard' layer. In order to precisely estimate the thickness of the layer peaks

with the smallest uncertainty were chosen for each wavelength. The ratio I_{hard}/I_{soft} as a function of penetration depth for chosen diffraction peaks is presented on a Fig. 7.33a, where an increase of contribution of I_{hard} intensity with decreasing penetration depth is seen. The results obtained for three different wavelengths and incident angles α coincide when they are plotted vs. τ. This proves that the I_{hard}/I_{soft} ratio really depends on the absorption phenomenon.

Knowing the ratio I_{hard}/I_{soft} ratios the layer thicknesses were calculated. Fig. 7.33b shows the estimated size of the layer as a function of the penetration depth. As it can be seen the thickness of the layer is about 1.38 μm and does not change for the data obtained with different experimental conditions (determined t thickness is constant for various depth τ, penetrated by the beam).

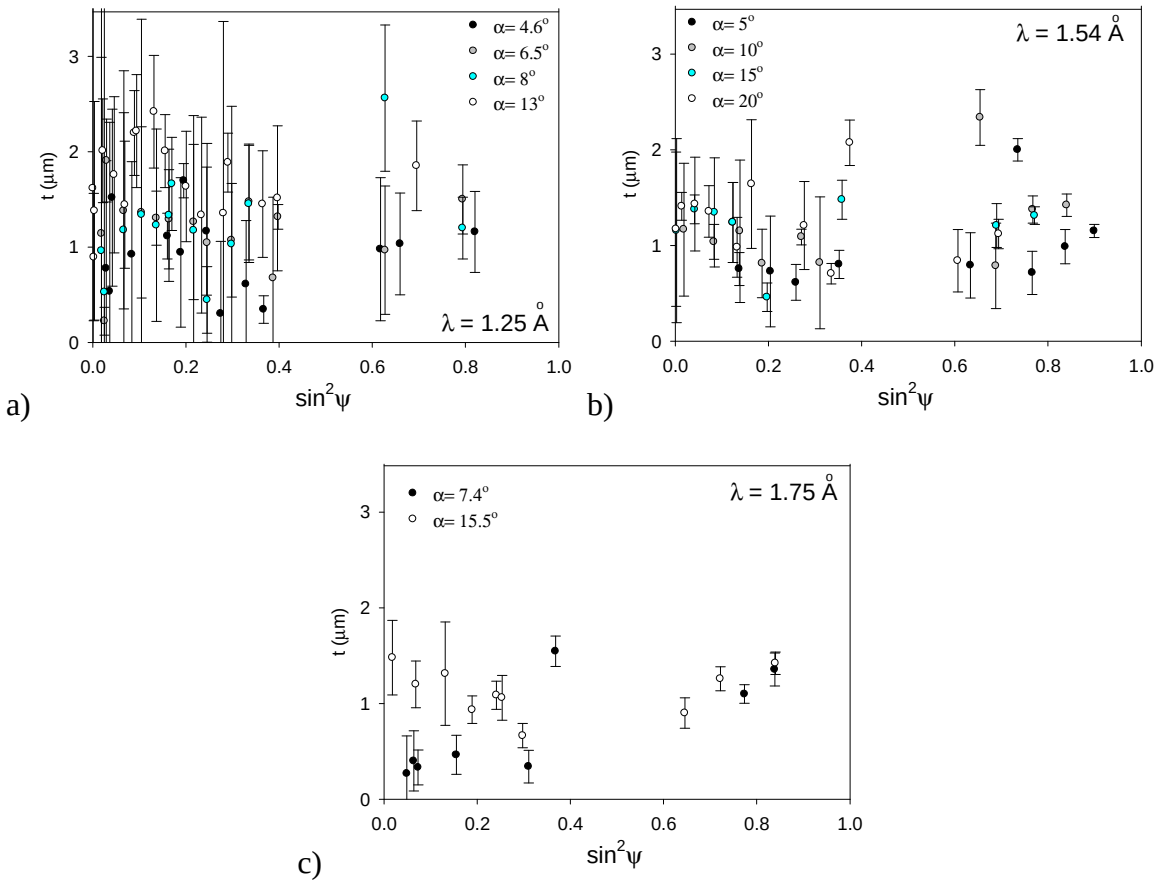

Fig. 7.32. The thickness of the layer calculated for all used wavelengths: 1.2527 Å (a), 1.5419 Å (b) and 1.7512 Å (c) and for different diffraction peaks.

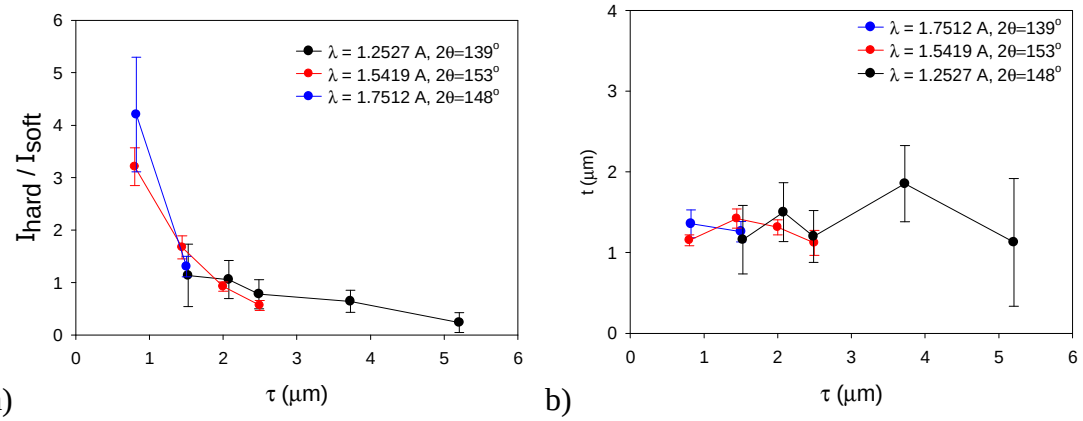

Fig. 7.33. The ratio I_{hard}/I_{soft} (a) and calculated layer thickness *t* (b) as a function of penetration depth for chosen diffraction peaks fitted with two pseudo-Voigt profiles.

After estimation of the layer thickness it is possible to present results from the synchrotron measurements as a function of the information depth $\bar{z}$ defined by Eq. 3.4. Fig. 7.34 presents the in-depth profile of stresses and lattice parameters. The results coming from both parts of the sample are gathered separately. As it can now be clearly seen there are two regions in the sample: the 'hard' region, where $\bar{z}$ is calculated for a layer having thickness t =1.38 μm and the 'soft' material for which $\bar{z}=\tau$ is defined for the infinite base material, starting at depth of 1.38 μm. The high compressive stresses is present in the layer of the thickness up to 1.38 μm, on the other hand the part of the sample, deeper than 1.38 μm, exhibits a small value of increasing tensile stress. Values of calculated lattice parameters a_0 and *a/c* are nearly constant in both parts (Fig. 7.34).

In the above analysis the sample was divided into two different parts having different properties and stresses. The reason of such treatment was that two peaks were seen and well separated from the diffraction profile. However, this approximation is artificial because the properties of the sample and stresses (for example FWHM) changes more or less smoothly. Therefore, it is necessary to compare the obtained results with another approach in which the stresses change gradually. It can be done, by using inverse Laplace transformation for the data obtained from the peak positions determined by the center of gravity method (presented in Fig. 7.29). The assumption of this approach is that the evolution of the stresses can be approximated by polynomial i.e., the step change of stress is not possible. Therefore, the results are 'smoothed' too much and the separation of

two profiles should not be seen in the diffraction peak. The result of the invert Laplace transform (using polynomial of 2 degree) together with the results of peak separation method are shown in Fig. 7.35. A quantitative agreement of both methods is seen, i.e. compressive stress close to the surface, zero stress at the same depth (2-3 μm) and tensile stress in the base material were obtained for both approaches. Also, the values of stresses are not very different. Concluding it can be stated that the results of the method with separation of two peaks are more reasonable because they have confirmation in peak profiles and some smoothing of the stress distribution between two separated parts of the sample should not introduce significant errors (a shown using invers Laplace method).

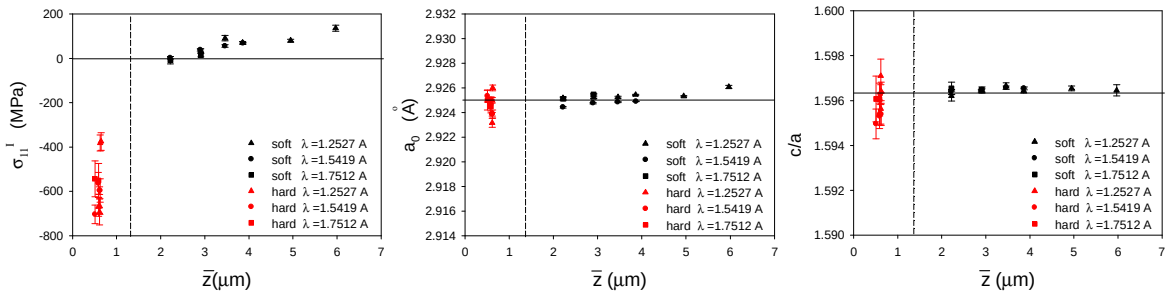

Fig. 7.34. The in-depth profiles of the stresses $\sigma_{11}^{I}(z)$, a_0 and c/a parameters, for Ti6Al4V sample. Results for different wavelengths after peak separation and with division into two regions in the sample separated by dashed vertical line.

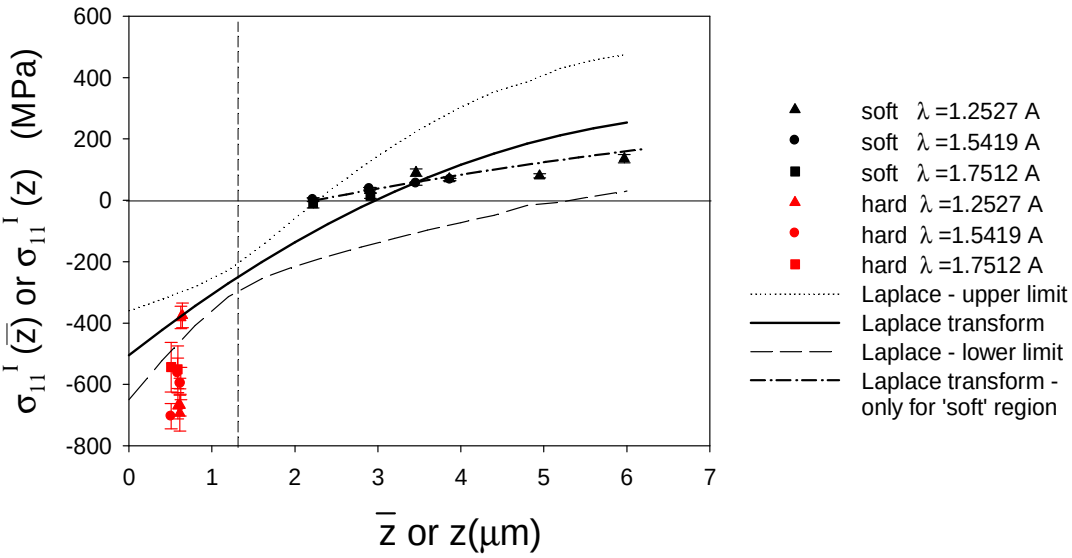

Fig. 7.35. The in-depth profiles of stresses for Ti6Al4V sample. Results after peak separation and with division into two regions in the sample (points, $\sigma_{11}^{I}(\bar{z})$) are compared with the in-depth stress profile (lines, $\sigma_{11}^{I}(z)$) as a function of real depth obtained with Laplace method (center of gravity for peak position).

Finally the root mean square strains $\sqrt{<\varepsilon^2>}$ corresponding to density of defects and influenced by the stress gradient were calculated using Williamson-Hall method independently for two separated peaks obtained from polished Ti6Al4V alloy (the LaB_6 powder was used as reference). As expected higher value of $\sqrt{<\varepsilon^2>} = 0.2\% - 0.3\%$ was obtained from the severely deformed layer in comparison with the base material ($\sqrt{<\varepsilon^2>} = 0.08\% - 0.1\%$). For the 'hard' region the $\sqrt{<\varepsilon^2>}$ strain does not depend on the value of penetration depth τ (in the margin of uncertainty), while small but systematic decrease of $\sqrt{<\varepsilon^2>}$ appears in the 'soft' region (Table 7.6). Indeed, the whole volume of 'hard' layer always contribute in the broad diffraction peak, while the gauge volume of the 'soft' part increases with larger penetration depth τ, showing small decrease of $\sqrt{<\varepsilon^2>}$ in deeper volumes measured using narrow peak.

The size of coherently diffracting domain was determined only in the case of the broad peak coming from 'hard' region, but still with large uncertainty (Table 7.6). Some results are not shown because uncertainty exceeds *D* value. In the case of the 'soft' part, the D size is too large to be determined in this experiment for all results, i.e., the experimental uncertainty exceeds few times the obtained *D* values.

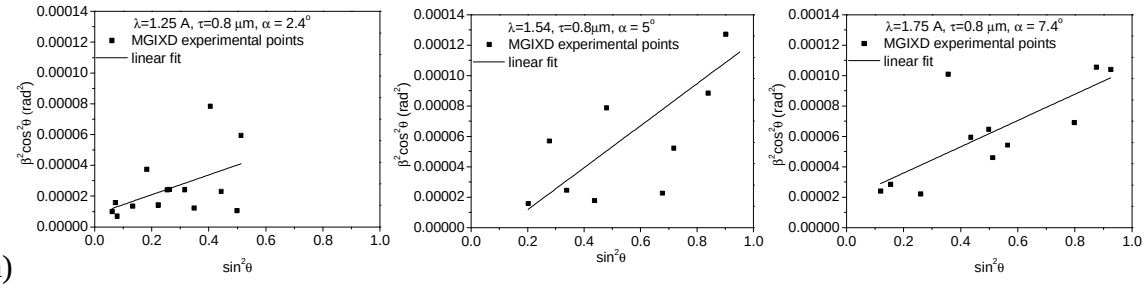

a)

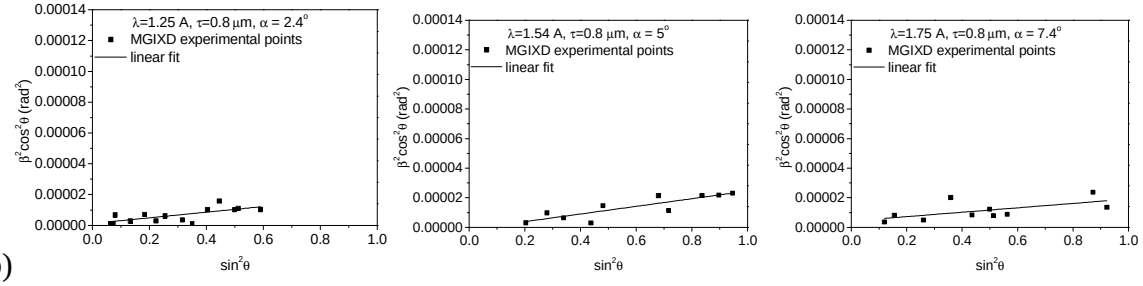

b)

Fig. 7.36. The linear function fitted to the experimental data in Williamson-Hall method for polished Ti6Al4V (Gauss approximation). Results compared for different wavelengths but for the same penetration depth from the 'hard' (a) and 'soft' (b) regions of the sample.

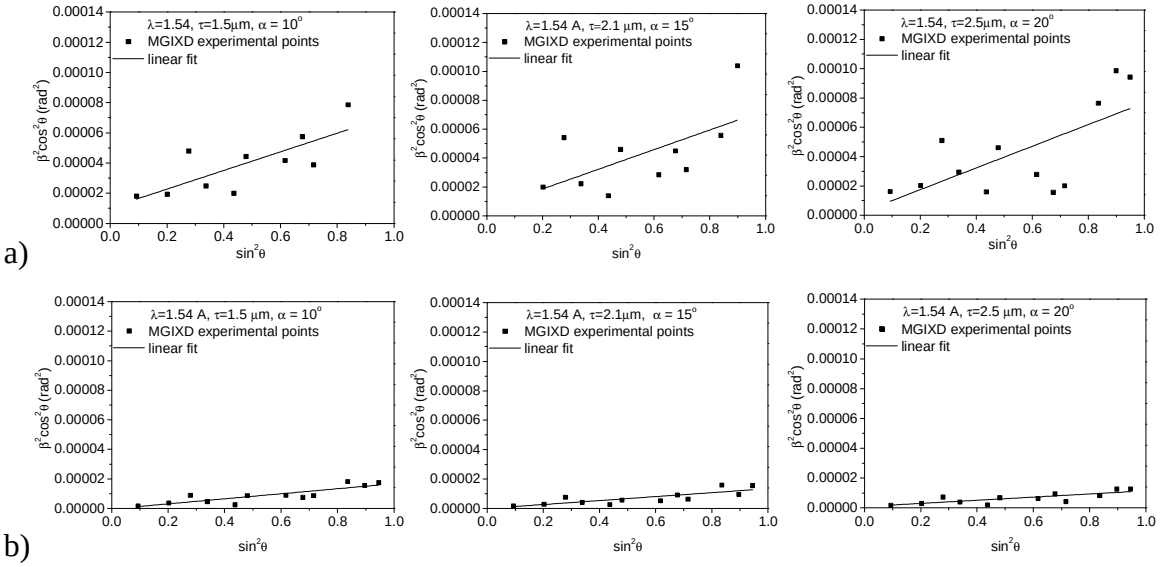

Fig. 7.37. Similar presentation as in Fig. 7.36, but the results are compared for the same wavelength (1.5419 Å) and for different incident angles α (i.e. for different depths in the sample). Plots for 'hard' (a) and 'soft' (b) regions are shown separately.

Table 7.6. The root mean square of the strain ($\sqrt{\langle \varepsilon^2 \rangle}$) and crystallite size ($D$) calculated with Williamson-Hall method for Al2017 polished samples (different wavelengths and incident angles).

λ Å	α (°)	τ (μm)	$\sqrt{<\varepsilon^2>}$		D (Å)	
Hard region						
1.2527	2.4	0.8	0.0020	±0.0005	441	±280
1.7512	7.4	0.8	0.0023	±0.0003	406	±149
1.5419	5	0.8	0.0029	±0.0004	---	----
1.5419	10	1.5	0.0020	±0.0003	478	±217
1.5419	15	2.1	0.0021	±0.0001	---	----
1.5419	20	2.5	0.0022	±0.0004	---	----
Soft region						
1.2527	2.4	0.8	0.0011	±0.0002	---	----
1.7512	7.4	0.8	0.0010	±0.0002	---	----
1.5419	5	0.8	0.0013	±0.0001	---	---
1.5419	10	1.5	0.0010	±0.0001	---	---
1.5419	15	2.1	0.0009	±0.0001	---	----
1.5419	20	2.5	0.0008	±0.0001	---	----

On the basis of presented results obtained measuring mechanically polished samples with synchrotron radiation on G3 spectrometer (DESY, HASYLAB), it appears that for three different wavelengths the same in-depth profiles of stresses $\sigma_{11}^{I}(\bar{z})$ were obtained analyzing shifts of the peak positions. What is more the results perfectly agree with those obtained previously using classical X-ray diffraction ($\lambda_{CuK\alpha 1}$=1.54056 Å). As the result, it was verified that absorption phenomenon limits the penetration depth of X-rays and stress gradient can be measured using MGIXD method. Furthermore, synchrotron radiation (λ=1.2527 Å) allowed to measure the stress profile for deeper regions in comparison with classical X-rays ($\lambda_{CuK\alpha 1}$=1.54056Å). In all measurements constant and independent on the depth values of a_0 and c/a were determined.

The analysis of peak profiles brings more information concerning dependence of the stress vs. real depth ($\sigma_{11}^{I}(z)$). In the case of polished Al2017, the asymmetry and/or shift of the peak correctly reflects the stress gradient calculated applying inverse Laplace transform for the $\sigma_{11}^{I}(\bar{z})$ function. On the other hand, two different regions having different microstructure were separated when diffraction peak was fitted by two pseudo-Voigt function. (it was clearly seen that the diffraction peak is composed from two profiles). Finally, the Wiliamson - Hall method was applied to determine evolution of the root mean square of the strain ($\sqrt{\langle \varepsilon^2 \rangle}$) from the depth. A small decrease of this value was found for polished Al 2017 sample and in the soft region of. Significantly, larger $\sqrt{\langle \varepsilon^2 \rangle}$ strain was measured in the severely deformed upper layer of polished Ti6Al4V alloy. The size of coherently diffracting domain (D) cannot be determined, because of large uncertainty.

7.3. ENERGY DISPERSION MEASUREMENT USING SYNCHROTRON RADIATION.

In the next experiment multireflection method was applied for the energy dispersion method in which white beam containing radiation having different wavelengths was used (λ (Å): 0.3–0.18/ E (keV): 40-68). The measurements were performed in polished (type I) and ground Ti (grade 2) samples on the EDDI beamline at BESSY synchrotron (Berlin, Germany). These specimens did not exhibit stress gradient when measured using laboratory diffractometer (see section 7.1). The synchrotron white beam was generated by the 7T-Wiggler and passed about 30 m through few optical components up to the place of the experiment. An absorber mask limits the beam diameter to 3.9 mm per 3.9 mm. In order to gain required characteristics of the beam, system of slits and filers is provided.

The stress analysis was performed using three different methods (the XSF were calculated by Kröner model):

- The first was the standard $sin^2\psi$ method (ψ - geometry) in which constant 2θ = 16° was used. Each $< a(\phi,\psi) >_{\{hkl\}}$ vs. $sin^2\psi$ plot was measured for different reflection *hkl* using appropriate wavelengths. Due to various absorption corresponding to different energies (and wavelengths) of radiation, each plot was determined for different average penetration depth. However, the penetration depth is not constant and varies vs. $sin^2\psi$.
- Universal plot method (described in section 3.1.2) was applied for 100 reflection and stresses close to the surface were determined.
- Using multireflection analysis it was possible to separate the data for chosen and constant penetration depth (within interval ±1μm). In this method only values $< a(\phi,\psi) >_{\{hkl\}}$ for the same penetration depth (different wavelengths and *hkl* reflections) were chosen to create one $\sin^2\psi$ plot. Using iteration fitting procedure based on Eqs. 3.23 and 6.1 the stresses were determined for constant depths.

The example $< a(\phi,\psi) >_{\{hkl\}}$ vs. $sin^2\psi$ plots for standard analysis are shown in Figs.7.38 and 7.39, while similar plots for multireflection method are presented in Figs. 7.40 and 7.41. The comparison of the in-depth stress profiles determined with all used methods of analysis, is presented in the Fig. 7.42.

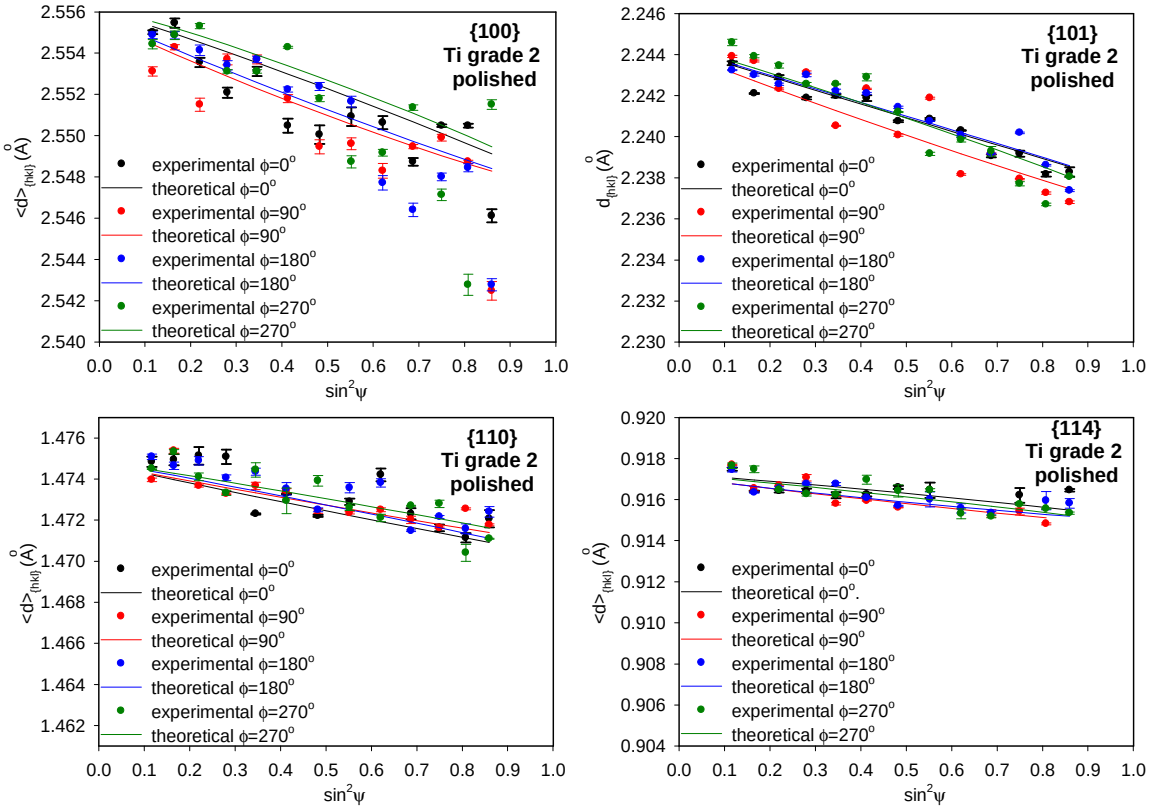

Fig. 7.38. The example of $\sin^2\psi$ plots for polished (type 1) Ti sample for standard analysis.

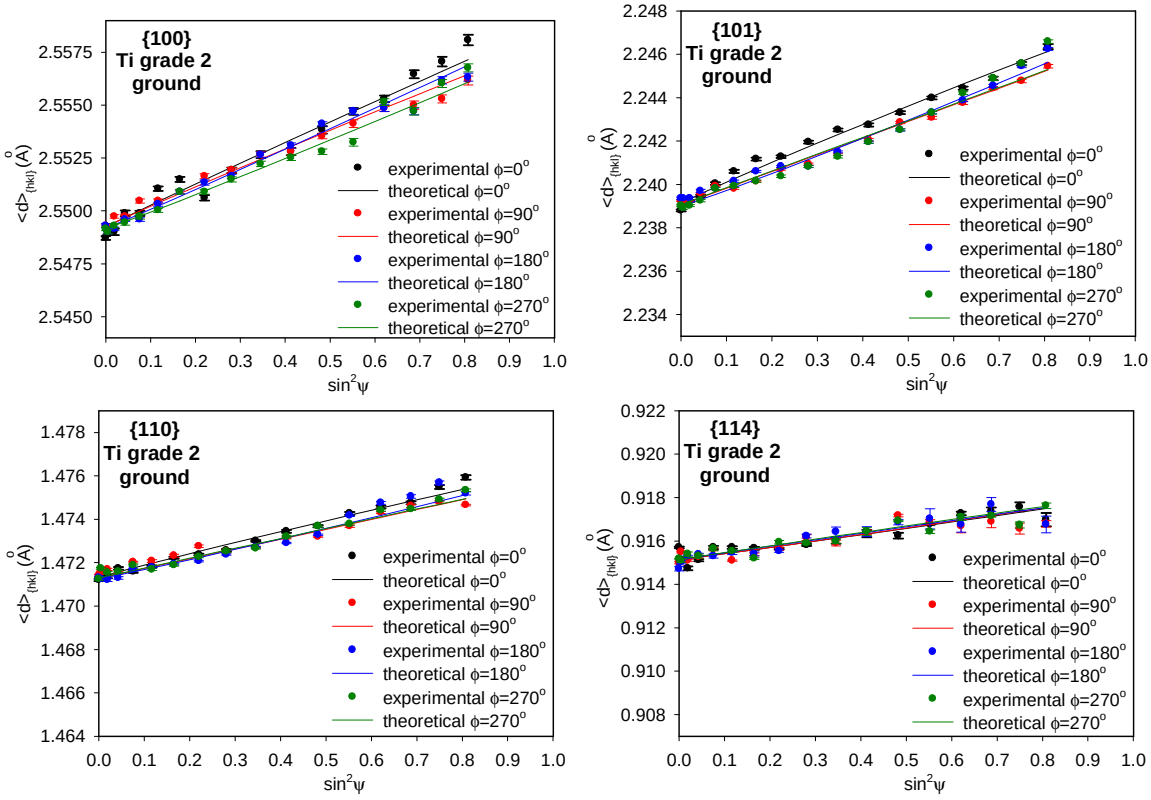

Fig. 7.39. The example of $\sin^2\psi$ plots for ground Ti sample for standard analysis.

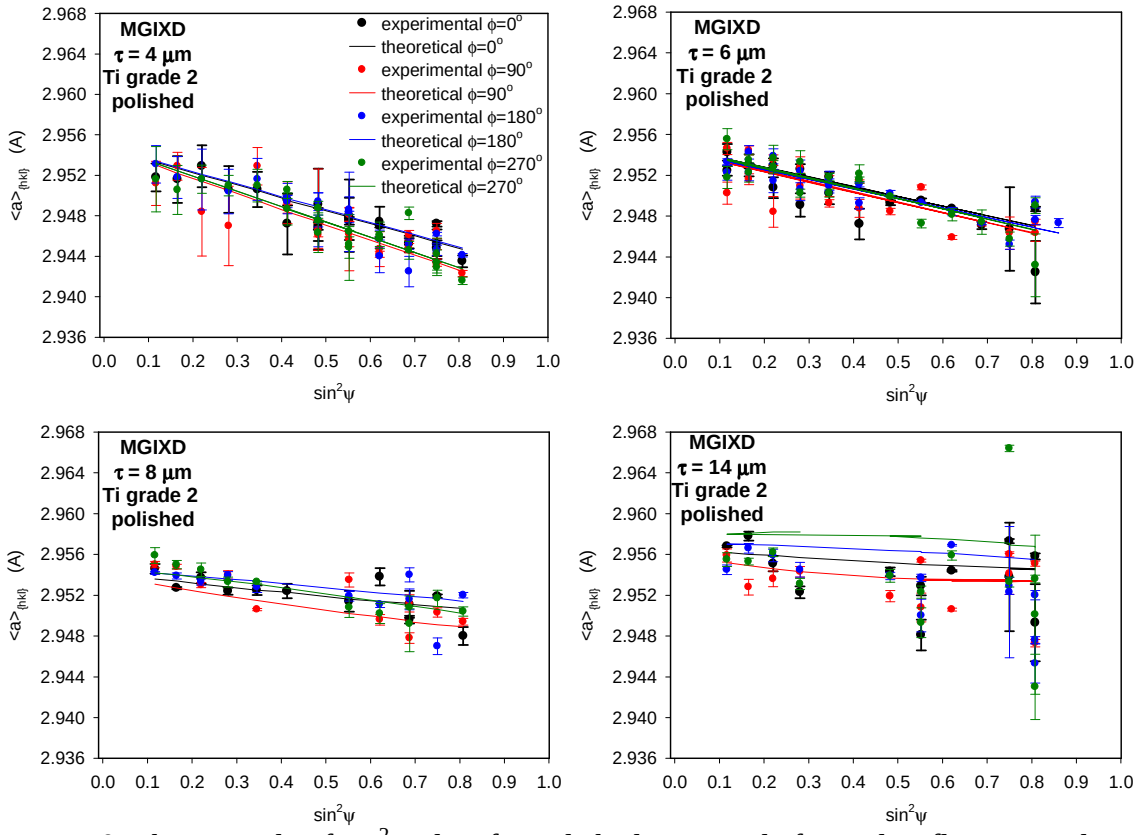

Fig. 7.40. The example of $\sin^2\psi$ plots for polished Ti sample for multireflection analysis.

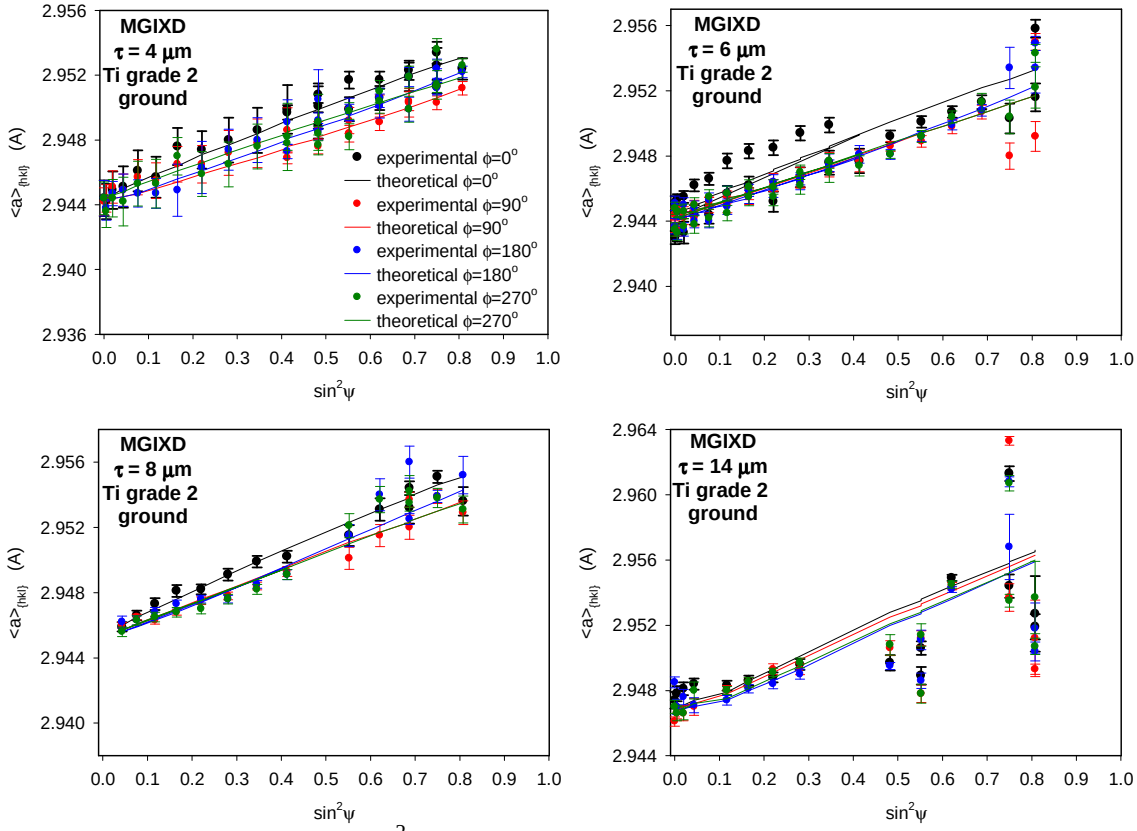

Fig. 7.41. The example of $\sin^2\psi$ plots for ground Ti (grade 2) sample for multireflection analysis.

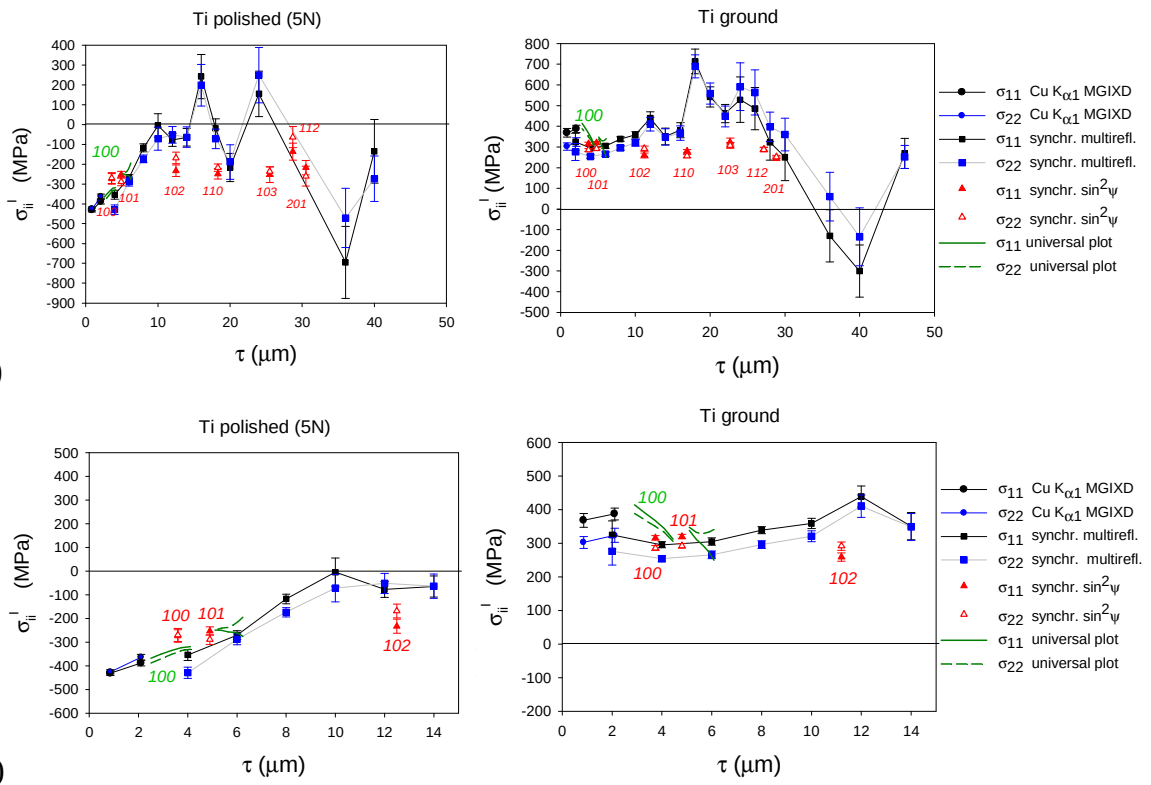

Fig. 7.42. The in-depth profile of stresses for polished (type I) and ground Ti (grade 2) sample. Comparison of the results from classical diffractometer (MGIXD) and synchrotron EDDI experiment, for which tree different methods of analysis were used (standard $\sin^2\psi$, multireflection, universal plot). Two different ranges of penetration depth are compared: a) 0-50 μm and b) 0-15 μm.

In the light of presented results (Fig. 7.42) it is visible that for the range of the penetration depth 0-50 the relevant spread of experimental points occurs. In view of the nature of these results it appears that the spread of the experimental points is caused by rather weak intensity of the large energy line which leads to poor experimental data fitting. Furthermore the deeper the penetration depth, the number of available reflections is decreasing since the small energy lines are no longer sensitive in this region. Narrowing the analyzed range of penetration depth to 0-15 μm shows the convergence of the results obtained from different methods in smaller depths. Moreover the synchrotron data perfectly agree with the results obtained on laboratory diffractometer (Cu K_α radiation) close to the surface. The results obtained for larger depth that 14 μm the experimental points exhibit significant spread and do not agree with the results of standard method.

Concluding, for the range of penetration depth 0-15 μm the results of different methods agree. Results obtained using with synchrotron radiation confirmed values of stresses measured close to surface using Cu K_α radiation. Moreover, it was shown, that the multireflection method, in which the experimental data are collected for the same depth in one plot, can be used for data obtained with white beam (EDDI).

7.4. CONCLUSIONS

Summarizing the results obtained with synchrotron radiation (MGIXD) it can be stated that using different wavelengths (energies) of radiation the same similar in-depth stress profiles were obtained. In addition the determined values of a_o and c/a vs. depth do not vary significantly with depth. For the first time also the multireflection method in which the data for the same penetration depth are selected was successfully used to analyze the EDDI data.

Perfect agreement was obtained between the measurements performed using synchrotron radiation as well as Cu K_α radiation on laboratory diffractometer (for MGIXD and also for EDDI methods). Certainly, synchrotron radiation with higher energies allowed measurements for larger depths in comparison with laboratory X-rays.

Synchrotron radiation (with better resolution) shows asymmetry of diffraction peak caused by stress gradient. If the asymmetry is small (polished Al2017) the analysis of this effect is difficult to analyze directly but inverse analysis, i.e. simulation of peak profile with stress gradient can be used as the confirmation of the stress measurements. It also happens that two regions exhibiting significant difference of microstructure can produce big asymmetry of the peak which can be fitted by two peaks. In this case the data can be separately treated for these regions.

The stress in-depth distribution vs. real depth z can be determined from stress profile measured as the function of information (or penetration) depth using inverse Laplace transform. In this work the limit of z for which the stress dependence is calculated was established using inverse analysis, i.e. comparing function $\sigma_{11}^{I}(z)$ integrated with the weight of intensity with experimental $\sigma_{11}^{I}(\bar{z})$. It should be also underline that it was not proven that the result of Laplace transform is unique. In the case of separated two peaks

corresponding to two regions in the sample, the thickness of the upper layer having different stress and microstructure can be determined analyzing contribution of intensities of these regions in the diffraction peak.

Finally the Wiliamson Hall analysis allowing determination of the root mean square strains $\sqrt{<\varepsilon^2>}$ and size of coherent domain *D* was used. It was found that the uncertainty of *D* is too large to obtain reasonable results when parallel geometry is used in MGIXD method. The values of $\sqrt{<\varepsilon^2>}$ measured using synchrotron and Cu K_α radiations agree very well. It should be stated that in the case of stress gradient, the $\sqrt{<\varepsilon^2>}$ value is influenced by third order stresses but also by the stress heterogeneity in the measured volume.

8. GENERAL CONCLUSIONS

The MGIXD (multireflection grazing incident X-ray diffraction) is one of the methods used for determination of in-depth stress distribution. Such measurement is possible due to small angle between incidence beam and sample surface, and consequently constant penetration depth of X-ray radiation in the studied material. The information depth can be changed by setting different angles of incidence. As it was presented in the thesis the MGIXD method has very important advantages in comparison with other diffraction methods of stress determination. The important feature of this method is that the lattice strains are measured in different crystallographic direction and next simultaneously used in analysis. This enables study of elastic anisotropy and choice of appropriate model of grains interaction for the interpretation of the experimental results. Furthermore not only stresses but also strain free a_0 and also c/a (for hexagonal structure) parameters and their in-depth variation can be determined. Finally in-depth evolution of the root mean square strain $\sqrt{<\varepsilon^2>}$ and crystallite size (coherent domain) can be studied using Williamson-Hall method. The main disadvantage of the MGIXD method is the requirement of perfect adjustment of the experimental setup. To obtain reasonable results the measurements must be performed using parallel beam configuration of the diffractometer.

In this work the MGIXD was developed and applied to measure in-depth stress distribution in coating and surface layers of the materials subjected to different mechanical treatments. The effect of physical and geometrical factors on the XSA was considered. The method of c/a parameter determination was proposed for hexagonal samples and the influence of stacking faults on the XSA was taken into account. Moreover in the thesis the mechanical properties of the polycrystals such as: elastic anisotropy of elastic constants and grain interactions were investigated. Different theoretical grain elasto-plastic interaction models were considered and applied in XSA. Finally, the MGIXD method was verified using synchrotron radiation and for the first time it was applied for EDDI experiment.

In the light of presented in thesis results, the following conclusions can be drawn:

- for the samples investigated in the thesis, the LPA correction did not influence significantly the results of XSA, even in the case of relatively broad diffraction peak. However this correction should be always applied when MGIXD is used beacause diffraction peaks having different 2θ positions are measured..
- The refraction can significantly influence the results of the MGIXD method. The new approach, presented in this thesis, takes into account the refraction effect as well as the accompanying wavelength change. It was shown that the effect of refractive index n<1 on the stress measurement strongly depends on value of the δ parameter (and thereby the type of material), wavelength, incident angle. The study of the literature indicates that also surface roughness can strongly affect the influence of refraction correction on XSA. This problem was not analysed in the thesis but study of the problem would be a valuable addition to the research.
- In the case of parallel beam geometry used for MGIXD method z-position imprecision does not significantly influence the obtained results, however special attention should be paid to adjust accurately the 2θ-zero position. Moreover, both statistical error and the misalignment error can be significantly reduced when the Göbel mirror is used in the primary optic of the diffractometer or synchrotron radiation is applied for measurements.

Secondly in the thesis following issues were developed:

- the method of *c/a* determination was proposed and tested for hexagonal samples with residual stresses (polished Ti - grade 2). It was shown that for the material having low elastic anisotropy the stresses, strain free parameter a_0 as well as *c/a* value can be determine using presented in this work self-consistent iteration method (the experimental values determined in the case of tensile as well compressive stresses were compared with those found in literature). Significantly better fitting of the theoretical values to experimental ones was obtained when *c/a* was adjusted.
- Probability of finding stacking fault ρ was determined for polished austenitic sample (alloy having low stacking fault energy). Reasonable values of ρ but with very large uncertainty were determined in the case compressive stress in the polished sample.

- The influence of XSF (X-ray stress factors) anisotropy on XSA was considered. Verification of the XSF was done by measuring lattice relative strains during 'in situ' tensile test. From the presented results it is evident that both experimental and calculated $<\varepsilon(\phi,\psi)>^{rel}_{\{hkl\}}$ vs. $sin^2\psi$ functions based on different *hkl* reflections exhibit nonlinearities in the case of elastically anisotropic samples (austenite stainless steel) but for elastically isotropic sample (titanium) this dependence is almost linear. Anisotropy of XSF was also observed on the $<a(\phi,\psi)>_{\{hkl\}}$ vs. $sin^2\psi$ plots obtained when the residual stresses were measured in ground Ni alloy, polished austenite stainless steel and CrN coating. The results presented in thesis, obtained using MGIXD and standard method, shows that Reuss and free surface grain interaction models are in the best agreement with the experimental results. Both models reflect in the best way the elastic anisotropy of the sample but the free surface model has a physical explanation in contrast to Reuss model.

Thirdly, in thesis the MGIXD method was verified using synchrotron radiation. In this aim two experiments were performed.

- In the first measurement performed at G3 spectrometer (DESY, Hamburg) three different wavelengths (energies) of radiation were used in MGIXD method. As the result:
  - almost the same in-depth stress profiles were obtained for all applied wavelengths.
  - The determined values of a_o and *c/a* vs. depth do not vary significantly with depth.
  - Due to its very good resolution of applied synchrotron radiation it was possible to observe the diffraction peak asymmetry caused by stress gradient.
  - The stress in-depth distribution vs. real depth *z* was determined from stress profile measured as the function of information (or penetration) depth using inverse Laplace transform. It should be underline that it was not proven that the result of Laplace transform is unique.
  - In the case of sample having strong diffraction peak asymmetry (polished Ti alloy) the separation of two peaks, corresponding to two regions in the

sample, was performed and the thickness of the upper layer having different stress and microstructure was determined analyzing contribution of intensities of these regions in the diffraction peak.

- The Wiliamson-Hall analysis showed that the uncertainty of *D* is too large to obtain reasonable results when parallel geometry is used in MGIXD method. The values of $\sqrt{<\varepsilon^2>}$ measured using synchrotron and Cu K_α radiations agree very well. It should be stated that in the case of stress gradient, the $\sqrt{<\varepsilon^2>}$ value is influenced by the third order stresses but also by the stress heterogeneity in the measured volume.

- For the first time also the proposed multireflection method (data selected for the same penetration depth) was successfully used to analyze the EDDI data. Very good agreement was obtained between the measurements performed using synchrotron radiation as well as Cu K_α radiation on the laboratory diffractometer (for MGIXD and also for EDDI methods). The great advantage of using high-energy synchrotron radiation was the possibility to measure stresses for larger depths in comparison with laboratory X-rays.

Concluding, it can be stated that MGIXD method is indispensable tool to study the distribution of stresses in the surface layers, but the applicability of this method is limited by factors such as refractive correction or interpretation problem associated with the anisotropy of elastic constants. On the basis of considered results, if MGIXD method is used, it is advised to perform the stress analysis with and without refraction correction and when the difference is significant the results should be rejected or accepted with so estimated large uncertainty. This is one of the limitations of MGIXD method which is significant for small incidence angle α. What is more, the special attention must be paid to accurate adjustment of the diffractometer (parallel beam configuration) and the 2θ - zero position must be carefully verified. It should be also underlined, that the reliable diffraction stress analysis is only possible when an appropriate grain interaction model is applied in calculation of XSF for anisotropic sample. On the bases of the results presented in this thesis it appears that free surface model is the one which not only correctly reflects the anisotropy of XSF well but also has a physical explanation concerning elastic interaction of the grains.

LIST OF PUBLICATIONS PUBLISHED BY AUTHOR

A1) Chwiej J., Janeczko K., Marciszko M., Czyżycki M., Rickers K., Setkowicz Z., *Neuroprotective action of FK-506 (tacrolimus) after seizures induced with pilocarpine: quantitative and topographic elemental analysis of brain tissue*, Journal of Biological Inorganic Chemistry; vol. 15, p. 283–289, 2010.

A2) Baczmański A., Marciszko M., Wierzbanowski K., Buturyn G., Bonarski J., Tarkowski L., *Application of Göbel mirror for stress measurement using grazing incidence geometry*, Materials Science Forum, vol. 652, p. 249–254, 2010.

A3) Marciszko M., Baczmański A., Zazi N., Chopart J., Lodini A., Wierzbanowski K., *Stress in aluminium alloys measured using Göbel mirror as a primary beam optics of X-ray diffractometer*, Materials Science Forum, vol. 681, p. 393-398, 2011.

A4) Marciszko M., Baczmański A., Wróbel M., Seiler W., Braham C., Donges J., Śniechowski M., Wierzbanowski K., *Application of multireflection grazing incidence method for stress measurements in polished Al–Mg alloy and CrN coating*, Applied Surface Science, vol. 226, p. 256-267, 2013.

A5) Marciszko M., Baczmański A., Wróbel M., Seiler W., Braham C., Donges J., Śniechowski M., Wierzbanowski K., *Multireflection grazing incidence diffraction used for stress measurements in surface layers*, Thin Solid Films, vol. 530 p. 81–84, 2013.

A6) Marciszko M., *Multireflection grazing incidence method for residual stress determination*, Proceedings of ISD Workshops, AGH University of Science and Technology, Kraków, 2013.

A7) Marciszko M., Stanisławczyk A., Baczmanski A., Wierzbanowski K., Seiler W., Braham C., Wróbel M., Szaraniec B., *In-depth distribution of stresses measured by multireflection grazing incidence diffraction*, Materials Science Forum – accepted for publication.

A8) Wroński S., Baczmanski A., Gaj A., Fitzpatrick M.E., Klosek V., Lodini A., Wierzbanowski K., Marciszko M., *Neutron diffraction study of elastoplastic behaviour of Al/SiCp metal matrix composite during tensile loading and unloading*, Materials Science Forum – accepted for publication.

REFERENCES

1. Hauk V., *Structural and Residual Stress Analysis by Nondestructive Methods*, Elsevier, Amsterdam, 1997.
2. Reimers W., Pyzalla A.R., Schreyer A., Clemens H., *Neutrons and Synchrotron Radiation in Engineering Materials Science*, WILEY-VCH Verlag GmbH & Co. KGaA, Weinheim, 2008.
3. Noyan I.C., Cohen J.B., *Residual Stress. Measurement by Diffraction and Interpretation*, New York, 1987.
4. Wagner C.N.J., Proc. Of Symp., *Local Atomic Arrangements studied by X-ray Diffraction*, Metall. Soc. Conferences, vol. 36, p. 219, 1966.
5. Darwin C.G., *The theory of X-ray reflection*, Phil. Mag., vol. 27, p. 315, 1914.
6. Cullity B.D., *Podstway Dyfrakcji Promieni Rentgenowskich*, Państwowe Wydawnictwo naukowe, Warszawa 1964.
7. Laue M., *Röntgenstrahlinterferenzen*, Akademische Verlagsgessellchaft, Frankfurt, 1960.
8. Bojarski Z., Łągiewka E., *Rentgenowska Analiza Strukturalna, Wydawnictwo Uniwersytetu Śląskiego*, Katowice 1995.
9. Rodriguez-Carvajal J., *An Introduction To The Program FullProf 2000*: http://www.ill.eu/sites/fullprof/php/tutorials.html (october 2011).
10. Kittel C., *Wstęp do Fizyki Ciała Stałego*, Państwowe Wydawnictwo Naukowe, Warszawa, 1976.
11. Warren B.E., Averbach B.L., *The effect of ColdWork Distortion on XRay Patterns*, J. Appl. Phys., vol. 21, p. 595, 1950.
12. Delhez R., Keijser Th.H., Mittemeijer E.J., *Accuracy of crystallite size and strain values from X-ray diffraction line profiles using Fourier series*, Proc. of Symp. on Accuracy in Powder Diffraction, N. B. S. Publ., Washington, vol. 567, p. 213, 1980.
13. Baczmański A., Braham C., Seiler W., *Microstresses in textured polycrystals studied by the multireflection diffraction method and self-consistent model*, Phil Mag., vol. 83, p. 3225, 2003.

14. Skrzypek S.J., Baczmański A., Ratuszek W., Kusior E., *New approach to stress analysis based on a grazing-incidence X-ray diffraction,* J. Appl. Cryst., vol.34, p.427, 2001.
15. Wertheim G.K, Butler M.A., West K.W., Buchmanan D.N.E., *Determination of the Gaussian and Lorentzian content of experimental line shape,* Rev. Sci. Instrum., vol. 45, p. 1369, 1974.
16. Young R.A., Wiles D.B., *Profile Shape Functions in Rietveld Refinements,* J. Appl. Cryst., vol. 15, p. 430, 1982.
17. Thompson P., Cox D.E., Hastings J.B., *Ritveld Refinement of Debye-Scherrer Synchrotron X-ray Data from Al2O3,* J. Appl. Cryst., vol. 20, p. 79, 1987.
18. Ghosh T.B., Sreemany M., *Application of Rachinger's method to separate overlapped doublets in the X-ray photoelectron spectrum,* Thin Solid Films, vol. 280, p.167, 1996.
19. Welzel U., Ligot J., Lamparter P., Vermeulen A.C., Mottemeijer E.J., *Stress analysis of polycrystalline thin film and surface regions by X-ray diffraction,* J. Appl. Cryst., vol.38, p. 1, 2005.
20. Baczmański A., *Stress fields in polycrystalline materials studied using diffraction and self-consistent modeling,* AGH, Kraków, 2005.
21. Bunge H.J., *Texture analysis in material science: Mathematical methods,* London: Butterworth, 1982.
22. Macherauch E., Müller P., *Das $\sin^2\psi$-Verfahren der röntgenographischen Spannungsmessung,* Z. Angew. Phys., vol. 13, p 305, 1961.
23. Möller H., Barbers J., *Röntgenographische Untersuchung über Spannungsverteilung und Ueberspannungen in Flußstahl,* vol 17, p. 157, 1935
24. Welzel U., Mittemeijer E.J., *Diffraction stress analysis of macroscopically elastically anisotropic specimens: On the concepts of diffraction elastic constants and stress factors,* J. Appl. Phys., vol. 93, p. 9001, 2003.
25. Press W.H., Teukolsky S.A., Vetterling W.T. Flannery B.P., *Numerical Recipes in C: The Art of Scientific Computing,* Second Edition, Cambridge University Press, 1992.

26. Cohen J.B., Hilliard J.E., *Local Atomic Arrangements studied by X-ray diffraction*, Metallurgical Society Conference, volume 36, 1965.
27. Bojarski Z., Bołd T., Instytut Metalurgii Żelaza, *Rentgenograficzne metody wyznaczania bloków metali polikrystalicznych*, Prace instytutow hutniczych, Zeszyt 1, Katowice,1970.
28. Ungar T., Gubicza J., Ribarik G., Borbely A., *Crystallite size distribution and dislocation structure determined by diffraction profile analysis: principles and practical application to cubic and hexagonal crystals*, J. Appl. Cryst., vol. 34, p. 298, 2001
29. Rachinger W.A., *A Correction for the α_1 α_2 Doublet in the Measurement of Widths of X-ray Diffraction Lines*, J.Sci.Instr., vol. 25, p. 254, 1948.
30. Klug H.P., Alexander L.E., *X-Ray Diffraction Procedures for Polycrystalline and Amorphous Materials*, New York, 1954
31. Stokes A.R., *A Numerical Fourier-analysis Method for the Correction of Widths and Shapes of Lines on X-ray Powder Photographs*, Proc. Phys. Soc., vol. 61, p. 382, 1948.
32. Hall W., *X-ray Line Broadening in Metals*, Proc.Phys.Soc. A, vol.62, p. 741, 1949.
33. Oleszak D., Olszyna A., *Określenie wielkości krystalitów I odkształeceń sieciowych w nanokompozycie NiAl-Al_2O_3 na podstawie poszerzenia rentgenowskich linii dyfrakcyjnych*, Composites, vol. 4, p.284, 2004.
34. Glockner R., Z. Techn. Phys., vol. 15, p. 421, 1934.
35. Bollenrath F., Hauk V., Osswald E., *Röntgenographische Spannungsmessungen bei überschreiten der Fließgrenze an Zugstäben aus unlegiertem Stahl*, VDI Z., vol. 83, p. 129, 1939.
36. Genzel Ch., *X-ray residual stress analysis in thin films under grazing incidence – basic aspects and applications*, Mat. Scienc. Tech., vol. 21, p. 10, 2005.
37. NIST Center for Neutron Research, The Residual Stress Measurement program at the NCNR: http://www.ncnr.nist.gov/instruments/darts/residual_stress.html (january 2013)
38. Genzel Ch, *Formalism for the evaluation of strongly non-linear surface stress fields by X-ray diffraction performed in the scattering vector mode*, Phys. Stat. Sol. (a), vol. 146, p. 629, 1994.

39. Genzel Ch., *Evaluation of Stress Gradients σij(z) from Their Discrete Laplace Transforms σij(τk) Obtained by X-ray Diffraction Performed in the Scattered Vector Mode*, Phys. Stat. Sol., vol. 156, p.353, 1996.

40. Behnken H., Hauk V., *Determination of steep stress gradients by X-ray diffraction results of joint investigation,* Material Science and Engineering A, vol. 300, p. 41, 2001.

41. Huang T.C., Predecki P.K., *Grazing-Incidence X-Ray Technique For Surface, Interface, And Thin-Film Analysis*, JCPDS-International Center for Diffraction Data, 1997.

42. Ch. Genzel, S. Krahmer, M. Klaus and I.A. Denks, *Energy-dispersive diffraction stress analysis under laboratory and synchrotron conditions: a comparative study*, J. Appl. Cryst., vol. 44, p. 1, 2011.

43. Genzel Ch., Stock C., Reimers W., *Application of energy-dispersive diffraction to the analysis of multiaxial residual stress fields in the intermediate zone between surface and volume,* Materials Science and Engineering A, vol. 372, p. 28, 2004.

44. Shiraiwa T., Sakamoto Y, *X-ray Stress Measurement and Its Application to Steel*, Sumito Serch., vol. 7, p.159, 1972.

45. Genzel Ch., Broda M., Dantz D., Reimers W., *A Self-Consistent Method for X-Ray Diffraction Analysis of Multiaxial Residual Stress Fields in the Near Surface Region of Polycrystalline Materials*, J. Appl.Cryst., vol. 32, p.779, 1999.

46. Genzel Ch., Denks J., Gibmeier J., Klaus M., Wagener G., *The materials science synchrotron beamline EDDI for energy-dispersive diffraction analysis*, Nuclear Instruments and Methods in Physics Research A, vol. 578, p. 23, 2007.

47. S.J. Skrzypek, A. Baczmanski, *Progress in X-ray Diffraction of Residual Macro-Stresses Determination Related to Surface Layer gradients and Anisotropy,* Adv. X-ray Anal., vol. 44, p. 134, 2001.

48. Baczmański A., Braham C., Seiler W., Shiraki N., *Multi-reflection metod and grazing incidence geometry used for stress measurement by X-ray diffraction*, Surface and Coating Technology, vol. 182, p. 43, 2004.

49. Wroński S., Wierzbanowski K., Baczmański A., Lodini A., Braham C., Seiler W., *X-ray grazing incidence technique – corrections in residual stress measurements – a reviw*, Powder Diffraction Suppl. 24, p.S11, 2009.

50. van Acker K., de Buyser L., Celis J.P., van Houtte P., *Characterization of thin nickel electrocoatings by the low-incident-beam-angle diffraction method*, J. Appl. Cryst., vol. 27, p. 56, 1994.
51. Quaeyhaegens C., Knuyt G., Stals L.M., Study of the residual macroscopic stress in TiN coatings deposied on various steel types (TuSA1), Surf. Coat. Technol., vol. 74/75, p. 104, 1996.
52. Predecki P., Zhu X., Ballard B., *Proposed methods for depth profiling of residual stresses using grazing incidence X-ray diffraction*, Adv. In X-ray Analysis, vol. 36, p. 237, 1993.
53. Kumar A., Welzel U., Mittemeijer E.J., *A method for the non-destructive analysis of gradients of mechanical stresses by X-ray diffraction measurements at fixed penetration/information depths*, J. Appl. Cryst., vol. 39, p. 633, 2006.
54. Erbachen T., Wanner A., Beck T., Vohringer O., *X-ray diffraction at constant penetration depth- a viable approach for characterizing steep residual stress gradients*, J. Appl.Cryst., vol. 41, p. 317, 2008.
55. Marciszko M., Baczmański A., Wróbel M., Seiler W., Braham C., Donges J., Śniechowski M., Wierzbanowski K., *Multireflection grazing incidence diffraction used for stress measurements in surface layers*, Thin Solid Films vol. 530, p.81, 2013.
56. Williamson G.K., Hall W.H., *X-ray line broadening from filed Al and W*, Acta Metallurgica, vol. 1, p. 22, 1953.
57. Mittemeijer E.J., Scardi P., *Diffraction Analysis of the Microstructure of Materials*, Springer Series in Materials Science, vol. 68, Heidelberg, 2004.
58. Peng J., *Determination des contraintes residueles dans des revetements par diffraction des rayons en faible incidence*, PhD thesis, L'école Nationale Supérieure D'Arts et Métiers, 2006.
59. Chihi T., Boucetta S., Maouche D., Behaviour of Di-Transition-Metal Nitride $Ti_{1-x}Zr_xN$ Alloy at high Pressure, Acta Physica Polonica A, vol. 116, p. 1085, 2009.
60. Fares M., Debili M.Y., *Structural Characterization of Nanostructured Nickiel Coated Carbon Fibers by X-Ray Line Broadening*, e-J. Surf. Sci. Nanotech., vol.6, p.258, 2008.

61. Collings E. W., *Materials properties Handbook, Titanium Alloys*, ASM International, 1994,
62. Birkholz M., *Thin Film Analysis by X-ray Scattering*, WILEY-VCH Verlag GmbH&Co. KGaA, Weinheim, 2006
63. Ceratti M., *Ph.D. Thesis*, Universite de Reims Champagne-Ardenne, France, 1993.
64. Simoms G., Wang H., *Single Crystal Elastic Constants and Calculated Aggregate Properties: A handbook*, second edition, The M.I.T. Press, Cambridge, Massachusetts and London, 1971.
65. Wolfram Demonstrations Project: http://demonstrations.wolfram.com (june 2011)
66. Inal K., Gergaud P., Francois M., Lebrun, J.-L., *X-ray diffraction methodologies of macro and pseudo-macro stress analysis in a textured duplex stainless steel*, J. of Scand. Metall., vol. 28, p. 139, 1999.
67. Fréour S., Gloaguen D., François M., Perronnet A., Guillén R., *Determination of single-crystal elasticity constants in a cubic phase within a multiphase alloy: X-ray diffraction measurements and inverse-scale transition modelling*, J. Appl. Cryst., vol 38, p. 30, 2005.
68. Voigt W., *Lehrbuch der Kristallphysik*, Leipzig, BG Teubner Verlag, 1928.
69. Reuss A., *Berechnung der Fließgrenze von Mischkristallen auf Grund der Plastizitätsbedingung für Einkristalle*, Z. Angew. Math. Mech., vol. 9, p. 49, 1929.
70. Kröner, E., *On the plastic deformation of polycrystals*, Acta Metall., vol. 9, p. 155, 1961.
71. Baczmański, A., Wierzbanowski, K., Tarasiuk, J., Lodini, A., *Determination of Residual Stresses by Diffraction Method in Anisotropic Materials*, Arch. Metall., vol. 42, p. 173, 1997.
72. Baczmański A., Skrzypek S.J., Braham C., Seiler W., *Wierzbanowski K.,Self-Consistent Diffraction Elastic Constants in Residual Stress Measurement with Grazing Incident Angle Geometry*, Arch. Metall., vol. 48, p. 137, 2003.
73. Brakman C.M., *The Voigt model case*, Phil. Mag. A, vol. 55, p. 39, 1987.
74. Bunge H.J., *Texture Analysis in Material Science: Mathematical Methods*., Butterworths&Co., London,. 1982.

75. Barral M., Lebrum J.L., Sprauel J.M., Maeder G., *X-ray macrostress determination on textured materials; use of the ODF for calculating the X-ray compliances*, Met. Trans. A, vol. 18A, p. 1229, 1987.
76. Eshelby J.D., *The determination of the elastic field of an ellipsoidal inclusion and related problems*, Proc. Roy. Soc., vol. A241, p. 376, 1957.
77. Kröner E., *Berechnung der elastischen Konstanten des Vielkristalls aus den Konstanten des Einkristalls*., Z. Phys., vol. 151, p.504, 1958.
78. Kneer G., *Über die Berechnung der Elastizitätsmoduln vielkristalliner Aggregate mit Textur*, Phys. Status Solidi B, vol. 9, p. 825, 1965.
79. Bollenrath F., Hauk V., Müller, *Zur Berechnung der Vielkristallinen Elastizitätskonstanten aus den Werten der Einkristalle*, Z. Metallkunde, vol. 58, p. 76, 1967.
80. Skrzypek S.J., *Nowe możliwości pomiaru makronaprężeń własnych materiałów przy zastosowaniu dyfrakcji promieniowania X w geometrii stałego kąta padania*, Uczelniane Wydawnictwo Naukowo-Dydaktyczne, Kraków, 2002.
81. François M., Ferreira C., Botzon R., *Reference specimens for x-ray stress analysis : the French experience*, Metrologia, vol. 41, p. 33, 2004.
82. François M., Ferreira C., Guillén R., *Approximate analytical formulae to evaluate the uncertainty in X-ray stress analysis*, Mat. Sci. Forum, vols. 490-491, p. 124, 2005.
83. Henke B.L., Gullikson E.M., Davis J.C., *X-ray interactions: photoabsorption, scattering, transmission, and reflection at E=50-30000 eV, Z=1-92*, Atomic Data and Nuclear Data Tables 54 no.2, p.181, 1993.
84. Hubbell J.H., Veigele W.J., Briggs E.A., Brown R.T., Cromer D.T., Howerton R.J., *Atomic Form Factors, Incoherent Scattering Functions and Photon Scattering Cross Sections*, J. Phys. Chem. Ref. Data 4, p. 471, 1975; erratum in 6, p. 615, 1977.
85. Hart M., Bellotto M., Lim G.S., *The refractive index correction in powder diffraction*., Acta Cryst., vol. A44m, p.193, 1988.
86. Lawrence Berkeley National Laboratory's Center for X-Ray Optics: http://www.cxro.lbl.gov/ (march 2013)

87. Ely T., Predecki P.K., Zhu X., Eatough M., Goehner R., Lucernoni R., *Measurement of the Refraction Correction for Asymmetric Grazing Incidence Xrd from Rough Surfaces and Powders*, Advences in X-ray Analysis vol. 39, p 381, 1998.
88. Ott M.H, Löhe D., *The influence of surface roughness on the refraction of X-rays and its effect on Bragg peak positions*, Advances in X-ray Analysis, vol. 46, p 232, 2003.
89. Holtz T., Dietsch R., Mai H., Brügemann L., *Application of Ni/C Göbel Mirrors*, Materials Science Forum, vols. 321-324, p. 179, 2000.
90. Gross M., Haaga S., Fietzek H., Herrmann M., Engel W., *Measurements in parallel – beam Geometry Achieved by a Göbel Mirror at Laboratory Source*, Materials Science Forum, vols. 278-281, p. 242, 1998.
91. Göbel H.E., *A new flat Goebel-mirror for the optimization of the primary beam in Bragg-Brentano diffraction geometry*, Microstructure Analysis in Material Science, p.15, 2005
92. Baczmański A., Marciszko M., Wierzbanowski K., Buturyn G., Bonarski J., Tarkowski L., *Application of Göbel Mirror for Stress Measurement Using Grazing Incidence Geometry*, Mater. Sci. Forum, vol. 652, p.249, 2010.
93. R. M. Wood, *The Lattice Constants of High Purity Alpha Titanium*, Proc. Phys. Soc., vol. 80, p.783, 1962.
94. Lutjering G., Williams J.C., *Titanium Alloys*, Springer, Heidelberg, 2003.
95. Wagner C.N.J., *Stacking faults by low temperature cold work in cooper and alpha brass*, Acta Metall., vol. 5, p. 427, 1957.
96. Paterson M.S., *X-ray diffraction by face-centered cubic crystals with deformation faults*, J.Appl.Phys., vol. 23., p.805, 1952.
97. Warren B.E, Warekois E.P., *Stacking faults in cold worked alpha-brass*, Acta Met., vol. 3, p. 473, 1955.
98. Velterop L., Delhez R., de Keijser Th.H., Mittemeijer E.J., Reefman D., *X-ray diffraction analysis of stacking and twin faults in fcc metals: a revision and allowance for texture and non-uniform fault probabilities*, J. Appl. Cryst., vol. 33, p.296, 2000.
99. Jegou S., Christiansen T.L., Klaus M., Genzel Ch., Somers M.A.J., *Determination of composition, residual stress and stacking fault depth profiles in expanded austenite with energy-dispersive diffraction*, Thin Solid Films, vol. 530, p. 71, 2013.

100. Baczmanski A., Lipinski P., Tidu A., Wierzbanowski K., Pathiraj B., *Quantitative estimation of incompatibility stresses and elastic energy stored in ferritic steel*, J. Appl. Cryst, vol. 41, p.854, 2008.

101. Bonarski J., Smolik J., Tarkowski L., Biel M., *Depth-profile of residual stresses in metallic/ceramic coatings*, Arch. Met. & Mat., vol. 53, p. 49, 2008.

102. Marciszko M., Baczmański A., Wierzbanowski K., Wróbel M., Braham C., Chopart J.-P., Lodini A., Bonarski J., Tarkowski L., Zazi N., *Application of multireflection grazing incidence method for stress measurements in polished Al.-Mg alloy and CrN coating*, Applied Surface Science, vol. 266, p.256, 2013.

103. Gall D., Shin C.S., Spila T., Oden M., Senna M.J.H, Greene J.E., Petrov I., *Growth of single-crystal CrN on MgO(001): Effects of low-energy ion-irradiation on surface morphological evolution and physical properties*, J. Appl. Phys., vol. 91, p. 3589, 2002.

104. Buijnsters J.G., Shankar P., Fleischer W., van Enckevort W.J.P., Schermer J.J., Meulen J.J., *CVD diamond deposition on steel using arc-plated chromium nitride interlayers*, Diamond Relat. Mater., vol. 11, p. 536, 2002.

105. Martinschitz K.J.,. Daniel R, Mitterer C., Keckes J., *Stress evolution in CrN/Cr coating systems during thermal straining*, Thin Solid Films, vol. 516 , p. 1972, 2008.

106. Peng R.L., Wang Y.D.,. Odén M, Almer J., *Residual Stress Analysis in both As-deposited and Annealed CrN Coatings*, Materials Science Forum, vols. 490–491, p. 643, 2005.

107. Bernier J.V., Park J.S., Pilchak A.L., Glavicic M.G., Miller M.P., *Measuring Stress Distribution in Ti-6Al-4V Using Synchrotron X-ray Diffraction*, Metallurgical and Materials Transactions A, vol.39A, p.3120-3133, 2008.

Ètude par diffraction des propriétés mécaniques et des contraintes résiduelles résultant de la transformation de matériaux polycristallins

RESUME : Les contraintes résiduelles sont les contraintes qui subsistent après l'élimination de la cause originelle des contraintes (forces externes, gradient thermique). L'ampleur et la répartition spatiale des contraintes résiduelles jouent un rôle primordial dans le comportement de la matière. Par conséquent, les méthodes expérimentales fiables pour la détermination des contraintes résiduelles sont d'une grande importance. Parmi les méthodes de détermination de ces contraintes, les techniques de diffraction détiennent une place spéciale. Leur spécificité la plus marquante est qu'elles sont non destructives et permettent de séparer les micro et macro contraintes résiduelles et d'étudier la répartition des contraintes dans l'échantillon.

Dans la première partie de cette thèse (chapitres 1-3), les méthodes de détermination des contraintes de diffraction sont introduites. Les principes de la distorsion du réseau, la taille des cristallites, l'analyse des contraintes en fonction du profil de pic de diffraction ainsi que la déformation du réseau mesurée sont décrits dans le chapitre 2. Ensuite, le chapitre 3 est consacré à une courte caractérisation de différentes méthodes pour la détermination des contraintes résiduelles en utilisant des rayons X (classique et synchrotron). Les méthodes expérimentales sont divisées en deux groupes, à savoir : le groupe, dans lequel la profondeur de pénétration des rayons X est constante ou deuxième pour lequel la pénétration varie au cours de la mesure. Sur la base des trois premiers chapitres, des objectifs de la thèse sont précisés dans le chapitre 4.

Les chapitres 5 - 7 présentent les résultats originaux de ce travail, en matière de développement et de test de la méthode de multireflection en incidence rasante (MGIXD) pour détermination des contraintes résiduelles sont présentés. Tout d'abord, les corrections les plus importantes des données expérimentales et des essais de dispositifs expérimentaux sont décrits (chapitre 5).

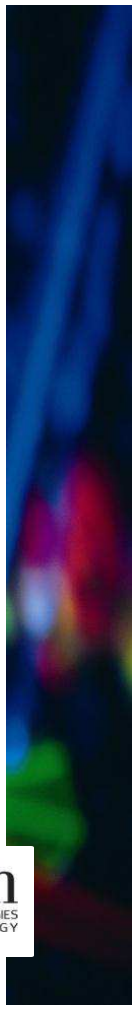

ARTS ET MÉTIERS ParisTech

ParisTech INSTITUT DES SCIENCES ET TECHNOLOGIES PARIS INSTITUTE OF TECHNOLOGY

Le chapitre 6 présente deux développements théoriques importants de la méthode MGIXD. Le premier, qui permet la détermination du paramètre c/a et qui améliore de manière significative la qualité de l'analyse des données expérimentales pour la structure hexagonale a été proposé et testé. Le second, dans lequel la densité des défauts d'empilement est prise en compte est appliqué. Qui plus est, une vérification de différents types des facteurs de contraintes (XSF) qui peuvent être appliquées pour interpréter les données expérimentales obtenues à l'aide du procédé MGIXD, est présentée. À la fin, le chapitre illustre des exemples de détermination des contraintes dans la couche de surface pour des matériaux ayant une haute et basse anisotropie des constantes élastiques monocristallines.

Dans le chapitre 7 la méthodologie de l'interprétation des données est développée afin de traiter les données obtenues non seulement pour différents angles d'incidence, mais aussi simultanément en utilisant différentes longueurs d'onde. Il est démontré que la nouvelle méthode élaborée est d'une part « multi-réflexion », et d'autre part « multi- longueur d'onde ». En outre, l'application de différentes longueurs d'ondes permet la vérification des mesures de MGIXD.

Le chapitre 8 rassemble tous les résultats présentés dans la thèse et formule des recommandations pratiques pour les utilisateurs de la méthode MGIXD.

Pour analyser les contraintes de premières ordre67, les déformation moyenne du réseau doit être déterminée à partir des changements de la position du pic de diffraction. C'est pour cela que la position exacte du pic de diffraction doit être déterminée avec une grande précision [1].

Il convient de préciser qu'avec l'utilisation des méthodes de diffraction, la déformation du réseau n'est pas mesurée directement mais, en fait, les distances interréticulaires $< d(\phi,\psi) >_{\{hkl\}}$ sont déterminées à partir de la position des pics de diffraction. Ces positions sont mesurées pour différentes orientations du vecteur de diffusion par rapport à l'échantillon, défini par les angles φ et ψ (Fig. 1).

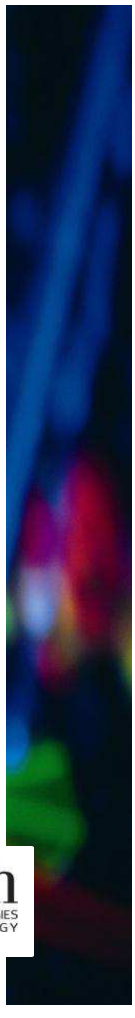

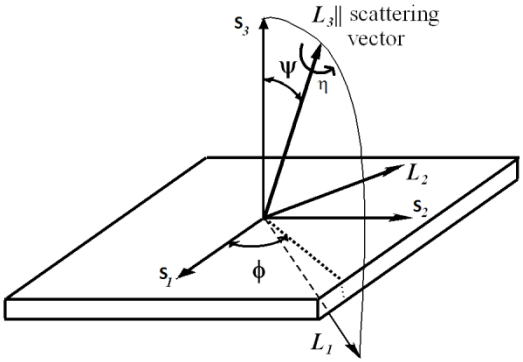

Fig.1. Orientation du vecteur de diffusion en ce qui concerne le système de l'échantillon S. Les angles ψ et ϕ définissent l'orientation du système de L (L_2 de l'axe est dans le plan de la surface de l'échantillon). En outre, η - rotation du système de L autour de vecteur de diffusion est affichée.

Après la transformation simple les distances interréticulaires peuvent être exprimées par les macrostresses σ_{ij}^I et $d_{\{hkl\}}^0$ - espacement réticulaire sans stress [1, 2, 3]:

$$< d(\phi,\psi) >_{\{hkl\}} = [\ F_{ij}\ (hkl,\phi,\psi,\ f)\,\sigma_{ij}^I\ ]\ d_{\{hkl\}}^0 + d_{\{hkl\}}^0 \qquad (1)$$

où F_{ij}(hkl,ϕ,ψ) sont XSF et dans le cas d'un matériau quasi-isotrope :

$$< d(\psi,\phi) >_{\{hkl\}} = \left[\begin{array}{l} \frac{1}{2} S_2^{hkl} \left\{ (\sigma_{11}^I - \sigma_{33}^I)\cos^2\phi + \sigma_{12}^I \sin 2\phi + (\sigma_{22}^I - \sigma_{33}^I) \right\} \sin^2\psi + \\ + S_1^{hkl} (\sigma_{11}^I + \sigma_{22}^I + \sigma_{33}^I) + \frac{1}{2} S_2^{hkl} \left(\sigma_{13}^I \cos\phi + \sigma_{23}^I \sin\phi \right) \sin 2\psi \end{array} \right] d_{hkl}^0 + d_{hkl}^0 \qquad (2)$$

Le calcul des contraintes en utilisant les équations affichées ci-dessus peut être effectué grâce à la méthode des moindres carrés et à l'ajustement des composantes de tenseur de contraintes ainsi que de $d_{\{hkl\}}^0$. Toutefois, l'ensemble du tenseur des contraintes (des contraintes principales) ne peut être calculé que si $d_{\{hkl\}}^0$ (sans stress paramètre) est connu. Heureusement, dans le cas de diffraction des rayons X pénétrant la mince couche de surface (grâce à une absorption élevée), nous pouvons supposer que les forces normales à la surface sont égales à zéro et de même σ_{33}^I = 0. Puisque l'une des contraintes

principales est connue, $d^{0}_{\{hkl\}}$ peut être ajusté et sa valeur peut également être déterminée.

La procédure des moindres carrés utilisée dans ce travail est basée sur la minimisation de la fonction de mérite appelée χ^2 qui est définie comme [4]:

$$\chi^2 = \frac{1}{N-M}\sum_{n=1}^{N}\left(\frac{< d(\phi_n,\psi_n) >^{exp}_{\{hkl\}} - < d(\phi_n,\psi_n >^{cal}_{\{hkl\}}}{\delta_n}\right)^2 \quad (3)$$

où : $< d(\phi_n,\psi_n) >^{exp}_{\{hkl\}}$ et $< d(\phi_n,\psi_n) >^{cal}_{\{hkl\}}$ sont les expérimentaux et la distance interréticulaire $\delta_n=\delta_n(< d(\phi_n,\psi_n) >^{exp}_{\{hkl\}})$ est l'erreur de mesure (écart-type) de la distance déterminée pour la mesure de la n-ième, N et M sont respectivement le nombre de points de mesure et des paramètres d'ajustement.

La valeur de χ^2 est une mesure de la qualité de l'ajustement, c'est à dire:

• $\chi^2 = 1$, signifie que le « bon choix » a été obtenu (il correspond à l'ajustement exactement dans les limites de l'incertitude expérimentale),

• $\chi^2 < 1$, les incertitudes de données expérimentales ($< d(\phi_n,\psi_n) >^{exp}_{\{hkl\}}$) sont surestimées ,

• $\chi^2 > 1$, les incertitudes de données expérimentales sont sous-estimées ou des valeurs $< d(\phi_n,\psi_n) >^{cal}_{\{hkl\}}$ (théoriques) calculées en fonction des facteurs $F_{ij}(hkl,\varphi,\psi)$ ne sont pas assez précises.

La présente thèse porte aussi sur, la méthodologie de mesures des contraintes en fonction de l'incidence d'un faisceau rasant de rayons X, à savoir: la méthode de multiréflection en incidence rasante (MGIXD) qui a été étudiée et développée. Cette technique est caractérisée par un angle d'incidence α faible et constant et par des orientations différentes du vecteur de diffusion (Fig. 2) [5-9].

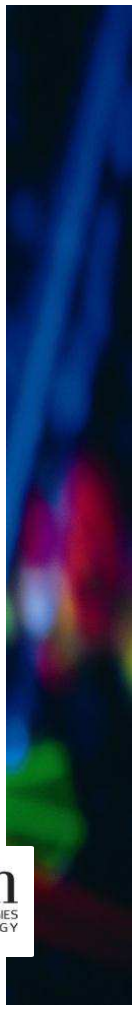

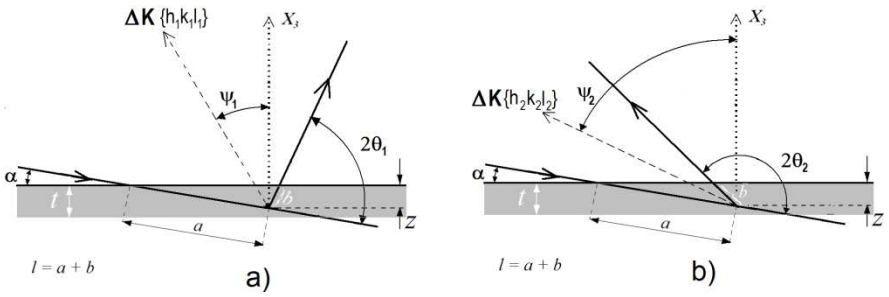

Fig.2. Géométrie de la méthode MGIXD-sin^{2}ψ. L'angle d'incidence α est fixé lors de la mesure alors que l'orientation du vecteur de diffusion est caractérisée par l'angle $\psi_{\{hkl\}}$.

Dans cette géométrie, le plan de diffraction est toujours perpendiculaire à la surface de l'échantillon. Le grand avantage de la méthode MGIXD (en comparaison avec les méthodes classiques) est que la profondeur de pénétration ne change pas pendant la mesure pour un angle d'incidence donné (α) (Fig. 3). En plus, la profondeur de pénétration peut être modifiée par un choix approprié de l'angle α, pour étudier les matériaux à différentes profondeurs en sous-couches de l'échantillon. Cela donne la possibilité de mesurer un gradient de contraintes dans les échantillons.

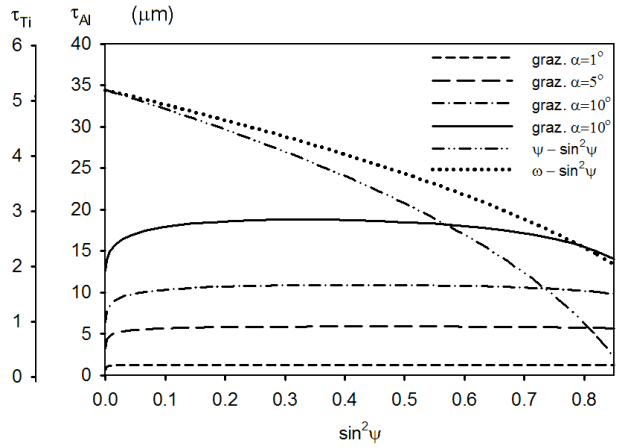

Fig. 3. La profondeur de pénétration (τ) vs sin^{2}ψ pour les géométries ψ et ω classique (montrée pour 2θ correspondant à 422 réflexions dans le cas d'Al) et pour la méthode MGIXD-sin2ψ (représentée pour quatre angles d'incidence). Deux échelles de τ correspondant à Al et Ti sont présentées.

Analogiquement à la méthode standard, des contraintes résiduelles peuvent être déterminées à partir des distances inter-réticulaires mesurées dans la direction du vecteur de diffusion, c'est-à-dire à condition que les angles soient différents $\psi_{\{hkl\}}$, $\theta_{\{hkl\}}$ et que d'un angle α soit constant. Toutefois, dans le cas de la méthode multi- réflexion, au lieu de $< d(\phi,\psi,\bar{z})>_{\{hkl\}}$, les paramètres équivalents de maille sont exprimés par macrostresses et constante a_0 pour les treillis libre de souche [9]:

$$< a(\phi,\psi,\bar{z})>_{\{hkl\}} = [\, F_{ij}\,(hkl,\phi,\psi)\,\sigma_{ij}^{I}(\bar{z})\,]\,a_0 + a_0 \qquad (4)$$

où :

pour la structure cristalline cubique:

$$< a(\phi,\psi,\bar{z})>_{\{hkl\}} = < d(\phi,\psi,\bar{z})>_{\{hkl\}} \sqrt{h^2+k^2+l^2} \qquad (4a)$$

pour la structure hexagonale :

$$< a(\phi,\psi,\bar{z})>_{\{hkl\}} = < d(\phi,\psi,\bar{z})>_{\{hkl\}} \left\{ \left[\frac{4}{3}(h^2+hk+k^2) \right] + \frac{l^2}{(c/a)^2} \right\}^{-1/2} \qquad (4b).$$

Dans le cas du procédé MGIXD, les mesures de distances inter-réticulaires sont effectuées dans le volume près de la surface, qui est limité par l'absorption du rayonnement. Pour définir ce volume, le trajet du faisceau de rayons X à travers l'échantillon doit être considéré. Les espacements interplanaires moyenes mesurés $< d(\phi,\psi,\tau)>_{\{hkl\}}$ égalent à:

$$< d(\phi,\psi,\bar{z})>_{\{hkl\}} = \frac{\int_0^t d(hkl,\phi,\psi,z)\exp[-\mu\, l(z)]\,dz}{\int_0^t \exp[-\mu\, l(z)]dz} \text{ et } l(z) = z\left(\frac{1}{\sin\alpha} + \frac{1}{\sin(2\theta_{\{hkl\}}-\alpha)} \right) \qquad (5)$$

où la formule ci-dessus peut être utilisée si une $\alpha >> \alpha_{cr}$ (α_{cr} est un angle critique de réflexion totale externe), z est la profondeur au-dessous de la surface et la moyenne est calculée par rapport au volume de tous les grains qui reflètent dans la trajectoire du faisceau, c'est-à-direà partir de la surface (z = 0) de l'épaisseur du revêtement (z = t). Si les contraintes sont mesurées dans un échantillon monolithique ou dans un revêtement d'épaisseur $t \to \infty$.

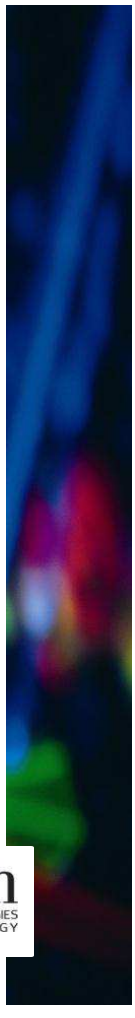

Le principal inconvénient de la méthode MGIXD est la résolution. La position du pic doit être déterminée avec précision. C'est pourquoi la géométrie du faisceau parallèle a été appliquée pour la détermination des contraintes. Le faisceau incident, sur diffractomètres classiques, a été collimaté par le miroir Göbel et les tests en configuration parallèle ont été réalisés pour la poudre d'aluminium. Les résultats présentés dans la thèse confirment que les erreurs statistiques et l'erreur d'alignement peuvent être considérablement réduites lorsque le miroir Göbel est utilisé dans l'optique primaire du diffractomètre (Tableau 1).

Tableau 1. Composante de contrainte résiduelle déterminée pour la poudre Al utilisant deux optiques de faisceau d'incidence : miroir Göbel ou fente (contraintes calculées excluant 111 et 200 réflexions comparées avec les résultats obtenus à partir de toutes les réflexions).

method	α (°) or *hkl*	$\bar{z}$ (μm)	primary beam config.	σ_{11}(MPa) all reflections	reflections 111, 200 excluded		
					σ_{11} (MPa)	a_0 (Å)	χ^2
MGIXD	α=5°	5.8	Göbel mirror	-5.0 ± 3.0	-1.6 ± 1.5	4.04936 ± 0.00003	0.05
			Slit	-22.1 ± 5.3	-16.0 ± 5.3	4.04973 ± 0.00009	0.55
	α=10°	10.8	Göbel mirror	-3.1 ± 3.2	-0.4 ± 1.1	4.04948 ± 0.00002	0.02
			Slit	-28.1 ± 6.4	-33.3 ± 5.6	4.04995 ± 0.00008	0.64
	α=15°	14.9	Göbel mirror	-3.0 ± 4.4	0.4 ± 3.8	4.04945 ± 0.00006	0.29
			Slit	-7.3 ± 6.1	-8.6 ± 7.3	4.04914 ± 0.00011	1.07
Standard	422	12-34	Göbel mirror	-2.1 ± 0.5		4.04946 ± 0.00001	0.65
			Slit	-0.5 ± 1.4		4.04903 ± 0.00004	3.08

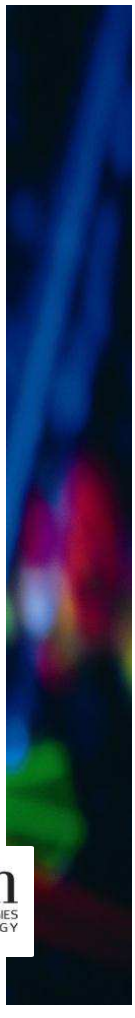

Dans le cas de la géométrie du faisceau parallèle utilisé pour la méthode MGIXD, les imprécisions sur la position z n'influencent pas de manière significative les résultats obtenus avec la méthode d'analyse par diffraction des rayons X (DRX). Afin de déterminer avec précision la position du pic de diffraction, des facteurs physiques doivent être pris en compte [1,2,3] : Lorentz-polarisation et le facteur d'absorption ainsi que la correction de réfraction. À la lumière des résultats présentés, l'influence de la correction LPA est généralement négligeable dans la méthode MGIXD (Tableau 2).

Tableau 2. Les contraintes (σ) et des constantes de réseau (a0) déterminées pour rectifié Al2017 et polies Ti grade 2 échantillons à partir des données expérimentales avec et sans correction LPA.

	calcul sans correction LPA	calcul avec correction LPA	différence
	rectifié Al 2017 (cubic)		
σ_{11}(MPa)	204.2 ± 4.8	206.9 ± 5.7	2.7
σ_{22}(MPa)	126.4 ± 4.8	129.4 ± 5.7	3.0
a_0 (Å)	4.04697 ± 0.00008	4.04698 ± 0.00010	0.00001
	poli Ti grade 2 (hexagonal)		
σ_{11}(MPa)	-411±11	-405.4 ±12.2	5.6
σ_{22}(MPa)	-405±11	-397.7 ±12.1	7.3
a_0 (Å)	2.9506 ±0.0001	2.9506 ± 0.0001	-
c/a	1.5881 ± 0.0003	1.5881 ± 0.0003	-

La réfraction des rayons X entre deux milieux différents peut influencer de manière significative la position du pic de diffraction. La déviation de la direction des vagues décrite par la loi de Snell-Descartes, provoque un changement dans la valeur de l'angle de diffraction Δ2θ et en plus une petite inclinaison Δψ de l'orientation du vecteur de diffusion. Jusqu'à présent, les seules solutions pour une correction de réfraction sont données dans le cas d'une surface lisse. Dans la thèse, la variation de l'angle de diffraction due à l'indice de réfraction n <1 est considérée, et la question de la correction de la réfraction a été examinée et comparée à des considérations présentées dans la littérature (par Hart et par Genzel) [10, 11]. Suite à la confrontation de «

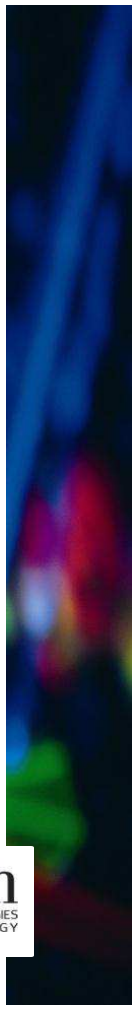

nouvelle formule » développée dans la thèse avec les approches proposées par Genzel et Hart (Fig. 4), on peut conclure que pour les grands angles d'incidence la «nouvelle approche» est conforme à celle proposée par Hart, mais elle en diffère par rapport à Genzel où l'effet de changement de longueur d'onde dans la réfraction a été négligé). Pour les petits angles d'incidence l'approche de la Genzel et celle proposée dans la thèse sont conformes, mais la formule de la Hart ne reflète pas correctement l'effet. Elle est causée par l'approximation imprécise pour les petits angles d'incidence.

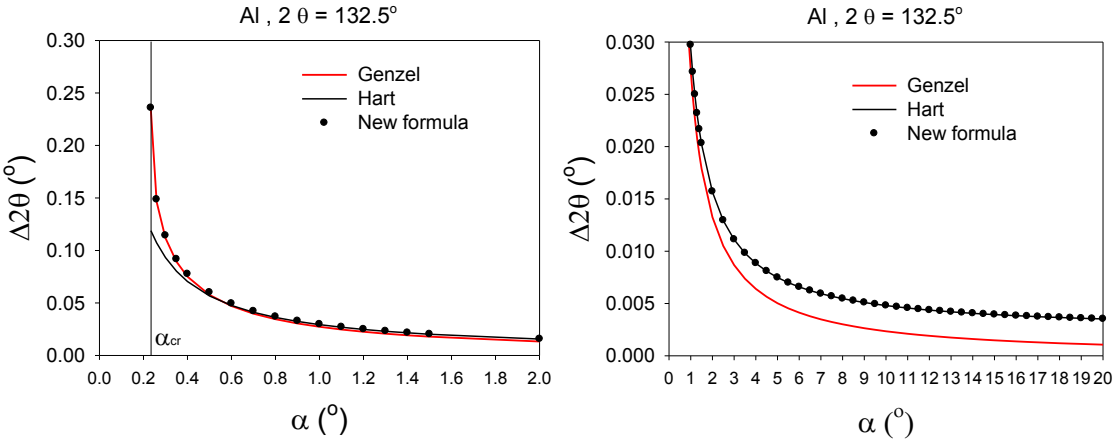

Fig. 4. Changement de la position du pic causé par la réfraction comparé pour Genzel, Hart approches et «Nouvelle formule» (α_{cr}=0.24°, Al échantillon et le rayonnement Cu).

L'effet de l'indice de réfraction n <1 sur la mesure de contrainte dépend fortement du type de matériau, la longueur d'onde, de l'angle d'incidence et de la rugosité de surface. Sur la base des résultats considérés, si la méthode MGIXD est utilisée, il est conseillé d'effectuer l'analyse des contraintes avec et sans correction de la réfraction et lorsque la différence entre les résultats obtenus est importante pour le paramètre désigné, les résultats doivent être rejetés. Cet effet est la limitation de la méthode MGIXD. Par conséquent, l'interprétation des résultats expérimentaux effectués avec la correction pour surface plane et sans correction fixe des limites pour les valeurs des contraintes et pour le paramètre a_0 dans l'échantillon étudié. Ces calculs doivent être toujours comparés afin de voir la gamme de l'angle d'incidence pour lequel la correction n'est pas significative (comme pour les échantillons présentés dans la figure 5).

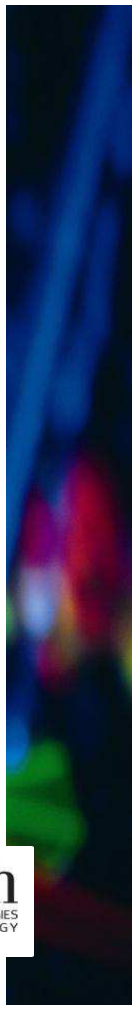

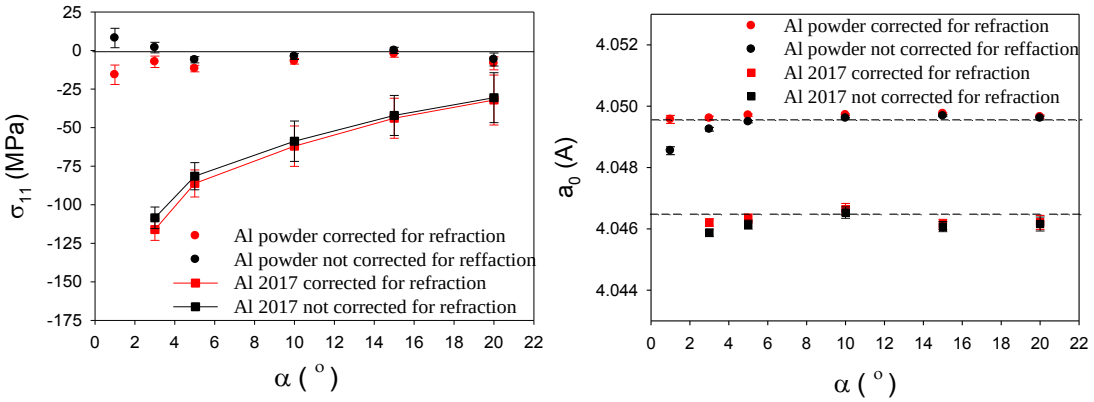

Fig. 5. Contrainte résiduelle et le paramètre a_o en fonction de l'angle α d'incidence déterminé avec et sans correction de la réfraction. La méthode MGIXD a été appliquée pour un alliage d'aluminium polie mécaniquement (Al 2017) et pour la poudre d'Al (Cu Ka rayonnement X-ray).

Dans ce travail, deux développements théoriques de la méthode MGIXD ont été présentés. Tout d'abord la procédure de détermination du paramètre de maille c/a a été proposée, ce qui améliore considérablement la qualité de l'analyse des données expérimentales dans le cas des échantillons de structure hexagonale. La méthode de détermination de ce paramètre a été testée sur un échantillon de Ti poli (grade 2) montrant une faible anisotropie élastique des contraintes. Le paramètre a_0 ainsi que c/a, peut être déterminé en utilisant la méthode présentée dans le travail : itérative d'auto- cohérent (les valeurs expérimentales déterminées dans le cas de contraintes en traction comme en compression ont été comparées avec la littérature).

Dans le cas de la structure cristalline cubique, des paramètres $<a(\phi,\psi)>_{\{hkl\}}$ expérimentaux de maille sont calculés directement à partir des distances mesurées $<d(\phi,\psi)>_{\{hkl\}}$. Par la suite, les paramètres d'ajustement σ_{ij}^{I} et a_0 peuvent être trouvés en ajustant les valeurs $<a(\phi,\psi)>_{\{hkl\}}$ obtenues à partir de l'équation à celles mesurées, comme dans la méthode standard. Toutefois, la procédure plus complexe de données expérimentales doit être appliquée pour la structure hexagonale puisque la valeur de paramètre c/a doit être connue a priori pour le calcule expérimental $<a(\phi,\psi)>_{\{hkl\}}$ de l'équation

théorétique. Cette difficulté peut être surmontée quand le procédé d'itération sera appliqué. Un meilleur ajustement des valeurs théoriques et expérimentales ont été obtenues de façon significative en cas c/a ajusté. Il convient de souligner que la valeur du c/a peut être estimée avec une bonne approximation pour le matériau élastique isotrope (Ti) ou si la XSF sont connus (mesurée ou contrôlée) [12].

Au début, le calcul des contraintes stressantes poli et rectifié Ti (grade 2) a été réalisée suite à l'utilisation des valeurs hypothétiques de c/a (le paramètre c/a est indiqué sur les figures 6 et 7). Dans ce cas-là, la valeur de c/a n'a pas été modifiée pendant la le traitement de données. Il est à remarquer que les points expérimentaux sont répartis loin des lignes obtenues en ajustant. Les XSF calculées grâce à l'application du modèle Kröner. Ensuite, la procédure d'auto-cohérent a été utilisé et la valeur c/a a été également ajustée. Les diagrammes $<a(\phi,\psi)>_{\{hkl\}}$ vs. $\sin^2\psi$ ci-dessous démontrent une meilleure entente entre les points théoriques et expérimentaux. Les valeurs du paramètre c/a et la χ2, déterminées en utilisant la procédure présentée, sont données dans les figures 6 et 7. On peut apercevoir que la valeur de χ2 diminue de manière significative lorsque les points expérimentaux se rapprochent aux courbes théoriques.

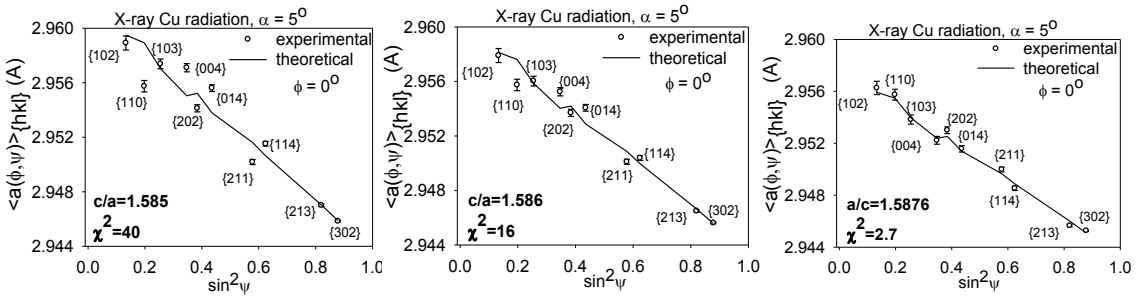

a) b)

c)

Fig.6. Le $<a(\phi,\psi)>_{\{hkl\}}$ vs. $\sin^2\psi$ graphes pour polie mécaniquement échantillon Ti (sous pression de 5 N), mesurées avec α = 5°. Sur les figures (a) et (b) les graphes théoriques ont été ajustés aux points expérimentaux déterminés avec valeur assumée de c/a, tandis que dans le cas de figure (c) c/a a été réglé. L'incertitude de la position de pointe a été supposée $\delta(2\theta)=0.01^o$.

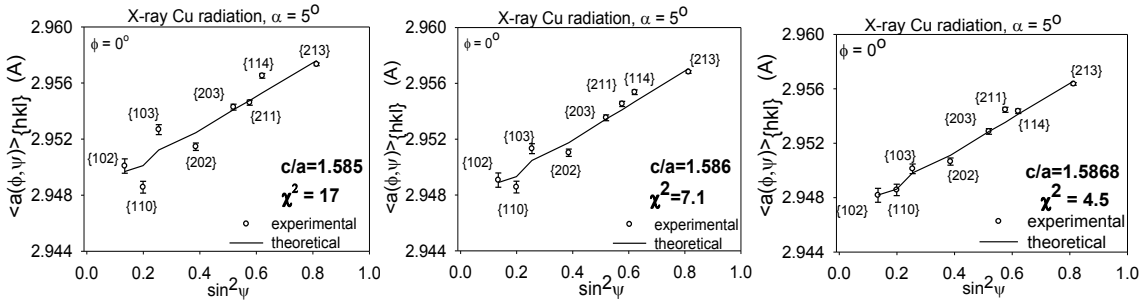

a) b) c)

Fig.7. Résultats similaires à la figure 6, mais pour rectifié échantillon Ti.

Deuxièmement, le développement prend en considération la présence de défauts d'empilement. Il a été montré que dans le cas des échantillons ayant une faible énergie de fautes d'empilement (cas d'acier inoxydable austénitique), la prise en compte de ces fautes d'empilement et la correction effectuée peut être bénéfique pour l'analyse par DRX. La probabilité de trouver le défaut d'empilement ρ a été déterminée pour l'acier inoxydable austénitique poli. Des valeurs raisonnables de ρ ont été déterminées dans la contrainte de compression dans le cas de l'échantillon poli. Le calcul similaire a été fait au préalable pour l'échantillon de sol (même en acier austénitique) par Baczmanski (2005) [9], qui a recu une valeur similaire de ρ. Cette méthode exige également la connaissance de XSF pour matériau anisotrope (comme l'acier inoxydable austénitique). C'est pourquoi il est important de vérifier les différents modèles de calculs XSF ce qui a été fait dans la thèse.

À part des contraintes résiduelles qui sont la raison du décalage du pic de diffraction par rapport à la position correspondante au réseau parfait, les raies de diffraction peuvent être influencées par l'empilement de défauts dans le matériau. Cet effet est particulièrement important pour les cristaux fcc ayant une faible énergie de défaut d'empilement (par exemple, les aciers austénitiques). Dans cette situation, l'amplitude du déplacement dépend de la probabilité de trouver le défaut d'empilement et de la réflexion hkl qui a été utilisée dans l'expérience. En l'absence des contraintes de seconde ordre d'incompatibilité :

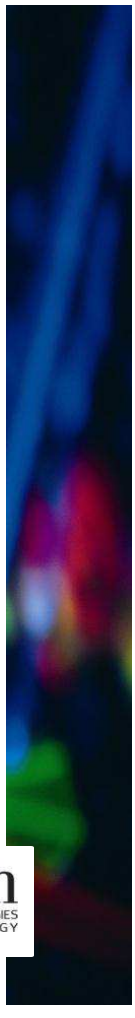

$$< a(\phi,\psi) >_{\{hkl\}} = [F_{ij}(hkl,\phi,\psi, f)\sigma_{ij}^{I} + \rho\, G(hkl)]\, a_0 + a_0 \qquad (6)$$

$$\text{avec} \quad G(hkl) \cong -\frac{\sqrt{3}}{4\pi(u+b)} \sum_{b} \frac{\pm(h+k+l)}{h^2+k^2+l^2}$$

où $\rho = \rho_s - \rho_d$, ρ_s et ρ_d sont les probabilités de trouver respectivement la simple et la double couche du défaut d'empilement, entre les plans voisins {111}, G(hkl) est le coefficient de la variation relative reflétant des distances intercausées par les défauts d'empilement pour les surfaces {hkl} de diffraction, tandis que b et u sont les numéros des composants de pointe qui sont respectivement affectés et non affectés par les défauts d'empilement..

À la fois la macrostress (Figure 8) et les défauts d'empilement provoquent les non-linéarités de la $<a(\phi,\psi)>_{\{hkl\}}$ vs. $sin^2\psi_{\{hkl\}}$ graphiques. Les macrostresses (500 MPa) influencent la pente ainsi bien que les non-linéarités de la courbe. En revanche, les défauts d'empilement augmenteent seulement les non-linéarités des graphique. Ce fait permet de séparer l'effet provenant des contraintes stressantes de celui relié aux défauts d'empilement et d'effectuer le calcul des valeurs de stress des contraintes et la probabilité de défauts

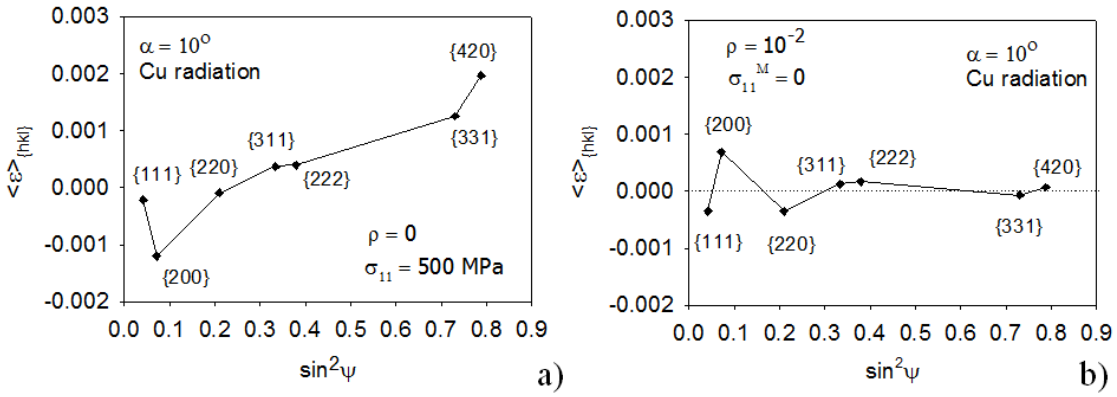

d'empilement en polycristallin.

Fig.8. Déformation du réseau calculées pour différentes réflexions hkl que l'effet de (a) contrainte uniaxiale et (b) la présence de fautes d'empilement sur les plans {111} pour l'échantillon austénitique (XSF ont été calculées en utilisant le modèle de surface libre [9].

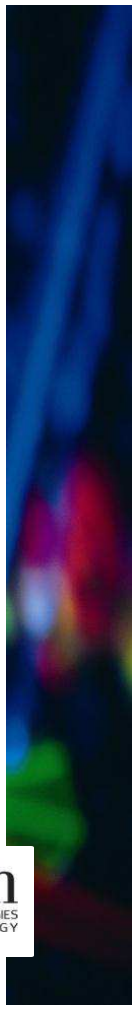

À la lumière des résultats présentés dans la thèse (Fig.9) il apparaît qu' il n'est pas nécessaire, pour un alliage de Ni prendre en considération la présence des défauts d'empilement dans l'analyse des contraintes. La valeur du paramètre ρ est dans la marge d'erreur égale à 0. Contrairement à l'acier inoxydable austénitique ayant une faible énergie de défauts d'empilement, il semble probable que la prise en compte de la présence de défauts d'empilement dans l'analyse des contraintes peut être bénéfique. Sans doute l'effet de défaut d'empilement améliore l'ajustement de la courbe théorique (calculée à partir du modèle d'interaction de grain choisi) aux points expérimentaux, mais il semble possible que cet effet entraîne le changement de la valeur XSF, qui peut maintenant différer de la valeur correcte.

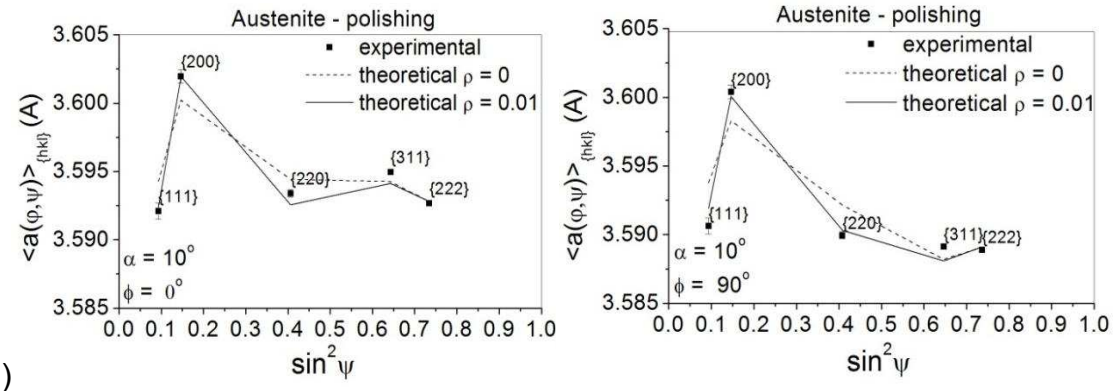

a)

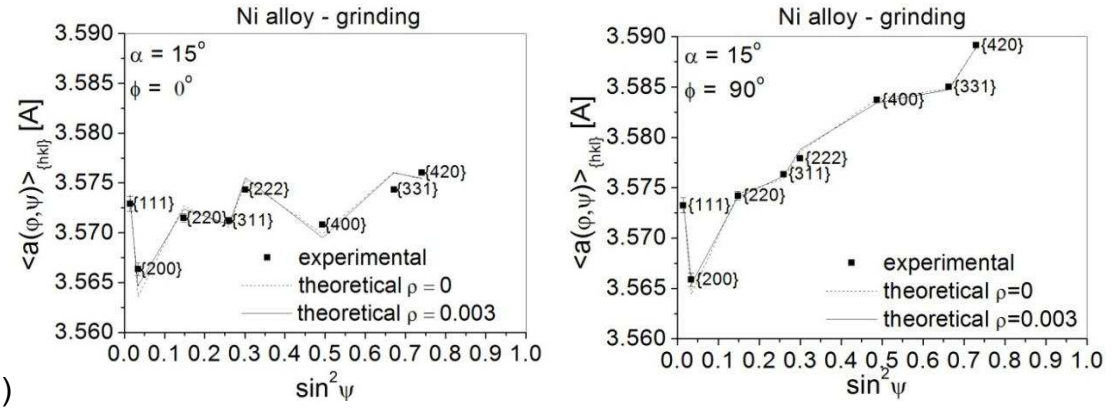

b)

Fig.9. Les paramètres $\langle a(\phi,\psi)\rangle_{\{hkl\}}$ ajustés aux points expérimentaux (en supposant $\rho \neq 0$ - ligne continue ou $\rho = 0$ - pointillés) pour l'acier poli inoxydable austénitique (AISI 316L) et d'alliage rectifié Ni (Inconel 690). XSF ont été calculés avec le modèle de surface libre en utilisant les fonctions de texture.

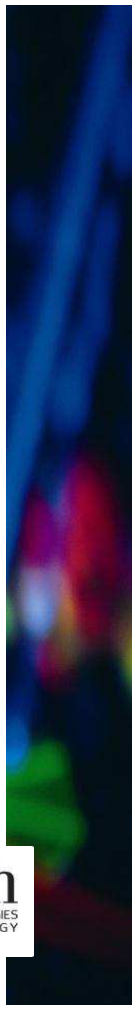

Pour étudier l'état des contraintes dans les matériaux polycristallins, les constantes d'élasticité radio-cristallographiques (CER ou XRayC) ou les facteurs de contraintes (XSF) doivent être déterminés [9, 12]. Dans le présent travail, les méthodes de diffraction des rayons X ont été appliquées pour mesurer les contraintes résiduelles dans les matériaux. Et outre, les CER et les facteurs XSF ont été utilisés pour interpréter des résultats. Les différents modèles théoriques d'interaction élasto-plastique entre les grains (Kröner, reuss, Voigt, surface libre) ont été pris en considération et appliqués dans l'analyse des contraintes (Fig. 10) [9].

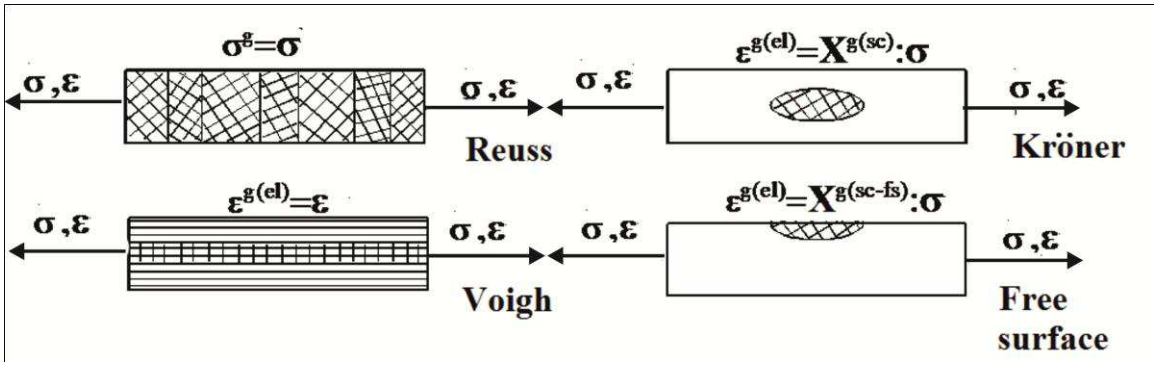

Fig. 10. Schéma de l'interaction entre les grains pour quatre modèles différents: a) Reuss - contrainte homogène, b) Voigt - déformation homogène c) Kröner - inclusion ellipsoïdale dans milieu homogène d) surface libre - inclusion ellipsoïdale placée près de la surface du milieu homogène [9].

La vérification des valeurs des XSF a été faite par les mesures des variations des distances interréticulaires lors des essais de traction dans le domaine élastique, pour l'échantillon anisotrope (en l'acier inoxydable austénitique) et pour l'échantillon isotrope (en titane). L'anisotropie des XSF a été également observée lors de la mesure des contraintes résiduelles dans un alliage de nickel réctifié, dans un acier inoxydable austénitique poli et dans un revêtement en CrN.

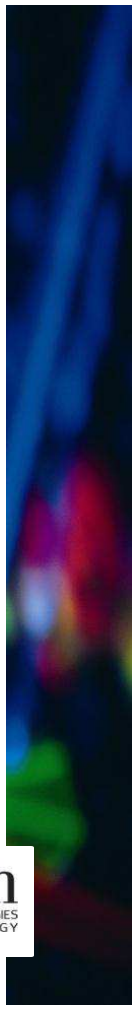

L'échantillon anisotrope (l'acier inoxydable austénitique).

Aux besoins de notre étude l'influence du modèle d'interaction des grains sur les valeurs de contraintes calculées en acier inoxydable austénitique (présentant une forte anisotropie élastique) a été soumise à une tension contrôlée (Σ_{11}= 50 MPa, 180 MPa et 300 MPa) pendant le chargement et le déchargement de la traction test. Pour chaque valeur de la charge, les contraintes résiduelles mesurées par la diffraction des rayons X ont été déterminées en utilisant le XSF calculé par quatre modèles (Kröner, Reuss, Voigt, surface libre) avec la fonction de distribution des orientations FDO ou ODF (orientation distribution function). Dans le cas du procédé MGIXD, les mesures ont été effectuées pour α = 20 ° (correspondant à la pénétration de profondeur τ = 2,9 um). La valeur initiale des contraintes calculées et des paramètres de maille pour l'échantillon non chargé sont rassemblés dans le tableau 3. Les $< a(\phi,\psi) >_{\{hkl\}}^{init}$ vs. $\sin^2\psi$ graphiques pour l'échantillon initial sont présentées dans la figure 11. Une petite compression et des contraintes de traction (comparables avec leurs incertitudes) ont été trouvées respectivement pour φ = 0 ° et φ = 90 °.

Tableau 3. Les valeurs initiales des contraintes et des paramètres de maille d'acier inoxydable austénitique non chargé.

modèle	α [°]	σ_{11} (MPa)	σ_{22} (MPa)	a_0 (Å)	χ^2
surface libre	20	-29± 18	27± 18	3.5937 ± 0.0001	1.5
Kröner		-27 ± 24	25 ± 23	3.5937 ± 0.0001	1.7
Reuss		-26 ± 16	25 ± 17	3.5937 ± 0.0001	1.5
Voigt		-26 ± 33	24 ± 31	3.5937 ± 0.0001	1.9

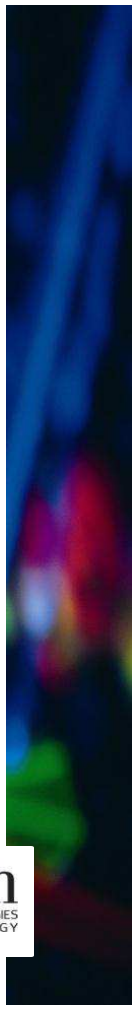

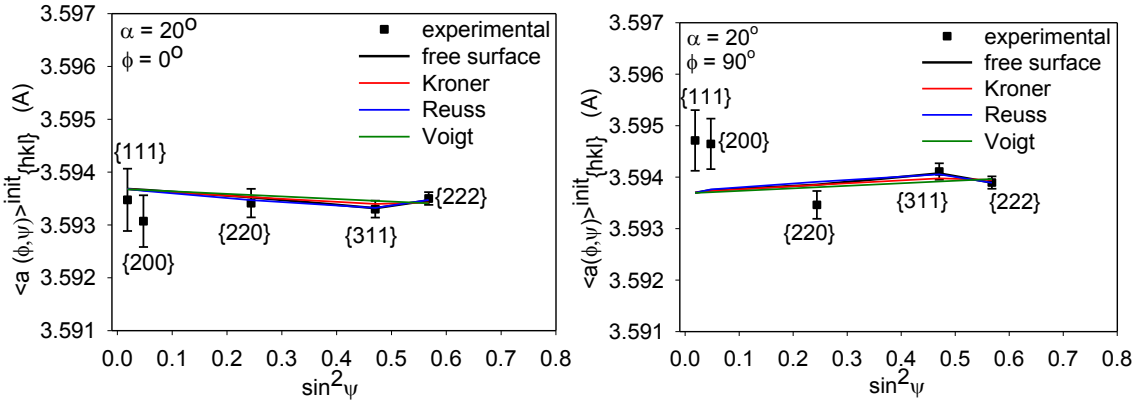

Fig. 11. Les graphiques $< a(\phi,\psi) >^{init}_{\{hkl\}}$ vs. $\sin^2\psi$ pour l'acier inoxydable austénitique initial non chargé (incertitude de la position du pic $\delta(2\theta) = 0.01^o$ a été prise en charge).

Les déformation relatifs du réseau $< \varepsilon(\phi,\psi) >^{rel}_{\{hkl\}}$ vs. $\sin^2\psi$ (pour α = 20 °) pour chaque charge et de quatre modèles grains d'interaction durant le chargement et le déchargement sont représentées respectivement sur les figures 12 et 13. Dans ces figures, les données expérimentales sont comparées avec les résultats de l'ajustement des moindres carrés basé directement sur la relation :

$$< \varepsilon(\phi,\psi) >^{rel}_{\{hkl\}} = F_{11}(hkl,\phi,\psi,f)\sigma^I_{11} + F_{22}(hkl,\phi,\psi,f)\sigma^I_{22}$$

où les valeurs σ^I_{11} et σ^I_{22} ajustées des contraintes peuvent être comparées respectivement avec les valeurs de contrainte appliquée Σ_{11} et $\Sigma_{22} = 0$ MPa .

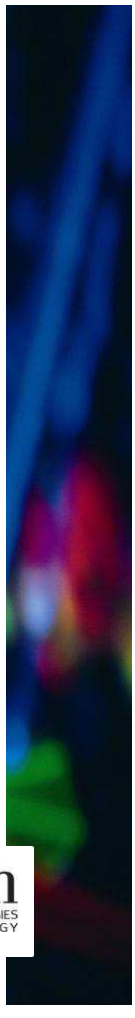

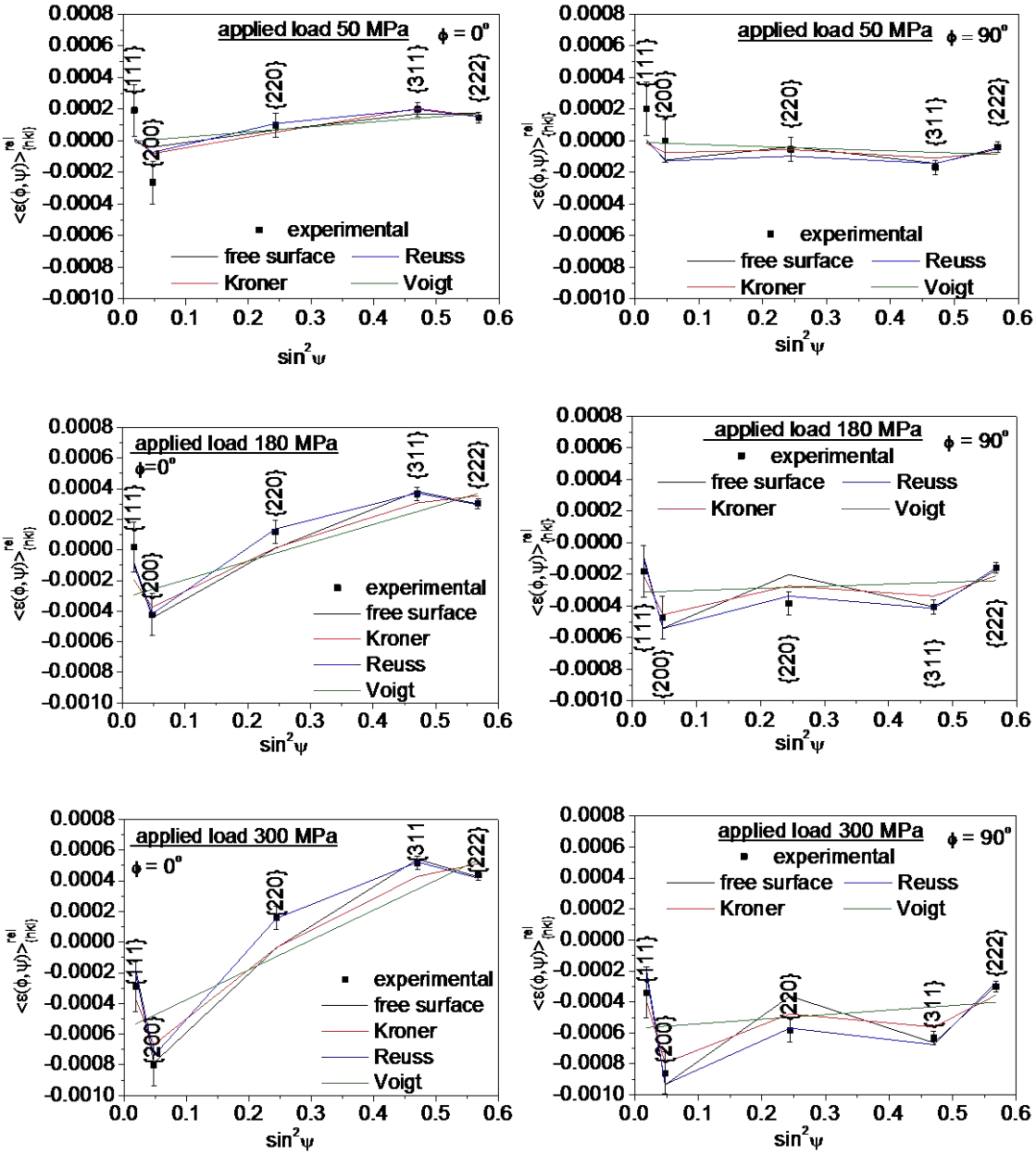

Fig. 12. Les défromations moyenne du réseau $<\varepsilon(\phi,\psi)>^{rel}_{\{hkl\}}$ vs sin²ψ (pour α = 20°) pendant le chargement de l'échantillon acier inoxydable austénitique. Les résultats expérimentaux sont équipés de XSF calculés par quatre modèles testés.

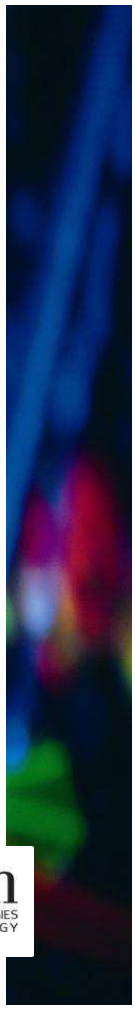

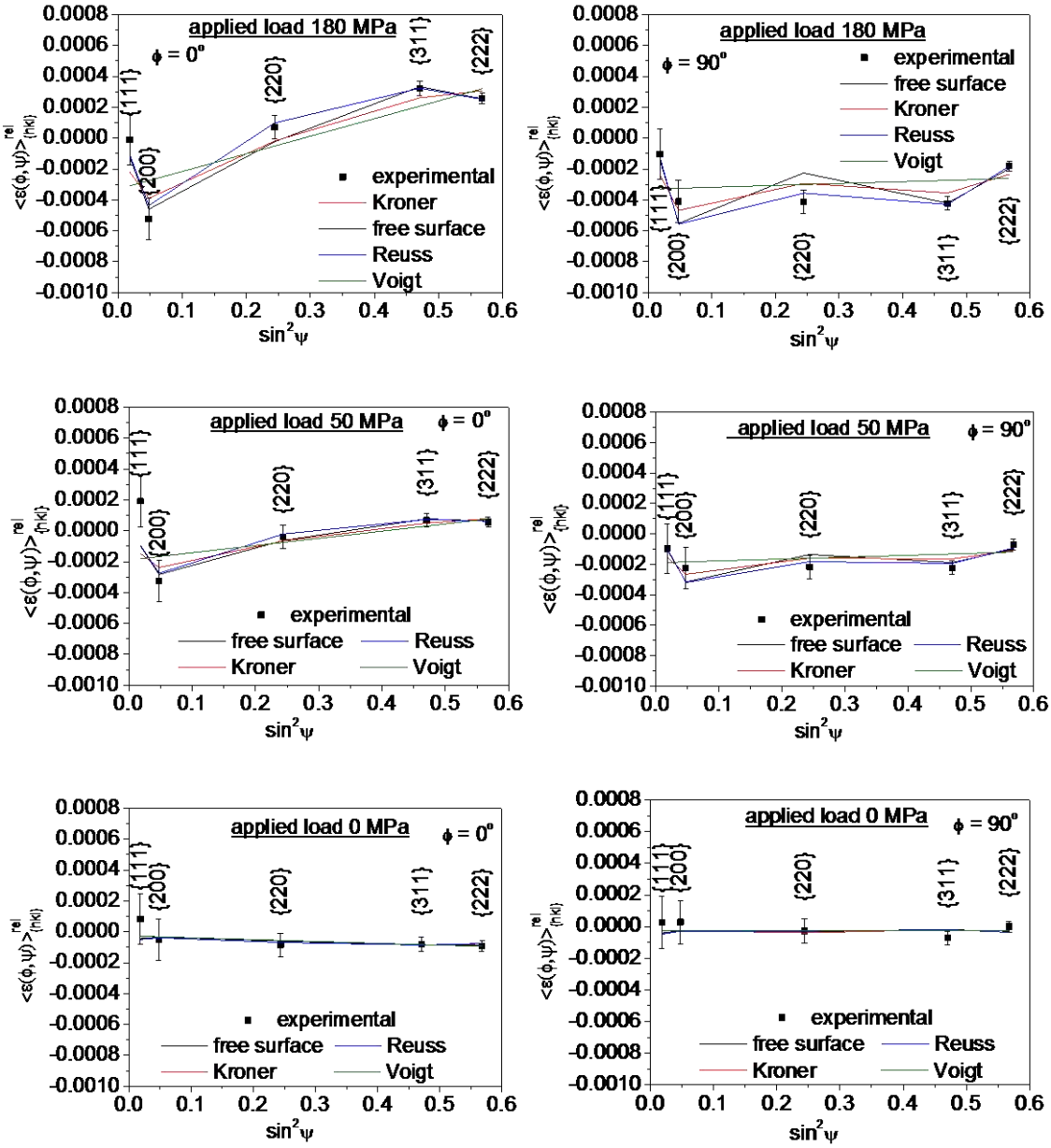

Fig. 13. Comparaison similaire comme dans Fig. 12 mais pour le déchargement de l'échantillon en acier inoxydable austénitique.

La non-linéarité des graphiques $\sin^2\psi$ dans les figures 12 et 13 est associée à une forte anisotropie élastique de l'échantillon. Comme on peut le déduire de ces graphiques, les déformations du réseau sont les plus faibles dans la direction <111> et les plus grandes dans la direction <200> pour charger l'échantillon austénitique. Ce résultat est en accord qualitatif avec l'évolution de ½ s_2 et s_1 valeurs pour différentes réflexions hkl (dans l'approche de matériau quasi-isotrope), ce qui explique la tendance observée. Si

l'interaction entre les grains est bien prédite les non-linéarités des courbes théoriques doivent refléter cette dépendance.

Nous voyons sur les graphiques $\sin^2\psi$ (figures 12 et 13) que les valeurs expérimentales ainsi que l' anisotropie élastique sont bien approchées par Reuss, Kröner et par le modèle de surface libre. La dépendance linéaire $<\varepsilon(\phi,\psi)>^{rel}_{\{hkl\}}$ vs. $\sin^2\psi$ prédite par le modèle Voigt ne peut être appliquée pour l'acier inoxydable austénitique ayant une forte anisotropie élastique. La comparaison quantitative de la qualité appropriée est donné par paramètre $\chi 2$ dont la valeur est comparée à la figure 14 pour toutes les charges appliquées et quatre modèles testés.

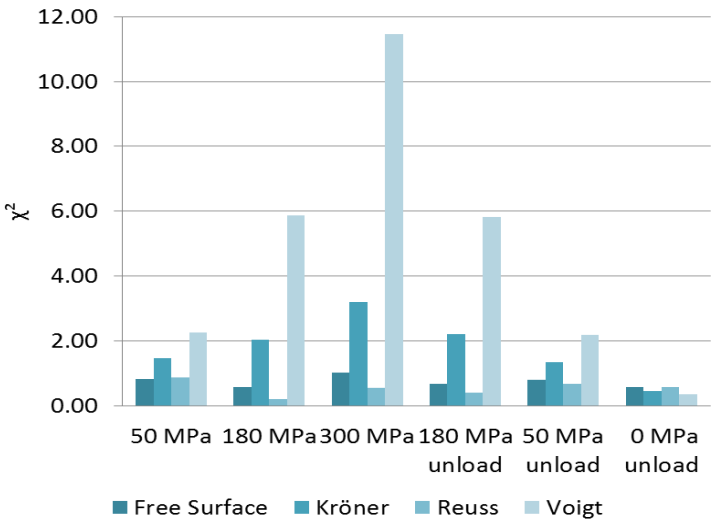

Fig. 14. Comparaison des valeurs de χ^2 pour quatre modèles d'interaction de différents grains pendant l'essai de traction de l'échantillon austénitique (chargement et déchargement).

On peut affirmer que χ^2 doit augmenter à condition que les différences entre les valeurs expérimentales et les résultats théoriques augmentent. Si un modèle donné prédit parfaitement XSF, la valeur de χ^2 est déterminée uniquement par les incertitudes expérimentales et il ne devrait pas augmenter pour des contraintes plus importantes appliquées (la déformation du réseau en raison de stress augmente par la même valeur que la souche prédite par la

théorie et en conséquence la distance entre elles ne change pas). Toutefois, si les valeurs de XSF ne sont pas correctement calculées par le modèle (même pour certaines orientations) la différence entre les distances interréticulaires théoriques et expérimentales agrandie avec l'augmentation de la charge appliquée provoque l'augmentation importante de la valeur de χ^2 (en raison de la quadrature dans la définition de χ^2).

Afin de déterminer le meilleur modèle la comparaison des contraintes recalculé à partir des données de diffraction avec des valeurs de la charge appliquée est présentée dans la Fig. 15, pour le chargement et le déchargement de l'échantillon. Les mesures ont été effectuées en utilisant deux méthodes suivantes : MGIXD ($\alpha = 20\ ^\circ$) et ψ géométrie standard. On peut voir que les processus de chargement et de déchargement sont exactement réversibles (points pour la même contrainte appliquée de chevauchement pour les deux méthodes expérimentales), c'est-à-dire, les mesures ont été effectuées dans la plage de déformation élastique. Il faut souligner que la bonne concordance entre les résultats obtenus avec les deux méthodes et des valeurs de la contrainte appliquée standard et MGIXD a été constatée dans le cas de la Reuss et du modèle à surface libre, il s'ensuit que les résultats obtenus avec les modèles obtenus avec Kröner et Voigt modèles s'écartent de la valeur de la contrainte appliquée. Pour les derniers modèles en particulier un grand écart entre les contraintes appliquées et re - calculé est vu dans le cas de mesures standard. Les pires résultats c'est-à-dire, le plus grand écart entre la contrainte appliquée et recalculée a été obtenu en cas du modèle Voigt utilisé.

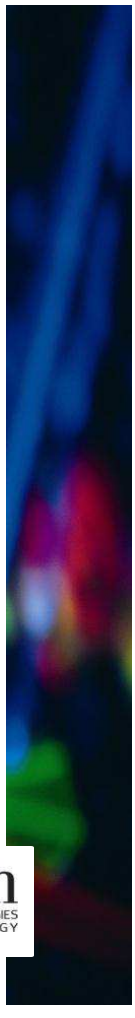

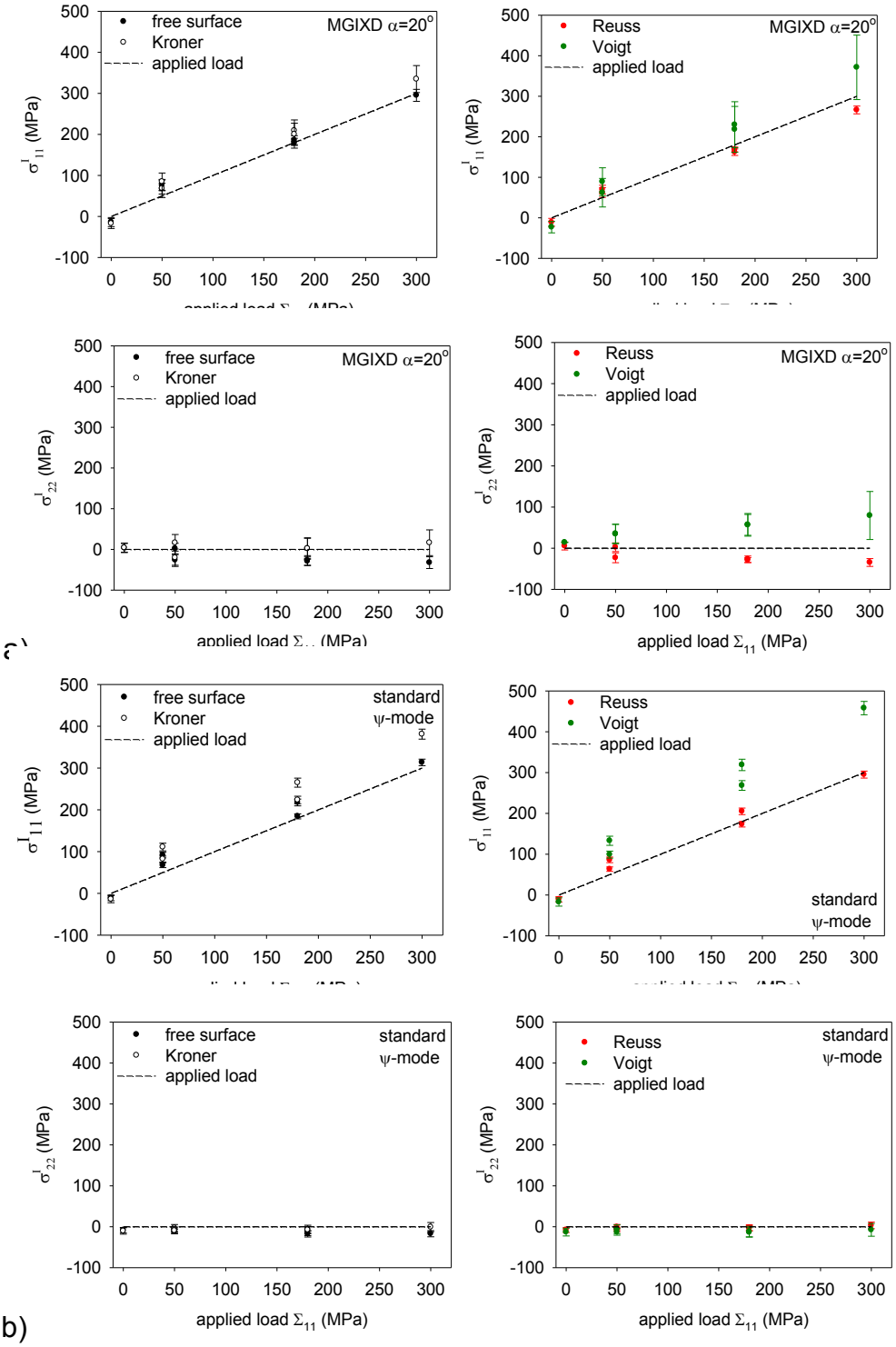

b)

Fig. 15. Comparaison des valeurs de contraintes σ_{11}^I et σ_{22}^I de re-calculé par rapport à la contrainte appliquée Σ_{11} et $\Sigma_{22} = 0$ MPa, respectivement (ligne en pointillés indique la valeur de la contrainte $\sigma_{11}^I = \Sigma_{11}$ ou $\sigma_{22}^I = \Sigma_{22} = 0$ MPa). Les résultats de chargement et de déchargement sont présentés et le point $\Sigma_{11} = 0$ MPa correspond à l'état après le déchargement. La méthode MGIXD (a) et la méthode standard - mode ψ (311 de réflexion) (b) ont été utilisées.

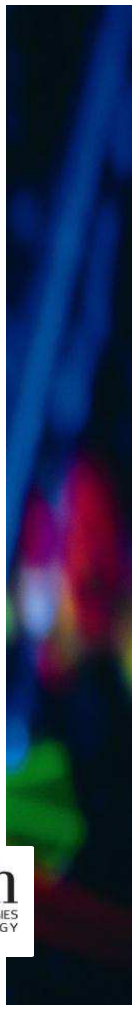

L'échantillon isotrope (titane).

Nous avons étudié comme le second échantillon étudié était Ti (grade 2), l'échantillon ayant une faible anisotropie élastique. Le titane a été soumis à une tension contrôlée (50 MPa, 150 MPa, 210 MPa) pendant le chargement dans l'essai de traction. Pour chaque valeur de la charge les contraintes mesurées par diffraction des rayons X ont été déterminées en utilisant le XSF calculé par quatre modèles avec la fonction ODF. Dans le cas du procédé MGIXD, les mesures ont été effectuées pour α = 10 ° et α = 20 ° (correspondant à la pénétration des profondeurs : τ = 1,6 et τ = um 2,5 um), tandis que le ω-géométrie a été utilisé pour les mesures classiques. La valeur initiale des contraintes calculées et des paramètres de maille pour l'échantillon non chargé sont rassemblés dans le tableau 4, tandis que les contre $\sin^2\psi$ graphiques pour l'échantillon initial sont présentés dans la figure 16 (méthode MGIXD). Les contraintes de compression de l'ordre de moins 30 MPa ont été trouvées pour φ = 0 ° et presque zéro stress pour φ = 90 °, respectivement.

Tableau 4. Les valeurs initiales des contraintes, des constantes de réseau de contrainte libre et c/a paramètres pour un échantillon non-chargé Ti (grade 2) - méthode MGIXD.

modèle	σ_{11} (MPa)	σ_{22} (MPa)	a_0 (Å)	c/a	χ^2
			α = 10°		
Surface libre	-30.9 ± 5.4	-4.7 ± 5.6	2.9511 ± 0.0001	1.5872 ± 0.0001	1.3
Kröner	-31.9 ± 5.4	-4.9 ± 5.6	2.9511 ± 0.0001	1.5872 ± 0.0001	1.3
Reuss	-30.2 ± 5.3	-4.4 ± 5.5	2.9511 ± 0.0001	1.5872 ± 0.0001	1.3
Voigt	-33.5 ± 5.6	-5.3 ± 5.7	2.9511 ± 0.0001	1.5872 ± 0.0001	1.4
			α = 20°		
Surface libre	-33.1 ± 8.2	10.7 ± 8.6	2.9514 ± 0.0001	1.5869 ± 0.0001	2.9
Kröner	-35.3 ± 8.2	10.4 ± 8.6	2.9514 ± 0.0001	1.5869 ± 0.0001	2.9
Reuss	-32.3 ± 8.0	11.4 ± 8.4	2.9514 ± 0.0001	1.5869 ± 0.0001	2.9
Voigt	-38.2 ± 8.4	9.4 ± 8.8	2.9514 ± 0.0001	1.5869 ± 0.0001	3.0

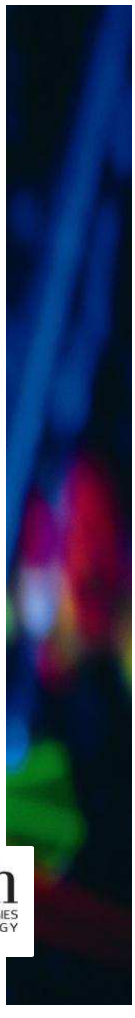

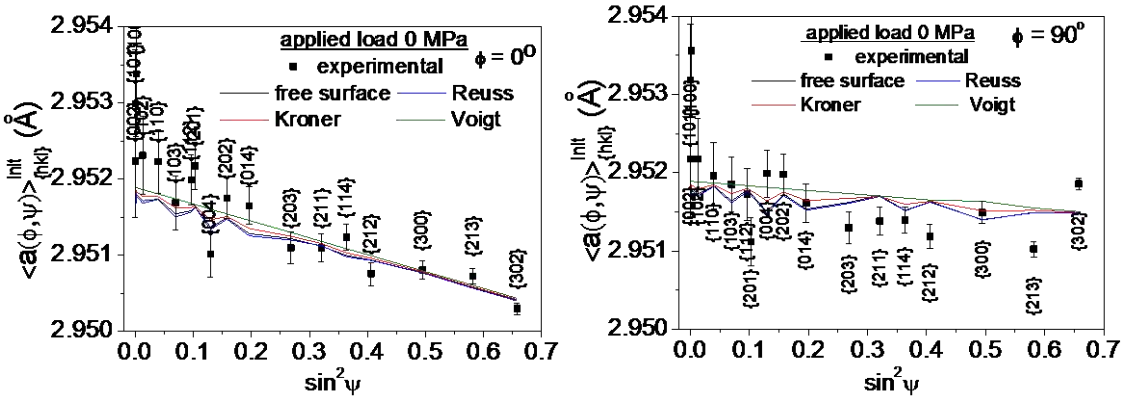

Fig. 16. Les $< a(\phi,\psi) >^{init}_{\{hkl\}}$ vs. $\sin^2\psi$ graphiques pour l'échantillon non chargé Ti (grade 2) mesuré à l'aide de MGIXD avec α = 20 ° (incertitude de la position du pic a été prise en charge).

Les résultats obtenus pour l'essai de traction sont représentés sur les figures suivantes :

• Fig. 17 - les déformation du réseau expérimentales relatives à treillis contre $< \varepsilon(\phi,\psi) >^{rel}_{\{hkl\}}$ vs. $\sin^2\psi$ pour α = 20 ° (méthode MGIXD),

• Fig. 18 - les valeurs du paramètre de bonté χ^2 pour α = 10 ° et α = 20 ° (méthode MGIXD) ;

• Fig. 19 – les valeurs des contraintes de re-calculé comparées avec celles appliquées.

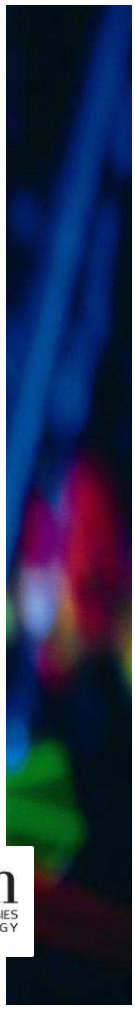

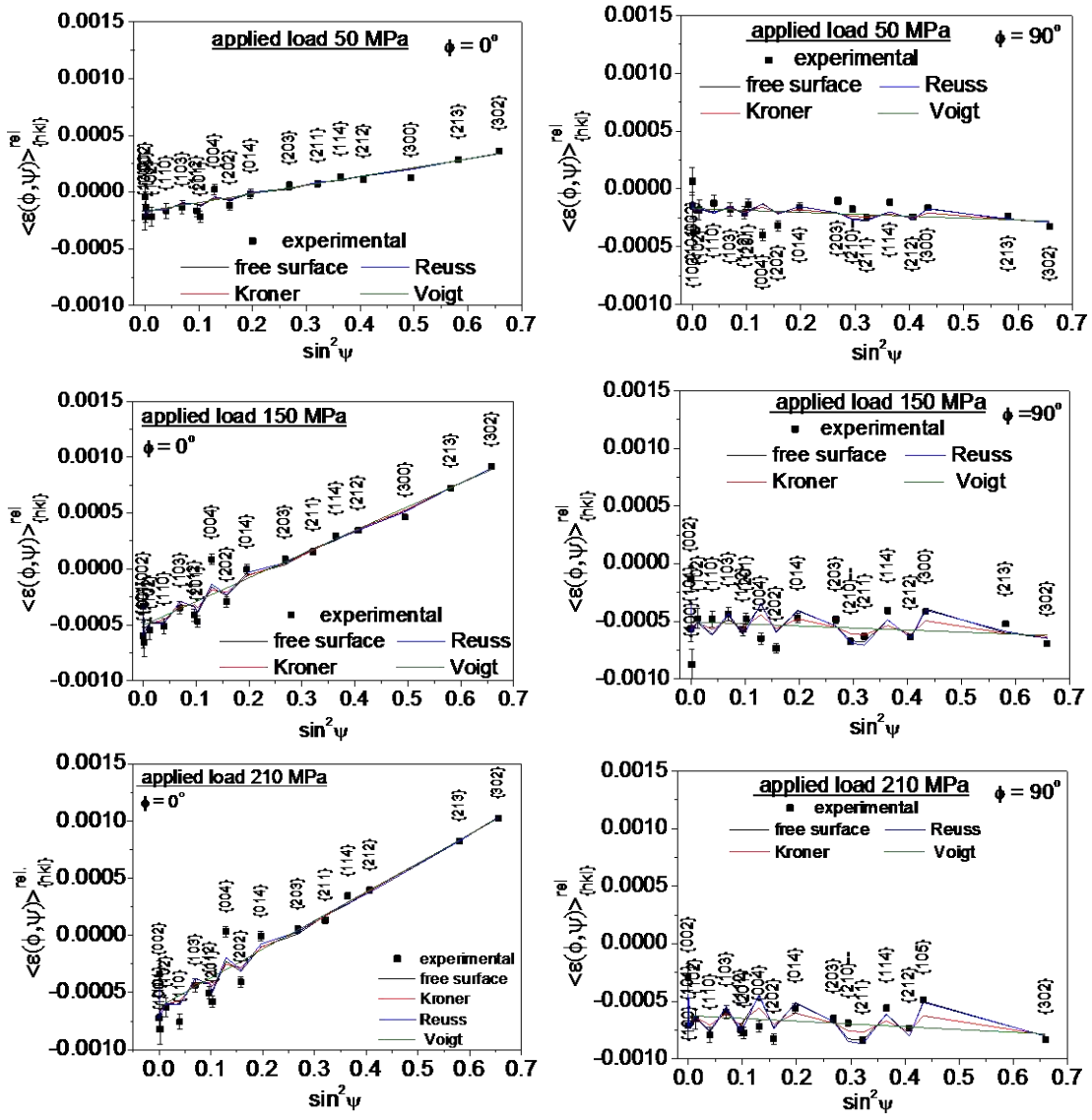

Fig. 17. $<\varepsilon(\phi,\psi)>^{rel}_{\{hkl\}}$ vs $\sin^2\psi$ (pour α = 20 °) pendant le chargement de l'échantillon de Ti. Les résultats expérimentaux sont ajustés avec XSF calculé par quatre modèles testés.

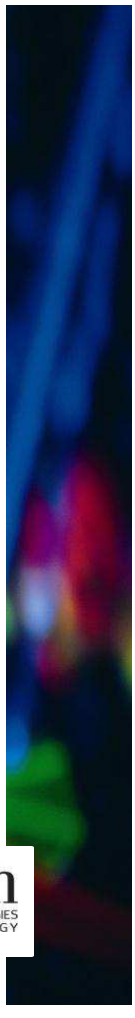

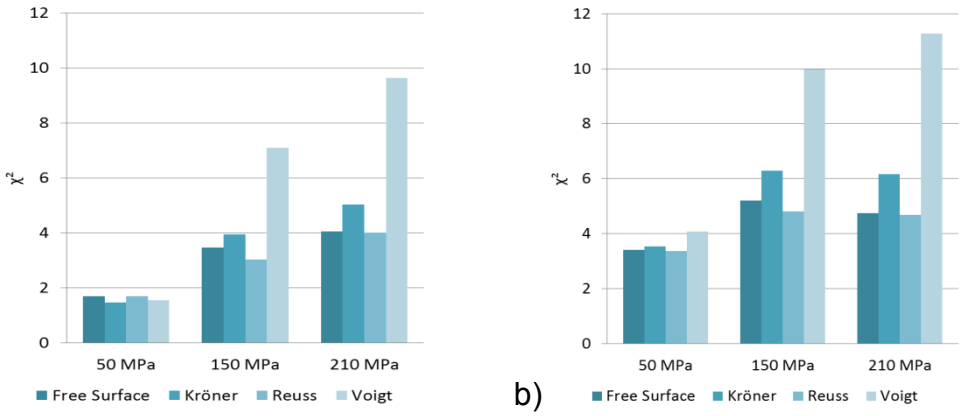

a) b)

Fig. 18. Comparaison des valeurs de χ ², quatre modèles d'interaction du grain au cours de la traction de l'échantillon de Ti pour α = 10 ° (a) et α = 20 ° (b) - méthode MGIXD.

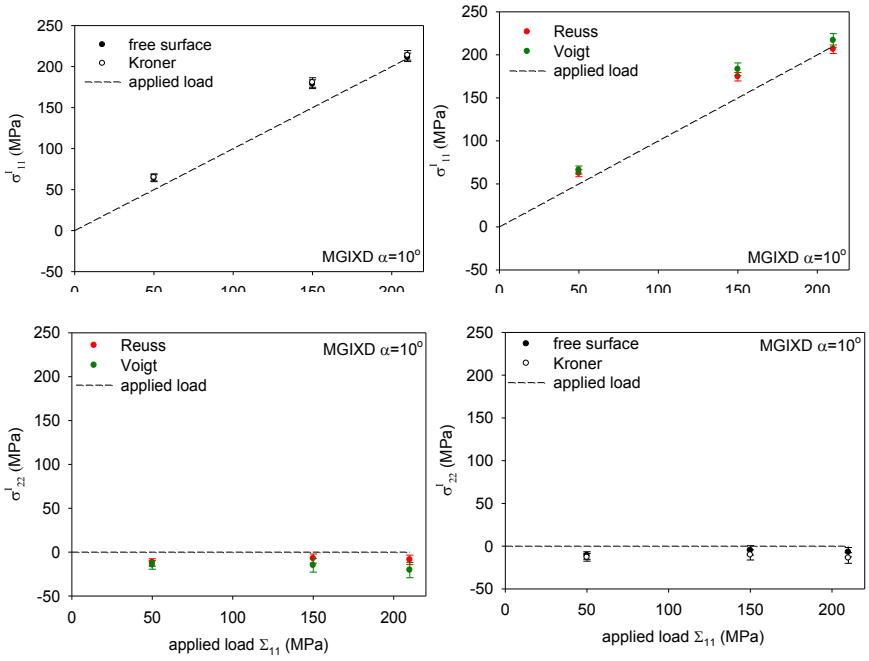

a)

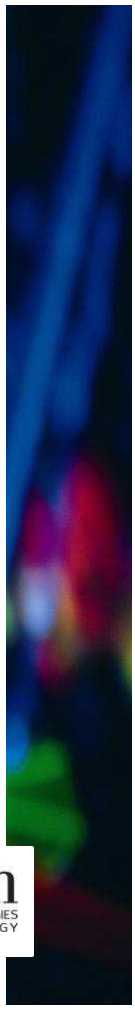

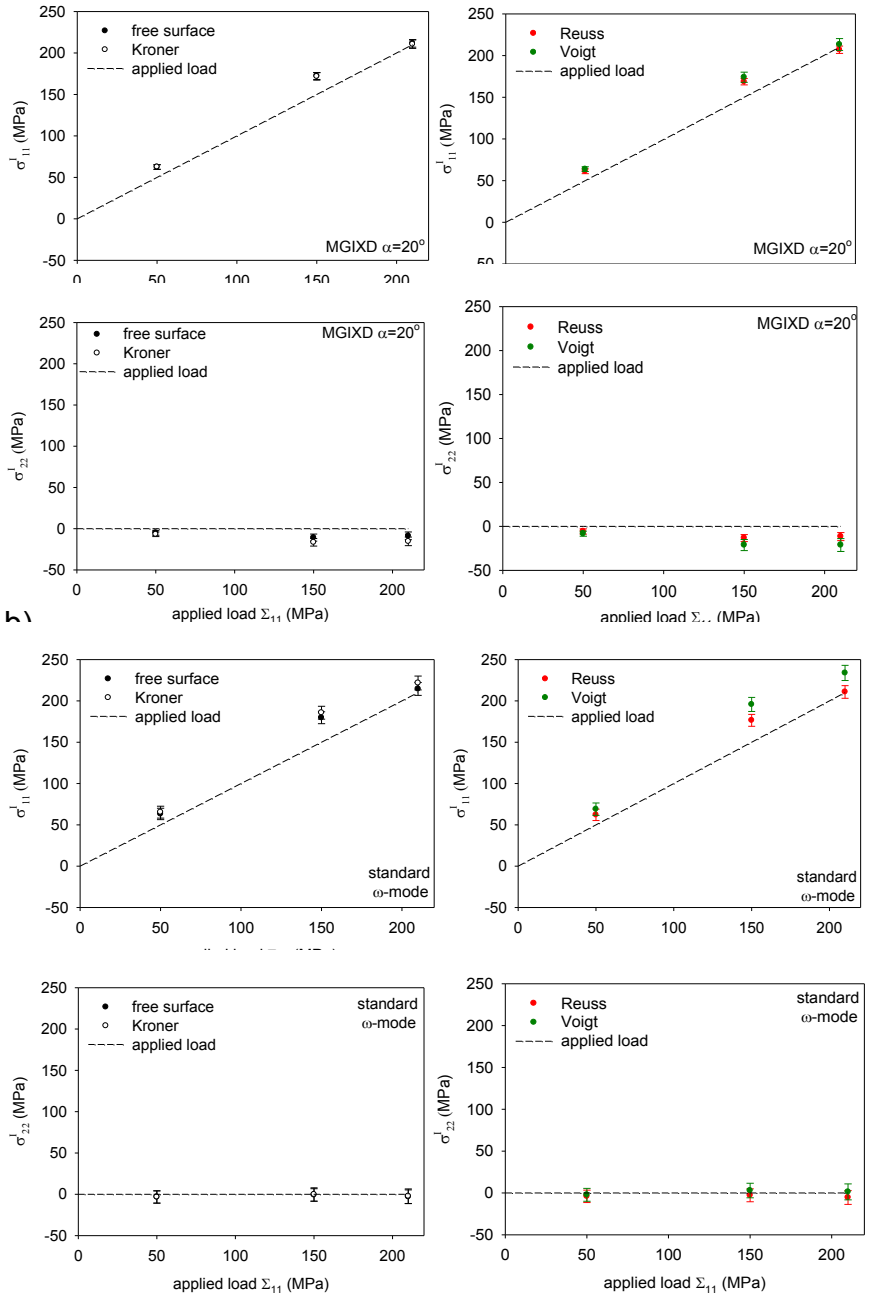

c)

Fig. 19. Comparaison des valeurs de contraintes σ_{11}^I et σ_{22}^I de re-calculé par rapport à la contrainte appliquée Σ_{11} et $\Sigma_{22} = 0$ MPa, respectivement (ligne en pointillés indique la valeur de la contrainte $\sigma_{11}^I = \Sigma_{11}$ ou $\sigma_{22}^I = \Sigma_{22} = 0$ MPa). La méthode MGIXD pour α = 10 ° (a), α = 20 ° (b) et la méthode standard avec ω-mode (213 réflexion) (c) ont été utilisées pour mesurer les contraintes dans l'échantillon chargé Ti.

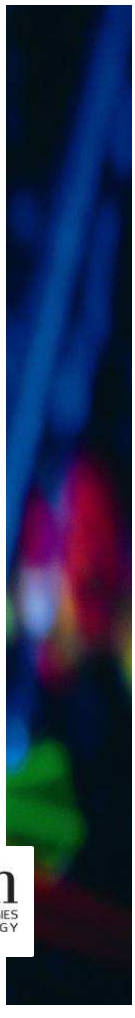

Ensuite, les échantillons ayant des contraintes de surface résiduelles importantes et non soumises à la charge externe ont été étudiés.

Tout d'abord, le tungstène élastiquement isotrope de l'échantillon (W) a été étudié. Pour générer le stress en surface de l'échantillon la surface a été polie manuellement (article de 2000 grains, polissage non directionnel). La méthode MGIXD et la méthode standard (géométries ω et ψ avec 321 réflexion) ont été appliquées à mesurer les déformations du réseau.

La comparaison des contraintes déterminée en utilisant de différentes XSFs et les valeurs du paramètre χ^2 obtenu de cette analyse est présentée dans la Fig. 20. Les $\sin^2\psi$ graphiques pour un exemple d'un angle incident α = 5° (méthode MGIXD) et des méthodes standards sont présentées dans la figure 21, tandis que la comparaison des graphes $\sin^2\psi$ pour différents angles α est démontrée sur la Fig. 22 (les XSF donnés par le modèle de surface libre ont été appliqués dans les calculs).

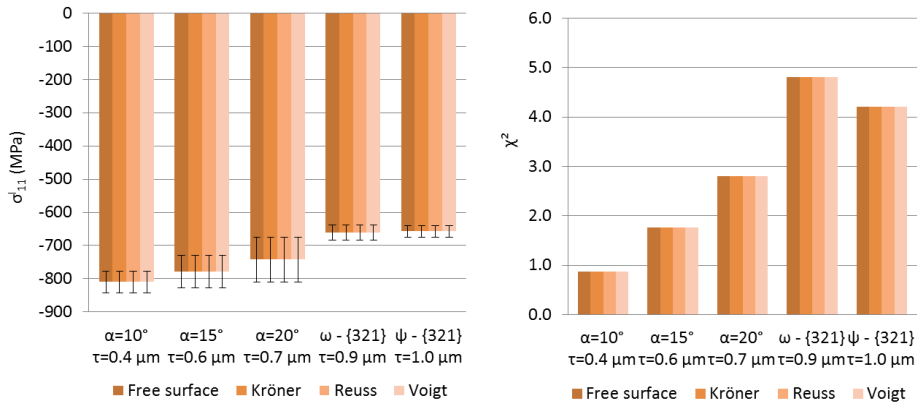

Fig. 20. Les valeurs de contraintes déterminées dans l'échantillon W poli en utilisant la méthode MGIXD et la méthode standard (a) et la comparaison des valeurs du paramètre χ^2 (b) pour quatre modèles d'interaction de grain.

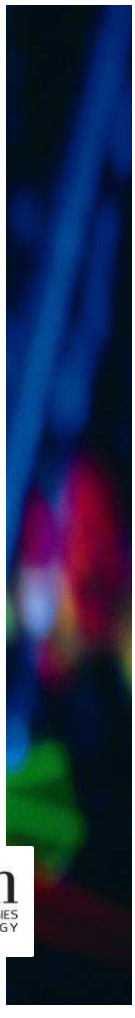

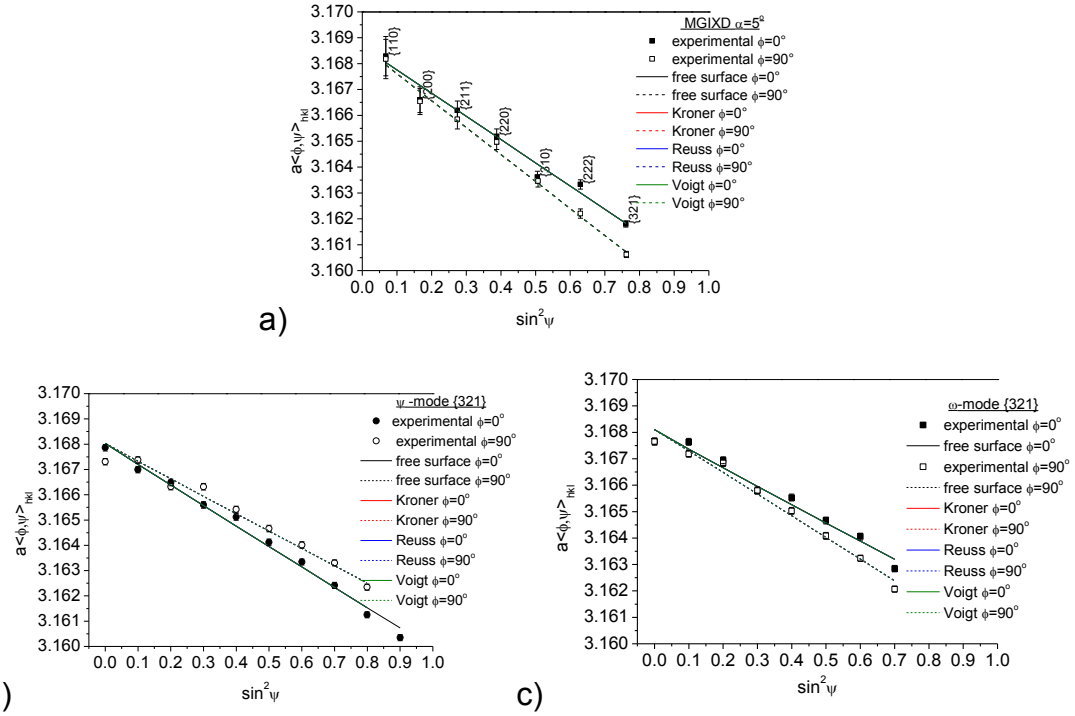

Fig. 21. Points expérimentaux et théoriques $<a(\phi,\psi)>_{\{hkl\}}$ vs sin²ψ pour l'échantillon W poli. Les mesures présentées pour MGIXD (α = 5°) (a) et ψ-mode standard (b) et ω-mode (c) méthodes (incertitude de la position du pic $\delta(2\theta)=0.01^{o}$ a été prise en charge).

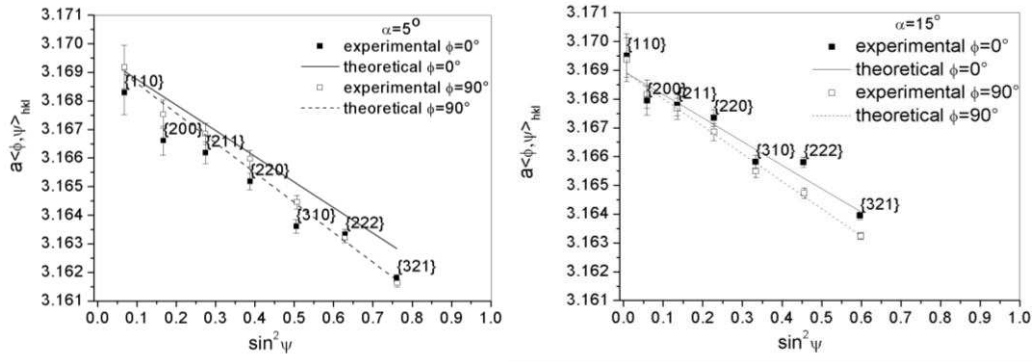

Fig. 22. Exemple de $<a(\phi,\psi)>_{\{hkl\}}$ vs sin²ψ graphiques pour l'échantillon W poli. Les résultats présentés pour la méthode MGIXD pour les angles d'incidence α = 5 ° et α = 15 °.

Deuxièmement, les échantillons ayant une forte anisotropie élastique ont été étudiés : réctifié Ni alliage, acier inoxydable austénitique poli et revêtement CrN. La méthode MGIXD et la méthode standard ont été appliquées pour déterminer les contraintes dans les échantillons mentionnés ci-dessus.

Seulement dans le cas de l'échantillon austénitique, les probabilités déterminées pour trouver le défaut d'empilement entre les plans voisins (ρ valeur) ont une influence significative sur les résultats et la valeur de l'incertitude. Par conséquent, le paramètre ρ a été réglé dans le cas de l'acier inoxydable austénitique poli, tandis que pour les autres échantillons ρ = 0 a été supposé. Le résultat de l'analyse des contraintes pour différents modèles d'interaction des grains considérés et pour tous les échantillons est présenté dans la Fig. 23, tandis que les valeurs de test de χ^2 sont présentées dans la Fig.24. L'exemple de graphiques $\sin^2\psi$, comparé pour tous les échantillons analysés est présenté dans la figure 25 (pour des modèles différents de grains d'interaction).

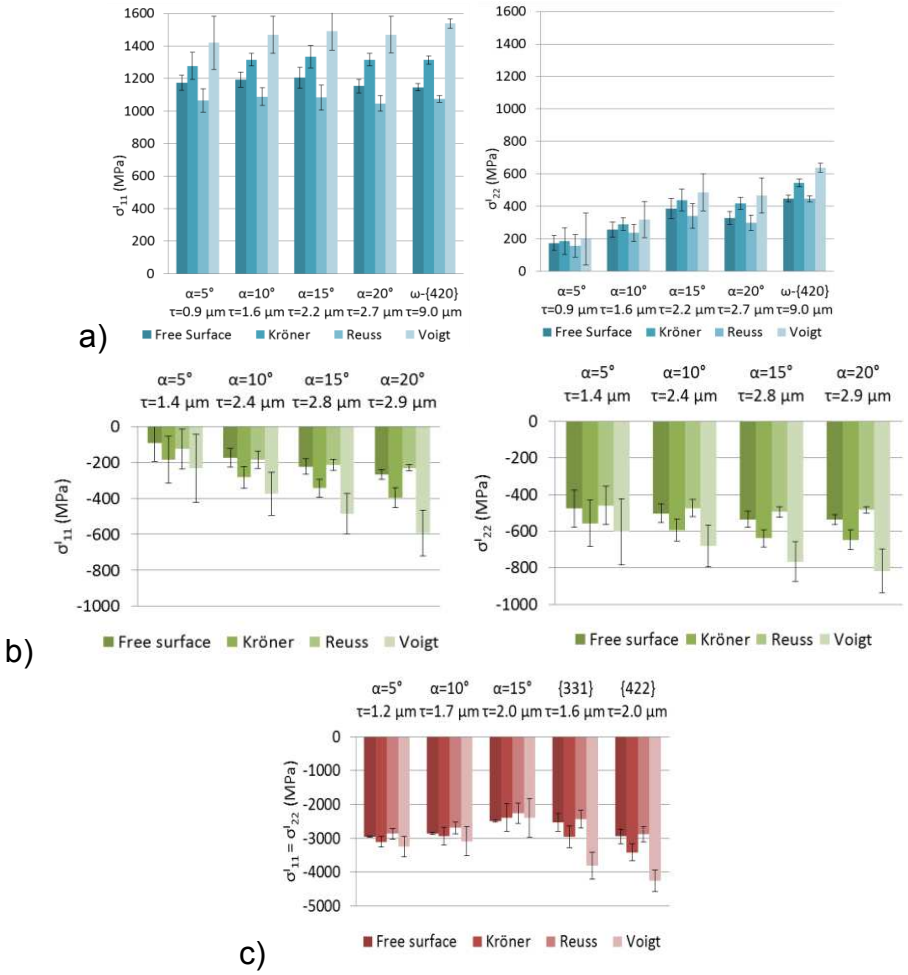

Fig. 23. Comparaison de l'influence de quatre modèles de l'interaction de grain appuyée sur les résultats des rayons X l'analyse des contraintes pour rectifié alliage de Ni (a), en acier poli inoxydable austénitique (b) et le revêtement CrN (c). Les résultats pour les angles différents d'incidence α sont comparés avec la méthode standard pour des réflexions hkl.

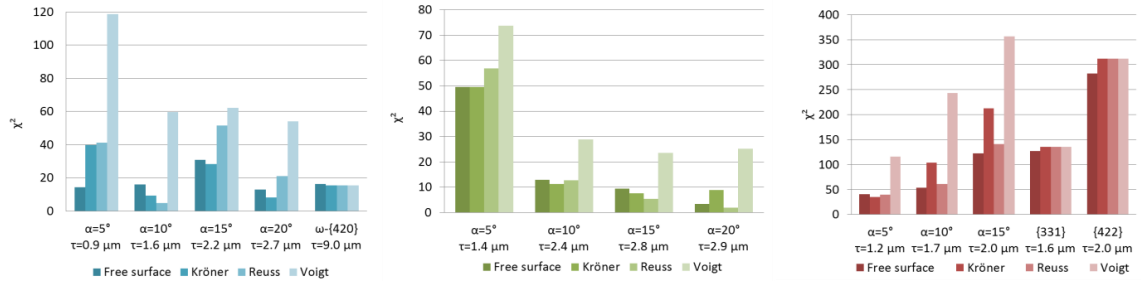

Fig. 24. Comparaison des valeurs du paramètre χ^2 pour différents modèles d'interaction de grain pour rectifié alliage de Ni (a), poli acier inoxydable austénitique (b), le revêtement CrN (c). Les résultats pour les différents angles d'incidence α sont comparés avec la méthode standard pour des réflexions hkl.

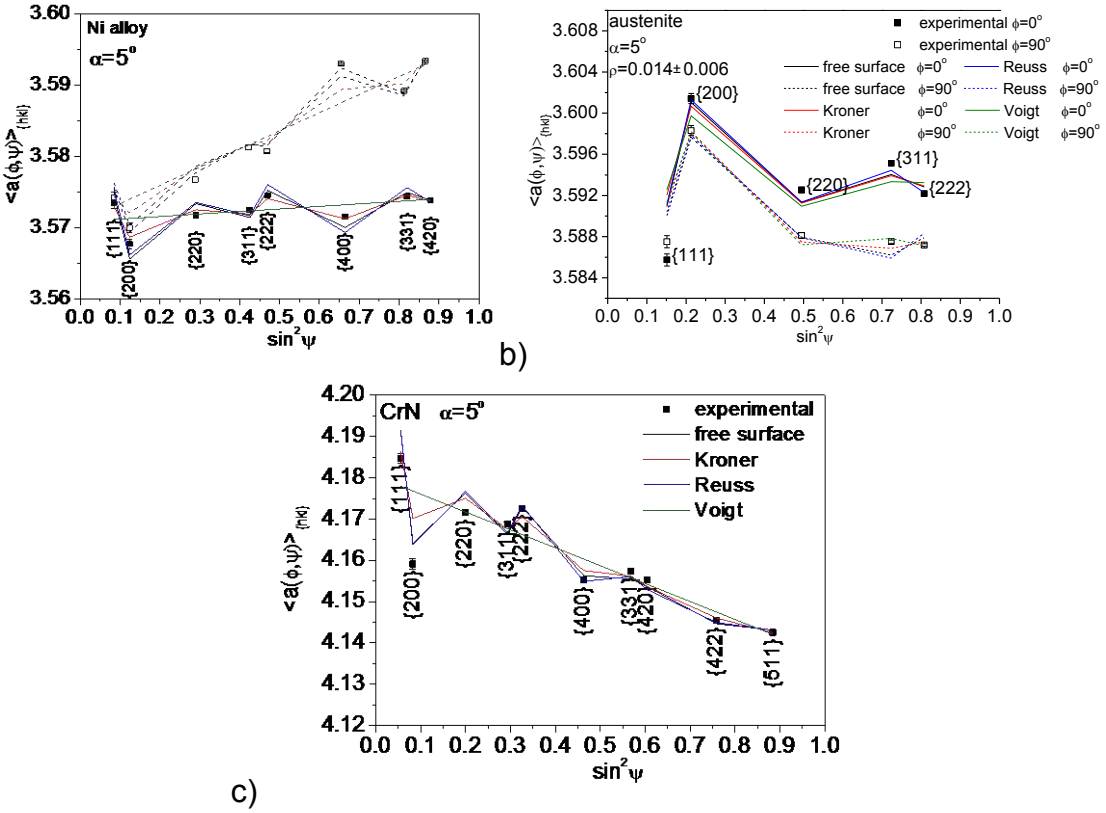

Fig. 25. Le $\sin^2\psi$ graphiques, comparé aux différents modèles d'interaction de grain, pour MGIXD α = 5° pour rectifié alliage de Ni (a), de l'acier inoxydable austénitique poli (b), le revêtement CrN (c). Seulement dans le cas de l'échantillon l'austénitique, le paramètre de ρ a été aménagé et déterminé (ρ = 0.014 ± 0.006).

Les résultats présentés dans la thèse, obtenus en utilisant la méthode MGIXD et la méthode standard, montrent que les modèles d'interaction de

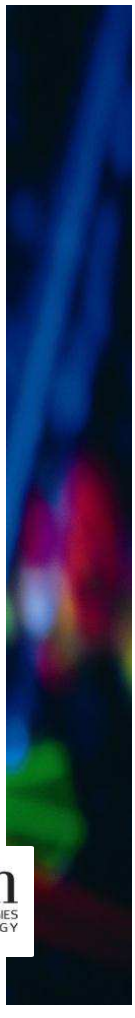

grains de types Reuss et de surface libre sont en meilleur accord avec les résultats expérimentaux. Ces modèles décrivent de la meilleure façon l'anisotropie élastique de l'échantillon, cependant le modèle de surface libre a une explication physique contrairement au modèle de Reuss.

Enfin, la méthode MGIXD a été vérifiée en utilisant le rayonnement synchrotron. La méthodologie de l'interprétation des données a été développée afin de traiter les données obtenues non seulement pour différents angles d'incidence, mais aussi simultanément en utilisant différentes longueurs d'ondes. Les résultats pour les échantillons présentant un gradient élevé de contrainte en profondeur (les résultats obtenus par diffraction des rayons X classique) ont été vérifiés en utilisant le rayonnement synchrotron. Trois longueurs d'ondes différentes (λ = 1.2527 Å, λ = 1.5419 Å et λ = 1.7512 Å) ont été choisies et les angles d'incidence (α), pour lesquels la profondeur de pénétration est la même, ont été calculés. Le premier échantillon étudié a été un échantillon en alliage Al2017 poli. Lorsque les pics ont été ajustés par la fonction de pseudo-Voigt, une très bonne concordance a été obtenue entre les données obtenues quand le rayonnement synchrotron (pour trois longueurs d'ondes différentes) a été utilisé ainsi que sur diffractomètre classique (Fig. 26)

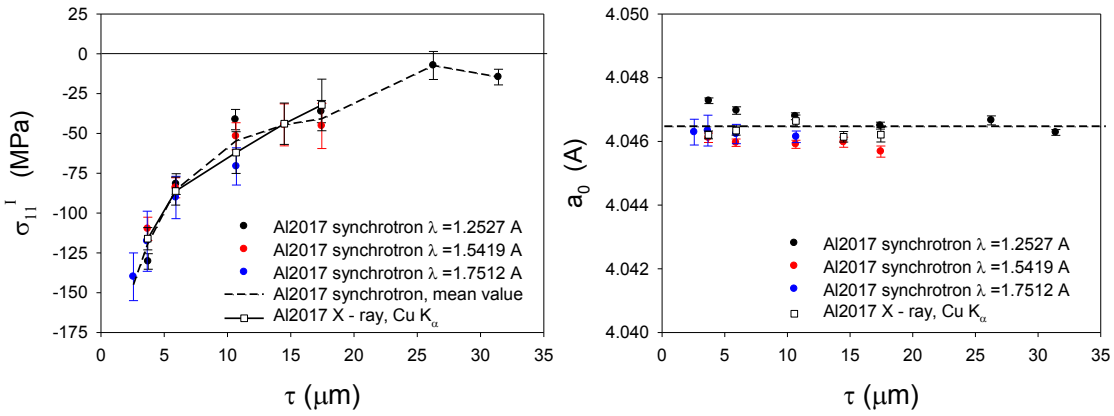

Fig. 26. Les profils en profondeur des contraintes et paramètre de maille sans contraintes a_0 pour l'échantillon Al2017 poli. Les résultats pour les différentes longueurs d'onde du rayonnement synchrotron et pour laboratoire diffractomètre sont présentés.

L'accord entre les résultats obtenus avec les différentes longueurs d'ondes permet de développer la méthode MGIXD. L'idée était de recueillir $\langle a(\phi,\psi)\rangle_{\{hkl\}}$ les valeurs correspondant à la même profondeur de pénétration τ sur la même tracé en $\sin^2\psi$. L'avantage de cette approche est que chaque point correspondant à une profondeur soit obtenu non seulement avec différentes réflexions hkl correspondant à différents angles d'incidence (multi-réflexion), mais aussi avec différentes longueurs d'ondes (multi-longueur d'onde). Ayant les valeurs moyennes des contraintes en fonction de la profondeur de pénétration, la variation de la contrainte en fonction de z – 'la vraie profondeur' peut être calculée en utilisant la transformée de Laplace inverse appliquée à la fonction polynomiale. Il a été constaté que les solutions ($\sigma_{11}^{I}(z)$) sont similaires pour des polynômes de 2ème et 3ème degré (Fig. 27).

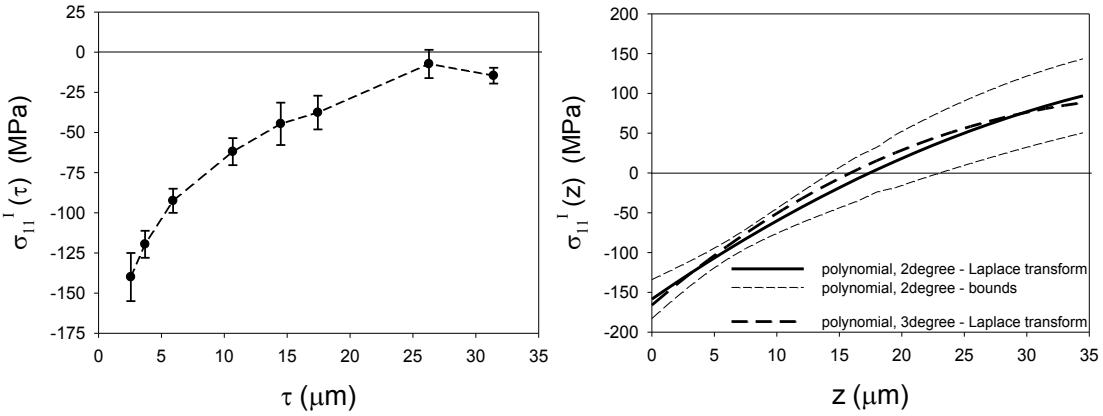

Fig. 27. Le profil de contrainte pour l'échantillon Al2017 poli pour tous les points expérimentaux obtenus pour trois longueurs d'onde différentes en fonction de τ - profondeur (a) et z pénétration - une réelle profondeur dans l'échantillon (b). Les limites d'incertitude sont données pour polynôme de degré 2.

Dans le but de révéler si le gradient de contrainte déterminé explique l'asymétrie des pics de diffraction obtenus en utilisant le rayonnement synchrotron, l'analyse inverse a été réalisée, c'est à dire, en supposant que la distribution des contraintes est déterminée, et les résultats expérimentaux ont été simulés. On peut en conclure que l'analyse inverse (intégration de la contrainte $\sigma_{11}^{I}(z)$ avec le poids de l'intensité) a permis de déterminer la

profondeur à partir de laquelle les contraintes influent sur les résultats de la diffraction, c'est à dire, pour laquelle, la contrainte $\sigma_{11}^{I}(z)$ été déterminée. En outre, l'analyse inverse appliquée pour les profils des pics a confirmé la répartition des contraintes données par $\sigma_{11}^{I}(z)$.

Le deuxième échantillon étudié a été un échantillon poli en alliage Ti6Al4V, présentant une forte asymétrie de pic de diffraction (Fig. 28).

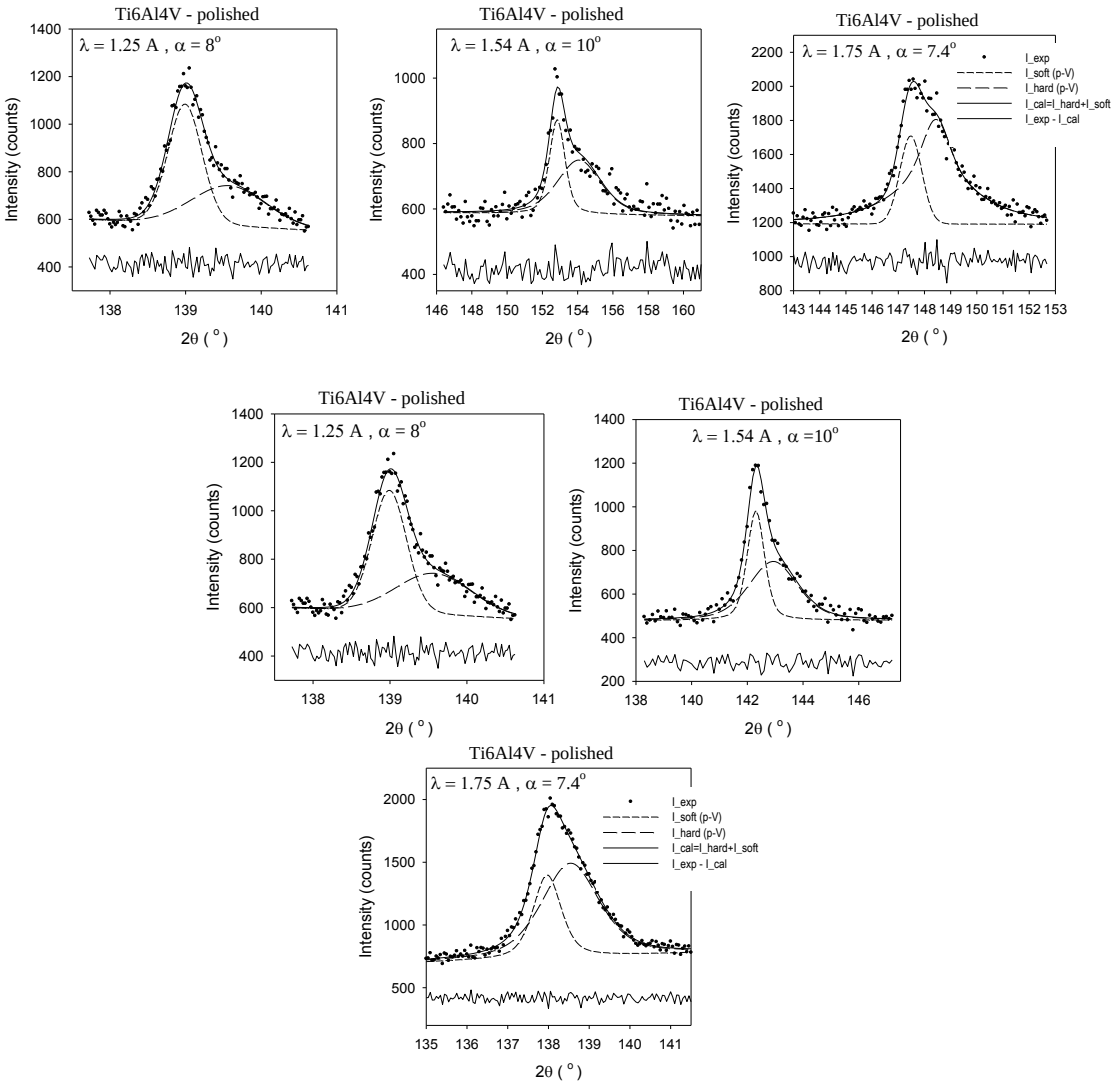

Fig. 28. Les profils exemple des pics pour plus moins les mêmes incidents angle α mais pour différentes longueurs d'onde et des profondeurs de pénétration. Deux fonctions pseudo-Voigt ont été ajustées aux données expérimentales.

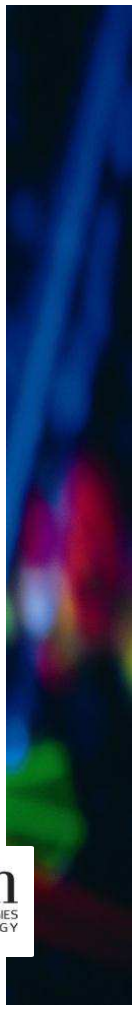

Cela suggère que deux régions irradiées de l'échantillon ont deux microstructures différentes, par exemple une couche de l'ordre de 0.5 à 1 µm, qui a été sévèrement déformée plastiquement (région de forte densité de dislocations) et, sous cette couche, le matériau de base ayant une densité de dislocations beaucoup plus faible (petite déformation plastique). Les pics de diffraction peuvent être aisément séparés en deux fonctions pseudo-Voigt ayant des positions et des largeurs intégrales différentes. Le profil en profondeur des contraintes est similaire pour les trois longueurs d'ondes différentes utilisées dans l'expérience. En outre, les résultats obtenus à partir de mesures au synchrotron ne sont pas loin de ceux obtenus sur diffractomètre classique (Fig. 29).

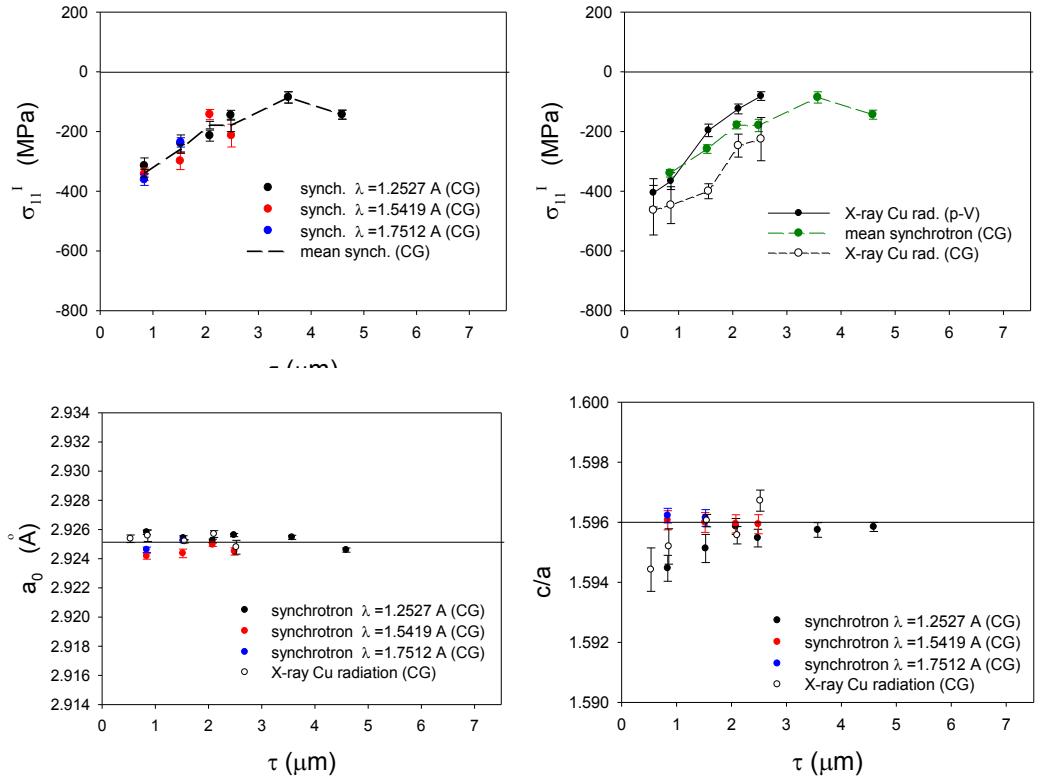

Fig. 29. Les profils en profondeur des contraintes, a_0 et c/a paramètres, pour l'échantillon Ti6Al4V. Comparaison pour trois longueurs d'onde différentes (synchrotron) et laboratoire diffractomètre en utilisant le réglage pseudo-Voigt (PV) et le centre de gravité (CG) pour déterminer la position du pic.

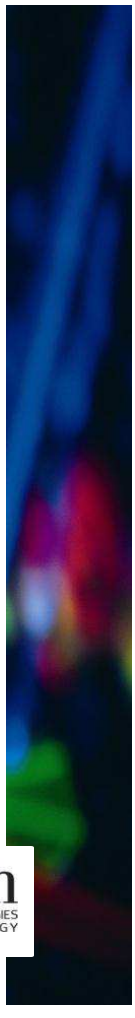

Sur la base de la loi d'atténuation exponentielle, il est possible de trouver l'épaisseur de la couche à partir des intensités relatives des pics de diffraction. Après l'estimation de l'épaisseur de couche (t = 1.38 µm), il est possible de présenter les résultats des mesures de rayonnement synchrotron en fonction de la profondeur de l'information estimée. De fortes contraintes de compression sont présentes dans la couche dont l'épaisseur atteint 1.38 µm, au-delà de 1.38 µm une légère augmentation de la contrainte de traction a été trouvée. Une autre approche dans laquelle les contraintes changent peu à peu a pu se faire, en utilisant la transformation de Laplace inverse. L'hypothèse de cette approche est que l'évolution des contraintes peut être approchée par un polynôme. Un accord quantitatif de ces deux méthodes a été noté, c'est à dire, une contrainte de compression à proximité de la surface, et une contrainte nulle à la même profondeur (2-3 µm) et une contrainte de traction dans le matériau de base ont été obtenues par ces deux approches. Aussi, les valeurs de contraintes ne sont pas très différentes.

L'analyse Wiliamson-Hall a été appliquée pour les données collectées, permettant de déterminer la moyenne quadratique des déformations $\sqrt{<\varepsilon^2>}$ et la taille des domaines cohérents D. Il a été constaté que l'incertitude sur D est trop grande pour obtenir des résultats raisonnables lorsque la géométrie parallèle est utilisée dans la méthode MGIXD. Les valeurs de $\sqrt{<\varepsilon^2>}$ mesurées en utilisant le rayonnement synchrotron et la radiation Cu K_α présentent une très bonne corrélation. Il convient de préciser que dans le cas de gradient de contrainte, la valeur $\sqrt{<\varepsilon^2>}$ est influencée par les contraintes d'ordre III mais aussi par l'hétérogénéité des contraintes dans le volume mesuré.

Ensuite, la méthode de multireflection a été appliquée avec la technique de dispersion d'énergie dans laquelle le faisceau blanc contenant un rayonnement ayant différentes longueurs d'ondes a été utilisé (λ (Å) : 0.3 à 0.18 / E (keV) : 40-68). L'analyse des contraintes a été réalisée en utilisant trois méthodes différentes : la méthode des $\sin^2\psi$ standard, la méthode de tracé universel basée sur l'analyse en multireflection. Pour des profondeurs de pénétration de l'ordre de 0-15 µm, les résultats montrent une convergence des

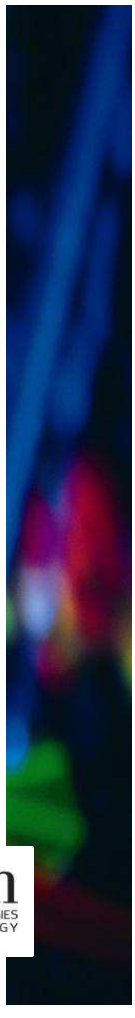

valeurs obtenues à partir de différentes méthodes dans les petites profondeurs (Fig. 30). En outre, les données du synchrotron sont en parfait accord avec les résultats obtenus sur le diffractomètre du laboratoire (radiation Cu K_α) près de la surface. Les résultats obtenus pour des profondeurs supérieures à 14 µm, les points expérimentaux montrent une dispersion importante et ne sont pas en accord avec les résultats de la méthode standard (Fig. 30).

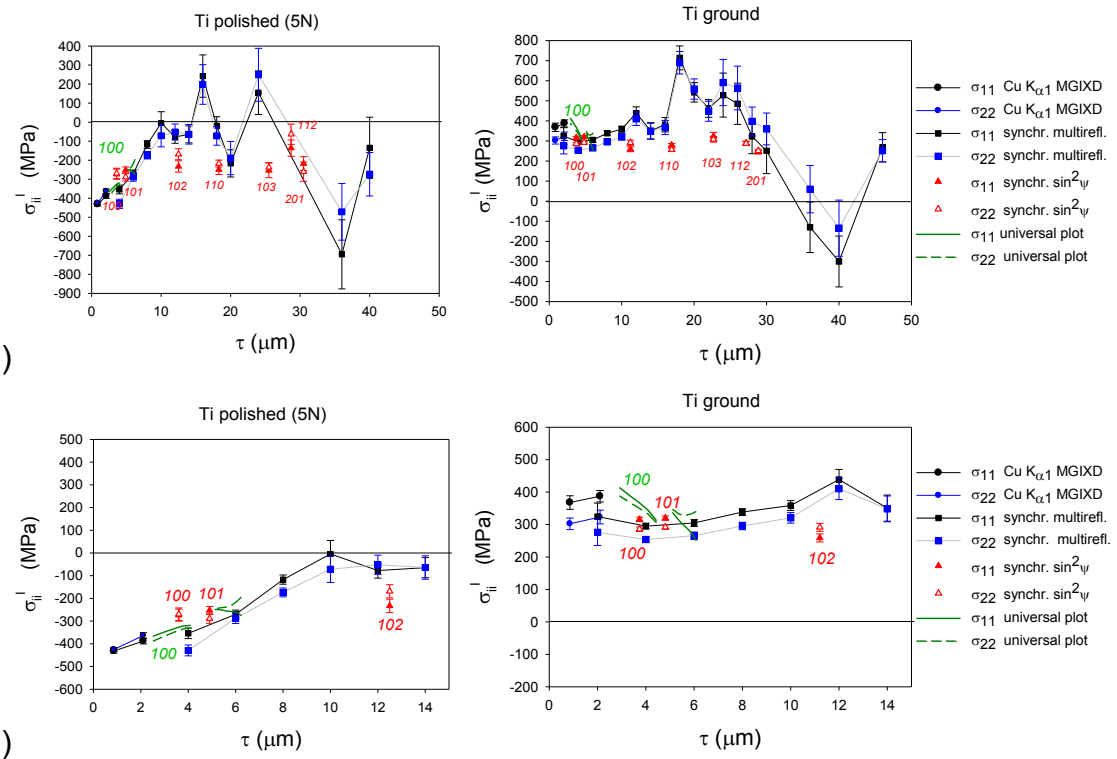

a)

b)

Fig. 30. Le profil en profondeur des contraintes pour poli et réctifié Ti (grade 2) échantillon. La comparaison des résultats de diffractomètre classique (MGIXD) et expérience de EDDI synchrotron, dont trois méthodes d'analyse différentes ont été utilisées ($\sin^2\psi$ standard, multireflection, 'universel plot'). Deux gammes différentes de la profondeur de pénétration sont comparées : a) de 0 à 50 um, et b) de 0 à 15 um.

Conclusion.

Pour conclure, on peut dire que la méthode MGIXD est un outil indispensable pour étudier la distribution des contraintes dans les couches de surface, mais l'application de cette méthode est limitée par des facteurs tels que la correction de réfraction ou le problème d'interprétation associée à l'anisotropie des

constantes élastiques. Sur la base des résultats considérés, si la méthode MGIXD est utilisée, il est conseillé d'effectuer l'analyse des contraintes avec et sans correction de la réfraction et lorsque la différence est significative les résultats devrait être rejetés ou acceptés à une grande incertitude. Il s'agit d' une des limitations de la méthode MGIXD qui est importante pour les petits angles d'incidence α . Qui plus est, l'attention particulière doit être accordée à un réglage précis du diffractomètre (configuration de faisceau parallèle) et la 2θ - position zéro doit être soigneusement vérifiée. Il faut également souligner que la fiabilité de l'analyse des contraintes de diffraction n'est possible que si le modèle d'interaction de grain approprié est appliqué dans le calcul des XSF pour l'échantillon anisotrope. Sur la base des résultats présentés dans cette thèse, il semble que le modèle de surface libre est celui qui reflète non seulement de manière correcte l'anisotropie de XSF, mais a aussi une explication physique concernant l'interaction élastique des grains .

Mots clés : contraintes résiduelles, diffraction des rayons X, méthode de l'incidence rasante, miroir Göbel

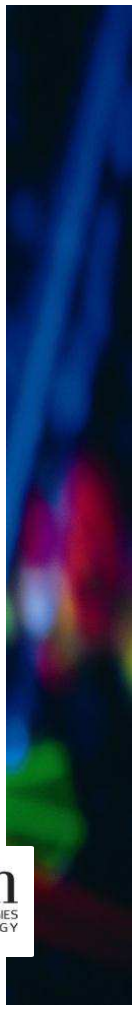

Références :

1. Hauk V., *Structural and Residual Stress Analysis by Nondestructive Methods*, Elsevier, Amsterdam, 1997.
2. Reimers W., Pyzalla A.R., Schreyer A., Clemens H., *Neutrons and Synchrotron Radiation in Engineering Materials Science*, WILEY-VCH Verlag GmbH & Co. KGaA, Weinheim, 2008.
3. Noyan I.C., Cohen J.B., *Residual Stress. Measurement by Diffraction and Interpretation*, New York, 1987.
4. Press W.H., Teukolsky S.A., Vetterling W.T. Flannery B.P., *Numerical Recipes in C: The Art of Scientific Computing*, Second Edition, Cambridge University Press, 1992.
5. Skrzypek S.J., Baczmański A., Ratuszek W., Kusior E., *New approach to stress analysis based on a grazing-incidence X-ray diffraction*, J. Appl. Cryst., vol.34, p.427, 2001.
6. Marciszko M., Stanisławczyk A., Baczmanski A., Wierzbanowski K., Seiler W., Braham C., Wróbel M., Szaraniec B., *In-depth distribution of stresses measured by multireflection grazing incidence diffraction*, Materials Science Forum – accepted for publication.
7. Marciszko M., *Multireflection grazing incidence method for residual stress determination*, Proceedings of ISD Workshops, AGH University of Science and Technology, Kraków, 2013.
8. Marciszko M., Baczmański A., Wróbel M., Seiler W., Braham C., Donges J., Śniechowski M., Wierzbanowski K., *Multireflection grazing incidence diffraction used for stress measurements in surface layers*, Thin Solid Films, vol. 530 p. 81–84, 2013.
9. Baczmański A., *Stress fields in polycrystalline materials studied using diffraction and self-consistent modeling*, AGH, Kraków, 2005.
10. Genzel Ch., *X-ray residual stress analysis in thin films under grazing incidence – basic aspects and applications*, Mat. Scienc. Tech., vol. 21, p. 10, 2005.
11. Hart M., Bellotto M., Lim G.S., *The refractive index correction in powder diffraction.*, Acta Cryst., vol. A44m, p.193, 1988.
12. Welzel U., Ligot J., Lamparter P., Vermeulen A.C., Mottemeijer E.J., *Stress analysis of polycrystalline thin film and surface regions by X-ray diffraction*, J. Appl. Cryst., vol.38, p. 1, 2005.

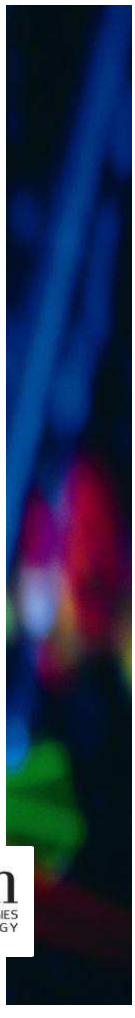

Diffraction study of mechanical properties and residual stresses resulting from surface processing of polycrystalline materials

ABSTRACT : Methodology of stress measurements with multireflection grazing incidence method (MGIXD) was investigated and developed. The parallel beam geometry was applied. The incident beam in classical diffractometers was collimated by Göbel mirror and the tests of parallel configuration were performed for Al powder. Results confirmed that both statistical error and the misalignment error can be reduced when the Göbel mirror is used. Physical factors were taken into account in XSA (X-ray stress analysis): Lorentz-polarization and absorption factor (LPA) and also refraction correction (RC). Results showed that the influence of LPA correction is minor in XSA but the RC can significantly influence analysis. In the thesis the issue of RC was considered and compared with approaches presented in the literature. In the thesis two theoretical developments of the MGIXD method were presented: the procedure of c/a parameter determination and the influence of stacking faults on the results was taken into account. It was shown that both developments significantly improves the quality of experimental data analysis. In the present work the problem of X-ray stress factors (XSF) used for the interpretation of XSA results was studied. Different theoretical grain elasto-plastic interaction models were considered and applied in XSA. Verification of the XSF was during tensile test for austenitic stainless steel and for the isotropic sample. Anisotropy of XSF was also observed in: ground Ni alloy, polished austenitic stainless steel and CrN coating. The results shows that Reuss and free surface grain interaction models are in the best agreement with the experimental results. Finally the MGIXD method was verified using synchrotron radiation and 3 different wavelengths. The methodology was developed to treat data not only for different incident angles but also using simultaneously different wavelengths. Stresses vs. z – 'real depth' was calculated using the inverse Laplace transform applied to polynomial function. Wiliamson-Hall analysis was applied for collected data. Next multireflection method was applied for the energy dispersion diffraction measurements in which white beam containing radiation having different wavelengths was used (λ (Å): 0.3–0.18/ E (keV): 40-68). The stress analysis was performed using three different methods: standard $sin^2\psi$ method, Universal plot method and by using multireflection analysis. In the range of penetration depth to 0-15 μm the convergence of the results obtained from different methods was gained. Moreover the synchrotron data perfectly agree with the results obtained on laboratory diffractometer (Cu K_α radiation) close to the surface. For depth larger than 14 μm the experimental points exhibit significant spread and do not agree with the results of standard method .
Keywords : residual stresses, X-ray diffraction, grazing incidence method, Göbel mirror.

Etude par diffraction des propriétés mécaniques et des contraintes résiduelles résultant de la transformation de matériaux polycristallins

RESUME : Méthodologie de mesures de contraintes avec la méthode multireflection pâturage d'incidence (MGIXD) a été étudié et développé. La géométrie du faisceau parallèle a été appliquée pour mensurations de stress. Le faisceau incident dans diffractomètres classiques a été collimaté par le miroir Göbel et les essais de configuration en parallèle ont été effectuées pour Al poudre. Les résultats confirmé que le erreur statistique et l'erreur d'alignement peuvent être réduits lorsque le miroir Göbel est utilisé. Facteurs physiques ont été prises en compte dans la CSX (analyse aux rayons X du stress): Lorentz - polarisation et facteur d'absorption (LPA) et aussi correction de la réfraction (RC). Les résultats montrent que l'influence de LPA est mineur dans CSX, mais la RC peut influencer de manière significative l'analyse. Dans la thèse de la question de RC a été examiné et comparé avec les approches présentées dans la littérature. Dans la thèse de deux développements théoriques de la méthode MGIXD ont été présentés: la procédure de détermination de paramètre c/a et l'influence des défauts d'empilement sur les résultats. Il a été montré que les deux développements améliore de manière significative la qualité de l'analyse des données expérimentales. Dans le présent travail le problème de la X -ray facteurs de stress (XSF) utilisés pour l'interprétation des résultats CSX a été étudiée. Différents modèles théoriques de grains élasto-plastique interaction ont été envisagées et appliquées dans la CSX. Vérification de la XSF durant l'essai de traction pour l'échantillon élastique anisotrope (en acier inoxydable austénitique) et pour l'échantillon isotrope (Ti - note2). Anisotropie de XSF a également été observée dans: rectifié alliage Ni, acier inoxydable austénitique poli et revêtement CrN. Les résultats montre que Reuss et modèle de la surface libre sont en meilleur accord avec les résultats expérimentaux. Enfin, la méthode MGIXD a été vérifiée en utilisant le rayonnement synchrotron et 3 longueurs d'onde différentes. La méthodologie a été développée pour traiter les données non seulement pour les différents angles d'incidence, mais aussi en utilisant différentes longueurs d'onde simultanément. Contraintes en fonction de «vraie profondeur» a été calculée en utilisant la transformée de Laplace inverse. Analyse Wiliamson-Hall a été appliquée pour les données. Méthode MGIXD a été appliqué pour les mesures de diffraction de dispersion d'énergie dans lequel le faisceau blanc a été utilisé: 0,3 à 0,18 Å. L' analyse des contraintes a été effectuée en utilisant trois méthodes différentes : la méthode de sin2ψ norme, la méthode de terrain universelle et en utilisant multireflection analyse . Dans la gamme de profondeur de pénétration à 0-15 um de la convergence des résultats obtenus à partir de différentes méthodes a été acquise . En outre, les données de synchrotron parfaitement en accord avec les résultats obtenus en laboratoire sur diffractomètre (rayonnement Cu Ka) à proximité de la surface . Pour profondeur supérieure à 14 um points expérimentaux présentent des variations importantes et ne sont pas d'accord avec les résultats de la méthode standard.
Mots clés : contraintes résiduelles, diffraction des rayons X, méthode de l'incidence rasante, miroir Göbel

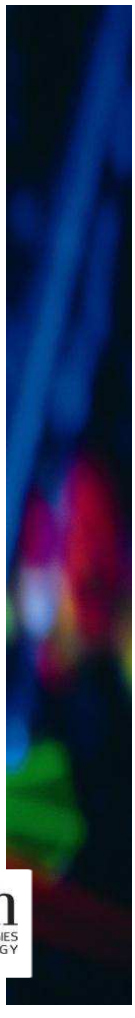

ARTS ET MÉTIERS ParisTech

ParisTech INSTITUT DES SCIENCES ET TECHNOLOGIES PARIS INSTITUTE OF TECHNOLOGY